GFZ Helmholtz Centre Potsdam

Freie Universität Berlin

Crustal structures in southern Madagascar and Sri Lanka in the context of Gondwana's assembly and break-up

A study based on surface wave dispersion and receiver functions

Jennifer Dreiling

Dissertation zur Erlangung
des Doktorgrades Dr. rer. nat.

Fachbereich Geowissenschaften
Freie Universität Berlin
November 2019

Thesis	Crustal structures in southern Madagascar and Sri Lanka in the context of Gondwana's assembly and break-up A study based on surface wave dispersion and receiver functions
submitted by	Jennifer Dreiling
in	November 2019
1st supervisor	Prof. Dr. Frederik Tilmann
2nd supervisor	Dr. Xiaohui Yuan
Date of Disputation	February 6, 2020
PhD committee	Prof. Dr. Frederik Tilmann (FU Berlin, GFZ Potsdam) Prof. Dr. Georg Rümpker (Goethe Universität Frankfurt) Prof. Dr. Serge A. Shapiro (FU Berlin) Jun. Prof. Dr. Eline Le Breton (FU Berlin) Dr. Xiaohui Yuan (GFZ Potsdam)

Thanks for your support!

I especially acknowledge my supervisor Frederik Tilmann for supporting me throughout the time of my studies. Thanks for the many constructive discussions and path-leading conversations that improved my scientific understanding, opened a different perspective to regard things, and taught me confidence in my academic work. Thanks for believing in me, and for considering me in the first place to join the seismology section at GFZ as PhD candidate. Also, for giving me the opportunity to participate in fieldwork campaigns in Sri Lanka, Italy and Austria, and to attend several conferences, such as EGU and AGU meetings.

Many thanks to Xiaohui Yuan for the lively discussions about scientific and non-scientific matters, and for copious comments on the manuscripts to our published articles. I thank Judith Bott for sharing her knowledge and experience to work related themes, for strategy advice, and also for the nice chats and inspirations.

My gratitude to Jörg Giese for taking the time to explain me the geologic processes that shaped Madagascar and for patiently answering all my excursive questions. Thanks to Robert Trumbull for his interest in our Sri Lanka study and for the vivid discussions about geologic interrelationships.

Cordial thanks to Elisa Rindraharisaona for being a good friend. I enjoyed our conversions sharing thoughts about work and life; they sometimes made my day.

Appreciation to Christian Haberland for his dedication, for organizing and managing the fieldwork campaigns in Sri Lanka and making it possible for me to participate. Also thanks to Mahinda Seneviratne for fieldwork related organization on site, and giving me an insight into Sri Lankan culture and history.

I am very grateful to my family and friends, especially my parents Josef and Beate, my sisters Michelle and Nadine, my niece Kiara and my soulmate Marius for mental support, distraction in stressful times, and for being as wonderful as they are. I especially want to thank Marius for his support in the final stage of my PhD.

Many thanks to my colleagues at GFZ for scientific exchange, and for chats and company during work breaks and section festivities.

Also thanks to Georg Rümpker, Serge Shapiro and Eline Le Breton for their interest in my research and being part of my PhD committee.

Last but not least, acknowledgements to the Geophysical Instrument Pool Potsdam for supplying seismological equipment for the field deployment, the GEOFON data center for hosting the project data, also to all fieldwork participants from the Institute and Observatory of Geophysics Antananarivo of Madagascar, the University of Frankfurt and the GFZ. Many thanks to the Geological Survey and Mines Bureau of Sri Lanka, who made it possible to deploy a temporary seismic network in Sri Lanka, and their employees for their local support and engagement during the fieldwork.

Abstract

Madagascar and Sri Lanka are key regions to understand the amalgamation and break-up of Gondwana; both islands were located centrally in the supercontinent and in the Pan-African Orogen. We determined crustal radial seismic anisotropy in southern Madagascar and the crustal velocity structure in Sri Lanka and compared our findings to those derived in other studies of Pan-African regions. We found major similarities, supporting the hypothesis that these once juxtaposed regions experienced major crustal unification through orogenetic processes.

We determined radial anisotropy (RA) in the crust of southern Madagascar from the differences between the speeds of vertically and horizontally polarized shear waves (V_{SV} and V_{SH}). The latter we derived from Rayleigh and Love surface wave dispersion determined from seismic ambient noise cross-correlations. The amalgamated Precambrian units in the east and the Phanerozoic Morondava basin in the west of southern Madagascar were shaped by different geodynamic processes: The crystalline basement was strongly deformed and metamorphosed to varying degrees during the assembly of Gondwana and the Pan-African Orogeny, whereas the Morondava basin was formed during the separation of Africa and Madagascar. The different developments are reflected in first order differences in the radial anisotropy structure.

In the Precambrian domains, positive RA ($V_{SV}<V_{SH}$) is found in the upper and lower crust, with a layer of negative RA ($V_{SV}>V_{SH}$) in between. The upper crustal anisotropy may reflect shallowly dipping layering within the Archean units and adjacent imbricated nappe stacks, whereas the lower crustal anisotropy likely represents fossilized crustal flow during the syn- or post-orogenic collapse of the Pan-African Orogen. The layer of negative RA may have preserved vertically oriented large shear zones of late Pan-African age. Within the Morondava basin, negative RA in the uppermost ~ 5 km could have been generated by steep normal faults, jointing, and magmatic dike intrusions. The deeper sediments and underlying crustal basement are characterized by positive RA. This is consistent with horizontal bedding in the sediments and with the alignment of fabrics in the basement created by extension during the basin formation.

The crust of Sri Lanka mostly consists of Precambrian rocks. We analyzed newly derived data from a temporary seismic network deployed in 2016–2017. Rayleigh wave phase dispersion from ambient noise cross-correlation and receiver functions were jointly inverted for the seismic structure using a transdimensional Bayesian approach.

We determined Moho interface depths between 30–40 km, with the thickest crust (38–40 km) beneath the central Highland Complex (HC). The thinnest crust (30–35 km) is along the west coast, which experienced crustal thinning through the formation of the Mannar basin. The majority of V_P/V_S ratios are within a range of 1.66–1.73 and predominantly favor a felsic bulk crustal composition with intermediate to high silica content. A major intra-crustal (18–27 km), westward dipping ($\sim$4.3°) interface with high V_S ($\sim$4 km/s) underneath is prominent in the central HC, continuing into the eastern Vijayan Complex (VC). The dipping discontinuity and

a low velocity zone in the upper crust of the central HC can be related to the HC/VC contact zone. They are also in agreement with the well-established amalgamation theory of Sri Lanka, described by a stepwise collision of the arc fragments during Gondwana's assembly, and deep crustal thrusting processes and a transpressional regime along the suture between HC and VC.

We found striking similarities of seismic properties between southern Madagascar and Sri Lanka, and southern India and East Antarctica as once juxtaposed Pan-African terranes. Their crustal thicknesses range between 35–40 km in regions with little to no influence of post-orogenic processes such as rifting or younger orogeny. Pan-African crust of all comparison studies agree to average crustal V_P/V_S ratios on the lower side (1.65–1.78), indicating felsic to intermediate bulk crustal compositions. Sri Lanka shows higher surface V_S (3.1–3.6 km/s) compared to average values in southern Madagascar (3.2–3.4 km/s) and southern India (3.2 km/s), which might be due to different burial depths and metamorphic grade of surface rocks during the Pan-African Orogeny, or different petrological compositions. A low velocity layer in the upper crust as we observe in central Sri Lanka is also present in other Pan-African terranes, and possibly was generated through retrograde metamorphic processes and fluid migration during the transpressive regime. The strong similarities of seismic crustal properties between these regions might be attributed to the region spanning unification of crustal structures through extensive common overprinting during the Pan-African Orogeny. Differences might be seen as consequence of autochtone terrane compositions, positions within the orogen, and individual reworking processes after the orogeny.

We developed a software (BayHunter), implementing a Bayesian inversion approach, to estimate a range of models that fit the data and outputs meaningful uncertainty estimations. BayHunter is a Python framework to perform a Markov chain Monte Carlo (McMC) transdimensional Bayesian inversion of surface wave dispersion and receiver functions. The algorithm follows a data-driven strategy and solves for the velocity-depth structure, the number of layers, noise scaling parameters and V_P/V_S ratio. BayHunter was developed and used for the inversion of seismic data in Sri Lanka.

Project I. Published as Dreiling et al. (2018): Dreiling, J., Tilmann, F., Yuan, X., Giese, J., Rindraharisaona, E. J., Rümpker, G., and Wysession, M. E. Crustal radial anisotropy and linkage to geodynamic processes: A study based on seismic ambient noise in southern Madagascar. Journal of Geophysical Research: Solid Earth, 2018. https://doi.org/10.1029/2017JB015273.

Project II. Submitted as Dreiling et al. (n.a.): Dreiling, J., Tilmann, F., Yuan, X., Haberland, C., and Seneviratne, S. W. M. Crustal structure of Sri Lanka derived from joint inversion of surface wave dispersion and receiver functions using a Bayesian approach. Journal of Geophysical Research: Solid Earth. Submission in 2019.

Project III. Published as Dreiling and Tilmann (2019): Dreiling, J. and Tilmann, F. BayHunter – McMC transdimensional Bayesian inversion of receiver functions and surface wave dispersion. GFZ Data Services, 2019. https://doi.org/10.5880/GFZ.2.4.2019.001. Available on GitHub: https://github.com/jenndrei/BayHunter

Kurzfassung

Madagaskar und Sri Lanka beherbergten zentrale Lokationen während der Pan-Afrikanischen Orogenese und im Superkontinent Gondwana, und sind somit Schlüsselregionen, um Details über die Amalgation und den Zerfall von Gondwana in Erfahrung zu bringen. Wir ermittelten die krustale seismische radiale Anisotropie in Südmadagaskar und die krustale seismische Struktur von Sri Lanka. Unsere Ergebnisse stellten wir in den Vergleich mit anderen Studien von Gondwana-Regionen und fanden weitreichende Ähnlichkeiten, welche die Hypothese unterstützen, dass die einst eng-benachbarten Regionen eine großskalige krustale Vereinheitlichung durch die Pan-Afrikanische Orogenese erfahren haben.

Wir bestimmten die radiale Anisotropie (RA) in der Kruste Südmadagaskars, basierend auf den Geschwindigkeitsunterschieden zwischen vertikal und horizontal polarisierten Scherwellen (V_{SV} and V_{SH}). Dazu invertierten wir Dispersionsgeschwindigkeiten der Rayleigh- und Love-Oberflächenwellen, welche wir durch Kreuzkorrelation seismischen Hintergrundrauschens ermittelten. Die akkretierten präkambrischen Einheiten im Osten und das phanerozoische Morondava Becken im Westen von Südmadagaskar wurden durch verschiedene geodynamische Prozesse geprägt: Das kristalline Grundgebirge wurde während des Zusammenschlusses von Gondwana in der Pan-Afrikanischen Orogenese stark deformiert und zu verschiedenen Graden metamorphisiert. Dahingegen waren Beckenbildungsprozesse (Sedimentation) im Morondava Becken erst mit der Separation von Afrika und Madagaskar abgeschlossen. Die unterschiedlichen geologischen Entwicklungen spiegeln sich erster Ordnung in der radialen Anisotropie-Struktur wieder.

Wir fanden in der oberen und unteren Kruste der präkambrischen Einheiten positive RA ($V_{SV}<V_{SH}$), mit zwischengelagerter negativer RA ($V_{SV}>V_{SH}$). Die Anisotropie in der oberen Kruste könnte flach einfallende Schichtung innerhalb des archaischen Gesteins und schuppenartige Deckenstapelung reflektieren, wohingegen die unterkrustale Anisotropie Strukturen eines Gravitationskollaps aufzeigt, die während oder nach dem orogenen Kollaps des Pan-Afrikanischen Gebirges erzeugt wurden. Im Gestein mit negativer RA könnten vertikal orientierte Scherzonen Pan-Afrikanischen Alters konserviert sein. Die negative RA in den oberen ~ 5 km des Morondava Beckens könnte durch steil einfallende Abschiebungen, Klüftung und magmatische Dyke Intrusionen (Gesteinsgänge) erzeugt worden sein. Die tieferen Sedimente des Beckens und das unterliegende krustale Grundgebirge sind durch positive RA charakterisiert. Dies ist konsistent mit horizontaler Schichtung in den Sedimenten und mit horizontaler Mineralausrichtung im Grundgebirge, hervorgerufen durch Extension während des Beckenbildungsprozesses.

Um die krustale Struktur vom großteilig präkambrischen Sri Lanka abzubilden, haben wir neue Daten eines temporären seismischen Netzwerkes (FDSN: 1A, 2016–2017) analysiert. Wir invertierten Phasengeschwindigkeiten von Rayleigh-Wellen aus Kreuzkorrelationen ambienten Hintergrundrauschens gemeinsam mit Receiver Funktionen. Dazu entwickelten wir eine Inver-

sionssoftware mit Bayesianischem Ansatz.

Wir ermittelten Mohotiefen zwischen 30–40 km, mit der mächtigsten Kruste (38–40 km) unterhalb des zentralen Highland Complexes (HC). Die dünnste Kruste (30–35 km) beobachten wir entlang der Westküste, welche krustale Verdünnung mit der Bildung des Mannar Beckens erfuhr. Die Mehrheit der V_P/V_S Verhältnisse liegt zwischen 1.66–1.73 und favorisiert eine felsische Gesteinskomposition mit einem Siliziumanteil von intermediär bis hoch. Auffällig im zentralen HC is eine intra-krustale (18–27 km), westwärts einfallende ($\sim$4.3°) Grenzfläche mit unterliegend hoher V_S ($\sim$4 km/s), welche sich in den Osten des Vijayan Complexes (VC) fortsetzt. Die geneigte Diskontinuität und eine Niedriggeschwindigkeitszone im zentralen HC können in Relation zur HC/VC Kontaktzone gesetzt werden und harmonieren mit der etablierten Amalgationstheorie von Sri Lanka. Diese ist beschrieben durch eine schrittweise Kollision von Inselbogenfragmenten, tiefkrustale Aufschiebungsprozesse und transpressionales Regiment entlang der Sutur zwischen HC und VC.

Die seismischen Eigenschaften in Südmadagaskar und Sri Lanka zeigen große Ähnlichkeiten zu solchen in Südindien und der Ostantarktis als ehemals eng-benachbarte Pan-Afrikanische Terrane. Krustale Mächtigkeiten liegen zwischen 35–40 km für Regionen ohne Einfluss postorogener Prozesse wie Rifting oder jüngere Orogenese. Pan-Afrikanische Kruste aller Vergleichsstudien zeigt niedrige durchschnittliche V_P/V_S Verhältnisse (1.65–1.78), welche auf eine felsische bis intermediäre gesamtkrustale Gesteinskomposition hindeuten. Sri Lanka zeigt höhere oberflächennahe Scherwellengeschwindigkeiten (3.1–3.6 km/s), im Vergleich zu Durchschnittswerten in Südmadagaskar (3.2–3.4 km/s) und Südindien (3.2 km/s). Diese könnten von den verschiedenen Versenkungstiefen des heute exponierten Gesteins während der Pan-Afrikanischen Orogenese oder von unterschiedlichen Gesteinszusammensetzungen herrühren. Eine Niedriggeschwindigkeitszone in der oberen Kruste wie wir in Sri Lanka abgebildet haben, ist ebenso in anderen Pan-Afrikanischen Terranen vorhanden. Diese könnte durch retrograde metamorphe Prozesse und Fluidmigration während des transpressiven Regiments generiert worden sein. Die starken Ähnlichkeiten seismischer Eigenschaften der Pan-Afrikanischen Regionen weisen auf weitreichende Vereinheitlichung der krustalen seismischen Strukturen hin, die durch extensives gemeinsames Überformen während der Pan-Afrikanischen Orogenese entstanden ist. Unterschiede können als Konsequenz autochtoner Terrankompositionen und individueller Überprägungsprozesse nach der Orogenese betrachtet werden.

Wir entwickelten eine Software (BayHunter) mit Bayesianischem Inversionsansatz, um eine repräsentative Menge möglicher Modelle abzuschätzen die die seismischen Daten erklären und Fehlerabschätzungen ermöglichen. BayHunter ist ein Open-Source Python Framework und basiert auf dem Markov-chain-Monte-Carlo-Verfahren. Die transdimensionale Bayesianische Inversion von Oberflächenwellendispersion und Receiver Funktion löst nach der Geschwindigkeits-Tiefen Struktur, der Anzahl der Schichten, Rauschparametern und dem V_P/V_S Verhältnis. BayHunter wurde für die Inversion der seismischen Daten in Sri Lanka verwendet.

Table of contents

List of Figures

List of Tables

Introduction

About this thesis

Motivation

The assembly of Gondwana and its subsequent break-up were two major events that shaped the continental landscape as it is today. Gondwana was the last supercontinent, before the landmasses broke apart. The Pan-African Orogeny, associated with the final assembly of Gondwana, strongly influenced the lithospheric rock units and structures, in particular those of terranes that were centrally located within the Pan-African collision, e.g., Madagascar and Sri Lanka. Especially the crustal structure can reveal information about the assembly of the continental fragments and their collisional and post-collisional deformation. Regional seismic data are able to shed light on the crustal velocity structure, so one can identify crustal thicknesses, major discontinuities and their spatial orientation, and vertical and lateral changes of crustal material; also typical or untypical behavior of crustal units can be identified in the frame of standard models.

In this work, we used the radial seismic anisotropy to emphasize the direction of structural alignment in southern Madagascar and to identify collisional and post-collisional deformation processes. For Sri Lanka, we used new seismic data and performed a joint inversion of surface wave dispersion and receiver functions to image seismic velocities and bulk crustal properties beneath the island. We developed software, implementing a Bayesian inversion approach, to estimate meaningful uncertainties from a range of models that fit the data.

Structure of the thesis

The thesis consists of three major parts, which are framed in overarching chapters to provide introductory and conclusive information. The three projects are:

I **Crustal radial anisotropy in southern Madagascar and linkage to geodynamic processes**
based on seismic ambient noise cross-correlation

II **Crustal structure of Sri Lanka**
based on surface wave dispersion and receiver functions

III **BayHunter - Bayesian inversion software**
a Python tool for transdimensional Bayesian inversion of surface wave dispersion and receiver functions

Introduction: The three projects use seismic data, but utilize different analysis methods for different study regions. While the first two studies are regional studies and use data from seismic stations in Madagascar and Sri Lanka, the latter is a software development project, where the

algorithm was validated by synthetic data. The geophysical fundamentals and the geologic frame that are relevant for each separate study are described in the general introduction. The focus lies on the overlap of the projects. The chapter includes foundations of seismic waves, their sources and analysis applications, and the amalgamation and break-up history of Gondwana highlighting positions of Madagascar and Sri Lanka. Note that each project includes an own introductory part, where special methodological background and/ or regional geology are worked out in more detail.

I Crustal radial anisotropy in southern Madagascar: We present one of the few seismic studies on Madagascar, focusing on the radial anisotropy within the crust. Radial anisotropy measures the difference between vertically and horizontally polarized shear-wave velocity, which we derived from Rayleigh and Love surface waves. The differences in Vs are predominantly caused by mineral alignment due to different stress and strain regimes in the past and therefore allow to infer past deformation processes within southern Madagascar.

The study is illustrated in five chapters. Within the introduction (chapter I.1), we define radial seismic anisotropy and application and interpretation possibilities, and provide geologic background to the assembly of southern Madagascar. The data section (chapter I.2) introduces the seismic data and its processing towards ambient noise cross-correlation to retrieve Green's functions of Rayleigh and Love surface waves. Group and phase velocities were measured for each wave type for subsequent tomographic inversion (chapter I.3). Tomographically derived group and phase velocity dispersion curves were then jointly inverted to retrieve Vs-depth models for V_{SV} and V_{SH} (chapter I.4). Finally, radial seismic anisotropy was computed from V_{SV} and V_{SH} and is discussed in the frame of geodynamic processes that formed Madagascar (chapter I.5).

II Crustal structure of Sri Lanka: We present the first large-scale passive seismic study conducted in Sri Lanka. We reveal the crustal velocity structure by joint inversion of surface wave dispersion together with receiver functions. The crustal thickness, intra-crustal features such as low and high velocity sections, and average crustal V_P/V_S tell us about the general bulk crustal composition, lateral and vertical changes of material and the relation to major geologic units identified at the surface.

Six chapters assemble the research. The introduction (chapter II.1) provides an overview of the major geologic complexes and their amalgamation to form Sri Lanka. The data section (chapter II.2) introduces the seismic data used within the study and addresses problems that occurred during operational time influencing data quality and quantity. The data was processed towards (1) ambient noise cross-correlation and phase velocity retrieval for the Rayleigh surface waves with subsequent tomographic inversion (chapter II.3), and (2) receiver function computation from earthquake signals (chapter II.4). The tomographically derived dispersion curves and the receiver functions were jointly inverted using a Bayesian approach (part III) to derive the crustal structure beneath Sri Lanka (chapter II.5). The observations are interpreted and discussed in the frame of the Pan-African Orogeny (chapter II.6).

III BayHunter - Bayesian inversion software: BayHunter is a Markov chain Monte Carlo (McMC) transdimensional Bayesian inversion software for inversion of surface wave dispersion and receiver functions. It solves for the velocity-depth structure, the number of layers, the seismic noise level and the average crustal V_P/V_S. The algorithm samples the parameter space based on the likelihood, which measures the probability to observe the data for a given model. The models sampled in the exploration phase, i.e., the second phase of the inversion defined by the number of iterations, assemble the posterior distribution and are representative for the parameters of interest.

The software development project is described in three chapters. The introduction (chapter III.1) describes Bayes theorem and the McMC sampling method. They set the foundation for the inversion tool BayHunter (chapter III.2), which is written in the Python programming language. The code was tested with synthetic data (chapter III.3) for validation.

Conclusion and outlook: Here, we weave together projects I and II in the greater frame of Gondwana's assembly and break-up. Seismic properties derived for southern Madagascar and Sri Lanka are compared to those of other Pan-African regions, i.e., southern India and East Antarctica. A summary and outlook conclude this chapter.

Contributions and difference to the papers

Part I of this thesis is published as peer-reviewed article in JGR[1]: Solid Earth (Dreiling et al., 2018). Part II is submitted for publication in JGR: Solid Earth (Dreiling et al., n.a.). Part III is published at the GFZ Data Services as software publication (Dreiling and Tilmann, 2019). For a journal publication, many details must be dropped or are often summarized with few sentences to stay within the limit of publication units and also to present an expedient and condensed version of the research. About 20–30 % of this thesis are unpublished and offer additional analyses and explanations to help the reader to better dive into the research and to better understand and follow the contents. Additional visuals, tables and explanations are especially given in the parts about seismic data (quality control) and tomographic inversion (parameter decisions), not to mention the introductory and conclusive chapters.

As parts of the thesis are published with co-authorships, I want to clarify the contributions of the authors to my research and the paper manuscripts. I performed all aspects of the research by myself, i.e., data processing towards surface wave dispersion and receiver function computation, travel time tomography and velocity-depth inversion with different codes, interpretation of results, and conceptional planning and development of Bayesian inversion code. F.T. provided the primary supervision, i.e., gave ideas, suggestions and discussed about additional analyses and testing, analytical and interpretative improvements and reviewed the manuscripts for contentual completeness. X.Y. was involved in lively discussions, gave suggestions, and reviewed the manuscripts. J.G. helped me understanding the geologic processes that shaped Madagascar and refined the geology section of the manuscript for project I. All authors discussed the results and provided comments on the manuscript they co-authored.

[1] Journal of Geophysical Research

Methodological background

To unravel the secret of the Earth's structure, the theory of seismic wave propagation is key. Seismic waves of different types can be generated through natural or man-made sources. Body waves propagate through the Earth, get reflected, refracted and transmitted at heterogeneities and carry valuable information about seismic properties and interfaces. Surface waves travel along the Earth's shell and contain important information of the medium along the propagation path. Seismometers can record those seismic disturbances, so that seismologists are able to unlock the encrypted information about the Earth's interior by applying processing and analysis strategies based on theoretical fundamentals. The following sections introduce basic theory about the properties and dynamics of seismic waves, the sources of seismic signals, and analysis methods to enhance key parameters of the Earth's structure; the methods are (1) ambient seismic noise cross-correlation and (2) receiver function computation.

Types and properties of seismic waves

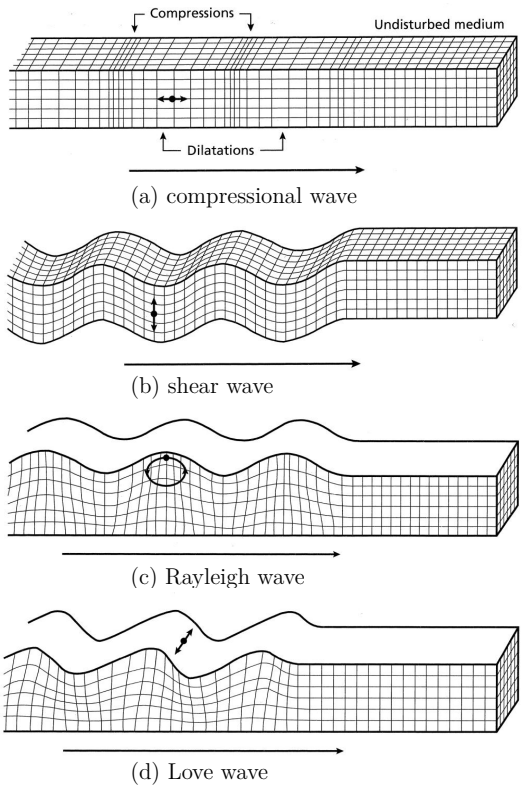

Figure 1: Particle motion of seismic body (a, b) and surface waves (c, d). Small black arrows indicate the oscillation of particles within the medium (Kearey et al., 2002).

A seismic wave can be understood as temporary elastic deformation of underground material and impulse-like propagation through the medium. The wave travels either through the medium (body wave) or at its surface (surface wave).

Figure 1 shows the two types of body waves (compressional and shear waves), and surface waves (Rayleigh and Love waves). Compressional waves (Fig. 1a) propagate by compressional and dilatational uniaxial strains in travel direction (Kearey et al., 2002), i.e., the particles oscillate back and forward parallel to the direction of wave propagation. They are also called longitudinal, primary and P-waves. Shear waves (Fig. 1b) propagate by pure shear strain, i.e., the particles oscillate transverse (perpendicular) to the direction of travel. They are also known as transverse, secondary and S-waves.

Rayleigh waves (Fig. 1c) are coupled P-SV waves and are polarized in the vertical propagation plane. They propagate along a free surface or along the boundary between two unlike solid media (Lowrie, 2007). The particle motion is elliptical and retrograde in a vertical plane, which is due to the phase shift between P and SV (Kearey et al., 2002). Love waves (Fig. 1d) are horizontally polarized shear waves (SH). Their particles move within a horizontal plane parallel to the free surface and perpendicular to the direction of wave propagation. Love waves travel by

multiple reflections between top and bottom of the low velocity layer near the surface (Kayal, 2006). If an SH ray strikes a near surface reflecting horizon at post critical angle, all the energy will be trapped within the wave guide (Lowrie, 2007).

The seismic properties of a wave include the seismic velocity, the frequency content, amplitude, attenuation and dispersion, and are related to each other. Here, we want to define the seismic velocity, considering P-wave (V_P) and S-wave velocity (V_S), and group (U) and phase velocity (c).

V_P and V_S are dependent on the elastic moduli to express longitudinal and transverse stress and strain relationship, i.e., the bulk modulus K and the shear modulus or rigidity μ, and the density ρ of the medium.

$$V_P = \left[\frac{K + \frac{4}{3}\mu}{\rho}\right]^{1/2} \qquad V_S = \left[\frac{\mu}{\rho}\right]^{1/2} \tag{1}$$

The seismic velocity of waves can be influenced by the temperature and pressure (depth), grain size and shape, texture, porosity, water content and anisotropy (micro scale), lithology, alteration zones, weathering and micro cracks among others (Altindag, 2012); those properties are summarized within the physical quantity of density, as we assume an ideal elastic and isotropic medium on the macro scale. P-waves always propagate faster than S-waves within the same medium. P-waves are able to travel through solids and fluids, as these are compressible. S-waves only exist in solids, because fluids do not support shear, and their rigidity is zero (Müller, 2007). The ratio of V_P and V_S is independent of density, and can be expressed by Poisson's ratio υ.

$$\upsilon = \frac{\lambda}{3K - \lambda} = \frac{\lambda}{2(\lambda + \mu)} \qquad \frac{V_P}{V_S} = \left[\frac{2(1-\upsilon)}{(1-2\upsilon)}\right]^{1/2} \tag{2}$$

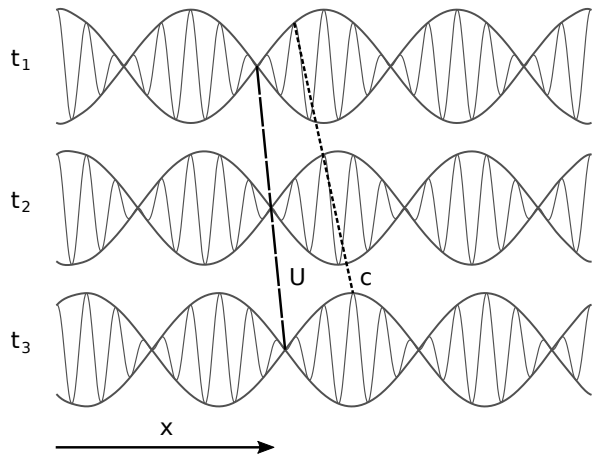

Figure 2: Conceptual image of group (U) and phase velocity (c). The phase (carrier) propagates faster than the group (envelope).

The velocity of surface waves depends on the wave's frequency (dispersion): The penetration depth of a wave is dependent on the frequency. Longer periods penetrate deeper into the Earth, and thus propagate with higher velocities. Higher frequencies (shorter periods) sample the shallower surface.

A surface wave package is represented by an amount of harmonic waves with different angular frequencies ω and wavenumbers k. The energy in the wave propagates as the envelope of the wave package with a speed called the group velocity U.

$$U(\omega) = \frac{\delta\omega}{\delta k} \tag{3}$$

The carrier, i.e., the individual waves, travel at the phase velocity c.

$$c = \frac{\omega}{k} \tag{4}$$

Therefore, the group velocity can be related to the phase velocity by:

$$U(\omega) = \frac{\delta\omega}{\delta k} = \frac{\delta ck}{\delta k} = c + k\frac{\delta c}{\delta k} = c - \lambda\frac{\delta c}{\delta\lambda} \tag{5}$$

with λ being the wavelength. If the wave is not dispersive ($\delta c/\delta\lambda = 0$) group and phase velocities are equal. For a normal dispersive wave, phase velocity increases with increasing wavelength ($\delta c/\delta\lambda > 0$) and the group velocity is slower than the phase velocity (Fig. 2). The shape of a wave package changes over time (and distance of travel) and forms a wave train, with longer wavelengths arriving first.

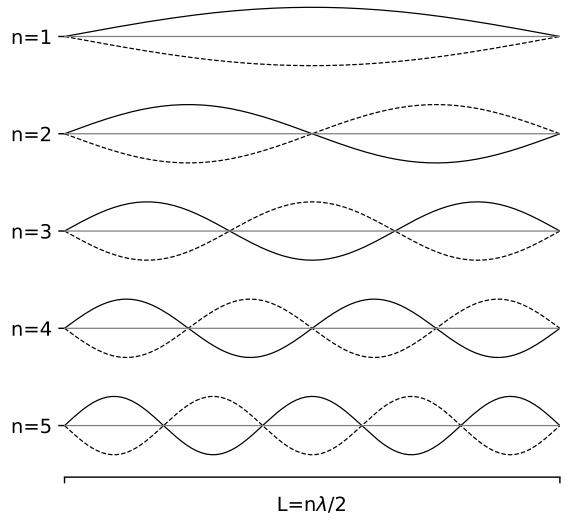

Figure 3: Normal modes of vibration of a string fixed on both ends. Solid and dashed lines indicate a phase shift of π. The fundamental mode is given by n=1 and higher modes by n >1.

Surface waves show *normal* modes of vibrations. A complicated vibration can thereby be represented by a number of superposed standing waves. The principle of modes can be illustrated by a one-dimensional excitation of a string fixed on both ends (Fig. 3). The displacement u of the string as a function of position x and time t can be described as

$$u(x,t) = \sum_{n=0}^{\infty} A_n U_n(x,\omega_n)\cos(\omega_n t) \tag{6}$$

which is the summation of standing waves or eigenfunctions $U_n(x,\omega_n)$, with weight A_n and eigenfrequency ω_n. For a homogeneous (uniform) string with length L, velocity v and zero displacement at the fixed ends of the string, follows

$$U_n(x,\omega_n) = \sin(n\pi x/L) = \sin(\omega_n x/v) \tag{7}$$

The eigenfrequencies are

$$\omega_n = n\pi v/L \tag{8}$$

$$\text{with} \qquad L = n\lambda/2 \tag{9}$$

Each spatial eigenfunction has an integral number of half wavelengths along the string; the string can only vibrate in these discrete modes. The fundamental mode is represented by $n = 1$, the overtones or higher modes (first, second, etc.) are given by $n > 1$.

Sources of seismic waves

Seismic sources can be subdivided into natural and man-made sources. Natural events include tectonic earthquakes, volcanic tremors, rock falls, collapse of cavities, storms, and microseism. Man-made sources include controlled explosions and vibrator activity, reservoir, mining and injection induced seismicity and cultural noise through heavy machinery, industry and traffic (Bormann et al., 2013b).

The signal used for seismic analysis is differently defined dependent on the analysis method and is retrieved from different seismic wave types from different seismic sources. Receiver functions are based on earthquake signals and body waves, and all three components (Z, N, E) of a seismogram are necessary for data processing and RF computation. For dispersion velocity analyses, surface wave signals can be derived from earthquakes, but also from cross-correlation of seismic ambient noise. Dependent on the type of surface wave used for the analysis, all components or only the vertical component must be available for data processing.

Earthquakes. An earthquake occurs, if stress (e.g., along plate boundaries) exceeds the strength of the material and the energy bottled as strain is released. The duration and amount of the stress and the strength of the material influence the magnitude of the event, which together with the focal mechanism are the most prominent characteristics that control the waveform and the initial amplitude of the seismic disturbance. The seismic energy propagates from the source as P- and S-waves through the Earth and as Rayleigh and Love waves along the surface, and may be recorded at the surface by a seismometer. In particular body waves experience reflection, refraction, transmission, and conversion at interfaces along their paths through the sub-surface

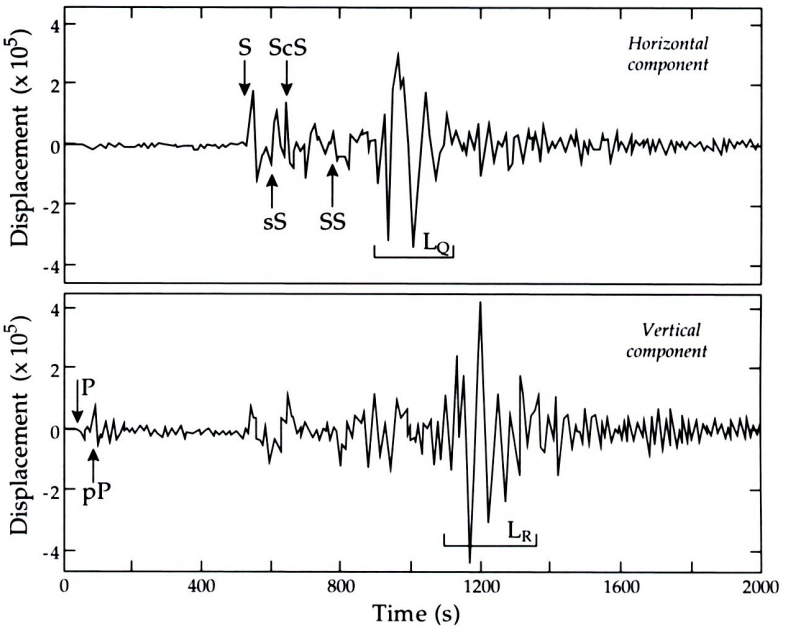

Figure 4: Broadband seismograms of an earthquake beneath Peru recorded at Harvard, Massachusetts. Shown are horizontal-component seismogram with clear SH phases (S, sS, ScS, SS, L_Q), and vertical-component seismogram with P, pP, SV and L_R arrivals (Lowrie, 2007).

and corresponding phases can be identified in a seismogram (Fig. 4), and are named after a nomenclature (see Bormann et al., 2013a), describing the path of travel through the Earth.

The broadband recordings (Fig. 4) show horizontal and vertical displacements caused by a deep event beneath Peru (May 24, 1991). The seismic body waves emitted by the earthquake traveled through deep regions of the mantle, hence several phases could be recorded. The horizontal-component seismometer can register P-, SH-, Rayleigh and Love waves. However, the amplitudes on a seismogram are affected by the instrument axis orientation to the wave path, the distance to the source and its focal mechanism, and the structure the waves traversed among others (Lowrie, 2007). For this event, the horizontal-component seismometer was oriented almost transverse to the ray path, so the P-wave arrival is barely perceptible on the record (Fig. 4, top). The first strong signal on the horizontal record is the direct S-wave, closely followed by numerous of other SH body wave phases (sS, ScS, SS) and the large-amplitude Love surface waves (L_Q). As the vertical-component seismometer has maximum sensitivity to vertical motions, P-, SV- and Rayleigh surface waves could be registered. The first phases on the vertical-component seismogram coincide to the P-wave arrivals (P, pP), followed by SV body wave arrivals and the Rayleigh surface-wave train (L_R). Dispersion for the surface waves is clearly identifiable by wave separation and period change along the wave train.

Seismic ambient noise. Sources of seismic waves related to background vibrations include natural and man-made sources and can produce cyclic and random noise. Seismic sources (borrowed from Bormann and Wielandt, 2013) include:

- ambient vibrations from natural sources (e.g., ocean microseisms, wind)
- man-made vibrations / cultural noise (e.g., from industry, traffic)
- secondary signals from wave propagation in inhomogeneous media (scattering)
- effects of gravity (e.g., Newtonian attraction of moving air masses in local atmosphere)
- signals from seismometer's sensitivity to ambient conditions (e.g., temperature)
- signals from technical imperfections or deterioration of sensor (e.g., corrosion, leakage currents, defective semiconductors)
- intrinsic self-noise of the seismometer (e.g., electronic and quantization noise)

Seismic noise proper ties to only ambient vibrations from natural sources; however, the mixing of those with noise amplitudes from man-made and instrument sources on a record is inevitable. Although earthquakes are natural sources of seismic waves, they often fall into a different category, as they are low-probability occurrences, determinable and isolatable, and can show amplitudes much higher than those of typical background vibrations. The frequency content of seismic disturbances differ from source to source. A summary (based on Peterson, 1993; Sleeman, 2006) is given below. Dominant noise sources are starred.

Short period seismic noise (>1 Hz, <1 s)

- local random noise (cultural noise) propagating mainly as surface waves (>1–10 Hz)*
- natural microseism at island and coastal sites show broader bandwidth (dominantly >1 Hz)
- local atmospheric turbulences (>1 Hz)

Long(er) period seismic noise (<1 Hz, >1 s)

- ocean microseisms (1–20 s, peaks at 5 and 18 s)*
- interaction of ocean waves with the ocean floor, e.g., storms at oceans generating swell- and surf-induced pressure fluctuations at the ocean bottom ($30 \cdot 10^{-3}$–1 Hz, 1–33 s)
- Rayleigh waves circling around the globe (7–$30{\cdot}10^{-3}$ Hz, 33–140 s)
- instrumental noise levels of seismic sensors (near and >2–$7{\cdot}10^{-3}$ Hz, 140–500 s)
- fundamental spheroidal Earth modes (2–$7{\cdot}10^{-3}$ Hz, 140–500 s)
- Earth tides, i.e., Earth rotation relative to the Moon (>12 h, peaks at 12 and 24 h)*
- Newtonian attraction of atmosphere (10^{-6}–10^{-3} Hz, 0.27–277 h)

Seismic analysis methods

Here, we want to introduce two analysis methods, which are (1) receiver functions to enhance the interface structure beneath a receiver, and (2) seismic ambient noise cross-correlation to isolate surface wave signals and retrieve absolute velocity information from dispersion analyses.

Receiver functions. When a seismic disturbance hits an impedance contrast in the medium (interface), it gets partially reflected, refracted and transmitted. A special case of the latter is the conversion (Fig. 5); parts of the compressional energy transforms into shear energy (P-to-S conversion) and vice versa (S-to-P conversion). Seismic time series can be processed in such a way, that converted waves (e.g., Ps) and their multiples (e.g., PpPs, PpSs) are isolated on the record (Figs. 6 and 7, bottom). After source effect removal, the time series of the converted phases image the interface structure along the ray path beneath the seismic station (receiver) and are called receiver functions. A receiver function can be converted to depth, assuming an average propagation velocity.

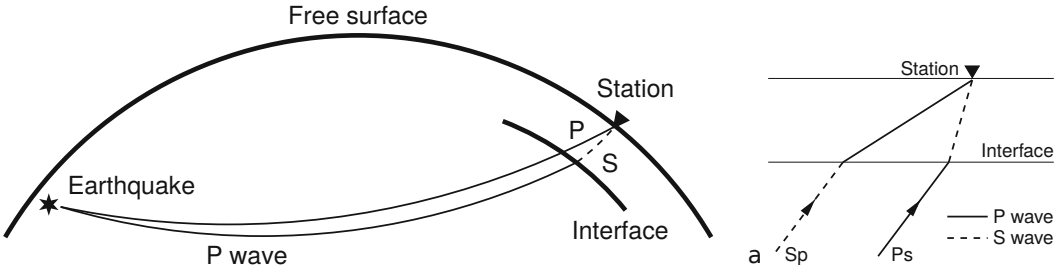

Figure 5: (left) Geometry of P receiver function; a plane P-wave emitted from a teleseismic event encounters interfaces below the receiver and partly converts into S-waves. (right) A closeup of the target area below a three-component station; sketch of ray paths of Ps and Sp converted waves (Kind and Yuan, 2011).

The processing of earthquake signal time series towards receiver functions includes multiple steps. The two main applications are the rotation and the deconvolution, as they isolate the primary and converted wave energy, and eliminate source and path effects, respectively. Frequency filtering, trimming and down sampling are also necessary to achieve good quality of the receiver functions. The processing steps are explained below for the computation of P receiver functions (P-to-S conversion).

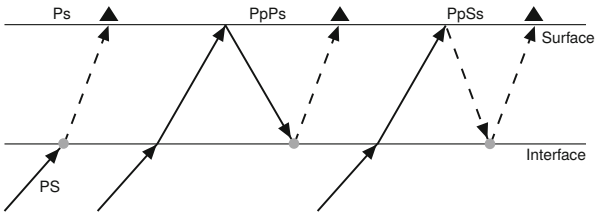

Figure 6: Ray paths of direct converted phase and crustal multiples from an incoming P-wave (Kind and Yuan, 2011).

Three-component seismic data are usually recorded in the ZNE geographic coordinate system. The rotation from the ZNE system into the LQT ray coordinate system isolates P- and S-waves on different components and hence separates the converted phases from its mother wave. The rotation is performed in three steps: (1) rotation of the coordinate system around the Z-axis with the back azimuth θ as rotation angle (ZNE→ZRT), (2) rotation of the coordinate system around the T-axis with the wave incidence angle i as rotation angle (ZRT→LQT) (Fig. 7, top), and (3) mirroring of the Q component to ensure the direction to point radially in opposite direction from the source (multiplication by -1). Thus, the phases that arrive as P-waves are isolated on the L component (mother wave, source component), the phases arriving as SV-wave are on the Q component and those arriving as SH-wave are on the T component (converted phases)(Fig. 7, bottom). Note that with Q⊥L the rotation does not perfectly separate P- and S-waves at the free surface, however, the influence of the free surface of the Earth is small and can be neglected in most cases (Bostock, 1998; Kind and Yuan, 2011).

Steps (1) and (2) of the rotation are performed by Equations 10 and 11. The full component rotations including step (3) for the Q component are described by Equations 12–14.

$$\begin{pmatrix} Z \\ R \\ T \end{pmatrix} = \begin{pmatrix} 1 & 0 & 0 \\ 0 & \cos(\theta) & \sin(\theta) \\ 0 & -\sin(\theta) & \cos(\theta) \end{pmatrix} \begin{pmatrix} Z \\ N \\ E \end{pmatrix} \tag{10}$$

$$\begin{pmatrix} L \\ Q \\ T \end{pmatrix} = \begin{pmatrix} \cos(i) & -\sin(i) & 0 \\ \sin(i) & \cos(i) & 0 \\ 0 & 0 & 1 \end{pmatrix} \begin{pmatrix} Z \\ R \\ T \end{pmatrix} \tag{11}$$

$$L = Z \cdot \cos(i) - N \cdot \sin(i) \cdot \cos(\theta) - E \cdot \sin(i) \cdot \sin(\theta) \tag{12}$$

$$Q = -Z \cdot \sin(i) - N \cdot \cos(i) \cdot \cos(\theta) - E \cdot \cos(i) \cdot \sin(\theta) \tag{13}$$

$$T = -N \cdot \sin(\theta) + E \cdot \cos(\theta) \tag{14}$$

For each event, the apparent incidence angle i and the back azimuth θ can be calculated directly from the data by diagonalizing the covariance matrix, or computed theoretically using a global Earth model (e.g., IASP91) and the locations of source and receiver. For a given ray parameter, the apparent incidence angle of the P-wave at the surface is only dependent on the S-wave velocity at the surface (Aki and Richards, 2002).

Earthquakes have different focal mechanisms and magnitudes and thus generate different waveforms and amplitudes. To make the receiver functions comparable and especially stackable to enhance the common receiver structure, such source effects need to be removed for each event. This is done through deconvolution in the time domain, in the frequency domain or through iterative deconvolution. The deconvolution in the frequency domain is a spectral division of the

Q by the L component (or the R by the Z component), i.e., SV/P, for P receiver functions (e.g., Langston, 1979) and vice versa for S receiver functions. A deconvolution considers the entire mother wave as the source-time function, which could unintentionally eliminate phases of the impulse response at the receiver site. For instance if deconvolving a long duration (e.g., 100 s) P component from the SV component, P multiples within the crust at the receiver site are also eliminated by the deconvolution (Kind and Yuan, 2011).

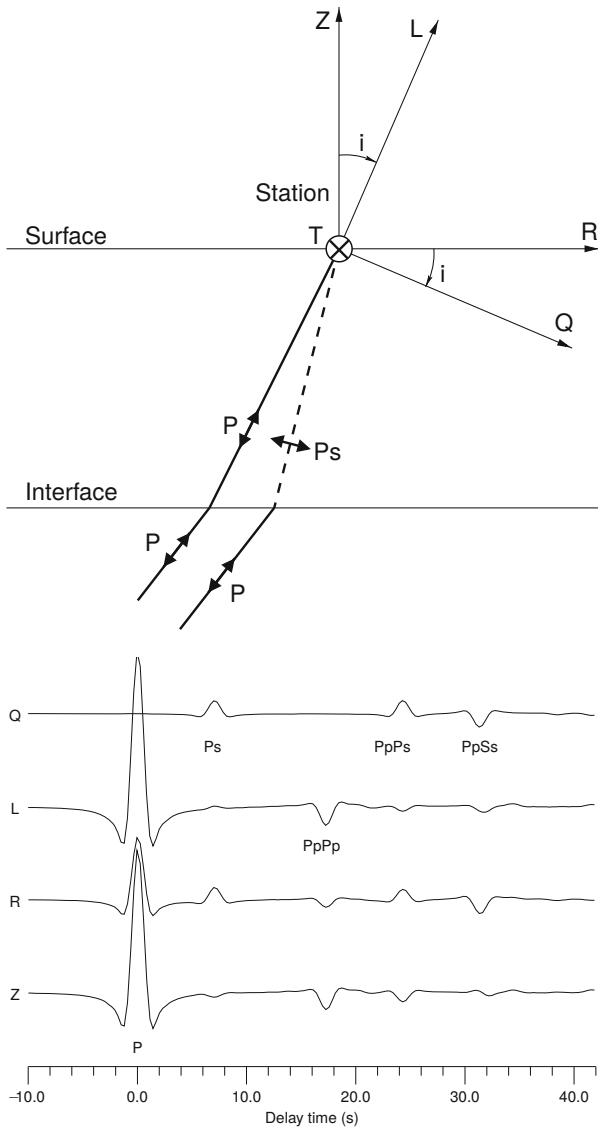

Figure 7: Rotation of vertical (Z) and radial (R) components around the incidence angle i into the LQ system. Phases arriving as P-wave (P, PpPp) are on the L component only. Phases arriving as SV-wave (Ps, PpPs, PpSs) are on the Q component. The SH-wave remains on the T component (Kind and Yuan, 2011).

The Fourier transform of the Q receiver function $RF_Q(\omega)$ is defined by

$$RF_Q(\omega) = \frac{Q(\omega)\overline{L}(\omega)}{\Phi_{ss}(\omega)} \tag{15}$$

$$\Phi_{ss}(\omega) = L(\omega)\overline{L}(\omega) \tag{16}$$

with the angular frequency $\omega = 2\pi f$, the Fourier transforms of the L and Q components $L(\omega)$ and $Q(\omega)$, and $\overline{L}(\omega)$ being the complex conjugate of $L(\omega)$ (based on Langston, 1979).

The deconvolution can be stabilized by using a water level c to avoid division by small numbers by replacing the small values in the divisor with a constant value. The constant is a fraction of the maximum spectral amplitude of the divisor, with the fraction given by the water level. The divisor therefore changes to:

$$\Phi_{ss}(\omega) = max\{L(\omega)\overline{L}(\omega), \\ c \cdot max[L(\omega)\overline{L}(\omega)]\} \tag{17}$$

The water level should be chosen as small as possible to avoid signal distortions of the receiver functions. The resulting spectra can then be inverse Fourier transformed without causing numerical problems if choosing an appropriate water level.

Furthermore, a Gaussian filter $G(\omega)$ is typically applied during the deconvolution, which operates as a lowpass filter and excludes high-frequency signals in the final time series.

$$RF_Q(\omega) = \frac{Q(\omega)\overline{L}(\omega)}{\Phi_{ss}(\omega)} \cdot G(\omega) \tag{18}$$

$$G(\omega) = e^{-\omega^2/4a^2} \tag{19}$$

with a as the Gaussian factor controlling the width. The Gaussian filter was chosen because of its smooth symmetric shape, the pulse-like character in the time domain (Fourier transform is also a Gaussian), and zero phase distortion (Langston, 1979).

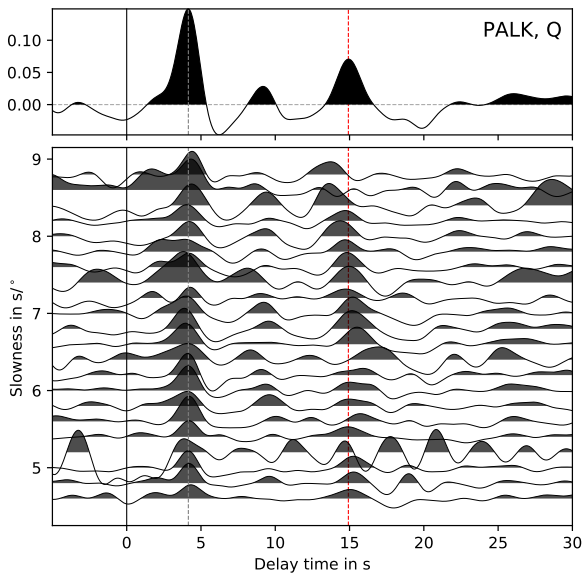

Figure 8: Q-RFs dependent on slowness and stack for a receiver located in central Sri Lanka (PALK). Gray and red vertical lines indicate Ps and PpPs phases at the RF-stack, respectively. PpPs arrivals show a strong moveout, while Ps are aligned.

After deconvolution the amplitudes are normalized to those of the incident phase (Kind and Yuan, 2011). The Q receiver function shows the P-to-S converted energy from each converter relative to the arrival of the main phase on the L component. The positive and negative amplitude peaks of the direct conversions correspond thereby to positive and negative velocity contrasts at the conversion interface.

To improve the signal-to-noise ratio of the converted phases on the Q component, RF traces from different events are stacked for the same receiver (Fig. 8). Thereby, common signals are added constructively, while random amplitudes interfere destructively.

As the events differ in depth and distance from the seismic station, each trace shows a different apparent incidence angle, i.e., the ray path length and the travel time increase with increasing angle and cause the converted phases and their multiples to arrive delayed from each other (Fig. 8). To encounter the effect of slowness, i.e., to align the phases, a moveout correction can be performed before stacking.

For receiver function analysis with source-receiver distances between 30–90°, slownesses are typically between 4–9 s/°. For the moveout correction, a reference slowness of usually 6.4 s/° is assumed, and the timescale of traces will be stretched or compressed relative to this slowness. The converted phases under investigation (e.g., Ps) are then parallel to the mother signal. The moveout correction for direct conversions amplifies the phase through optimal constructive summation in the stack. However, surface multiples become shifted with respect to each other and thus are destructively superimposed (Kind and Yuan, 2011).

The final receiver function stack is often used for forward modeling or inversion applications

to image the interface structure beneath the receiver. However, absolute velocities are necessary to constrain the interface depths due to velocity-depth trade-off.

$H\kappa$-stacking is a method to determine the crustal thickness (H) and V_P/V_S ratio (κ) beneath a station from receiver functions, assuming an average crustal V_P (Zhu and Kanamori, 2000). Thereby, receiver function amplitudes are stacked at predicted arrival times of the Moho converted phase and crustal reverberations (Ps, PpPs, and PpSs+PsPs). The delay times of those phases (t_{Ps}, t_{PpPs} and $t_{PpSs+PsPs}$) are related to H and κ as follows (Eqs. 20–22).

$$H = \frac{t_{Ps}}{\sqrt{\frac{1}{V_S^2} - p^2} - \sqrt{\frac{1}{V_P^2} - p^2}} \tag{20}$$

$$H = \frac{t_{PpPs}}{\sqrt{\frac{1}{V_S^2} - p^2} + \sqrt{\frac{1}{V_P^2} - p^2}} \tag{21}$$

$$H = \frac{t_{PpSs+PsPs}}{2\sqrt{\frac{1}{V_S^2} - p^2}} \tag{22}$$

with p being the ray parameter of the incident wave. The $H\kappa$-stacking is performed by

$$s(H, \kappa) = w_1 r(t_1) + w_2 r(t_2) + w_3 r(t_3) \tag{23}$$

with $r(t)$ is the receiver function and t_1, t_2, and t_3 the predicted arrival times for phases Ps, PpPs, and PpSs+PsPs corresponding to H and κ. w_1, w_2, and w_3 are weighting factors with $\sum w_i = 1$. The stacking function $s(H, \kappa)$ reaches a maximum at correct H and κ, so that the phases are coherently stacked.

Ambient noise cross-correlation. Seismic ambient noise in the Earth shows diffuse wavefields that are composed of waves with random amplitudes and phases propagating in many different directions (Fig. 9). Through cross-correlation of such background noise between station pairs, dispersive wave trains coherent to ballistic surface waves can be revealed (Shapiro and Campillo, 2004). They contain the response functions of the medium along the ray path between the stations and can be used for dispersion velocity analyses.

The Green's function between two stations is extractable by correlation and stacking of the signal over an appropriate long time period. The full Green's tensor after rotation from the ZNE into the ZRT coordinate system contains cross-correlograms between each of the components between the two stations (see Eq. 29). The Green's functions including the vertical and radial components, i.e., ZZ, ZR, RZ, RR, represent to first order the Rayleigh surface wave, while the transverse component combination, i.e., TT, represents to first order the Love surface wave.

After Bensen et al. (2007) several processing steps before the cross-correlation are recommended to improve the signal: (1) removal of instrument response, mean and trend from the raw data, application of bandpass frequency filter and trimming of seismic traces to daily segments, (2) normalization in the time and frequency domain.

Time domain normalization eliminates seismic signals that are not ambient noise, to reduce

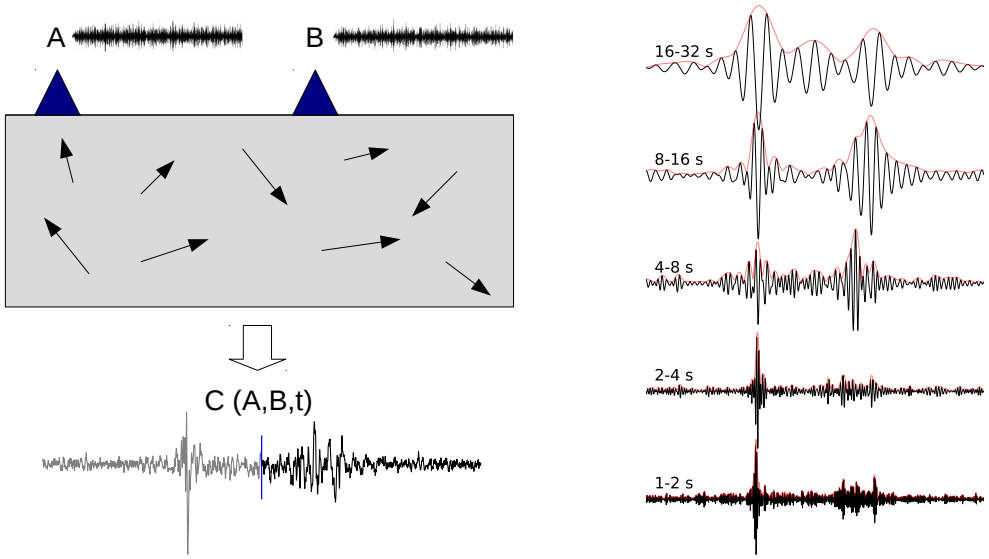

Figure 9: (left) Principle of ambient noise cross-correlation where stations A and B form source and receiver pairs: the seismic ambient noise fields are recorded at A and B (top) and cross-correlated (bottom), showing causal and acausal signal parts in black and gray, respectively. Each part shows the response function of the waves traveling between the stations in opposite directions. $C(A, B, t)$ corresponds to the cross-correlogram between A and B over time t. (right) Frequency filtering of the correlogram for different intervals with envelope in red. The envelope can be used to estimate the frequency dependent group velocity.

their effect on the cross-correlation. Those signals include earthquakes, instrumental irregularities and non-stationary noise sources close to the stations. The procedures in the time domain are for instance, one-bit normalization, clipping of the waveform, absolute mean normalization or water-level normalization. Frequency domain normalization, also spectral normalization or whitening, equalizes the amplitudes of the spectra for the frequencies of interest. Hence, frequencies with weak amplitudes are amplified and dominating frequencies are weakened.

Surface wave signals are used for dispersion analyses (Fig. 9, right). Therefore, group and phase velocity dispersion can be measured.

Group velocity dispersion. Group velocity dispersion as measured in this study, is based on the multiple-filter technique described by Dziewonski et al. (1969). Thereby, the seismic surface wave time series $s(t)$ is Gaussian filtered to retrieve $s_{\omega_0}(t)$ at the center frequency ω_0. The filtering is performed in the frequency domain.

$$S_{\omega_0}(\omega) = S(\omega) \cdot G(\omega_0) \tag{24}$$

with $S(\omega)$ and $S_{\omega_0}(\omega)$ being the Fourier transforms of $s(t)$ and $s_{\omega_0}(t)$, respectively. $G(\omega_0)$ is the Gaussian window as given by Equation 19.

The envelope $e_{\omega_0}(t)$ is computed by adding the squared amplitudes of $s_{\omega_0}(t)$ and its Hilbert-Transform H, and taking the square-root (Kanasewich, 1981).

$$e_{\omega_0}(t) = \sqrt{s_{\omega_0}(t)^2 + H(s_{\omega_0}(t))^2} \tag{25}$$

The time at the maximum envelope corresponds to the group travel time of the wave package (dominantly at ω_0), and can be used together with the travel distance to compute the group velocity. Multiple filters are applied to retrieve the group velocity dispersion curve.

Phase velocity dispersion. For phase velocity measurements, we follow the approach proposed by Ekström et al. (2009), and measure the velocity directly from the zero crossings of the real part of the correlation spectrum (after Aki, 1957). Methods that are based on a modified formulation of earthquake-based methods (Bensen et al., 2007; Herrmann, 2013; Yao et al., 2006) use a high frequency approximation, which introduces a phase shift at high frequencies (e.g., Yao et al., 2006), and require minimum inter-station distances (r) larger than 3 wavelengths (λ) to satisfy the far-field approximation (Lin et al., 2008; Yao et al., 2006). The method after Ekström et al. (2009) does not need a high frequency approximation and minimum inter-station distances are reduced to $\sim\lambda$.

Aki (1957) found that the azimuthally averaged normalized cross spectrum $\bar{\rho}(r, \omega_0)$ varies as the Bessel function J (Eq. 26).

$$\bar{\rho}(r, \omega_0) = J_0\left(\frac{\omega_0}{c(\omega_0)} r\right) \tag{26}$$

with J_0 being the first order Bessel function and $c(\omega_0)$ the phase velocity at frequency ω_0. The cross spectra derived from the correlation of stochastic horizontally propagating waves between station pairs at different azimuths show great similarities. Aki (1957) argued that a single station pair spectrum can replace $\bar{\rho}(r, \omega_0)$ under the assumption of a sufficiently isotropic stochastic noise wavefield. Thus, the leading term in the real part of the spectrum is dominant.

From a cross-correlation function, phase velocities can be obtained by matching the real part of the correlation spectrum to a Bessel function. Only locations of zero crossings are considered, as they should be insensitive to variations in the spectral power of the background noise. The phase velocity for the ZZ component can be computed by

$$c(\omega_n) = \frac{\omega_n^r}{z_n} \tag{27}$$

with ω_n being the angular frequency of the n-th observed zero crossing, and z_n the n-th zero crossing of the first order Bessel function. As noise in the spectrum can cause missed or extra zero crossings, a set of phase velocity estimates is computed by

$$c_m(\omega_n) = \frac{\omega_n^r}{z_{n+2m}} \tag{28}$$

where $m \in \mathbb{Z}$ indicates those zero crossings. m is multiplied by 2 to only consider zero crossings of the same kind, i.e., negative-to-positive or positive-to-negative ones.

For a uniform source distribution, the full correlation tensor C for Rayleigh and Love waves

in two dimensions is (after Haney et al., 2012):

$$C = \begin{pmatrix} ZZ & ZR & ZT \\ RZ & RR & RT \\ TZ & TR & TT \end{pmatrix}$$

$$C = \begin{pmatrix} \varepsilon_R(\omega)\eta^2 J_0(\omega\tau_R) & -\varepsilon_R(\omega)\eta J_1(|\omega|\tau_R) & 0 \\ \varepsilon_R(\omega)\eta J_1(|\omega|\tau_R) & \begin{matrix}\varepsilon_R(\omega)[J_0(\omega\tau_R)-J_2(\omega\tau_R)]/2 \\ +\varepsilon_L(\omega)[J_0(\omega\tau_L)+J_2(\omega\tau_L)]/2\end{matrix} & 0 \\ 0 & 0 & \begin{matrix}\varepsilon_L(\omega)[J_0(\omega\tau_L)-J_2(\omega\tau_L)]/2 \\ +\varepsilon_R(\omega)[J_0(\omega\tau_R)+J_2(\omega\tau_R)]/2\end{matrix} \end{pmatrix} \tag{29}$$

with $\tau_R = r/c_R$, $\tau_L = r/c_L$; ε_R and ε_L are uniform source intensities; the indices R and L indicate the Rayleigh and Love wave, respectively. η is the Rayleigh wave ellipticity defined by Z/R. J_0, J_1 and J_2 are the zeroth, first and second order Bessel functions.

The Bessel function to match the ZZ component is J_0, while the RZ and ZR components correspond to J_1. The RR and the TT components are not purely represented by Rayleigh and Love wave velocities, respectively, but a superposition of both. J_2 is asymptotically equal to $-J_0$ and thus, the Rayleigh wave is dominant in RR and the Love wave is dominant in TT at high frequency. To measure Rayleigh wave phase velocities from RR and Love velocities from TT, the Bessel function difference $(J_0 - J_2)$ is used.

Phase as well as group velocity dispersion measurements offer absolute velocity information and are therefore often inverted jointly with receiver functions to receive the V_S-depth structure beneath the receiver. As Rayleigh waves are vertically and Love waves horizontally polarized shear waves, they are sensitive to V_{SV} and V_{SH}, respectively. These velocities can be used to derive radial seismic anisotropy.

Radial seismic anisotropy. A discrepancy between V_{SV} and V_{SH} in the same medium is described as polarization anisotropy, radial seismic anisotropy or transverse seismic isotropy (Fig. 10). They are used as synonyms and emphasize different ideas of the same: The naming polarization anisotropy is based on the anisotropic velocities of the differently polarized waves, i.e., vertically and horizontally polarized shear wave velocities. Radial anisotropy in a spherical reference system describes anisotropic properties along the radial (vertical) axis. The transverse isotropic medium has a vertical symmetry axis and shows isotropic behavior in the perpendicular transverse direction, i.e., independent from the azimuth in the horizontal symmetry plane. Radial anisotropy can be contrasted with azimuthal anisotropy, which shows anisotropic properties within the horizontal plane (Shapiro et al., 2004).

We define V_{SV} and V_{SH} for a transverse isotropic medium and want to recall Hooke's law:

$$\sigma_{ij} = \sum_{k=1}^{3}\sum_{l=1}^{3} c_{ijkl}\varepsilon_{kl} \tag{30}$$

with the stress matrix σ_{ij}, the srain matrix ε_{kl}, and the elasticity tensor or elastic moduli

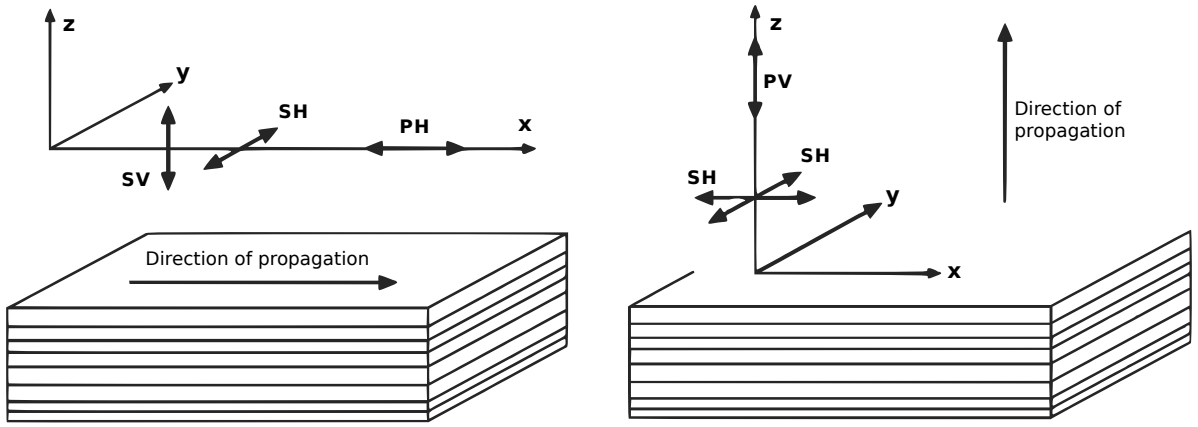

Figure 10: Effects of radial anisotropy in a layered medium. (left) Directions of particle motions for P- and S-waves traveling along x in the plane of layering. The S-wave oscillating within the plane of layering has a velocity of V_{SH}, which is faster than that of the S-wave oscillating across the layers (V_{SV}). (right) Directions of particle motions for P- and S-waves traveling along z perpendicular to the layering. Both S-waves have the same velocity; the P-wave velocity V_{PV} is less than V_{PH}. A consequence of the horizontally layered medium is that V_S inferred from the dispersion of Love waves, which are SH-waves, is different than that from Rayleigh waves, which involve SV-waves (modified after Stein and Wysession, 2003).

being c_{ijkl}, where i,j,k and l correspond to 1, 2 or 3, indicating x, y or z directions, respectively. Inherent symmetries of σ, ε, and c reduce the 81 constants to 21 independent elastic constants and allow representation of the 3x3x3x3 tensor c_{ijkl} by a 6x6 matrix C_{mn}, as defined in Equations 31 and 32.

$$C_{mn} = \begin{pmatrix} c_{1111} & c_{1122} & c_{1133} & c_{1123} & c_{1113} & c_{1112} \\ c_{2211} & c_{2222} & c_{2233} & c_{2223} & c_{2213} & c_{2212} \\ c_{3311} & c_{3322} & c_{3333} & c_{3323} & c_{3313} & c_{3312} \\ c_{2311} & c_{2322} & c_{2333} & c_{2323} & c_{2313} & c_{2312} \\ c_{1311} & c_{1322} & c_{1333} & c_{1323} & c_{1313} & c_{1312} \\ c_{1211} & c_{1222} & c_{1233} & c_{1223} & c_{1213} & c_{1212} \end{pmatrix} \tag{31}$$

or

$$C_{mn} = \begin{pmatrix} C_{11} & C_{12} & C_{13} & C_{14} & C_{15} & C_{16} \\ C_{21} & C_{22} & C_{23} & C_{24} & C_{25} & C_{26} \\ C_{31} & C_{32} & C_{33} & C_{34} & C_{35} & C_{36} \\ C_{41} & C_{42} & C_{43} & C_{44} & C_{45} & C_{46} \\ C_{51} & C_{52} & C_{53} & C_{54} & C_{55} & C_{56} \\ C_{61} & C_{62} & C_{63} & C_{64} & C_{65} & C_{66} \end{pmatrix} \tag{32}$$

with m and n as pairs of indices, $m = (i, j)$ and $n = (k, l)$. For an isotropic material, the elastic properties at a given point in the medium are the same in all directions and only two independent constants, the Lamé constants λ and μ, describe the elastic moduli:

$$c_{ijkl} = \lambda\delta_{ij}\delta_{kl} + \mu(\delta_{ik}\delta_{jl} + \delta_{il}\delta_{jk}) \tag{33}$$

Any elastic material with more than two constants is considered anisotropic. In a transversely isotropic medium, at least five elastic constants are required to properly describe the elastic response (Anderson, 2007). As we assume a vertical rotational axis, we can set $C_{11} = C_{22}$, $C_{31} = C_{32}$, $C_{44} = C_{55}$ and $C_{66} = (C_{11} - C_{12})/2$ (Lubarda and Chen, 2008), and the elasticity matrix is defined by the five independent elastic moduli A, N, L, C, and F (Love, 1927).

$$C_{mn} = \begin{pmatrix} A & A-2N & F & 0 & 0 & 0 \\ A-2N & A & F & 0 & 0 & 0 \\ F & F & C & 0 & 0 & 0 \\ 0 & 0 & 0 & L & 0 & 0 \\ 0 & 0 & 0 & 0 & L & 0 \\ 0 & 0 & 0 & 0 & 0 & N \end{pmatrix} \tag{34}$$

$A = \lambda_H + 2\mu_H$, $N = \mu_H$, $L = \mu_V$, and $C = \lambda_V + 2\mu_V$, where the indices H and V indicate the horizontal and vertical direction, respectively. The fifth constant F requires additional information (see below). The wave speeds are derived by:

$$V_{SH} = \left[\frac{N}{\rho}\right]^{1/2} \qquad V_{PH} = \left[\frac{A}{\rho}\right]^{1/2} \tag{35}$$

$$V_{SV} = \left[\frac{L}{\rho}\right]^{1/2} \qquad V_{PV} = \left[\frac{C}{\rho}\right]^{1/2} \tag{36}$$

with PH and SH being waves that propagate and are polarized in the horizontal direction, and PV and SV being waves that propagate and are polarized in the vertical direction (Fig. 10). F is defined by $\rho(2V_{P45}^2 - V_{PH}^2 - 2V_{SV}^2)$, where V_{P45} corresponds to a P-wave in a direction of 45° to the x-y plane (Wong et al., 2008).

Radial seismic anisotropy (RA) can be estimated from the anisotropic parameter $\xi = N/L$ (Anderson, 1961), which is 1 for isotropic material, and generally >1 for layered structures:

$$\xi = \frac{N}{L} = \left[\frac{V_{SH}}{V_{SV}}\right]^2 \qquad RA = (\xi - 1) \cdot 100\ \% \tag{37}$$

Geologic background

This section provides an overview of the assembly and break-up of Gondwana and the role of Madagascar and Sri Lanka within this framework. Each part of this thesis will include a study-specific geology background section on its own, so that here we only give a short introduction to the major episodes of the formation and break-up of Gondwana (Tab. 1). The time spans given are approximations and slightly differ from study to study. Nevertheless, our focus are structures inferred from amalgamation and separation processes, and not the exact timing of those processes.

The supercontinent Gondwana formed through collisional events between the component cratons of West and East Gondwana (Fig. 11); West Gondwana is thereby represented by fragments assembling Africa and South America, and East Gondwana by fragments assembling what

Table 1: Major episodes of the formation and break-up of Gondwana. Given time spans are approximations and slightly differ from study to study.

900–850 Ma	Supercontinent Rodinia broke apart (Stern, 1994).
750–490 Ma	Gondwana formation, i.e., amalgamation of African and South American terranes with Antarctica–Australia–India (Meert, 2003; Meert and Lieberman, 2008; Stern, 1994).
320 Ma	Gondwana merging with Laurussia (Veevers, 2004), with subsequent collision of Siberia to form supercontinent Pangea.
290 Ma	Limestones, deposited during the oldest marine transgression within central Gondwana (Wescott and Diggens, 1997), show that parts of the orogen were by then eroded to sea level (Emmel et al., 2008).
185–100 Ma	Stepwise break-up of supercontinent, including Gondwana terranes (Veevers, 2004).
90 Ma	Final phase of Gondwana break-up, separation of Madagascar from India-Seychelles.

is known today as Australia, Antarctica, India, Madagascar and Sri Lanka. Madagascar and Sri Lanka occupy key positions, as they were located in the center of the collision zone.

The Pan-African collision forming Gondwana created multiple orogens along the craton boundaries, as shown in Figure 11. The East African Orogeny (∼750–620 Ma; Meert, 2003) was the main stage in the Neoproterozoic assembly. The orogen resulted from the accretion of numerous juvenile arcs and a few older continental fragments in the Arabian–Nubian shield region

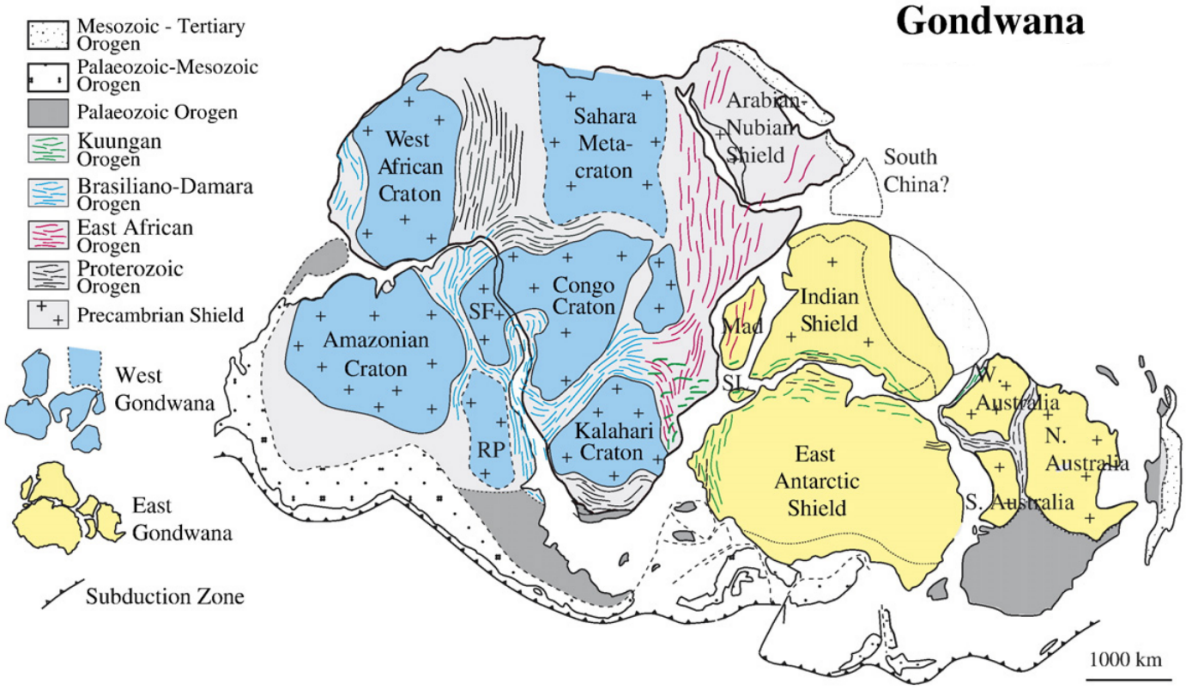

Figure 11: Assemblage of cratons and orogens, evolving through the stepwise collision of West (blue) and East Gondwana (yellow). See text for details (Meert and Lieberman, 2008).

(870–690 Ma Stern, 1994) and oblique continent–continent collision between eastern Africa with an ill-defined collage of continental blocks including parts of Madagascar, Sri Lanka, Seychelles, India and East Antarctica (Meert, 2003). The Kuungan Orogeny (570–530 Ma; Meert, 2003) involved the coastal margins of East Antarctica, India, Sri Lanka, southern Madagascar and south-eastern Africa. The Brasiliano Orogens represent the suture between Africa and South America, which formed through the closure of the Adamastor Ocean (Gray et al., 2008). The protracted Brasiliano Orogeny (600–530 Ma; Meert and Van der Voo, 1997) and the closure of the Damara Belt are related to the final assembly of the Gondwana supercontinent and extended to at least ∼490 Ma (Meert and Lieberman, 2008).

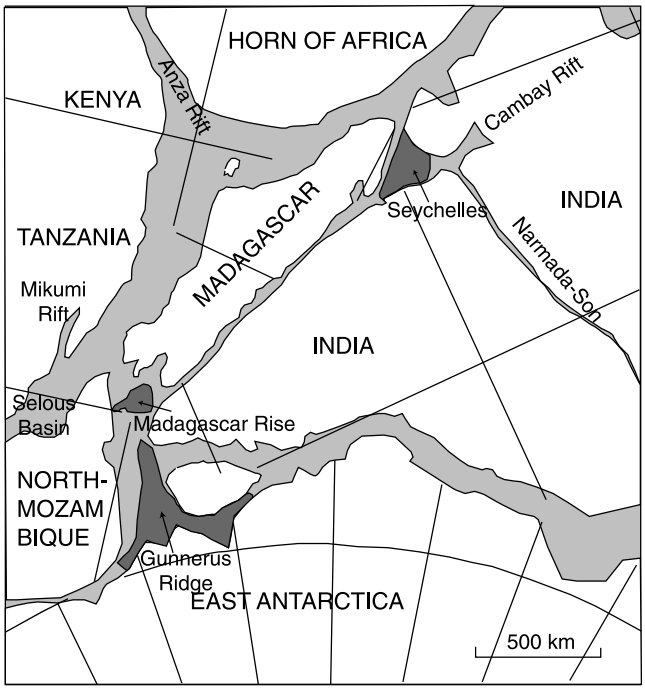

Figure 12: Reconstruction of Gondwana fragments at 200 Ma. Shown are geometrically rigid Precambrian crustal fragments (white), originally continental rocks that have been extended and lost from outcrop by rifting (light gray), and areas that are largely submarine, partly Precambrian (dark gray) (Seward et al., 2004).

Strong Pan-African non-coaxial strain obliterated most of the older structures and also brought early fabrics into parallelism according to the strain directions (Kehelpannala, 1997). The continental collisions led to crustal thickening and uplift, beginning 750–700 Ma for the East African Orogen, propagating eastwards with time (Stern, 1994). The thickening was followed by orogenic collapse and escape tectonics until ∼540 Ma, the latter causing major rift basins in the northern East African Orogen and environs. The development of those rift systems directly led to sea-floor spreading and the formation of an ocean basin to the north at ∼550 Ma (Stern, 1994).

The supercontinent Pangea was assembled by closing the Tethys Ocean and merging Gondwana and Laurussia in ∼320 Ma (Veevers, 2004), followed by the collision with Sibiria in late Permian (∼260?–250 Ma). A reconstruction of relative locations of major Gondwana fragments at 200 Ma is illustrated in Figure 12. The initial break-up of Pangea is dated to 185 Ma (Veevers, 2004). The break-up, as the assembly, was a stepwise process.

The Gondwana break-up is proposed to have started between East Antarctica and the Antarctic Peninsula, in the Weddell Sea (pre-late Jurassic, 180–160 Ma; LaBrecque and Barker, 1981), and propagated clockwise around Antarctica (Lawver et al., 1991). Jokat et al. (2003) reveal that first oceanic crust of the South Atlantic, i.e., between Africa and Antarctica, has formed around 155 Ma.

Intra-continental rifting in Madagascar began in Early Permian (300–270? Ma) with the development of intra-continental pull-apart basins through strike-slip displacement close to the

Vohibory domain (Schandelmeier et al., 2004), and initiated the separation between Africa and Madagascar (and the rest of East Gondwana). The kinematic character along the south-western coast of Madagascar gradually changed from transtensional sag dynamics to purely tensional tectonics, i.e., normal faulting, by ∼250 Ma (Schandelmeier et al., 2004). While the first rifting episode led to a continental failed rift, the second is characterized by a rift locus migration towards the west (Geiger et al., 2004), continuous rifting, and the break-up from Africa along a strike-slip boundary. At ∼155 Ma, Madagascar (and the rest of East Gondwana) started to drift southwards along that transform fault (Fig. 13a). Sedimentary basins (e.g., the Morondava basin) developed along Madagascar's coast line as marine conditions prevailed. By 118 Ma Madagascar reached its present position relative to Africa (Seward et al., 2004).

Separation of Greater India from East Gondwana started ∼136 Ma north-east of Australia-Antarctica through a mid-ocean ridge that progressively propagated from north to south and reached the southern tip of India at ∼126 Ma (Fig. 13a, b) with simultaneous separation of Sri

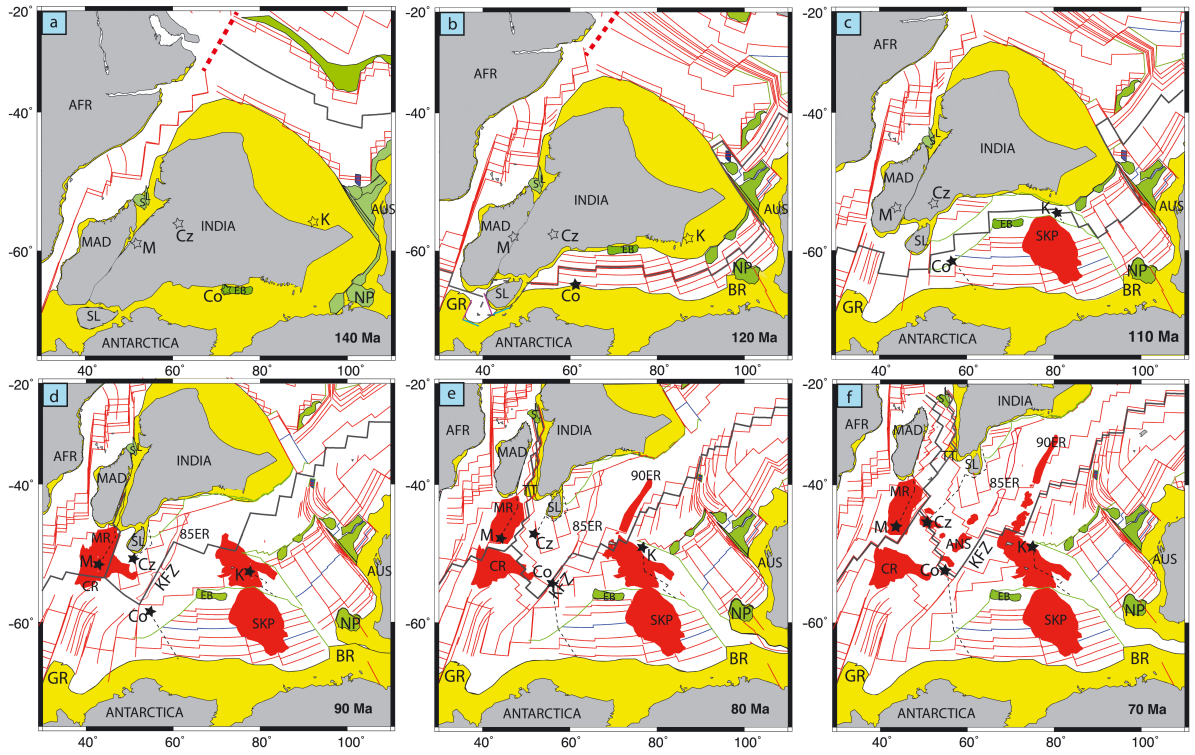

Figure 13: Mercator-projected reconstructions of the southern Indian Ocean at (a) 140 Ma, (b) 120 Ma, (c) 110 Ma, (d) 90 Ma, (e) 80 Ma, and (f) 70 Ma, constructed with Antarctica fixed in present-day coordinates. Shown are pseudo-faults (light green lines), extinct ridges (light blue lines), COB (thin black line, filled in yellow), continental microfragments (filled in green), isochrons (red lines), East African-Tethyan transform fault (thick red dashed line), spreading centers (thick dark gray lines), and hotspot tracks (thin black dashed lines). Continental material above sea level is outlined in gray, and large igneous provinces are shown in red. 85ER: 85°E Ridge, 90ER: 90°E Ridge, AFR: Africa, AUS: Australia, BR: Bruce Rise, CR: Conrad Rise 4000 m isobath, Cr: Crozet Hotspot, EB: Elan Bank, KP: Kerguelen Plateau, KFZ: Kerguelen Fracture Zone, L: Laxmi Ridge, MAD: Madagascar, MR: Madagascar Ridge 3500 m isobath, NP: Naturaliste Plateau, S: Seychelles, SL: Sri Lanka, TT: Terrace near Trivandrum. Black/hollow stars show the locations of hotspots fixed in their present-day locations, including Conrad (Co), Crozet (Cr), Marion (M) and Kerguelen (K) (Gibbons et al., 2013).

Lanka from the Gunnerus Ridge (East Antarctica). The separation induced an anticlockwise motion for India at a pole located near Sri Lanka and forced the formation of a transform boundary in the sea floor north-west of Greater India and east of Africa (red dashed line in Fig. 13a, b). The sea floor spreading between Africa and Madagascar provided space for Greater India's motion. The anticlockwise rotation induced a minor overlap between India and Madagascar (Fig. 13c), with subsequent break-up at ∼100 Ma (Seward et al., 2004, and references therein) and sea floor spreading between them from south to north from 94 to 84 Ma (Fig. 13d; Gibbons et al., 2013).

The Mannar basin, a pre-cratonic failed rift basin, developed between India and Sri Lanka since 165 Ma (Kularathna et al., 2015). A great amount of rifting together with strike slip movement and anticlockwise rotation (∼45°) of Sri Lanka (Kularathna et al., 2015) unzipped Sri Lanka fully from India by ∼116 Ma (Gibbons et al., 2013). The Indian subcontinent, including Sri Lanka, drifted north-eastwards and collided with the Eurasian plate at ∼59 Ma (Hu et al., 2016) to form the Himalayan Orogen.

Both Madagascar and Sri Lanka experienced massive reworking through the Pan-African Orogeny and individual post-orogenic shaping. Each of the Gondwana terranes experienced own complicated amalgamation processes parallel to the Pan-African collision, including a different number of fragments from different ages and origins.

Madagascar is composed of Archean and Proterozoic domains, which predominantly consist of magmatic and metamorphic rocks (Antananarivo domain), domains of island arc settings (Ikalamavony domain), and igneous rocks and supracrustal formations (Anosyen and Androyen domains). During the Pan-African Orogeny, the Precambrian crust was extensively reworked under amphibolite to granulite facies conditions, and a sedimentary basin formed during the later separation from Africa. Most of Sri Lanka is assembled by Neoproterozoic (<∼1 Ga) arcs, incorporating rocks as old as 2–3 Ga (Highland Complex). The fragments assembling Sri Lanka were accreted by thrust tectonics during a transpressional Pan-African regime, and today show amphibolite to granulite facies rocks.

The amalgamation of southern Madagascar and Sri Lanka is described in detail in the introductary chapter of the corresponding project, i.e., chapter I.1 for Madagascar, and chapter II.1 for Sri Lanka.

Project I

Crustal radial anisotropy in southern Madagascar and linkage to geodynamic processes – based on seismic ambient noise cross-correlation

Published as Dreiling et al. (2018): Dreiling, J., Tilmann, F., Yuan, X., Giese, J., Rindraharisaona, E. J., Rümpker, G., and Wysession, M. E. Crustal radial anisotropy and linkage to geodynamic processes: A study based on seismic ambient noise in southern Madagascar. Journal of Geophysical Research: Solid Earth, 2018. https://doi.org/10.1029/2017JB015273.

1 Introduction

The island of Madagascar occupied a key region in both the assembly and break-up of Gondwana. Hence, numerous geological investigations have been carried out in and adjacent to Madagascar to understand the evolution of the former supercontinent (e.g., Bardintzeff et al., 2010; Coffin and Rabinowitz, 1988; Fritz et al., 2013; Geiger et al., 2004; Tucker et al., 2011, 2014). Due to a lack of seismological data, little was known about the sub-surface structure, except for studies below four of the permanent broadband stations (Rindraharisaona et al., 2013) and a model for the central region (Rambolamanana et al., 1997). Recently, several temporary passive seismic deployments have been conducted in Madagascar (Fig. I.1), including the SELASOMA (Tilmann et al., 2012), MACOMO (Wysession et al., 2011) and RHUM-RHUM experiments (Barruol et al., 2017). They allow to image the seismic signatures of past geodynamic events in the crust and lithosphere of southern Madagascar.

We use data recorded by these experiments to characterize the radial seismic anisotropy in the crust of southern Madagascar. Our determinations of V_{SV} and V_{SH} are based on the vertically polarized Rayleigh and horizontally polarized Love surface wave, derived by seismic ambient noise cross-correlation. Radial seismic anisotropy can reveal information about anisotropic features in the crust, which can be associated to major geologic and tectonic processes.

Contents. We define radial seismic anisotropy and its correlation to intrinsic and extrinsic anisotropy, and describe the geologic and tectonic development of southern Madagascar (chapter 1). In chapter 2 the utilized seismic data are introduced and processed for subsequent ambient noise cross-correlation to retrieve Green's functions for Rayleigh and Love surface waves. Respective group and phase velocity dispersion curves were measured and tomographically inverted (chapter 3). Also, checkerboards were computed to estimate the dimensions of resolvable features. The group and phase velocity dispersion curves derived by tomography were jointly inverted for the velocity-depth structure (chapter 4). Final results of V_{SV}, V_{SH}, and RA are presented in chapter 5. It follows an interpretation and discussion about the radial anisotropy findings in southern Madagascar, and the linkage to past geodynamic processes.

Appendices I.A–I.C provide additional information.

1.1 Radial seismic anisotropy

Radial seismic anisotropy is a description of the dependence of wave speed on the direction and polarization of the seismic wave field. We estimate vertically and horizontally polarized shear wave velocities (V_{SV} and V_{SH}) from Rayleigh and Love wave dispersion, respectively, and compute radial anisotropy (RA) as stated in Equation I.1.

$$\xi = \left[\frac{V_{SH}}{V_{SV}}\right]^2 \qquad RA = (\xi - 1) \cdot 100\ \% \tag{I.1}$$

In an isotropic medium, V_{SV} and V_{SH} are equal. A negative radial anisotropy indicates a faster seismic velocity of vertically polarized shear waves ($V_{SV}>V_{SH}$), while a positive radial anisotropy implies a faster velocity of the horizontally polarized waves ($V_{SV}<V_{SH}$).

Velocity anisotropy can be produced by the intrinsic properties of the single minerals of crustal and mantle rocks, if these align along their crystallographic axes, which is known as crystallographic preferred orientation (CPO). The alignment results from finite strain in the dislocation creep regime (e.g., Karato and Wu, 1993). Because alignment is not perfect and the anisotropic properties of the different constituent minerals sometimes interact destructively, the anisotropy of the bulk rock is usually much less than that of its minerals. Effective anisotropy can also result from isotropic constituents, if heterogeneities on a scale much smaller than the wavelength show preferred orientations; such anisotropy from shape-preferred orientation (SPO) can arise from aligned microcracks, layering, or the organization of melt in dikes or sills. In many cases, the development of SPO is governed by the current or paleo-stress field (Wang et al., 2013).

Radial anisotropy in the shallow crust (<5–10 km) is primarily associated with the presence of oriented microfractures and cracks (Luo et al., 2013; Tatham et al., 2008; Weiss et al., 1999). Mid-crustal anisotropy is often attributed to the CPO of micas, i.e., biotite and muscovite (e.g., Nishizawa and Yoshino, 2001). Although micas crystallize into the monoclinic crystal system, they show a hexagonal type of anisotropy on crustal scales. An important contributor to anisotropy in the lower crust is amphibole (Kitamura, 2006; Tatham et al., 2008). Amphiboles have monoclinic and orthorhombic crystal systems, but are, as with micas and most of the deep crustal minerals, quasi-hexagonal (Weiss et al., 1999).

Many geodynamic processes can be correlated with either compressional or extensional tectonics: both regimes can cause alignment, reorientation, recrystallization and growth of minerals oriented perpendicular – or at defined angles – to the stress direction. Although many studies of radial anisotropy relate compressional regimes to vertical and extensional regimes to horizontal alignment of crustal materials, both regimes can produce very variable orientations of minerals and anisotropy signatures that contradict these simplifications; in each case, vertical and horizontal preferred orientations need to be seen in relation to the geodynamic background at the specific location. While a negative anomaly suggests anisotropic features that are steeply dipping to subvertical (60–90°), a positive radial anisotropy implies that the anisotropic features are subhorizontal to shallowly dipping (0–30°) (Xie et al., 2013). The strength of radial anisotropy (RA in Eq. I.1) is a measure of the consistency of material alignment (CPO), the degree of organization, and the contrast in material properties (SPO).

1.2 Geodynamic background

The geology of southern Madagascar is characterized by the crystalline basement, which covers the eastern two thirds of the island and comprise Archean and Proterozoic units, and by the sedimentary Morondava basin in the west (Fig. I.1). Both the crystalline basement and the Morondava basin are in some places intruded by Cretaceous volcanics, with significant outcrops along the east coast, in the area around Volcan de l'Androy in the south, and in the central Morondava basin (Roig et al., 2012). The formation of each unit is associated with a major

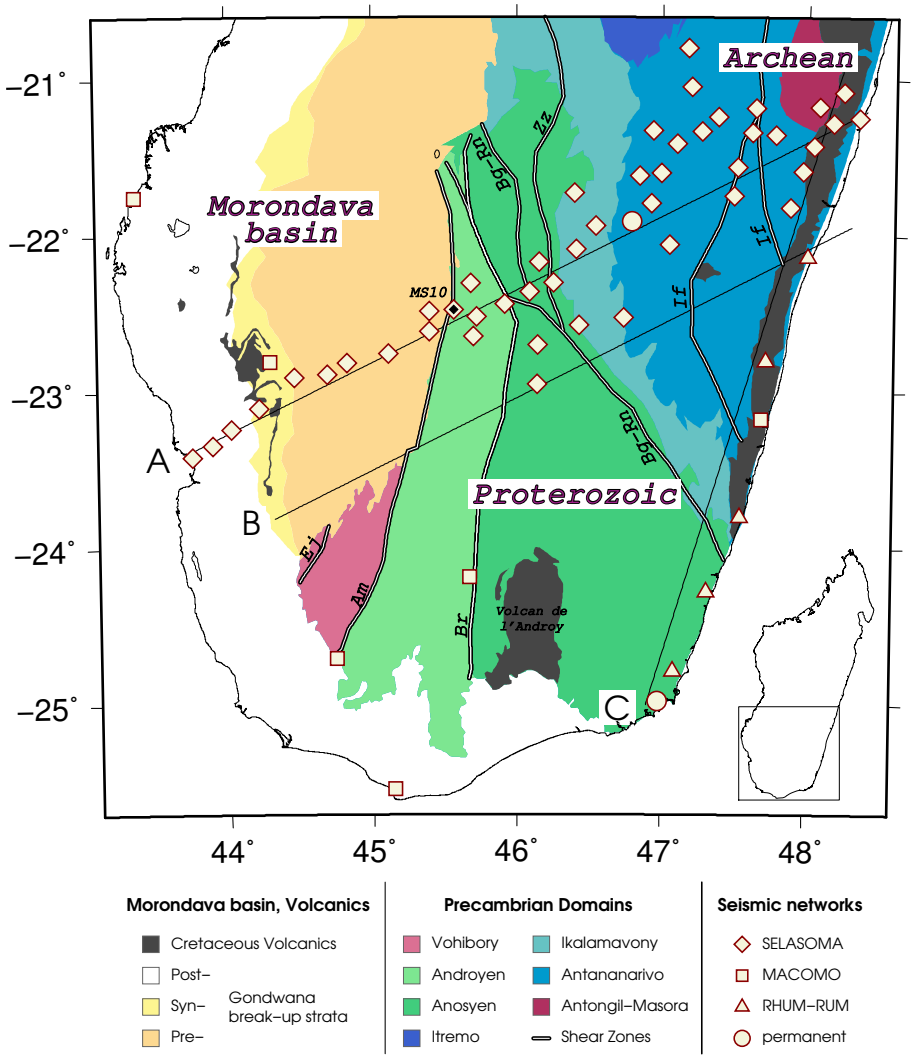

Figure I.1: Simplified surface geology of southern Madagascar after Boger et al. (2008a,b,c); Roberts et al. (2012); Tucker et al. (2011). Illustrated shear zones after Martelat et al. (2000): Ampanihy (Am), Bongolava-Ranotsara (Bg-Rn), Beraketa (Br), Ejeda (Ej), Ifanadiana (If), and Zazafotsy (Zz). Note that the shear zones represented here as lines often represent broader zones of deformation. Lines A-C signify locations of cross sections shown in Figures I.28–I.30. Map data after Rindraharisaona et al. (2017).

episode in the geologic history of Madagascar: the crystalline basement represents the assembly of Gondwana finalized by the Pan-African Orogeny, the Morondava basin reflects the separation of Africa and Madagascar but also earlier failed rifting episodes, and Cretaceous volcanism accompanies the separation of Madagascar from India and the Seychelles.

The formation of **proto-Madagascar** was accomplished through the accretionary convergence of the Proterozoic southern domains (Vohibory, Androyen, Anosyen, Ikalamavony) and the Archean units (Antananarivo, Antongil/Masora)(Fig. I.1). The stepwise accretion involved the subduction of back-arc basins and intervening oceans. The Ikalamavony domain is interpreted as the volcano-sedimentary sequence of a magmatic arc accreted to the Antananarivo-Masora domains prior the Pan-African Orogeny in earliest Neoproterozoic time, subsequently followed by the formation of a passive continental margin with the deposition of associated sediments (i.e.,

Itremo) (Boger et al., 2014). Renewed eastward subduction of the Mozambique Ocean in Cryogenian time (720–635 Ma) triggered magmatism (e.g., Tucker et al., 2014) and sedimentation of the future Anosyen domain sediments within an active fore-arc environment (Boger et al., 2014). Following the model of Boger et al. (2015), the intra-oceanic island arc of the Vohibory domain collided with the micro-continent of the Androyen domain between 650–610 Ma, forming the Ampanihy shear zone, and preceding the final collision and formation of the Beraketa shear zone between the eastern amalgamated domains of Masora/Antananarivo/Ikalamavony/Anosyen and the western amalgamated fragment of the Androyen/Vohibory.

During the **Pan-African Orogeny** all the basement units were finally assembled (e.g., Tucker et al., 2014). The Pan-African Orogen was finalized in the compressional stress regime during the final Gondwana-forming collision between roughly 590–530 Ma, accompanied with syn- to post-tectonic granitic magmatism of the Ambalavao suite (e.g., Tucker et al., 2014). The finite strain pattern dominating the Precambrian of southern Madagascar is defined by large areas comprising shallowly dipping to subhorizontal foliations with E-W-trending stretching lineations. These are bordered by an extensive, anastamosing shear-zone network that was active during late-stage Pan-African transpressional tectonics (Lardeaux et al., 1999; Martelat et al., 2000). Most of the shear zones visible today are located within the Proterozoic domains and are characterized by kilometer-wide zones of steeply dipping, highly strained rocks. While the Ampanihy and Beraketa shear zones represent terrane boundaries, the Ejeda, Bongolava-Ranotsara, Ifanadiana and Zazafotsy shear zones run intra-domainly (GAF-BGR, 2008). All these shear zones feature tight- to isoclinal folds and are highly flattened crustal-scale zones resulting from the Pan-African collision. The Ranotsara zone shows ductile sinistral deflection confined to its central segment and prominent NW-SE-trending brittle faulting along most of its length (Schreurs et al., 2010). The shear zones appear to be rooted in a zone of much more broadly distributed deformation in the mantle (Reiss et al., 2016).

The collisional event caused crustal shortening and thickening (60–70 km), with subsequent thinning by a combination of lower crustal delamination (Rindraharisaona et al., 2017), gravitational spreading (de Wit et al., 2001; Fitzsimons, 2016; Giese et al., 2017) and upper crustal removal through erosion and exhumation (Giese et al., 2011; Seward et al., 2004). The central part of the East African Orogen reached thermal equilibrium between 500–350 Ma (Emmel et al., 2008) and Early Permian (∼290 Ma) limestones, deposited during the oldest marine transgression within central Gondwana (Wescott and Diggens, 1997), show that parts of the orogen were by then eroded to sea level (Emmel et al., 2008).

Compressive intraplate stress related to far-field stresses (effective mechanical coupling of orogenic belt and continental foreland) caused reactivation of basement faults, triggered the opening of intracontinental pull-apart basins through strike-slip displacement close to the Vohibory domain and initiated the **separation of Africa and Madagascar** (Schandelmeier et al., 2004). The Ampanihy shear zone in particular appears to have influenced the opening of the southern Morondava basin. The kinematic character forming the Morondava basin gradually changed from transtensional sag dynamics to purely tensional tectonics (normal faulting) by the Early Triassic (Schandelmeier et al., 2004). The Phanerozoic sedimentary basin was formed in two rifting episodes in the Permo-Triassic and Jurassic, respectively (Geiger et al., 2004, and ref-

erences therein): The continental failed rift (Karoo rift) resulted in moderately thinned crust and sedimentary infill; however, especially the Isalo formation, reaches a thickness of 5000–6000 m (Wescott and Diggens, 1998). The second rifting stage is characterized by the East Africa/ Madagascar rift locus migration towards the west (Geiger et al., 2004), the continuous rifting, and the break-up from Africa along a strike-slip boundary with passive margin formation. Co-existing NW-directed, low-angle normal faults effectively thinned the crust below the western Madagascan island (Andriampenomanana et al., 2017). The break-up was accompanied by the deposition of thick sedimentary sequences with a maximum thickness of 10 km (Pratt et al., 2017; Rindraharisaona et al., 2017). The strata exposed in the Morondava basin are classified, from east to west, as pre-, syn-, and post-Gondwana break-up sequences (Geiger et al., 2004).

Late Cretaceous volcanism (∼90 Ma) along Madagascar's east coast relates to the **separation of Madagascar from India-Seychelles** and thus the final phase of the stepwise break-up of Gondwana. Extensional rifting developed a volcanic margin and might have caused a thinner crust along the east coast through crustal extension (Rindraharisaona et al., 2017). Basaltic and rhyolitic magmas intruded the crust and formed dikes not only where volcanic outcrops are found, i.e., along the eastern margin, the Volcan de l'Androy in the Anosyen domain, and within the pre- and syn-Gondwana break-up strata of the Morondava basin (Fig. I.1), but also within the basement of the Vohibory, Androyen, Anosyen, Ikalamavony and Antananarivo domains (GAF-BGR, 2008; Martelat et al., 2014; Roig et al., 2012; Storey et al., 1995). Isotopic analyses suggest that a deep magma source plays an important role in the formation of the flood basalts (Storey et al., 1995, 1997). Neogene and Quaternary tectonic reactivation resulted in renewed volcanic activity and uplift (Roberts et al., 2012; Storey et al., 1995).

Table I.1 summarizes the geologic dynamics of tectonic processes that are important for interpreting radial anisotropy.

Table I.1: Summary of geochronological events forming the four units assembling southern Madagascar, i.e., Archean, Proterozoic, Morondava basin, and volcanics. Events rely on compressional and extensional processes, which affected the crustal structure and radial anisotropy.

Time	Archean	Proterozoic	Morondava basin	Volcanics
>610 Ma	**Formation of proto-Madagascar** Compression and accretion of terranes.			
590-530 Ma	**Pan-African collision** Compression. Folding, faulting and crustal thickening (60−70 km). Reactivation and creation of faults. Crustal thinning by delamination, gravitational collapse and erosion. Contemporary extension.			
∼290 Ma	**Post-collisional state** Pan-African Orogen partly eroded to sea-level.		**Separation from Africa** Extension. Rifting, crustal stretching and thinning. Sedimentation.	
∼90 Ma			Marion hotspot activity and dike intrusion.	**Separation from India** Extension. Rifting, crustal stretching and thinning. Flood basalt and dike formations.

2 Seismic data

We utilized seismic data from 61 three-component stations from different seismological projects (Tab. I.2, locations in Fig. I.1). The SELASOMA passive seismic experiment provides the majority of our data. Twenty-five broadband stations formed a SW-NE directing, 530 km long profile from Toliary to Mananjary across southern Madagascar with inter-station distances of 15−20 km. Another 23 short-period stations located in the south-eastern part of the island supplemented the profile from April 2013 to May 2014. The linear RHUM-RUM array covers the south-east coast of Madagascar and the MACOMO and permanent stations are distributed widely across the island.

Table I.2: Seismological networks in southern Madagascar used in this study. The SELASOMA passive seismic experiment provides the majority of our data.

Project	Project Description
SELASOMA (2012–2014)	SEismological signatures in the Lithosphere/ Asthenosphere System of Southern MAdagascar · German Research Centre for Geosciences, Potsdam, Germany · Tilmann et al. (2012)
MACOMO (2011–2013)	MAdagascar-COmoros-MOzambique · Washington University, St. Louis, USA · Wysession et al. (2011)
RHUM-RUM (2012–2014)	Réunion Hotspot and Upper Mantle · Université de La Réunion, France · Barruol et al. (2017)
	Permanent stations · GEOSCOPE (1982) · GEOFON (1993)

The seismic stations used in this study are summarized in Table I.3. Table I.A1 provides additional meta information.

Table I.3: Seismic stations and time span used in this study. The stations are broadband, except where marked SP (short period). SR: sampling rate (Hz). See also Table I.A1.

Network*	Stations	No	SR	Time span
ZE	MS01–MS25	25	50, 100	04/2012 – 05/2014
(SP) ZE	AM01–AM23	23	50	04/2013 – 05/2014
XV	MMBE, LONA, AMPY, CPSM, BKTA, MAHA	6	40	04/2012 – 09/2013
YV	RUM1–5	5	50, 100	09/2012 – 09/2014
G, GE	FOMA, VOI	2	20	04/2012 – 09/2014

* ZE–SELASOMA; XV–MACOMO; YV–RHUM-RUM; G–GEOSCOPE; GE–GEOFON

Pre-processing and cross-correlation. The raw data were baseline corrected by removing the linear trend and the mean. A lowpass filter was applied prior to decimation to prevent aliasing effects; the threshold was set to 85 % of the new Nyquist frequency (2.125 Hz). The data was down sampled to a sampling rate of 5 Hz with subsequent instrument response removal.

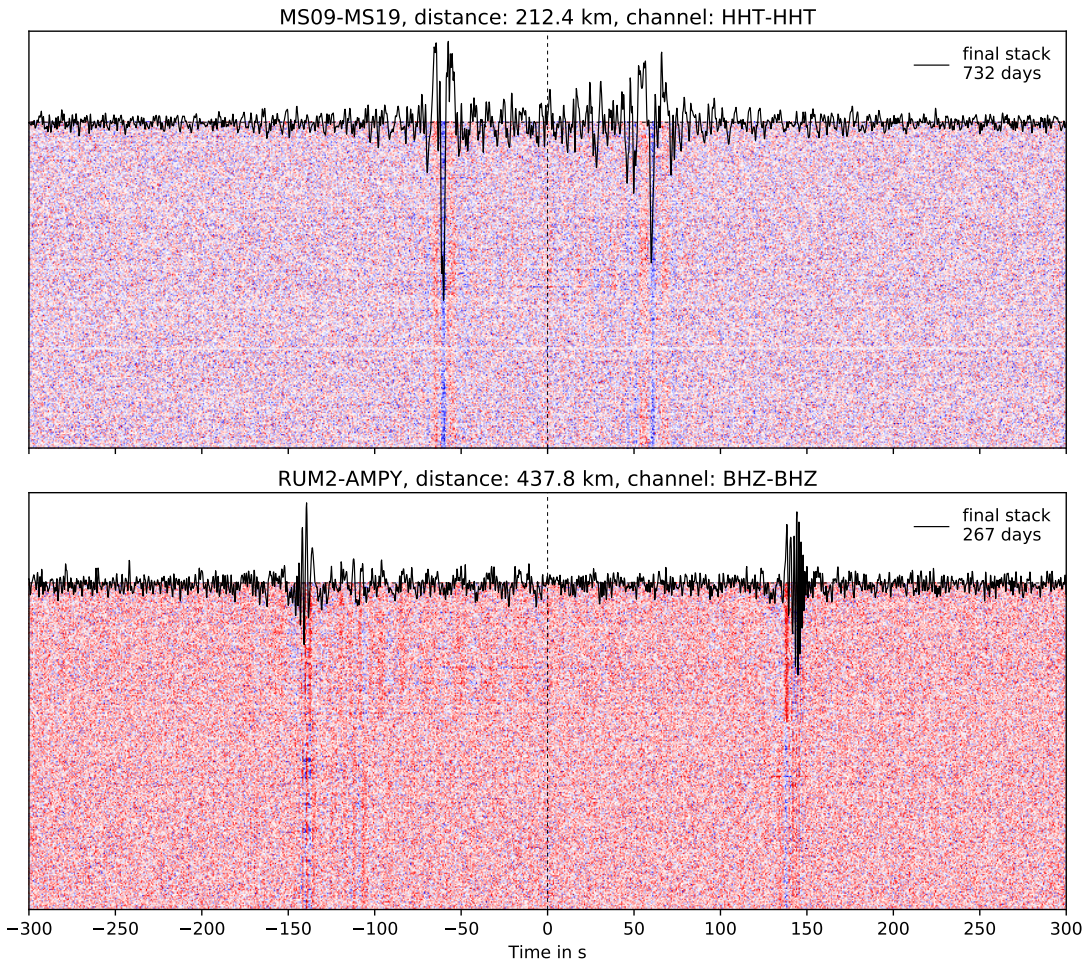

Figure I.2: Green's functions over time (colored area) and final stack (black line) for station pairs MS09-MS19 and RUM2-AMPY with inter-station distances of 212 and 438 km, respectively. Illustrated are Love (top) and Rayleigh (bottom) surface waves, which show average propagation speeds of 3.5 and 3.1 km/s. Note that the final stacks are for a different number of days (732 and 267, respectively). A frequency bandpass filter of 1–35 s was applied.

For ambient noise cross-correlation, we considered the pre-processing procedures suggested by Bensen et al. (2007). The instrument corrected data were clipped at 3 standard deviations, and bandpass filtered between 0.01–1.25 Hz. Then, spectral whitening and 1-bit normalization was applied. The cross-correlation was performed by correlating 1 hour segments of all station and component combinations and subsequent rotation of the full Green's tensor stream from the ZNE into the ZRT coordinate system. The correlograms of each station pair from one day were added to daily stacks.

Final Green's functions were computed by stacking the daily stacks for the time period available (3–747 days; median: 353 days). This resulted in 1847 correlogram stacks for each of the components. The vertical-vertical (ZZ) and transverse-transverse (TT) components were considered for Rayleigh and Love surface waves, respectively.

Green's functions and signal strength. Figure I.2 shows the development of Green's functions over time for the station pairs MS09-MS19 and RUM2-AMPY. Illustrated are the TT and ZZ components, showing strong symmetry for the causal and acausal parts. The surface

wave arrival is clearly visible throughout the entire time period at 60 and 140 s. The average propagation speeds of the waves between the two stations of each pair are 3.5 km/s for the Love, and 3.1 km/s for the Rayleigh wave.

The surface wave arrival times are constant over time. However, temporal changes, e.g., seasonal variations (alternation of rainy and dry season) or changes of noise source properties should not be underestimated. The influence of these variations are discussed in section 3.1, when measuring period dependent propagation velocities of the waves.

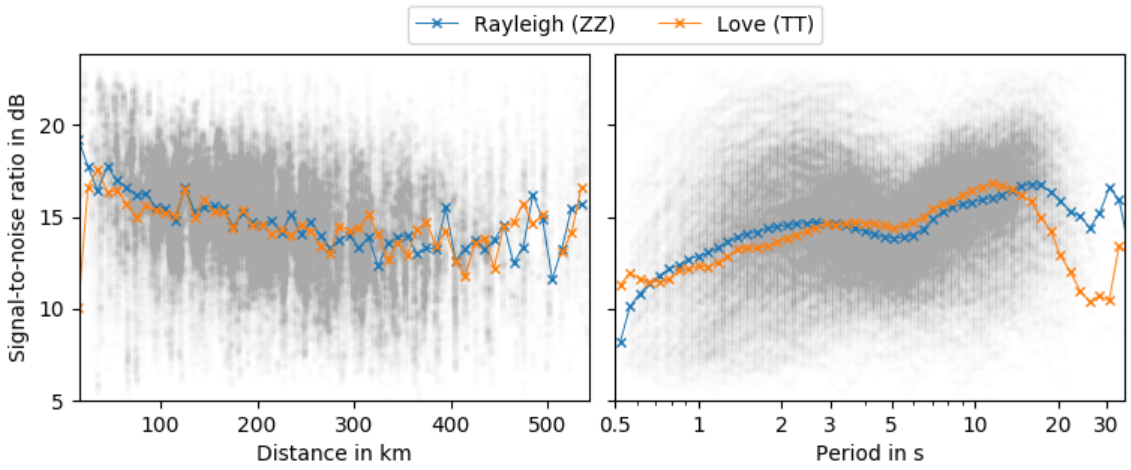

Figure I.3: Signal-to-noise ratios for symmetric Green's functions from all station pairs. SNRs are sorted by inter-station distance and filter period. Gray symbols show data for the Rayleigh component. Colored lines show bin-meaned SNRs for Rayleigh (blue) and Love waves (orange).

As a quality measure, period dependent SNRs were computed for each symmetric Green's function. The signal is defined as the maximum amplitude within the window of group speed velocities between 1–4.5 km/s. The noise was computed by the root-mean-square within the time window between 350–550 s of the trace. If the signal window exceeds 350 s, the noise window start was shifted to the end of the signal window. SNRs for Rayleigh and Love waves are shown in Figure I.3 and are sorted by inter-station distance and period.

The signal strength is strongly dependent on the inter-station distance; close stations show high SNRs, decreasing with increasing distance between the stations. SNRs dependent on the period reveal two major peaks of increased signal strength at ∼2.5 and ∼13 s of period, which could reflect the secondary and primary micro-seism peaks, respectively. Rayleigh and Love waves show relatively similar average SNRs, except for the shortest (<0.7 s) and longest periods (>14 s), where few measurements are available.

Moveout velocity. Figure I.4 shows Rayleigh and Love surface wave record sections, with station MS10 at zero distance. MS10 is located at the boundary between the Phanerozoic sedimentary basin in the west and the Precambrian crystalline crust in the east; hence, we can expect different behaviors of waves propagating through the two major units. Waves traveling through the basin show a much longer wave train compared to the waves propagating through the hard rock. This is due to the low velocities of basin sediments and the property of dispersion.

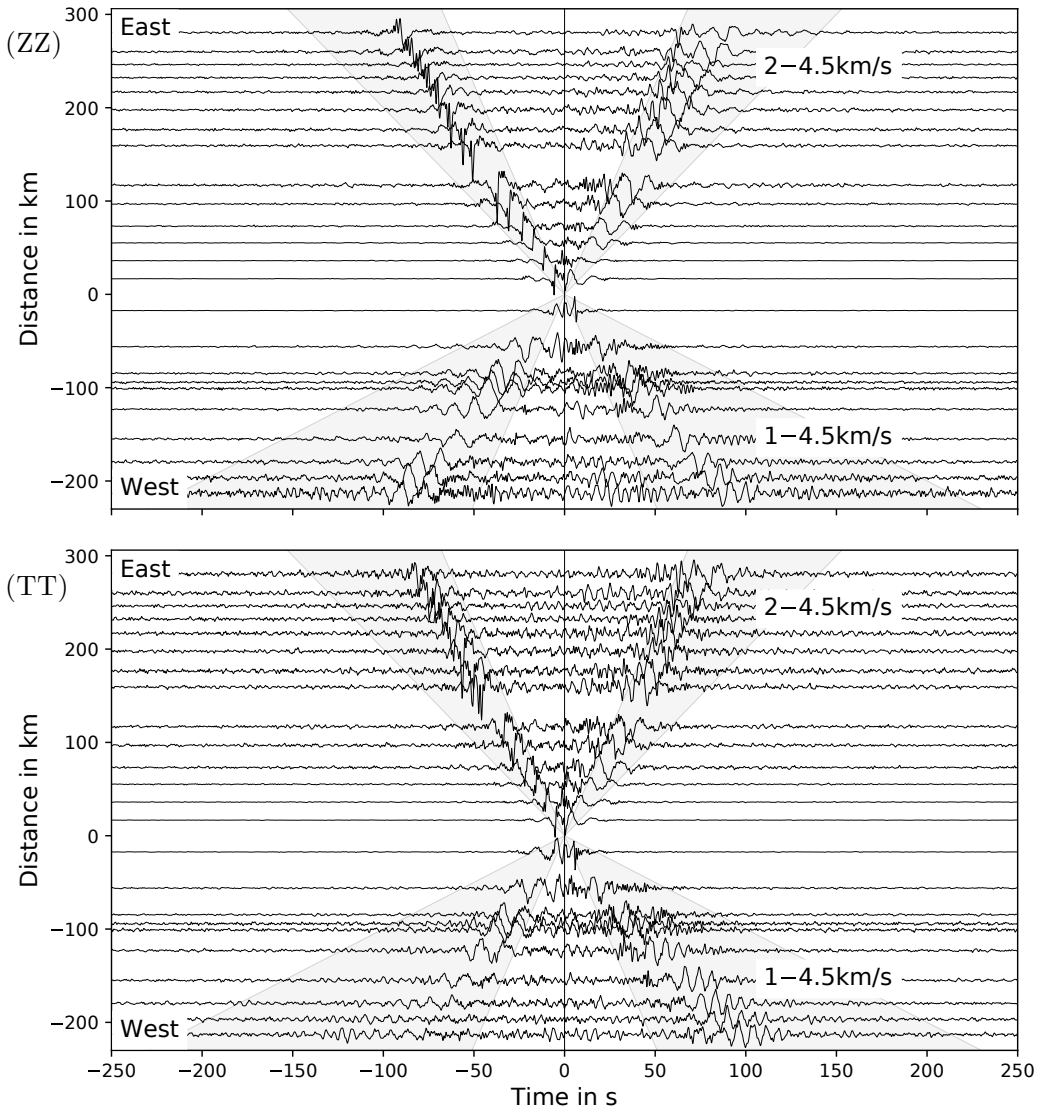

Figure I.4: Record section of Rayleigh (ZZ) and Love wave (TT) correlograms with station MS10 at zero distance. Positive and negative distances are relative to MS10 and represent the inter-station distances of stations located to the east and west, respectively. (MS10, as marked in Fig. I.1, is located at the boundary between the sedimentary basin to the west and the Precambrian units to the east). Correlograms have been filtered with a bandpass (1–35 s).

While shorter period waves sample the surface and travel with slower sedimentary velocities (late arrival times), the longer period waves sample the deeper crust (basement) and propagate with higher velocities. The eastern Precambrian units of southern Madagascar contain little to no sediments, and waves travel with steady high velocities throughout the crust. The strong dispersion visible in the west is not existent in the east.

There are also distinct differences between Rayleigh and Love waves. Rayleigh waves propagate much slower reaching moveout velocities of about 3 km/s, while Love waves show moveout velocities as high as 4 km/s.

3 Surface wave dispersion and tomography

3.1 Group velocity measurements

Dispersion curves. To avoid errors introduced by automatic picking routines, we decided for a manual picking procedure. The fundamental mode group velocity dispersion was obtained by application of narrow bandwidth Gaussian filters (multiple-filter analysis) following Dziewonski et al. (1969). The applied filters range between 0.5–50 s with 150 discrete filter periods, log-spaced within the given span. As the causal and acausal parts show good symmetry (see chapter 2), both parts were taken into account. Instead of adding the negative and positive time lag to compute a symmetric component (as in Bensen et al., 2007), their energy (envelope) was added. This ensures constructive adding of the traces and avoids destructive summation.

Examples of multiple-filter analyses are shown in Figures I.5 and I.6 for three station pairs for Rayleigh and Love wave, respectively. Each station pair was evaluated visually. If a period−group velocity dependence was obvious and clear, the dispersion curve was picked. If the picking was unclear for the entire trace or in specific period ranges, the station pair or the specific period range was discarded.

After Bensen et al. (2007), we considered only periods, where a minimum of three wavelengths propagated within the inter-station distance Δ to ensure a sufficient separation of the surface wave package from precursory arrivals and noise, and to satisfy the far-field approximation (Xie et al., 2013). As indicated in chapter 2 the wave propagation velocity can be as high as 4 km/s. For computing the maximum reliable period T_{max} for each station pair, a velocity of 4 km/s was considered. Reliable periods T are defined by

$$T < T_{max} = \Delta/12 \text{ s} \tag{I.2}$$

The three wavelength criterion was applied after picking. Two types of group velocity dispersion are observed for southern Madagascar:

(1) Increasing velocities with increasing periods; ray paths are (completely or partly) through the sedimentary basin, e.g., MS01–MS08 (Figs. I.5a, I.6a).

(2) Constant velocity throughout all of the periods; ray paths travel through Precambrian units, e.g., MS17–MS09 and MS12–BKTA (Figs. I.5b,c, I.6b,c).

Figure I.7 (bottom plots) show all retrieved dispersion curves in the study area, distinguished by the region the ray is traveling through, i.e., the Morondava basin, Proterozoic, Archean and Cretaceous volcanics with geologic borders as in Figure I.1. Each of these regions is described below based on the dispersion measurements. Note that the number of dispersion curves picked in each region is significantly different (Tab. I.4).

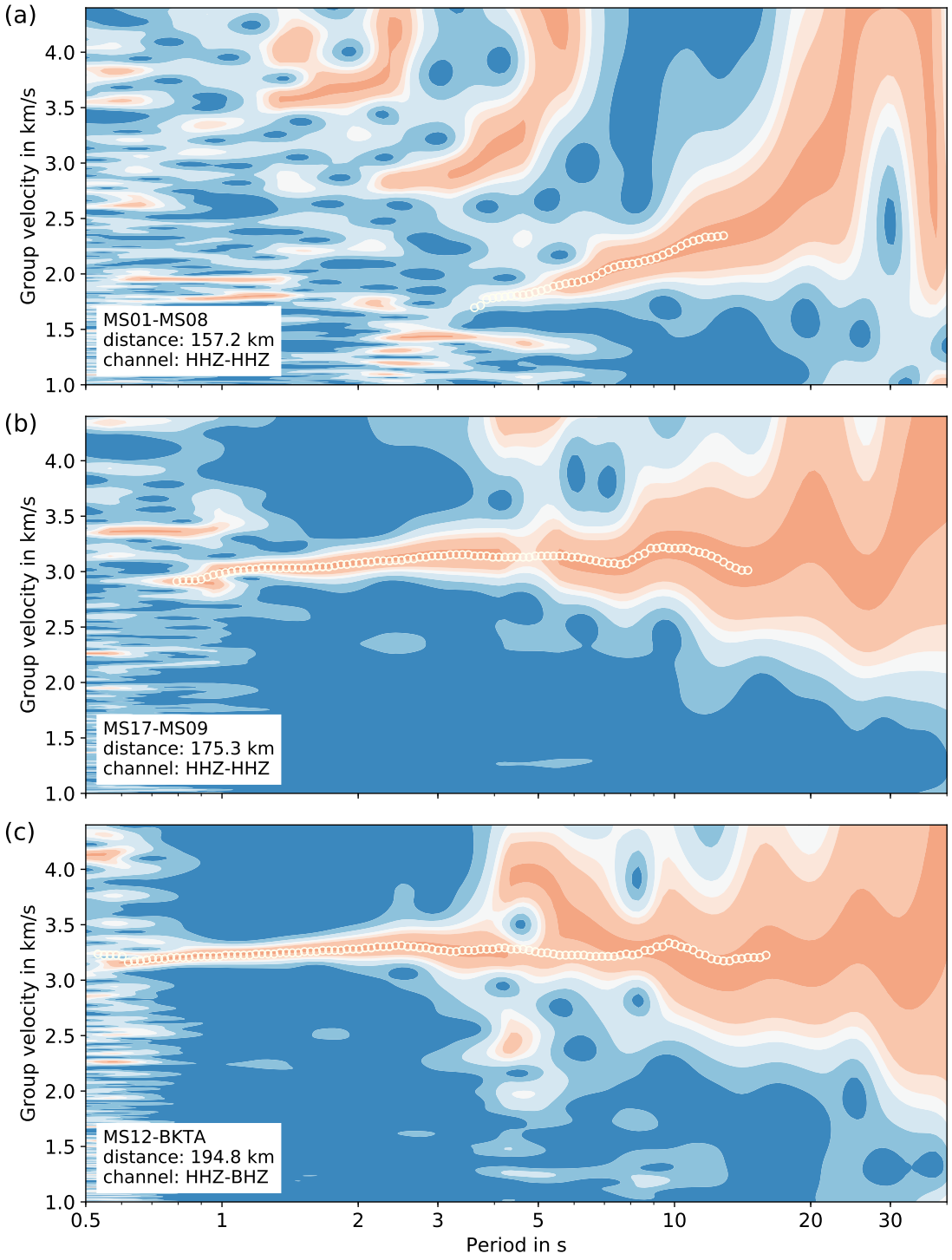

Figure I.5: Multiple-filter analysis for three different station pairs for the Rayleigh wave. Each trace is normed to its maximum. White symbols are manually picked dispersion velocities (after application of the three wavelength criterion). The darkest orange contour band shows the 97.5 % amplitude interval used for uncertainty estimation.

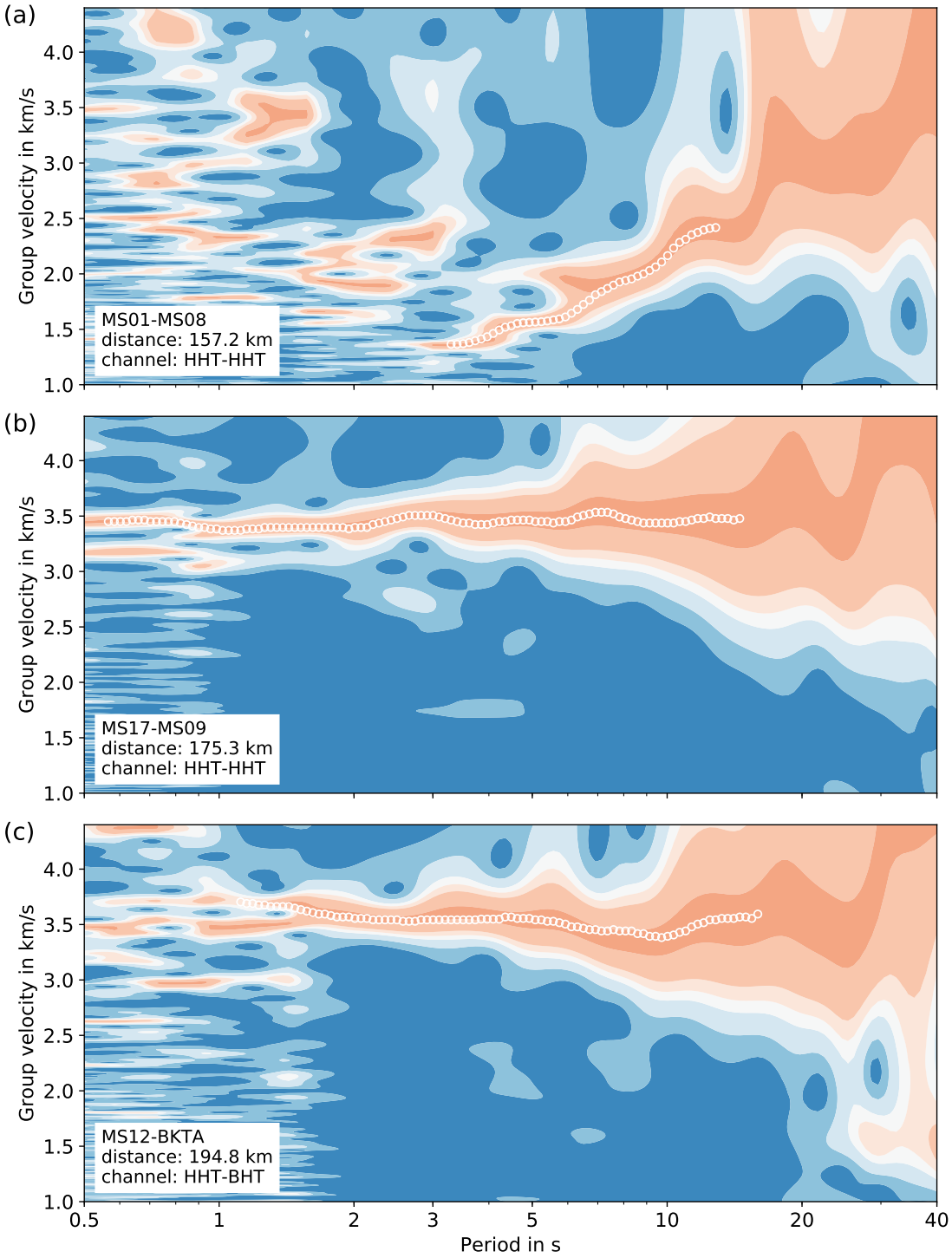

Figure I.6: Multiple-filter analysis for three station pairs for the Love wave. See caption of Figure I.5.

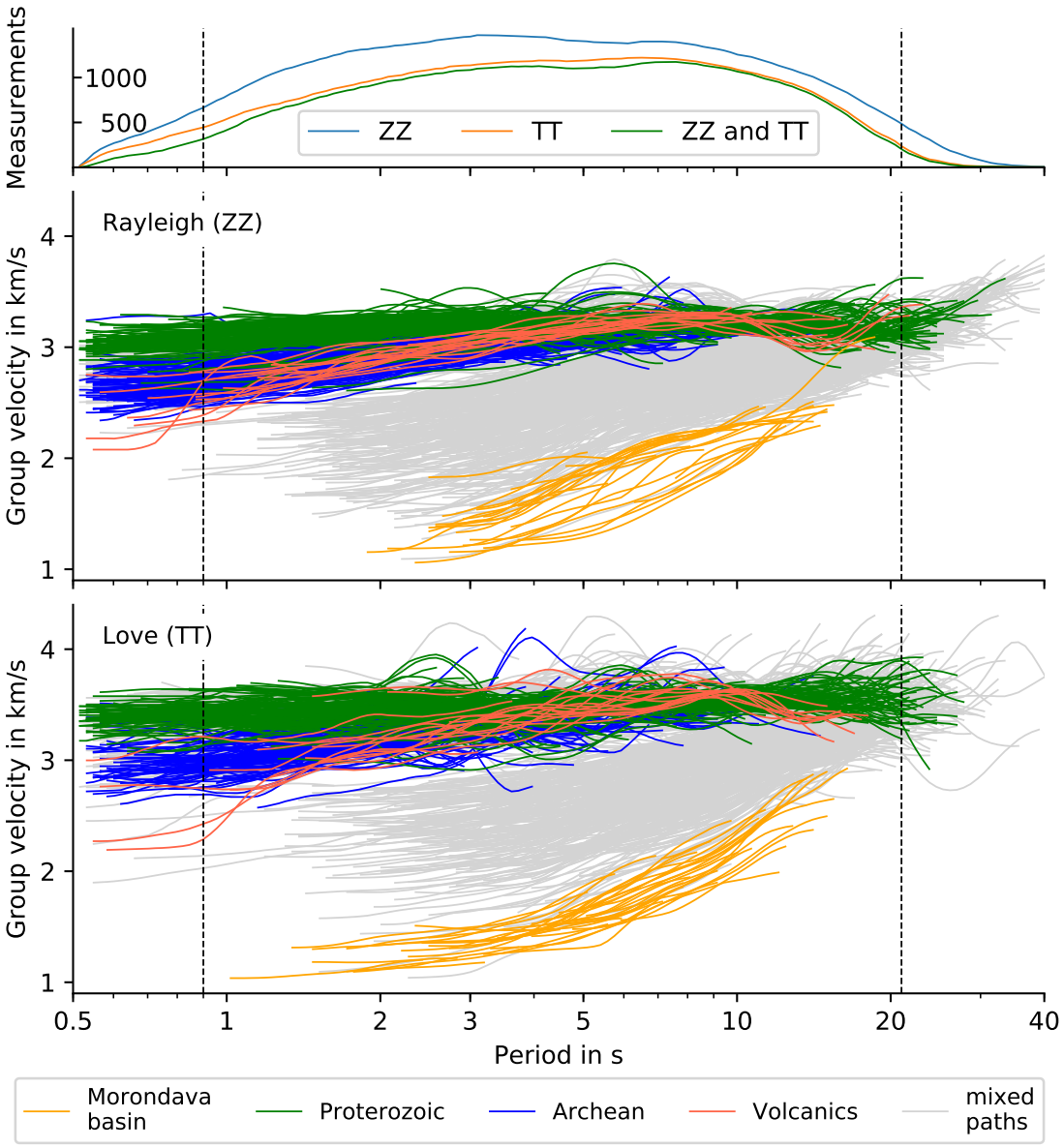

Figure I.7: (top) Number of group velocity measurements for Rayleigh (blue) and Love waves (orange), and number of common ray paths (green). (bottom plots) Group velocity dispersion curves colored after ray path region, i.e., the Morondava basin, Proterozoic, Archean and Cretaceous volcanics (see Fig. I.1). Gray colored dispersion-relations represent station pairs and their ray paths within southern Madagascar crossing geologic borders. Dashed lines indicate the interval (periods: 0.9–21 s) chosen for tomography.

Morondava basin: The measured group velocities cover a relatively broad range: Due to thick sediments they are as low as 1 km/s. With increasing periods the velocities increase continuously up to 2.5–3 km/s. Rayleigh and Love wave velocities behave similarly throughout the period range. Dispersion curves were determined between 1–15 s of period.

Proterozoic: The velocity range is narrow compared to the Morondava basin and to the Archean region. The majority of Rayleigh wave velocities are 3–3.3 km/s with slightly lower velocities for periods shorter than 1 s. For Love waves, velocities dominantly are 3.2–3.6 km/s. Dispersion curves could be determined for periods between 0.5–23 s.

Archean: The velocities show a much wider range in comparison to the Proterozoic region. For Rayleigh waves, the majority of velocities are 2.5–3.3 km/s with lower velocities for the shorter periods (<2 s). Love wave velocities range between 2.7–3.9 km/s. Dispersion relations could be estimated for periods between 0.5–13 s.

Cretaceous volcanics: Group velocities are placed at the lower velocity border in the Archean region. For Rayleigh waves, the velocities increase from ∼2.7 to 3.1 km/s between periods of 1.3–7 s and remain constant at 3.1 km/s up to 11 s. Love waves show a broader range of velocities, which are generally higher and reach 3.5 km/s.

mixed paths: This label is a collective for ray paths crossing geologic borders; the waves sample at least two units while traveling between the stations. Hence, the velocities cover a wide range between 1.5–3.5 km/s for the Rayleigh and 1.5–3.9 km/s for the Love waves. Velocity measurements include periods up to 40 s.

Table I.4: Number of measured group velocity dispersion curves corresponding to the major geologic regions.

Region	Rayleigh wave	Love wave
Morondava basin	28	36
Proterozoic	181	165
Archean	153	126
Volcanics	20	19
mixed paths	1324	1149
southern Madagascar	1706	1495

The number of group velocity measurements per period is illustrated in Figure I.7 (top). For Rayleigh waves, they vary between 2–1476, with the period of the maximum pick number being 3 s. For Love waves, they are between 1–1239, with the period of the maximum number of picks being 6.5 s. The greatest number of group velocity measurements are within the period range of 1–15 s, with a down drop at 4–7 s. This can be explained by the signal-to-noise ratios (Fig. I.3), which show a similar period dependency. The period range taken into account for further analysis is limited by a minimum group velocity pick number of 200, and is based on actual tomography results. An appropriate number of ray paths and a balanced path distribution are obtained for periods between 0.9–21 s.

Travel time uncertainty estimation. Temporal changes of the seismic ambient noise fields, such as seasonal effects, wandering noise source locations, amplitude over time, and to a minor extent wave velocity differences, influence the properties of the waves traveling between seismic stations. Through stacking of the correlograms, these effects will be balanced out by constructive summation of the arrival time signal and destructive summation of random amplitudes, but are still existent in the Green's functions, if temporal changes are stable over a longer time period.

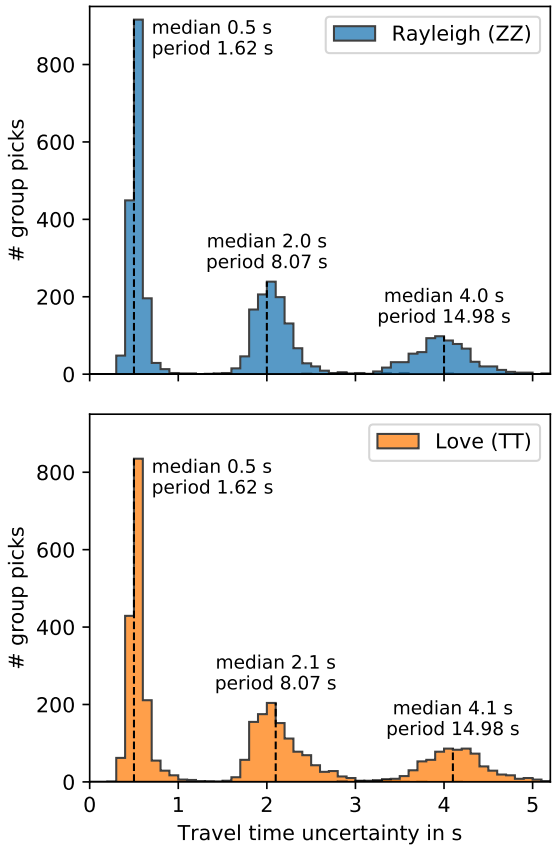

Figure I.8: Relative travel time uncertainties for periods of ∼1.6, 8 and 15 s, estimated by the half width of the arrival time peak at 97.5 % of its maximum amplitude. The travel time uncertainties are as precise as 0.2 s, congruent with the sampling interval of the data.

An indicator for the correlograms' stability is the width of the arrival time signal's envelope in the final stack: If there was no change in travel time velocity (at a specific period) throughout the entire time period, the final surface wave stack will show a sharper signal (at this period) compared to a surface wave from a region which experienced large variations. Also, effects of unbalanced symmetry of the causal and acausal parts are captured in the stacked surface wave signal. Hence, the sharpness of the wave arrival can be used as a comparative measure of quality for surface wave signals from different station pairs, and thus provide a weight for travel time tomography.

We used an automatic process to estimate the relative travel time uncertainty for each period and station pair. Thereby, we measured the half-width of the arrival-time envelope peak at 97.5 % of its maximum amplitude. Cotte and Laske (2002) and Harmon et al. (2007) used thresholds of 98 % and 85 %, respectively, to best serve their data. Time uncertainties are illustrated in Figure I.8 for three different periods. The dominant effect on the envelope peak width is controlled by the period of the Gaussian filter. The broadening due to timing variations of the wave over time exists as a secondary effect. Hence, we can compare the relative errors within, but not between periods. The range of uncertainties and the median are slightly higher for Love waves.

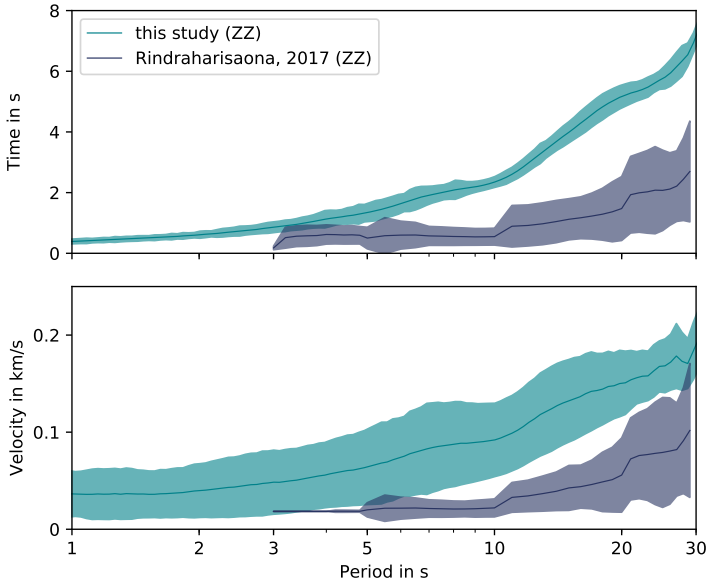

Figure I.9: Time and velocity uncertainties derived by this study and Rindraharisaona et al. (2017) for the Rayleigh wave component. Our uncertainties are on average 3 times larger.

Figure I.9 shows a comparison between the uncertainties for Rayleigh waves derived in this study and uncertainties from Rindraharisaona et al. (2017), where errors are estimated from seasonal changes. Our data-driven estimations of time and velocity uncertainties are 2–4 times as large as their estimates with an average ratio of 3.

As the tomography package (FMST) accounts for relative ray path weighting, we used the values from our method.

Travel time tomography. The travel time tomography was performed using the Fast Marching Surface wave Tomography package (FMST; Rawlinson and Sambridge, 2005), which uses a finite-difference solution of the Eikonal equation to solve the forward problem, and implements a subspace inversion to solve the inverse problem. The procedure is iterated several times, such that the ray paths and travel times adapt to the changing model.

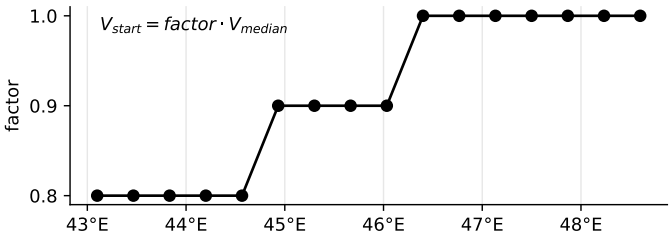

Figure I.10: Initial velocity model for tomographic inversion. Velocities increase towards the east, to imitate the geological units in southern Madagascar. The median velocity is dependent on the period.

The inversion grid covers the area shown in Figure I.1 (43.1 to 48.6°E, 25.7 to 20.6°S) and is represented by 13 x 16 nodes with cell dimensions of about 47 and 37 km in longitude and latitude directions, respectively. The larger number of grid cells along the latitude is motivated by the dense station spacing in W-E direction. As initial velocity model a staircase model was used (Fig. I.10), defined by a stepwise increase of velocities towards the east. The start velocities are based on the median group velocity from the data, which is dependent on the period.

The initial velocity model has a significant influence on the tomography results and the travel time residuals between observed and computed travel times. We first applied two constant velocity starting models based on the median and mean velocity for each of the periods: But basin supporting ray paths were declared as outliers (see below) and removed as they do not fit the median and mean velocities well enough. As a result, the western regions became sparse in ray coverage and the border between the Morondava basin and the Proterozoic unit ended far to the west, incompatible with geologic surface evidence. To suppress the inversion shifting this geologic boundary towards an unrealistic direction, we also tested the application of higher weights for ray paths in the basin and crossing basin boundaries. Our solution to improve the results (and to avoid introducing additional parameters) was the usage of the staircase starting velocity model.

Other parameters that control the inversion are mainly the damping and smoothing factors. Also important are the number of iterations and the percentage of outliers that will be removed. Based on initial tests, we chose a smoothing factor of 3, a maximum number of 7 iterations, and an allowance of 1.5 % outliers. Outliers are removed at the 3rd and 5th iteration and are not recycled in ensuing iterations.

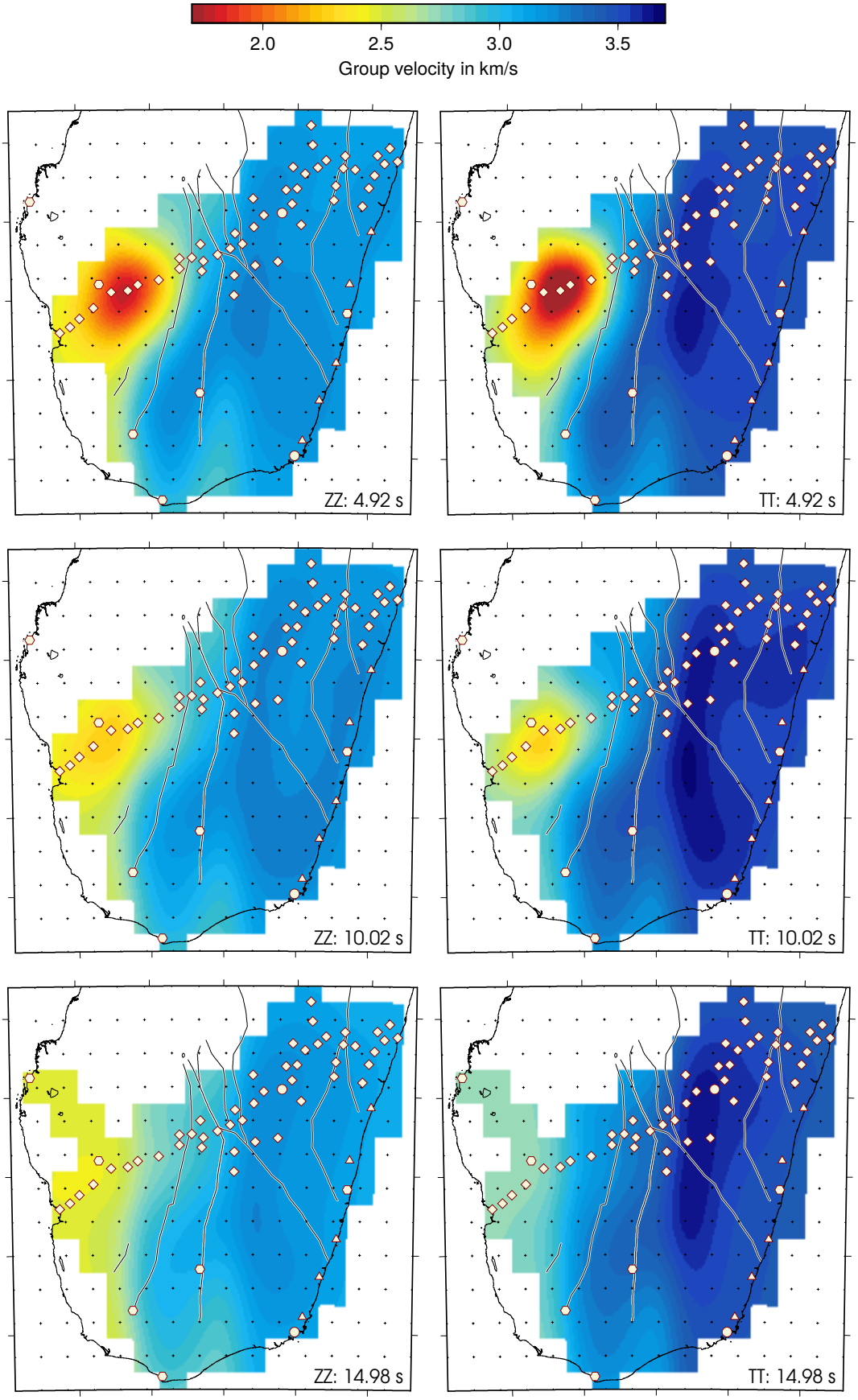

Figure I.11: Tomographic inversion results for Rayleigh and Love wave group velocities for different periods. Black crosses indicate grid cell nodes. Grid cells are only colored if rays are propagating through. Black lines correspond to shear zones, red symbols to seismic stations.

In order to find the optimum damping factor for each period, we constructed trade-off curves from a set of 25 trial values (log-spaced between 0.01–1000). The computed data misfits and model variances form L-curves (Fig. I.B1), with optimum damping factor chosen to minimize both. Because optimum damping factors for Rayleigh and Love waves are similar, we used their mean value for the tomography. Optimum damping factors for all periods are shown in Figure I.13, and are between 5–147 for the periods of 0.9–21 s.

Figures I.11 and I.B2 show tomographic results for Rayleigh and Love group velocities for periods of 1, 5, 10, 15 and 20 s, with corresponding travel time residuals in Figure I.12. Independent from the period and the wave type, the western part of the southern island is characterized by low velocities (1.3−2.7 km/s), corresponding to the Morondava basin west of the Ampanihy shear zone. The central and eastern parts of southern Madagascar show much higher velocities (2.7−3.7 km/s). Slightly increased velocities are observed between the central shear zones Beraketa and Bongolava-Ranotsara, often continuing north crossing the latter fracture zone. For the Morondava basin, Rayleigh and Love waves show similar low velocities for the shorter periods. For the longer periods, Love waves are slightly faster. In the Precambrian regions, Love waves are generally about 0.2−0.5 km/s faster than the Rayleigh waves.

Figure I.13 summarizes period-specific parameters from group velocity tomography. The number of ray paths and the damping factor show a vague but no apparent correlation. Generally it is observed that more data require a higher damping factor to achieve a balance between data and model variance. The median group velocities for Love waves are ∼0.3 km/s faster than for Rayleigh waves throughout all of the periods. For periods longer than 20 s the velocities increase strongly for Rayleigh and moderately for Love waves; this effect is due to the rapid thinning of velocity information at longer periods (compare Fig. I.7). These values are outside the period interval considered for reconstructing dispersion curves.

The RMS travel time residuals are as low as 1.1 s and do not exceed 3.5 s until periods of 15.5 s (Love waves). The misfits are constantly increasing from periods of 12 s, reaching a maximum of 8.7 s (Rayleigh) and 15 s (Love) at 32.5 s period. Beyond the period of 21 s the travel time misfits rapidly climb up for both wave types, which can be explained by the steadily decreasing number of data and the increasing uncertainties at those high periods. Residuals for

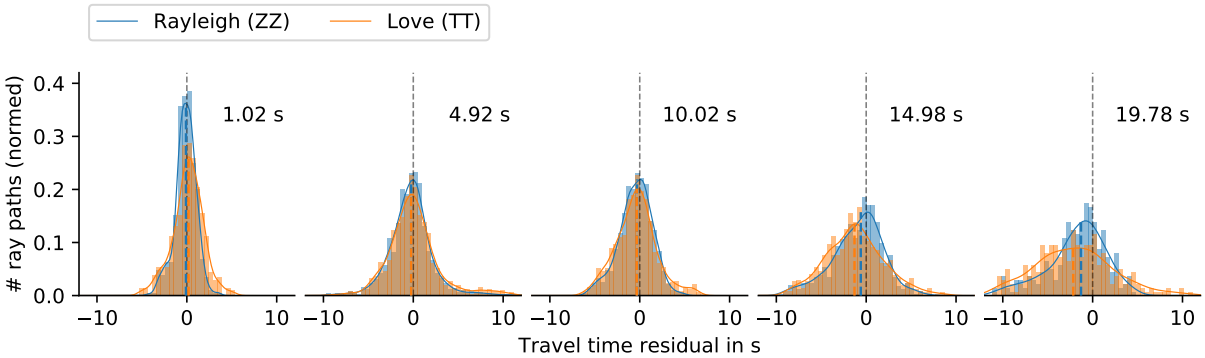

Figure I.12: Travel time residual distributions from tomographic inversions of Rayleigh and Love wave group velocities at periods 1, 5, 10, 15 and 20 s (Figs. I.11 and I.B2). The colored dashed lines correspond to the mean residuals.

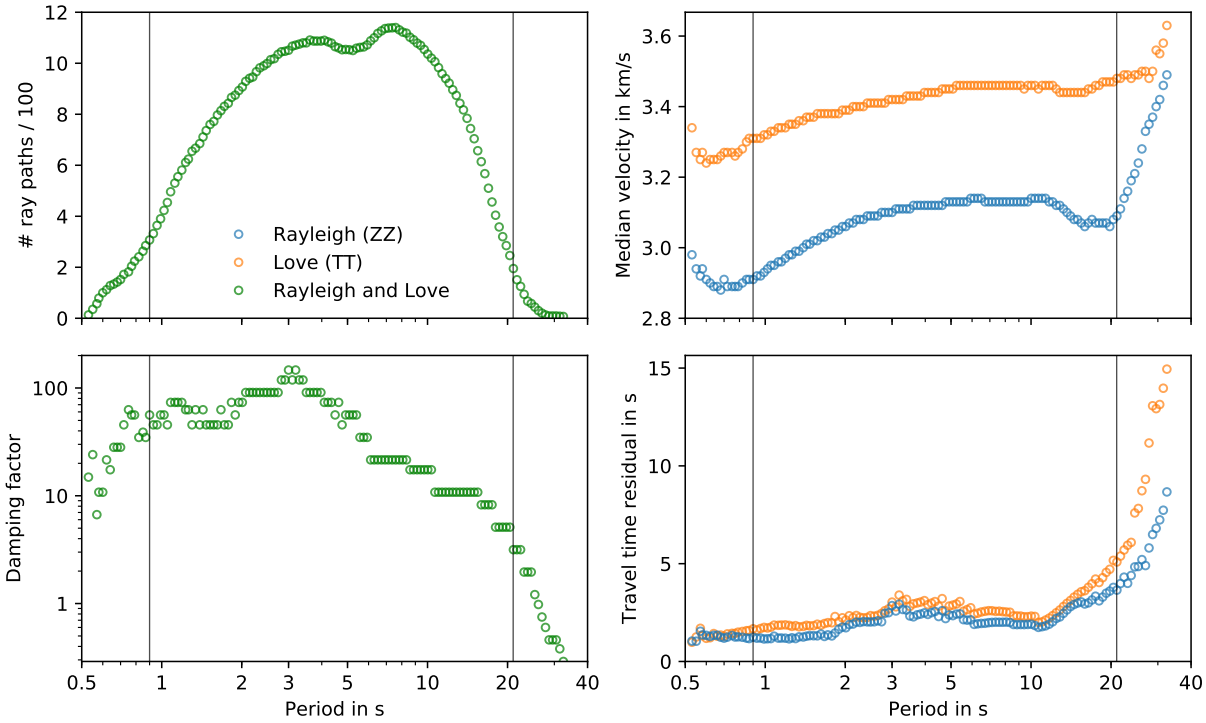

Figure I.13: Number of ray paths (excluding outliers), median velocities, optimum damping factors and average RMS travel time residuals from tomographic inversions of Rayleigh and Love wave group velocities. Vertical lines indicate the interval (periods: 0.9–21 s) for further analysis.

periods of 0.9–21 s are between 1.1–3.8 s (Rayleigh) and 1.6–5.1 s (Love) and show mean values of 2.1 and 2.6 s, respectively.

3.2 Phase velocity measurements

Dispersion curves. Phase velocities offer additional information to group velocities and also stabilize the velocity-depth inversion (section 4.2). Properties of group velocities that make it preferable to use phase velocity observations are listed below (from Boschi et al., 2012).

(1) The envelope peak is less precisely defined than the phase of the carrying sinusoidal wave.

(2) Group velocity depends on, and is in turn used to image, structure over a narrower and shallower depth range than phase velocity. Phase velocity is particularly helpful to resolve larger depths (fundamental mode).

(3) A group velocity measurement requires a wider time window than a phase velocity measurement, and contamination by interfering phases is thus more likely.

Phase velocities were determined by zero crossings of the real part of the correlation spectrum (Aki, 1957; Ekström et al., 2009). The computation leads to an amount of period–phase velocity dependencies due to the 2π ambiguity (Fig. I.14). Hence, average phase velocity dispersion was computed (Prieto et al., 2009), and used as a guide for individual dispersion curve picking. As our study area provides a variety of dispersion behaviors (Fig. I.7), reference curves were computed for each ray path region (Morondava basin, Proterozoic, Archean, volcanics), and for

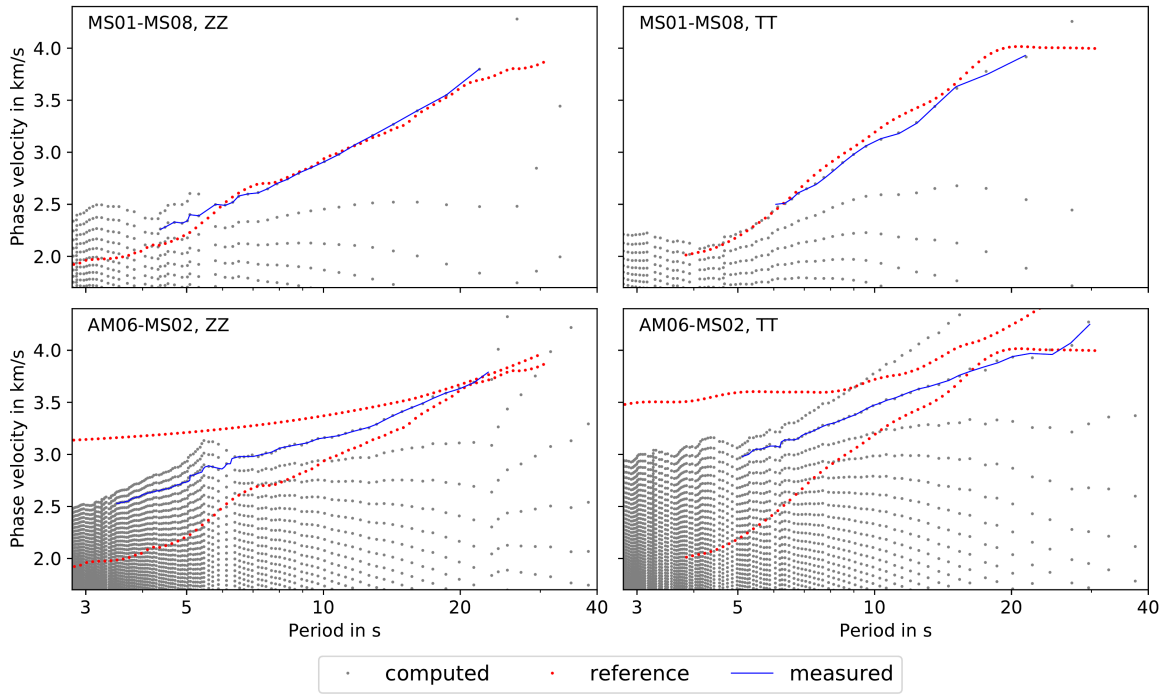

Figure I.14: Measurements of phase velocities for two station pairs from the Rayleigh and Love components. Gray dots: amount of computed period–phase velocity dependencies due to 2π ambiguity. Red dots: reference curve or interval. Blue line: measured phase velocities.

each component. For region crossing ray paths, both the basin and Archean reference curves were considered (Fig. I.14, bottom). We measured phase velocities using the tool GSpecDisp (Sadeghisorkhani et al., 2017).

Phase velocities were picked, as long as they result in a smooth and continuous curve (Fig. I.14); this includes cycle skipping velocities. To validate the measured velocities (group and phase), theoretical group velocities were computed from the measured phase velocities, and compared with the measured group velocities (Fig. I.15). Phase velocities were interpolated to match the discrete periods where group velocities are available. The measured and theoretical group velocity curves show a consistent trend, which verifies the velocity values themselves and the methods for obtaining them. The theoretical velocities oscillate around the picked group dispersion curves with differences <0.2 km/s. The two station pairs illustrated in Figure I.15 show representative examples for the complete data set, which shows velocity differences <0.3 km/s.

Figure I.16 (bottom plots) shows phase velocity measurements for the study area, for Rayleigh and Love waves, respectively. The numbers of extracted dispersion curves are summarized in Table I.5. In comparison to group velocities (Tab. I.4), about 21 % less Rayleigh and 27 % less Love wave measurements were taken.

Morondava basin: The phase velocities are as low as 2 km/s. With increasing periods the velocities increase continuously up to 4 km/s. Dispersion curves could be determined between periods of 2.5–25 s (Rayleigh) and 2.5–20 s (Love).

Proterozoic: Velocities increase from 3.2 to 4.2 km/s (Rayleigh) and from 3.5 to 4.5 km/s (Love) within the period range of 1–35 s. Dispersion relations were measured between 1–40 s.

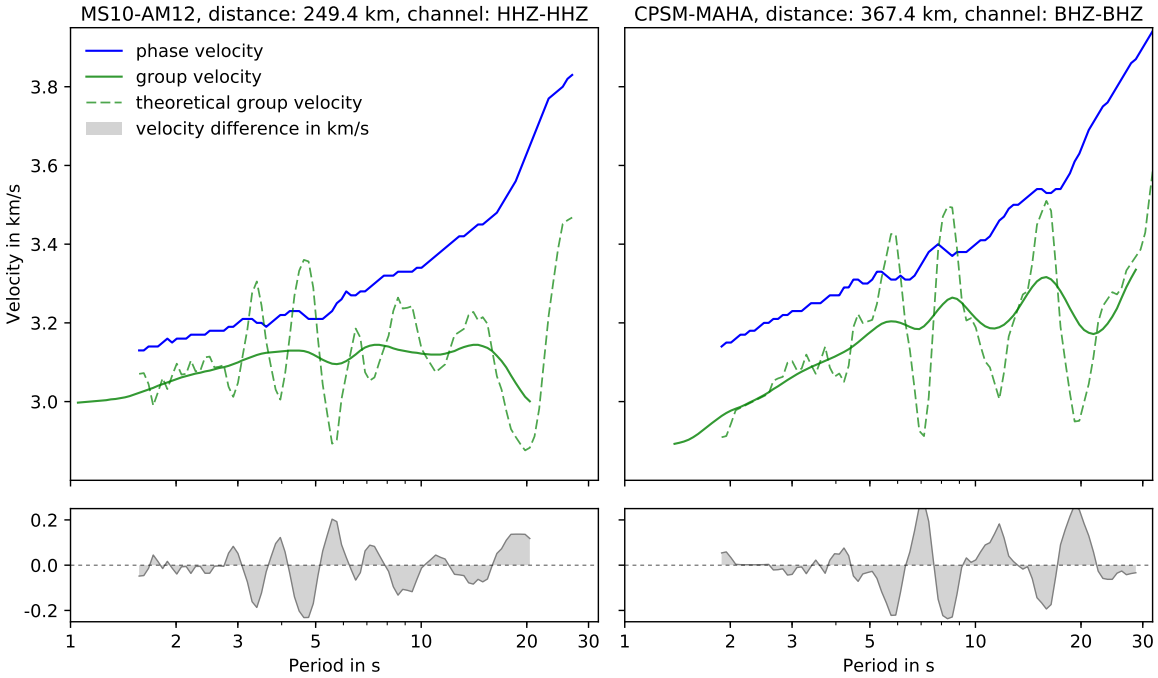

Figure I.15: (top) Measured group and phase velocities (solid lines) and theoretical group velocities (dashed line) computed from phase velocity measurements for two station pairs. A smoothing over three samples was applied to the phase velocity curve. (bottom) Difference of measured and theoretical group velocities.

Archean: The velocity range is much wider in comparison to the Proterozoic region. For Rayleigh waves, the majority of velocities are between 2.8–4.0 km/s. Love wave velocities are between 3.0–4.4 km/s. The periods covered are between 1–32 s.

Cretaceous volcanics: Phase velocities show intermediate values within the range of the two Precambrian units. Rayleigh wave velocities increase from 3 to 3.7 km/s between periods 1–26 s, and Love wave velocities from 3.2 to 4 km/s between periods of 1–20 s.

mixed paths: The velocities show a broad range between 2.3–4.5 km/s with Love waves around 0.2 km/s faster than Rayleigh waves for all periods.

Table I.5: Number of measured phase velocity dispersion curves corresponding to the major geologic regions.

Region	Rayleigh wave	Love wave
Morondava basin	42	44
Proterozoic	149	119
Archean	142	111
Volcanics	19	12
mixed paths	994	801
southern Madagascar	1346	1087

Figure I.16 (top) illustrates the period dependent number of measured phase velocities. The shape of those curves differ from that of the group velocities (Fig. I.7, top). A strong increase of measurements is observable from ∼6 s period. At shorter periods less velocity measurements

were accomplished due to the high ambiguity through increasing density of phase cycles and an increasing number of step-like velocity changes between adjacent zero crossings (Fig. I.14).

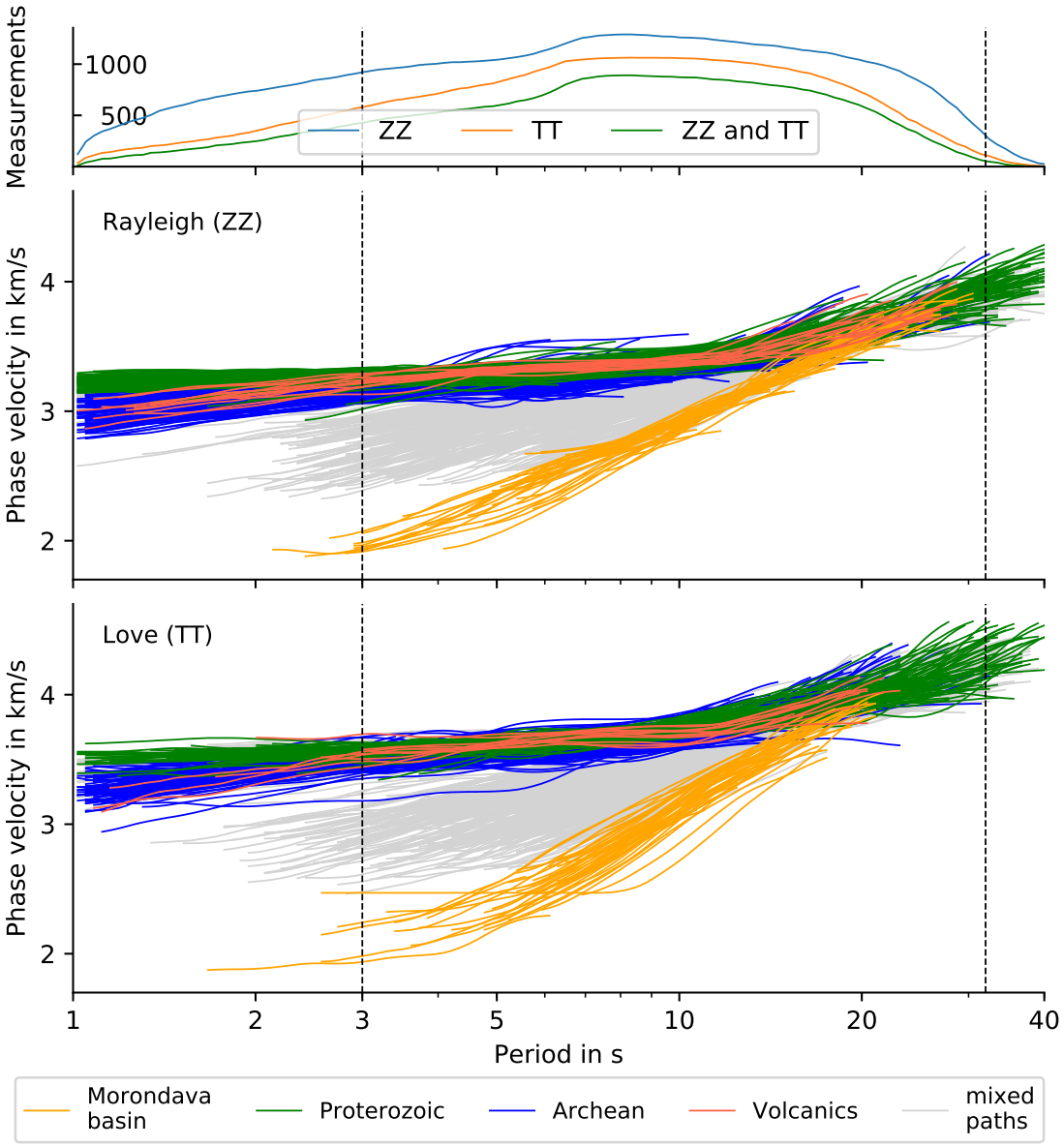

Figure I.16: (top) Number of phase velocity measurements, and (bottom) phase velocity dispersion curves colored after ray path region. The periods chosen for tomography are 3–32 s. See caption of Figure I.7.

Travel time tomography. The travel time tomography for phase velocities was performed using the FMST package as described in section 3.1. The inversion grid parametrization, the starting velocity model, number of iterations, smoothing factor and the percentage of outliers are equal to the group velocity tomography. Travel times for each period were equally weighted. Damping factor trade-off curves (Fig. I.B3) were constructed from a set of 25 trial values (log-spaced between 0.01–1000). The optimum damping factors received for Rayleigh and Love waves are similar, hence, a mean value was computed for each period. Damping factors for all periods are shown in Figure I.19 and range between 8–56 for periods of 3–32 s.

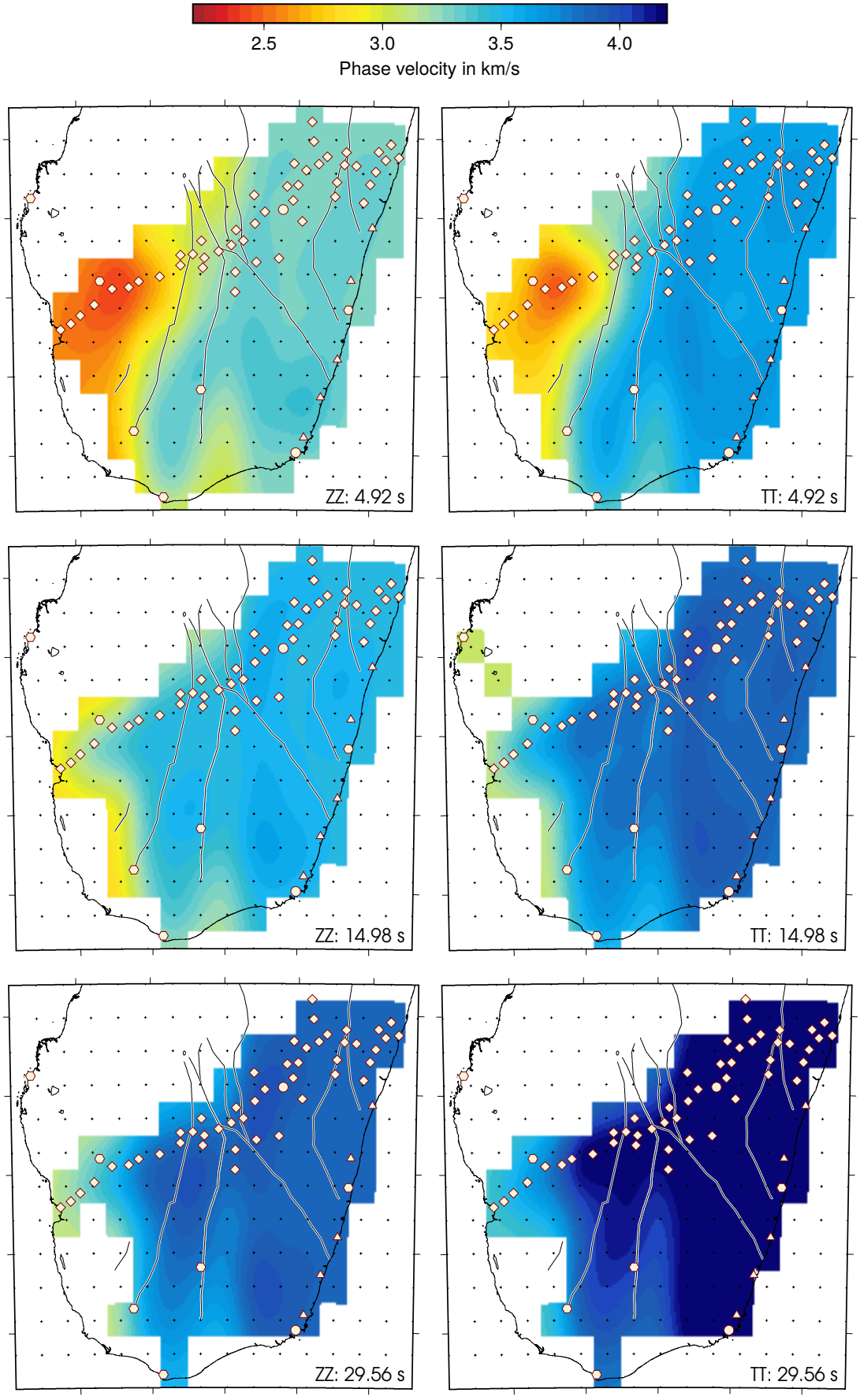

Figure I.17: Tomographic inversion results for Rayleigh and Love wave phase velocities for different periods. See caption of Figure I.11.

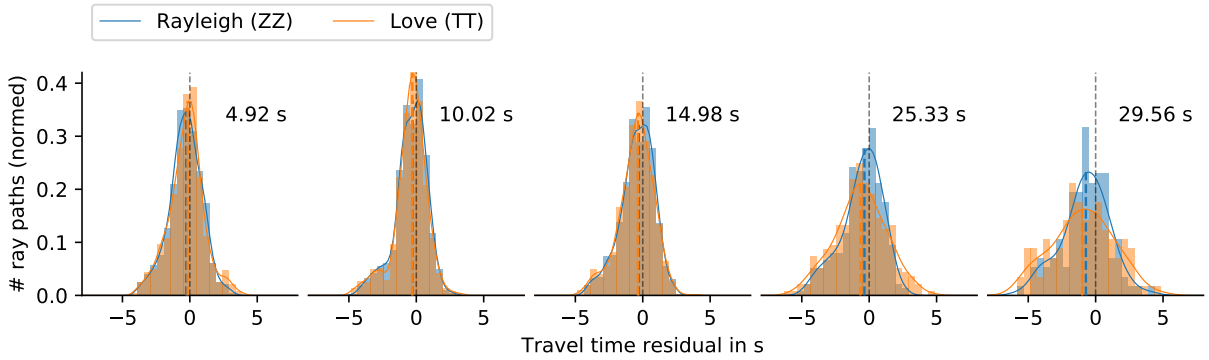

Figure I.18: Travel time residual distributions from tomographic inversions of Rayleigh and Love wave phase velocities at periods of 5, 10, 15, 25, and 30 s (Figs. I.17 and I.B4). The colored dashed lines correspond to the mean residuals.

Tomography results for Rayleigh and Love waves are shown in Figures I.17 and I.B4 with corresponding travel time residuals in Figure I.18. The western part of the southern island is characterized by low velocities (2.2–3.2 km/s), corresponding to the Morondava basin west of the Ampanihy shear zone. The central and eastern parts of southern Madagascar show much higher velocities (3.2–4.3 km/s). Slightly higher velocities are observable between the central shear zones Beraketa and Bongolava-Ranotsara, often continuing north crossing the latter fracture zone (periods <10 s). For the higher periods, high velocity anomalies additionally occur between the Ampanihy and Beraketa shear zones, and west of the Ampanihy shear zone. The velocity contrast between the Phanerozoic and Precambrian units decreases with longer periods, as the basin gives way to the basement. Also, Love waves show higher velocities than Rayleigh waves.

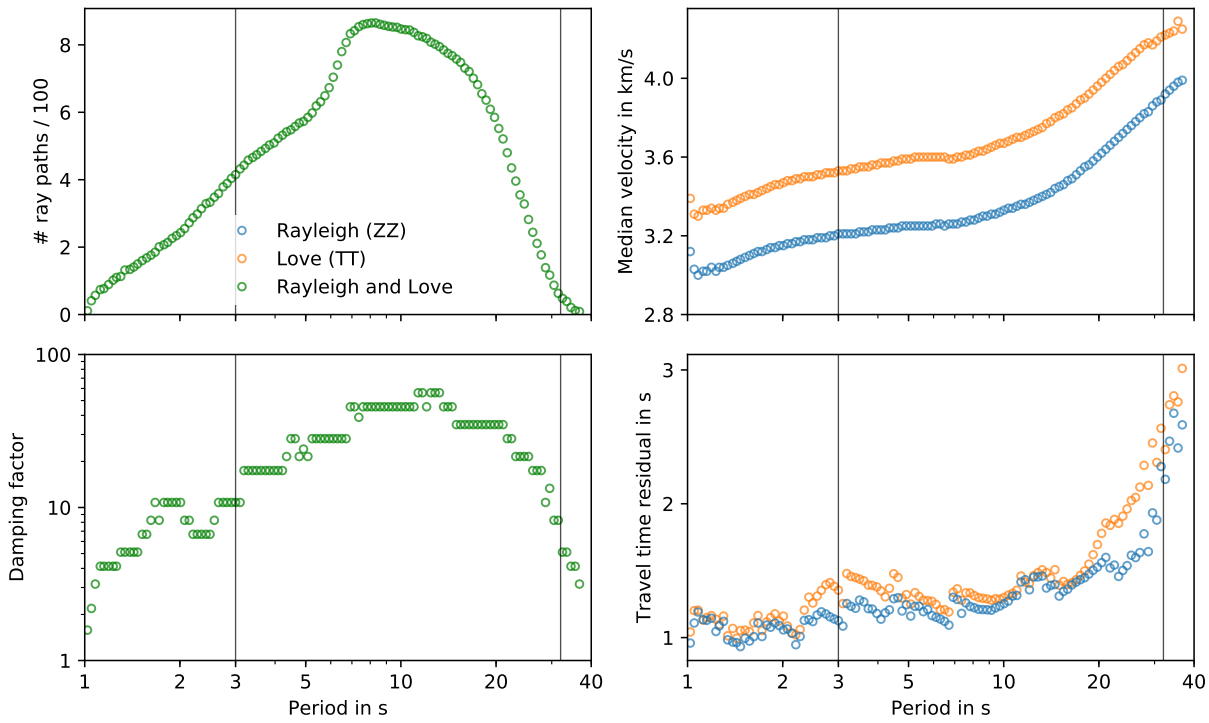

Figure I.19: Number of ray paths (excluding outliers), median velocities, optimum damping factors and average RMS travel time residuals from tomographic inversions of Rayleigh and Love wave phase velocities. Vertical lines indicate the interval (periods: 3–32 s) for further analysis.

Figure I.19 displays period-specific parameters from phase velocity tomography. The number of ray paths and the damping factors correlate, i.e., a larger amount of measurements demanded a higher damping to achieve an optimum balance between data misfit and model roughness. The median phase velocities of Love waves are ∼0.3 km/s faster than those of the Rayleigh waves throughout the complete period range. Between periods of 3–32 s the travel time residuals are between 1.1–2.3 s for Rayleigh, and 1.2–2.6 s for Love waves, and show a mean of 1.3 and 1.5 s, respectively. Travel time residuals are significantly smaller compared to those from group velocity tomography. This is expected, as the phase of a wave is more precisely defined (Boschi et al., 2012) and measurements are more stable and coherent within a each period.

3.3 Checkerboard tests

For the interpretation of the results, it is important to know the dimensions of resolvable features. Hence, checkerboard tests were performed based on the actual ray path coverage. Because of the common ray paths, the results of the tests apply to both Rayleigh and Love wave inversions. Checkerboards covering 1 x 1, 2 x 2, 3 x 3 and 4 x 4 grid cells were created, with each grid cell the size of about 47 x 37 km. The checkerboard mean velocity was set to 3.0 km/s with a perturbation of ± 0.30 km/s. Gaussian noise was added to the synthetic observed data.

Initial and recovered models for group and phase velocities are displayed in Figure I.20. The checkerboard tests reveal that the largest features, i.e., 4 x 4 (188 x 148 km) and 3 x 3 (141 x 111 km) grid cell sized structures, can be recovered for both group and phase velocities independent of period and geographic location.

Structures as small as 2 x 2 grid cells (94 x 74 km) are recoverable along the main profile A and the coastal profile C (see Fig. I.1 for profile locations) for the entire period range of group velocities, and for phase velocities up to 22 s. Some smearing effects are visible in the north-west and south-west, where the number of crossing paths are limited by the sparser station distribution. For phase velocities with periods longer than 22 s, the pattern is strongly smeared in NW-SE direction, which results from an underrepresentation of rays traveling in a perpendicular direction (NE-SW). The 1 x 1 checkerboard is not recovered.

Interpreted structures, such as the Morondava basin or the velocity anomalies in central southern Madagascar, have dimensions of at least 80–100 km, and are within the scope of our resolution.

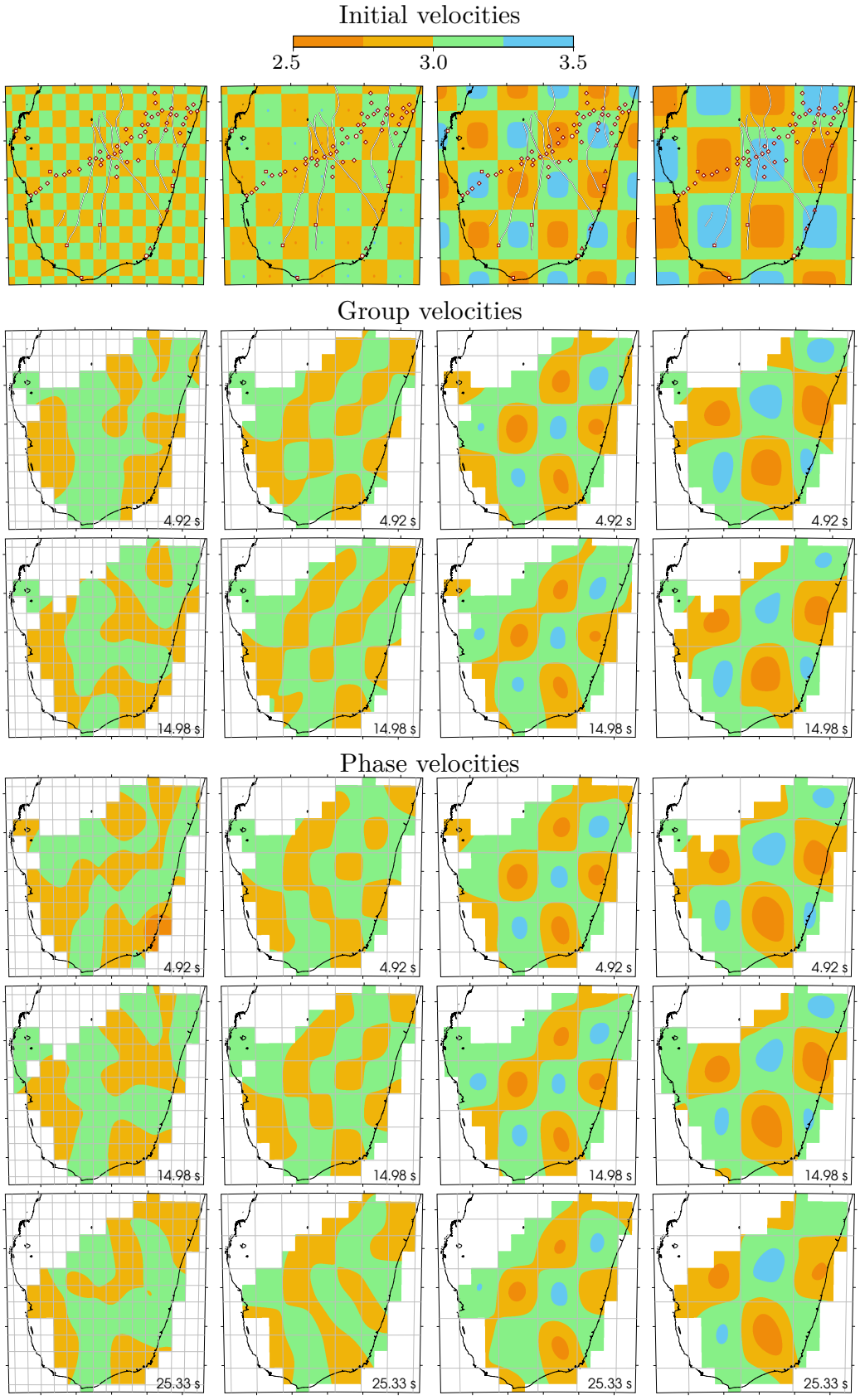

Figure I.20: 1 x 1, 2 x 2, 3 x 3 and 4 x 4 checkerboard tests for group and phase velocity tomography. The upper row shows the initial, the rows below the recovered velocity models.

4 Velocity-depth inversion

4.1 Data and parametrization

We extracted 96 dispersion curves for southern Madagascar from the 208 grid nodes. Dispersion relations are shown in Figure I.21 for group and phase velocities, Rayleigh and Love waves and are color coded by their geologic region. The number of tomographically derived dispersion curves varies between the regions: 19 (Morondava basin), 42 (Proterozoic), 25 (Archean), and 10 (Cretaceous volcanics).

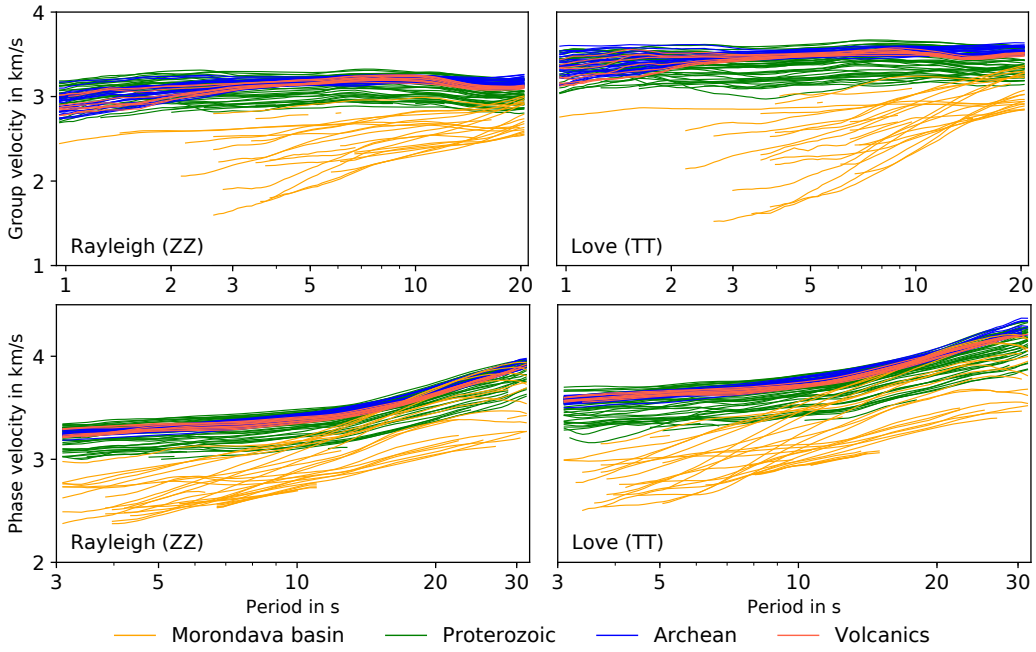

Figure I.21: Tomographically derived group and phase velocity dispersion curves color colored after ray path region. See caption of Figure I.7. The curves were smoothed (moving window with width of 7 period values) and trimmed to the period bands of interest (0.9–21 s and 3–32 s).

For velocity-depth inversion of dispersion curves, we used `CPS/surf96` (Herrmann and Ammon, 2002), which is based on a linearized least-squares approach. The tomographically derived dispersion curves were inverted at each grid node and separately for Rayleigh and Love waves; a joint inversion fitting Rayleigh and Love wave dispersion measurements with one shear wave velocity model – which would imply an isotropic crustal structure – was not feasable. The separate inversion of Rayleigh and Love wave dispersion is an appropriate approach for extracting V_{SV} and V_{SH}.

The following list shows the steps and order of performance for the velocity-depth inversions. The inversions were performed for each grid node and different starting models. Tests regarding depth sensitivity and surface resolution were conducted at selected grid nodes covering different geologic regions.

(1)	test: parametrization	initial velocity models and parameters
(2)	group velocity inversion	R→L and L→R
(3)	joint group and phase velocity inversion	R→L and L→R
(4)	test: inversion robustness	depth sensitivity, surface resolution, and inversion order

The additions R→L and L→R specify the inversion order scheme: For the R→L ordered inversions, the first inversion was applied to the Rayleigh wave data. The subsequent Love wave inversion used the final velocity structure derived from Rayleigh wave inversion as a start model. The latter Love wave inversion should introduce different velocities only when required by the data. For L→R ordered inversions, we performed the Love wave inversion first, followed by the inversion of Rayleigh wave data, using the final velocity structure derived from Love wave inversion as the starting model.

As our inital velocity models are based on Rindraharisaona et al. (2017), who used Rayleigh waves, our preferred inversion scheme is R→L. Hence, this study focuses on results from this scheme. Results of L→R ordered inversions are shown in section 4.3 and appendix I.B.

Initial velocity models. Ten initial velocity models were created (Fig. I.22), each containing 24 layers. While the uppermost five layers have thicknesses of 0.5 km (4 layers) and 1 km (1 layer), the layers underneath have thicknesses of 2.5 km, down to a depth of 50.5 km. The start models labeled `hs3.2`, `hs3.5`, `hs3.8` and `hs4.0` represent half space models with V_S of 3.2, 3.5, 3.8 and 4.0 km/s, respectively. `lgradient` and `sgradient` are simple gradient models with a low and a steep gradient. The realistic models are based on Rindraharisaona et al. (2017); we bundled their final velocity structures dependent on their geographic location and computed a median model as representative V_S-model for each of the four regions (see Fig. I.22).

The initial models were tested at four grid nodes, covering each of the geologic regions in southern Madagascar. For the majority of the inversions, the simple half space models failed; they show extensive velocity anomalies and are joined by large misfits. The gradient and realistic initial velocity models show well constrained results and small misfits. Figure I.23 displays the results of group velocity inversions at the four grid nodes. For each location, the velocity structures (V_{SV} and V_{SH}) are very similar down to a depth of 20 km and rather independent from the starting model. The calculated *RA*-depth structures agree in their overall trend and algebraic sign. Independent from the grid node location, the Precambrian starting models resulted in the smallest misfits. The similarities of the velocity models and the RMS misfits derived from Precambrian starting models are expected, as these initial models are also relatively similar (Fig. I.22, bottom left).

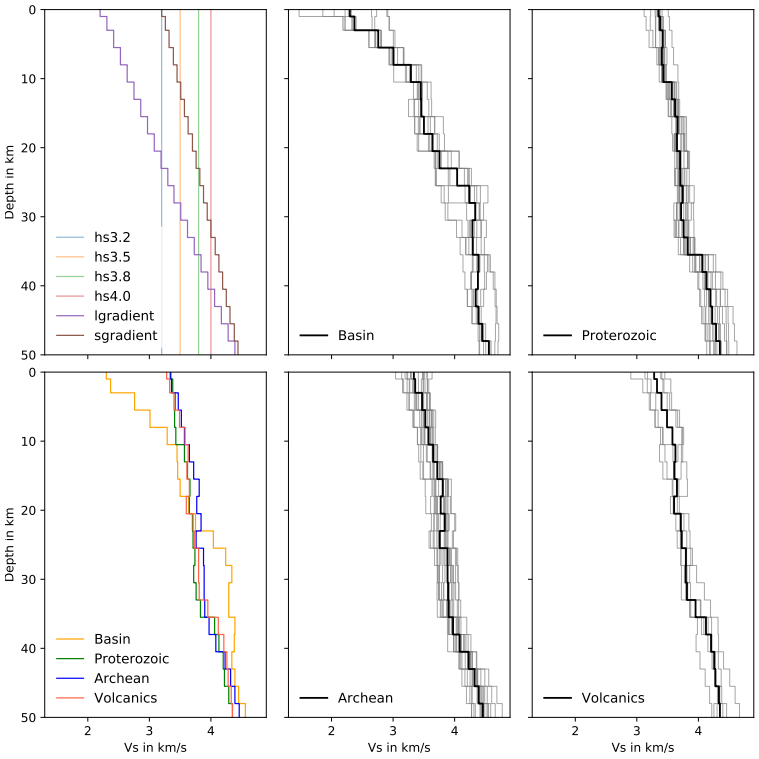

Figure I.22: Initial velocity models for inversion: (left) Simple half space and gradient models (top), and region dependent realistic velocity structures (bottom). (center and right) Velocity models from Rindraharisaona et al. (2017) (gray) and median models (black) as final realistic models for four regions. The median was computed from 10, 15, 17 and 6 velocity structures within the Morondava basin, Proterozoic, Archean and volcanic region, respectively.

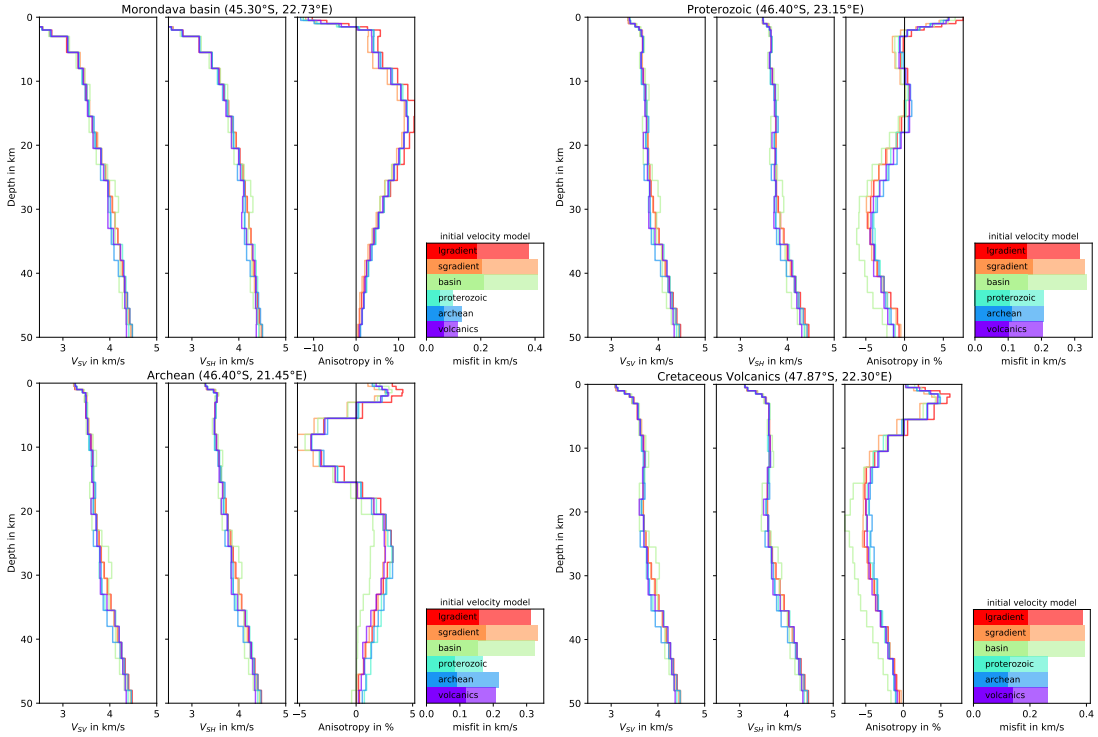

Figure I.23: V_{SV}, V_{SH} and RA from group velocity inversion (R→L) based on different initial models at four grid nodes. Initial velcoity models are `lgradient`, `sgradient`, `basin`, `proterozoic`, `archean`, and `volcanics` (Fig. I.22, left). The column diagram shows the RMS inversion misfits for Rayleigh (dark shade) and Love wave inversion (light shade).

From starting model testing, we draw the following conclusions:

(1) The half space starting models lead to anomalous velocity-depth structures and large misfits; they are discarded.
(2) The inversions with gradient and realistic starting velocity models result in similar velocities down to 20 km depth.
(3) The group dispersion curves (<21 s) cannot image the velocity structure below a depth of ∼20 km.
(4) *RA*-depth structures derived from inversions with gradient and realistic starting models agree in their overall trend and absolute values.
(5) Group, and joint group and phase velocity-depth inversions will be performed with the grid node dependent starting model, i.e., the location of the grid node determines which of the four realistic starting models is used.

Inversion parameters were defined by the initial model test. We used a damping factor of 5, differential smoothing, causal inversion coupling, and a number of 100 iterations. For the tomographically derived dispersion curves, we defined an equal velocity uncertainty for each period.

4.2 Joint group and phase velocity-depth inversion

Figure I.24 shows data fits and velocity-depth structures at three different grid nodes. The panel from each location shows (left) observed group and phase velocity dispersion curves for Rayleigh and Love waves, including initial and final fitted curves, and (right) the initial and final V_{SV}- and V_{SH}-depth structures for both inversions. The first inversion at each grid node (Rayleigh wave inversion) requires large model changes to fit the observed data. For the second inversion (Love wave inversion), the initial models for the Proterozoic and Archean regions fit the data very well. Only minor velocity changes at shallower depths are required to explain the data. At the basin grid node, larger adjustments of velocities are necessary.

Figure I.C1 shows results from only group velocity inversion for the same grid nodes. The difference is mainly the sensitivity of the dispersion data to depth, which is down to ∼30 km when including phase velocities compared to ∼20 km for group velocities only.

Radial anisotropy can already be estimated from the right columns (V_{SH}-plots), as the initial model represents the final V_{SV} structure. In the Morondava basin, we clearly see faster V_{SV} in the uppermost layers (negative *RA*), and faster V_{SH} underneath and down to 30 km (positive *RA*). The other grid nodes show weaker velocity differences between V_{SV} and V_{SH}, which hints towards weaker anisotropy.

Velocity and radial anisotropy maps at 18, 23 and 28 km are displayed in Figure I.25. The results for depths <20 km are almost identical to those from the group velocity inversion (see Fig. I.C2). The velocities are generally lower in the west compared to the east. The low-to-high velocity contact is close to the Beraketa shear zone. At 13 km and deeper, low V_{SH} follows along the Beraketa shear zone towards the Zazafotsy shear zone in the north.

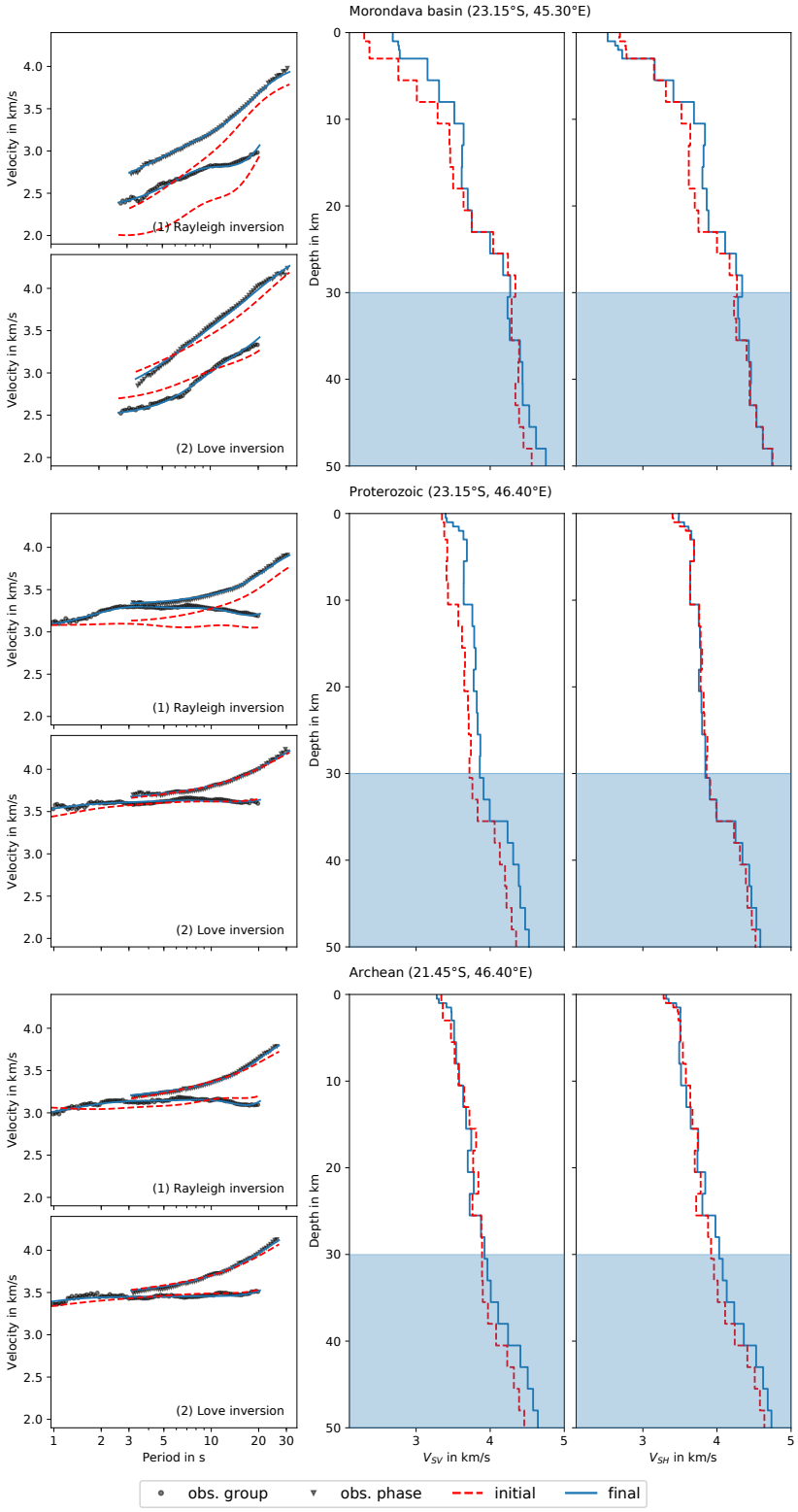

Figure I.24: Group and phase velocity dispersion curve inversion results for grid nodes in the Morondava basin, Proterozoic and Archean region. (left) Observed data and modeled dispersion curves for initial and final velocity models, and (right) corresponding V_{SV}- and V_{SH}-depth structures. Blue shaded area marks depths of low sensitivity.

The shallower depths (< 5 km) show generally negative RA for the western and positive RA for the eastern part of southern Madagascar. For depth between 5–20 km, the pattern is inverse,

i.e., positive *RA* in the Morondava basin and the Androyen domain and generally negative *RA* in the other Precambrian domains. Beneath 20 km depth, the *RA* is dominantly positive. Figures I.28–I.30 show cross sections of *RA* along profiles A–C from joint velocity inversion. Radial seismic anisotropy derived by different starting models can be found in Figures I.C3 and I.C4.

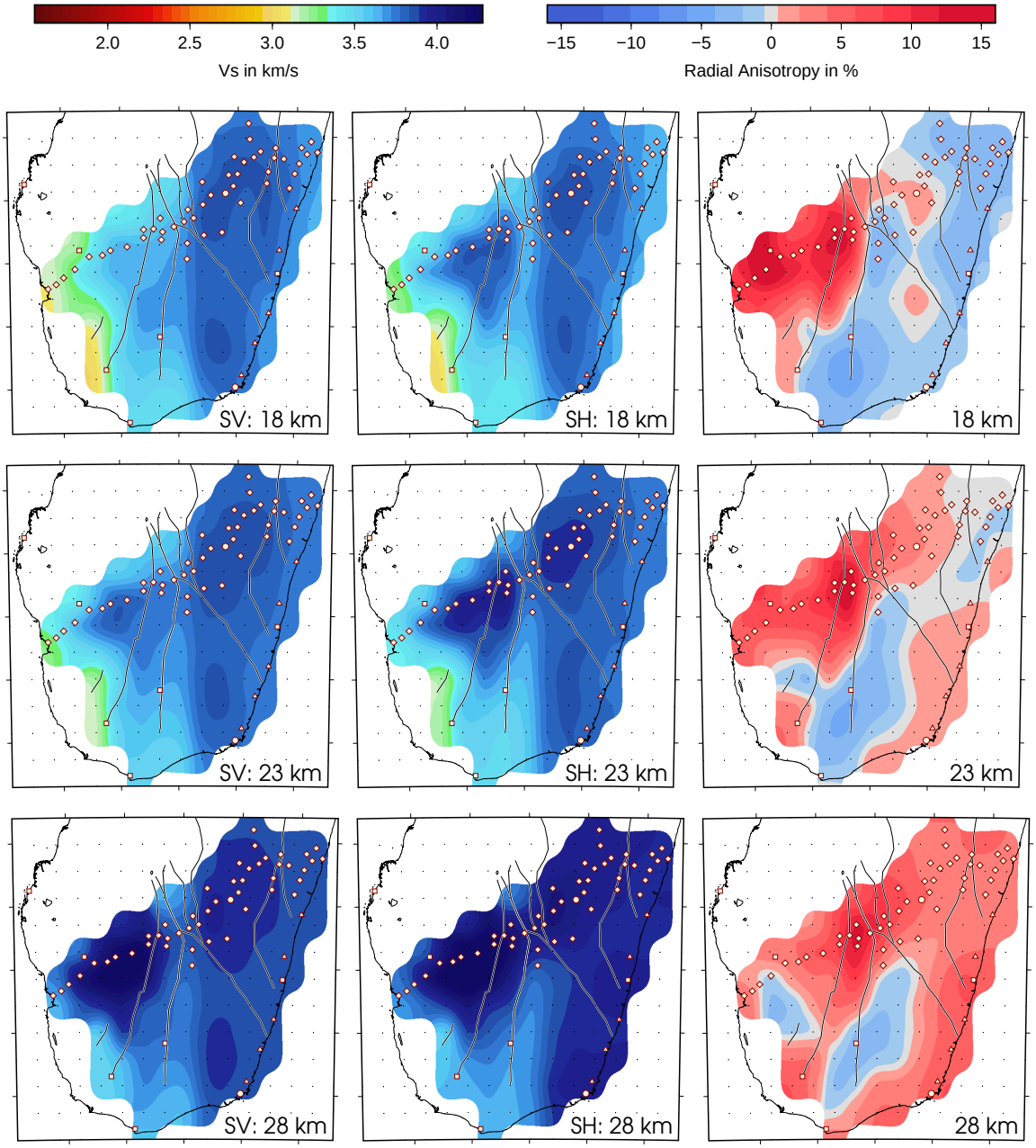

Figure I.25: V_{SV}, V_{SH} and *RA* at 18, 23 and 28 km of depth. For shallower depths, maps from joint inversion are almost identical to those derived by group velocity inversion (Fig. I.C2). *RA* is negative if $V_{SV}>V_{SH}$ and positive if $V_{SV}<V_{SH}$.

4.3 Testing inversion robustness

To evaluate the quality of the inversion results and possible error sources, we performed multiple tests to quantify: (1) the depth sensitivity of the data, (2) the introduction of *RA* anomalies in sedimentary settings, and (3) random inversion perturbations generated by the inversion order. The results of the depth sensitivity tests were already anticipated in section 4.2.

Depth sensitivity. We define the final V_S structure at a grid node as the base model for the test. The base model was modified (see example in Fig. I.26) to estimate the influence of the velocity structure on the dispersion curves. Therefore, the base model velocities of single layers

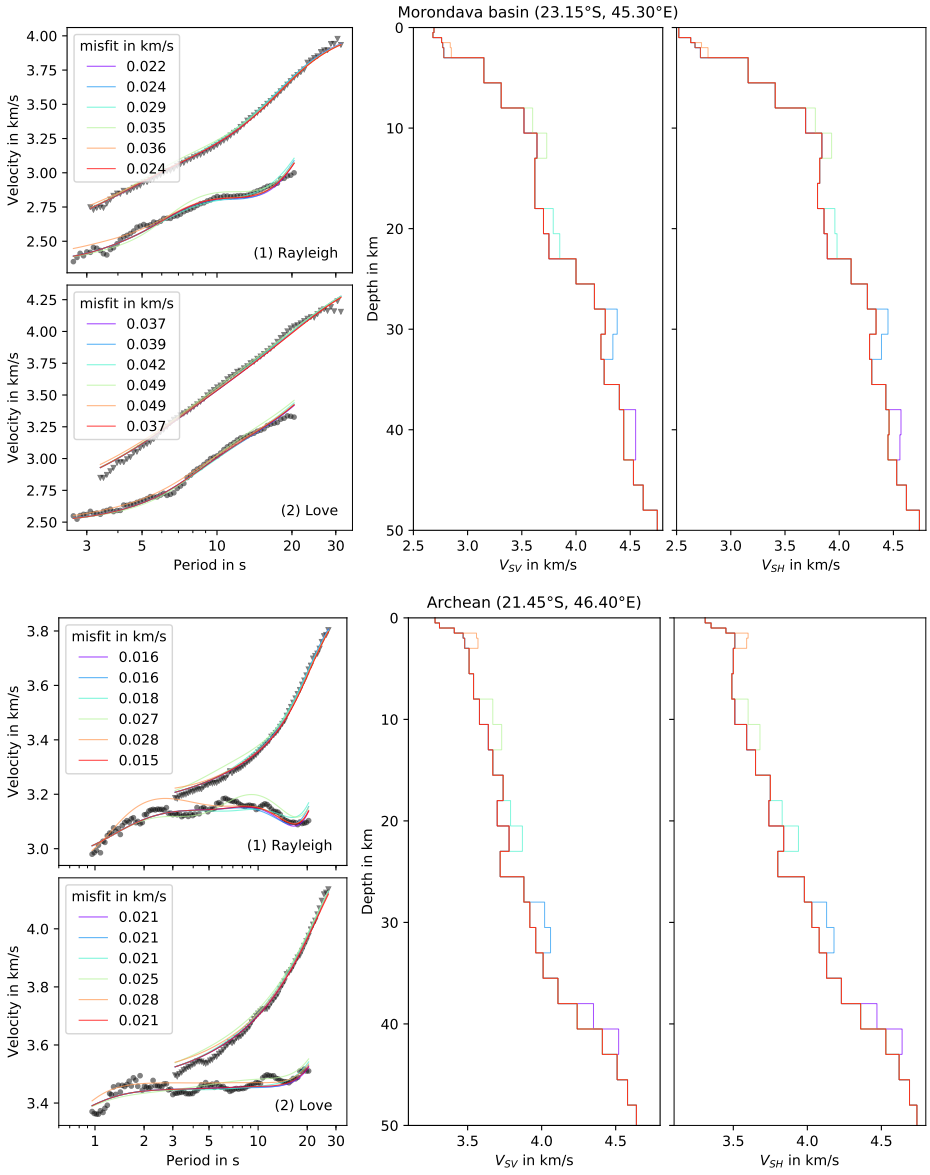

Figure I.26: The influence of velocity-depth model modifications on the dispersion curves and their fit. Layer velocities of the base model (red) were modified by 2.5 % (colors). Modifications beyond depths of ~30 km have little to no influence on the dispersion curve at the measured periods and on the misfits.

and two layers were perturbed between -5 and 5 %. Figure I.26 shows the base model with +2.5 % velocity modifications of two layers, centered at 2.5, 10.5, 20.5, 30.5 and 40.5 km depth. The shallow depth modifications of the base model influence the modeled dispersion curves at the shorter periods, which is directly measurable in the RMS misfits. For the alterations at the depth of 2.5 km, the misfits are 30–50 % higher than the base model misfits. They decrease with increasing depth of the modification. At a depth of ∼30 km, the velocity modifications only have little to no influence on the modeled dispersion curves at the measured periods and on the misfits. Hence, we conclude that the measured data are only sensitive to the velocity structure above 30 km, and that our inversion results can be trusted down to that depth. Other modification depths and percentages draw towards the same conclusion.

Near surface model parametrization. The negative shallow anisotropy observed in the Morondava basin is surprising because usually sub-horizontal layering is found in sedimentary basins. Here, we test whether this could have spuriously arisen from (1) the coarse layer parametrization at the surface and (2) the different depth sensitivity kernels of Rayleigh and Love waves. We evaluate the radial anisotropy which is generated by the two properties, and how they relate to our inversion results. Therefore, we created a base model by replacing the uppermost 5.5 km of the initial basin model (Fig. I.22) by fine isotropic layers of random thicknesses (10–500 m) and sedimentary velocities oscillating around a velocity gradient (2.3–3.3 km/s).

We modified the base model by low or high velocity zones with random velocities between 1.55–3.70 km/s. High velocity volcanic intrusion layers are not uncommon in the Morondava basin. We include low velocity layers to see whether they introduce different anomalies. For each modification, we computed "observed" dispersion relations, inverted the data with parameters and work flow as described above, and computed RA. Mostly positive anisotropies are introduced, independent of the sign of the initial velocity change. The inversions rarely introduce negative RA anomalies, and in the cases that they do, the negative anisotropy only extends to depths shallower than 1.5 km. Also, the inclusion of multiple zones of high and/or low velocities shows similar results. We therefore conclude that the negative basin surface anisotropies are required by the data, as they reach percentages much higher than seen in this test.

Inversion order scheme. We compared the velocity-depth inversion results dependent on the inversion order scheme (Fig. I.27). If the two inversion order schemes were to cause differences in the inferred SV and SH velocities and thus the RA pattern, then the inversion would be influenced by random artifacts rather than real structures. Most differences between R→L and L→R inversions are small (±1 %). The differences exceeding this value are focused on (1) the mantle structure beneath the Morondava basin (<8 %) and (2) within the sedimentary basin (-10–4 %). The sedimentary basin, however, shows equal-signed RA in both inversion orders, with stronger anomalies for the R→L inversion order. The features we interpret only show minor differences and agree in the sign of the anomaly.

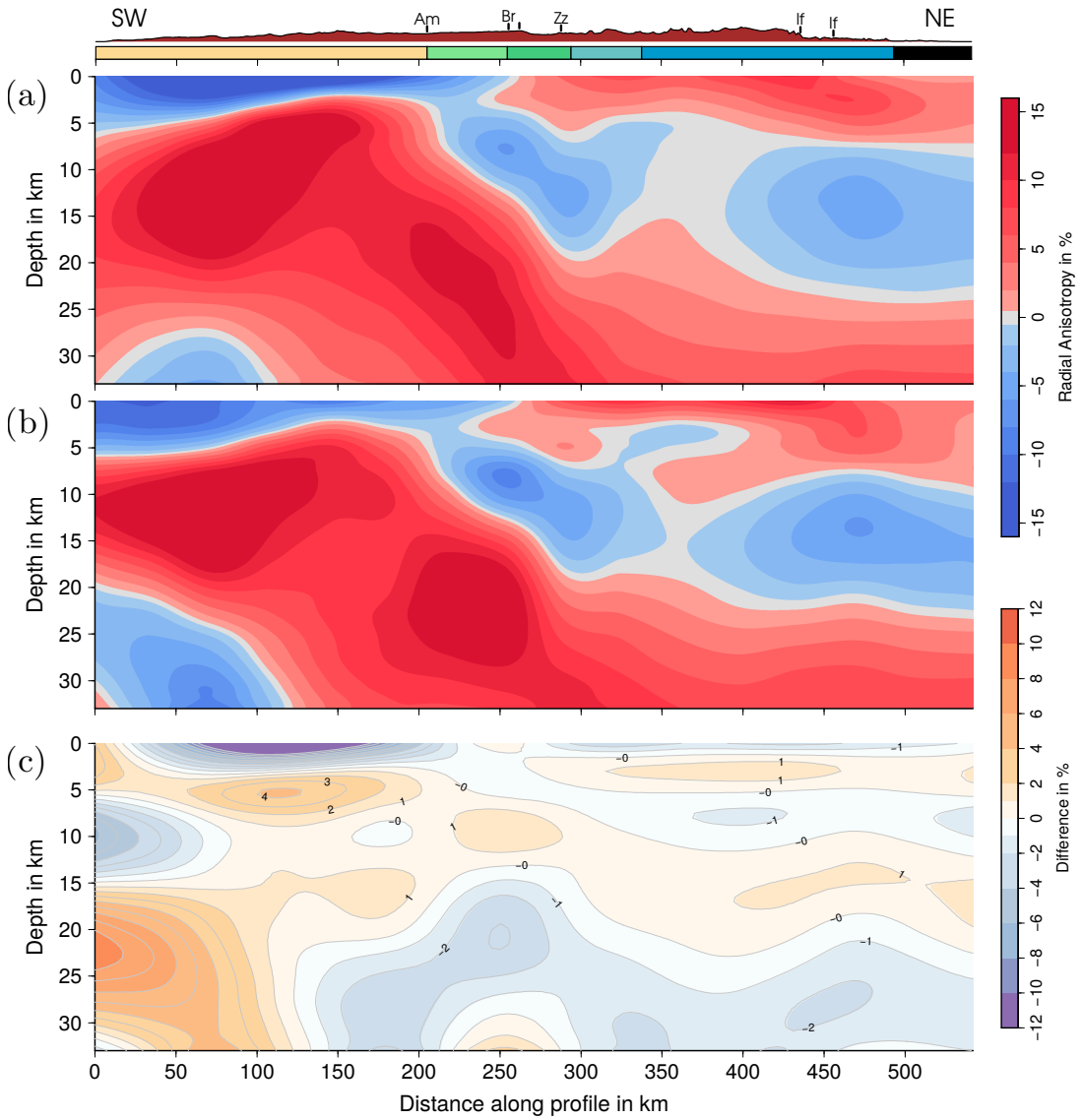

Figure I.27: Radial anisotropy structure along profile A derived from (a) R→L and (b) L→R ordered inversion. Deviations are illustrated in (c).

5 Shear wave velocity and radial anisotropy

In this chapter three representative cross sections of mean V_S (of V_{SV} and V_{SH}) and RA within our study area are discussed (Figs. I.28–I.30). The locations of profiles A–C are displayed in Figure I.1. The profiles are chosen to cover the regions that are best resolved by station coverage. Although profiles A and B run parallel and are only 60 km apart, they show slightly different dimensions of velocity and anisotropy features, corresponding to the surface geologic units. While profile A covers large parts of the Morondava basin and the Archean unit, profile B has a longer intersection with the Proterozoic unit. Profile C is located along the east coast and crosses the Proterozoic and the Archean units, including the Cretaceous volcanic cover.

We consider all features discussed in the following as robust results of the inversion. This was evaluated by several tests: (1) the structural resolution of velocity anomalies (checkerboard tests), (2) the influence of the starting velocities on the depth inversion, (3) the depth sensitivity of the data, (4) the possible introduction of RA artifacts in the shallow Morondava basin, and (5) the influence of the inversion order.

5.1 Final results

The velocity sections along profiles A and B (Figs. I.28, I.29, top) show V_S generally increasing with depth. The low velocities (<3.1 km/s) in the west extending to depths up to 10 km represent the Morondava basin. The middle crust is characterized by intermediate velocities along the east coast and high velocities beneath the Archean and the directly adjacent (eastern) Proterozoic units. A strong lateral velocity change can be seen in the central Proterozoic unit, where the major shear zones are located. Profile C (Fig. I.30, top) more-less only shows a velocity gradient from surface to depth, and also a lateral velocity change from 3.8 to 3.4 km/s in the middle crust (10–20 km depth) from south to north.

The radial anisotropy along the profiles A and B (Figs. I.28, I.29, bottom) shows a complex pattern of positive and negative anomalies, which is almost the opposite when comparing the basin and the Precambrian region. Although the anisotropy pattern of the two cross sections looks slightly different, they are congruent with regard to the surface geology. A pronounced negative radial anisotropy (>-12 %) is revealed in the shallow part of the Morondava sediments with a thickness of 5 km beneath the western basin, thinning to 2 km below the eastern basin. The deeper basin and entire crust below it show a very high positive anisotropy, the strongest in the study region (>12 %). The mantle below the basin appears to show negative anisotropy, but it is close to the limit of our resolution. The Moho of Rindraharisaona et al. (2017) roughly follows the 5 % anisotropy contour.

The Precambrian units show a completely different depth dependency of RA: the uppermost upper crust (top 5–8 km) is characterized by moderate positive values (mostly <6%), down to 20 km depth, underlain by the middle crust with a moderately negative anisotropy (>-6%) and a lower crust with a positive anisotropy again. Beneath the Proterozoic units (Androyen,

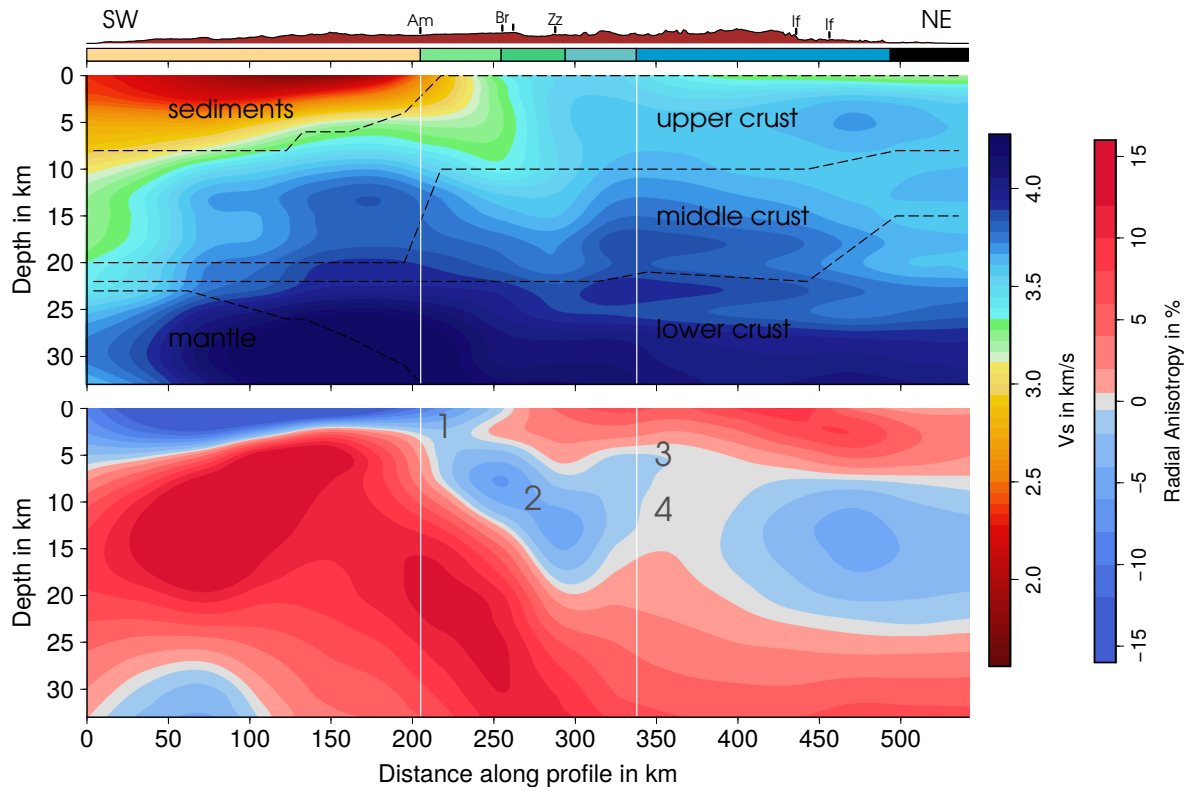

Figure I.28: Cross sections of mean V_S and *RA* along profile A as indicated in Figure I.1. Dashed lines (top plot) mark the crustal structure derived by (Rindraharisaona et al., 2017). White lines indicate the vertical projection of surface contacts between the Morondava basin and the Proterozoic and Archean domains. Note that the actual orientation of contacts between these domains may not be vertical and may not extent through the entire depth range indicated. Features 1–4 are described in the text. The topography plot shows additional geologic divisions color coded as the units in Figure I.1, except for the Morondava basin, which is unicolored. Elevation profile is based on etopo1 (Amante and Eakins, 2009).

Anosyen), an easterly dipping negative anomaly (Fig. I.28, feature 2) seems to connect the shallow Morondava basin to the Precambrian middle crust, but because of the very different lithology, it is likely that the root causes are different. The anomaly dives from 5 km in the west down to a depth of 19 and 25 km in the east along profiles A and B, respectively.

At the transition between the Proterozoic and Archean terranes (feature 3) the negative anomaly extends closer to the surface, reducing the thickness of the overlying positive anisotropy by 3 and 5 km in profile A and B at 320–380 km and 250–350 km, respectively. Within the negative *RA* layer in this part of the model (feature 4), the negative anisotropy is weaker (0–2%) in comparison to the adjacent units (2–6%). The anisotropy maps in Figure I.C2 emphasize the differences between the basin in the west and the Precambrian domains in the east.

Profile C (Fig. I.30, bottom) shows a laterally nearly homogeneous layered anisotropy pattern: positive in the upper (< 8 km), negative in the middle (8–21 km) and positive in the lower crust (>21 km). This contribution is equivalent to the general Archean anisotropy pattern, although the middle-to-lower crustal contact is shifted to lie within the negative anisotropy using the boundaries defined by Rindraharisaona et al. (2017). The thickness of the shallow layer with positive anisotropy increases from 2 km in the south to 8 km in the north with the largest

change approximately at the southern boundary of the volcanic units.

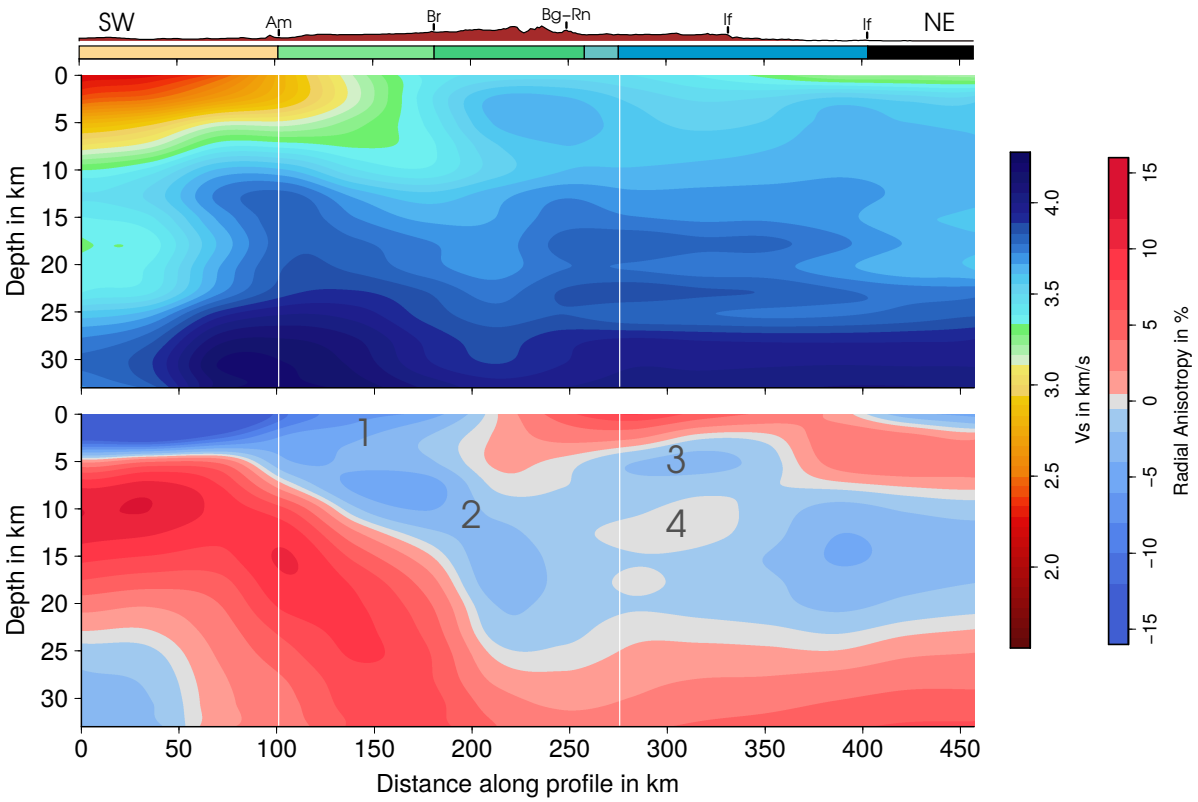

Figure I.29: Cross sections of mean V_S and RA along profile B. See caption of Figure I.28.

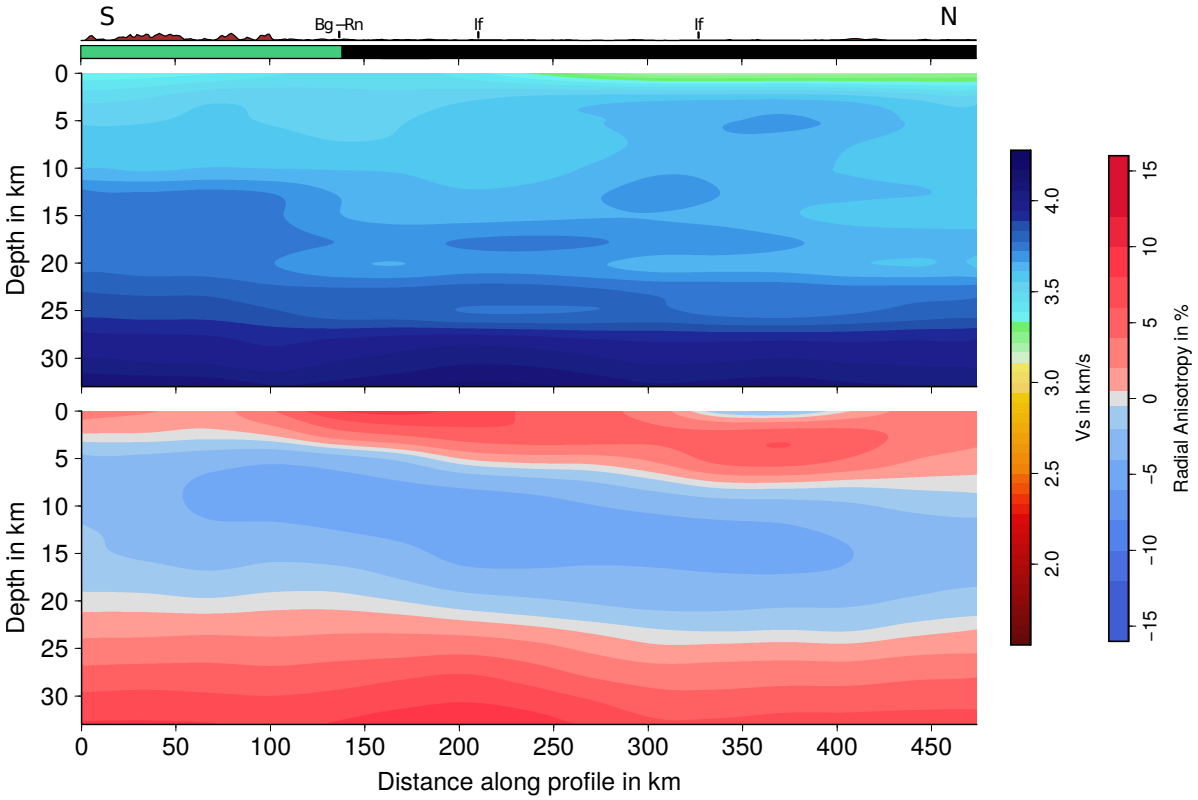

Figure I.30: Cross sections of mean V_S and RA along profile C. See caption of Figure I.28.

5.2 Interpretation and discussion

We obtained the radial anisotropic pattern for each of the major geological regions. The Proterozoic and Archean terranes reflect individual tectonic events of accretion and collision until they share a common history after amalgamation during the Pan-African collision (< 590 Ma). Along the east coast, additional volcanic pre-rift indicators, such as dikes and flood basalts from the Cretaceous, can be found (Storey et al., 1995). In contrast, western Madagascar underwent long-term rifting and sedimentary basin formation since 300 Ma. Our interpretation of the current anisotropy pattern will consider inherited pre-Pan-African architecture, the Pan-African collision, which has modified most of the crust (Tucker et al., 2014), and the post-orogenic tectonic evolution.

Proterozoic and Archean. The Precambrian domains (including the eastern coast) show a broadly similar anisotropy pattern, suggesting a strong influence of the late collisional and Gondwana forming event, the Pan-African Orogeny, on the generation of this background anisotropy. The Precambrian units are characterized by steep or openly folded domains interrupted by kilometer-wide zones of steeply dipping, highly strained rocks and contact zones (Martelat et al., 2000; Tucker et al., 2011, and references therein). These shear-zone structures are able to produce negative anisotropy if the fabric produced by shearing is sub-vertical. The Androyen and parts of the Anosyen domain show a negative surface anomaly (Fig. I.C2, feature 1), which we assign to the strong isoclinal folding and vertical foliations within the shear zones (GAF-BGR, 2008). The negative anisotropy shaping the intermediate depth range of eastern Madagascar (4–21 km) could thus also reflect Pan-African vertical structures that were fossilized during subsequent lithospheric cooling (Walker et al., 2004) as manifested also by intra- and inter-domain shear zones across the southern island.

Preceding the final Pan-African collision, the Itremo- and Ikalamavony domains were thrusted eastward onto the Antananarivo domain in central and southern Madagascar, respectively, forming an imbricated and relatively flat-lying nappe stack (e.g., Giese et al., 2017; Tucker et al., 2007). During the Pan-African Orogeny, this nappe stack, as well as the Antananarivo domain in its footwall were intruded by large volumes of granitoid rocks of the Amabalavao suite (e.g., Tucker et al., 2014) resulting in large isotropic plutonic intrusions, but also in form of foliation-parallel sills. Pan-African shortening affected this transitional part from the Proterozoic to the Archean domains (e.g., Giese et al., 2017), but its intensity decreases towards the east. This results in shallowly to moderately dipping foliation planes and open angle folds and preservation of inherited compositional layering between orthogneisses and supracrustal formations within the Antananarivo domain (GAF-BGR, 2008), which could explain the faster V_{SH} and thus a positive *RA*.

However, most of the Precambrian surface outcrops originated from middle-to-lower crust of the Pan-African Orogen and were buried to a depth of 25–35 km (Androyen domain; Jöns and Schenk, 2011) and 18–30 km (Anosyen domain; Horton et al., 2016, and references therein) presumably at the time of tectonic thickening of the crust (Horton et al., 2016). According to Horton et al. (2016), concentrated radiogenic heat production caused an extreme thermal anomaly in the middle crust (around 30 km) of southern Madagascar, which could have weakened

it and initiated syn- or post-orogenic crustal flow driven by the gravitational potential energy of the Pan-African Orogen. Evidence for late to post-orogenic extension in this region of the Malagasy crust can be seen in low-angle extensional detachment faulting (Collins et al., 2000) and extensional reactivation of shallowly dipping ductile thrust contacts (Giese et al., 2017). Ductile flow is the main cause for textural alignment of minerals in metamorphic rocks (Rabbel et al., 1998) and is therefore also a plausible mechanism for the observed positive *RA* now observed in the shallowest layers in the eastern part of southern Madagascar, remembering that these rocks were in the middle crust at the beginning of the orogenic collapse.

Gravitational collapse is not only associated with mid-crustal ductile flow, but also with channeled lateral flow in the lower crust. Many studies point towards the latter, as this mechanism can accommodate collapse without surface extension being necessary (Rey et al., 2001, and references therein). The Tibetan plateau is the best modern analogue for the Pan-African collision zone (Fitzsimons, 2016; Horton et al., 2016). Radial anisotropy of the Tibet/ Himalaya region was examined in several studies (e.g., Chen et al., 2009; Duret et al., 2010; Guo et al., 2012; Huang, 2014; Shapiro et al., 2004). These studies typically observed a mid-to-lower crustal positive radial anisotropy. Duret et al. (2010) found a positive anomaly at 15–45 km depth, and Shapiro et al. (2004) found one at 25–50 km depth. Ambient noise studies discovered similar upper limits and even deeper lower limits for their study areas. Guo et al. (2012) found positive anisotropy in the mid-crustal layer of southern Tibet ($>$ 25 km, limited by the maximum resolved depth of 35 km). Chen et al. (2009) analyzed the Qinghai-Tibet Plateau and surrounding regions and found almost exclusively positive anisotropy at a depth range of 18–75 km in the Himalayan, Lhasa, and Qiangtang Blocks. Huang (2014) observed widespread positive anisotropy in zones (with low wave speeds) in the middle and lower crust ($\sim$20 km – Moho) of the southeastern Tibetan Plateau. The positive mid-to-lower crustal *RA* observations there are generally interpreted as crustal channel flow. It is likely that the positive anisotropy characterizing the Madagascan Precambrian basement at 20–30 km depth today was generated through similar mechanisms during the Pan-African collapse, when the layers were buried at depths of around 40–60 km. The anisotropic fabric formed in the Precambrian during the orogeny and subsequent collapse thus appears to have been preserved, even as the top layers of the crust were removed by erosion.

The *RA* structure of the **Proterozoic** and its interpretation differ in some important details from the adjacent Archean units. (1) The east-dipping negative-positive anisotropy contrast within the Androyen and Anosyen domains (feature 2 and below) could be due to the composition of the crustal rocks causing a weaker rheology during final collision and indentation of the Antananarivo-Antongil-Masora block (Schreurs et al., 2010), resulting in much stronger deformation during shortening compared to the adjacent domains further east. With this in mind, the dipping anomaly (feature 2) could be the expression of the final Pan-African collision and suturing of the Mozambique Ocean, which was subducted eastward below the Anosyen-Ikalamavony-Antananarivo-Masora domains (Boger et al., 2015). The anomaly may thus simply trace the Androyen domain into the crust. (2) The extension of the Proterozoic negative anomaly to the surface (feature 1) might be the expression of the strongly upright folded and horizontally shortened large-scale vertical shear zones seen in the surface geology (GAF-BGR,

2008). Also, teleseismic shear-wave splitting combined with forward-modeling revealed a ∼150-km-wide zone with a fast direction of azimuthal anisotropy -40° and up to 12% (azimuthal) anisotropy (Reiss et al., 2016). The later rifting, initiating and forming the Morondava basin in western Madagascar, could have overprinted mid-crustal shear-zone signatures below the negative anomaly within the Proterozoic domains by horizontal stretching; we note that the dipping negative *RA* anomaly occurs in the region of the largest gradient in Moho depth, increasing from about 28–38 km (profile A at 180–280 km in Fig. I.28).

The Morondava basin. The positive radial anisotropy in the crust beneath the sediments is the expected consequence of long-lasting extension over a time of about 150 Ma. The basin formed as a result of horizontal stretching and thinning of the crust, likely permitting mineral alignment along the deformation direction. Based on the absence of fast lower crustal velocities in the thinned crust below the basin, Rindraharisaona et al. (2017) argued that the crustal thinning might have been accomplished by exhumation of lower crust along a low-angle detachment; this motion would likewise be expected to result in sub-horizontal mineral alignment. The western basin is the only place in our model where surface waves of the examined period range are sensitive to the structure of the mantle. Tests here show some dependence on the details of the inversion procedure (Fig. I.27), as this part of the model is close to the limit of resolution. Nevertheless, it is clear that negative *RA* is present in the mantle below the basin.

In the basin sediments themselves, the deeper positive *RA* is expected from SPO of alternating horizontal layers of different seismic velocities. The shallow negative *RA* is surprising, though, as there is no way to produce it from the SPO of isotropic layers. However, negative *RA* in the near-surface in basin settings is not that unusual. Chen et al. (2009) found values of -5 ± 3% down to depths of 8 km and deeper in the major Tarim and Qaidam basins adjacent to the Qinghai-Tibet Plateau. Shirzad and Shomali (2014) reported a negative anisotropy in the shallow (< 2 km) Tehran basin of Iran, which they explained by the vertical alignment of cracks along the surface. Although the shallow Morondava basin contains jointing and is also spiked with rather steeply dipping normal faults (GAF-BGR, 2008), this might not be the exclusive explanation for the strong negative surface anisotropy, as the spacing between the faults is relatively wide and might not be able to generate an anisotropic effect stronger than the sedimentary layering itself. Instead, Cretaceous dike intrusions could generate strong lateral velocity contrasts within the sediments, which, with a minimum thickness and spacing, could overprint the *RA* signature of horizontal sedimentary layering. The presence of outcrops of cross-cutting Cretaceous dikes in the Cretaceous and parts of the adjacent Jurassic strata in the southern Morondava basin (Roig et al., 2012; Storey et al., 1995) support this hypothesis for the western Morondava basin. Of course, the presence of surface outcrops of dikes implies that intrusions must be present throughout the sedimentary package, and this would influence the anisotropy. The positive *RA* in the deeper parts of the basin might also be enhanced by the intrusions, if they are organized predominantly as sills rather than dikes (Jaxybulatov et al., 2014).

No surface outcrops of volcanic rocks have been mapped in the eastern Morondava basin. However, it is conceivable that the Ejeda-Bekily dike swarm (between the Volcan de l'Androy and the Ejeda SZ) has intruded into the sediments, traversing the southernmost part of the Morondava basin without penetrating the recent surface, but supporting the negative surface

anisotropy. From a geological point of view, it seems rather unlikely that the young dike intrusions stop directly at the Ejeda shear zone (e.g., as illustrated in Roig et al., 2012). As the Cretaceous dikes are obviously located in the western part of the Morondava basin, we propose that a combination of magmatic intrusions, normal faults, and jointing is responsible for the negative surface anisotropy in the basin.

The Cretaceous volcanics. The radial anisotropy pattern along the east coast does not show a difference compared to the general Archean one. The large intrusions and flood basaltic extrusions do not seem to influence the signature of the radial anisotropy, although the velocities in the middle crust along the coast are smaller relative to the Archean ones (Fig. I.28). However, this region is at the edge of our study area and has a rather narrow width, so the surface waves with paths along the east coast would still be influenced by the Archean structure.

Project II

Crustal structure of Sri Lanka – based on surface wave dispersion and receiver functions

Submitted as Dreiling et al. (n.a.): Dreiling, J., Tilmann, F., Yuan, X., Haberland, C., and Seneviratne, S. W. M. Crustal structure of Sri Lanka derived from joint inversion of surface wave dispersion and receiver functions using a Bayesian approach. Journal of Geophysical Research: Solid Earth. Submission in 2019.

1 Introduction

Sri Lanka occupied a key region in both the assembly and the multistage break-up of Gondwana. Many petrological, geochemical and geochronological studies have been conducted to reconstruct the processes acting during the amalgamation. However, little is known about the seismic structure of the island. Until mid 2016, only three permanent seismic stations existed on the island. Pathak et al. (2006) and Rai et al. (2009) analyzed receiver functions from the permanent station PALK and estimated Moho depths and V_P/V_S ratios. Mishra et al. (2006) modeled gravity anomalies within Sri Lanka and other continental fragments of Gondwana to determine the crustal thickness and density structure beneath the island.

In 2016–2017 the Geological Survey and Mines Bureau (GSMB) of Sri Lanka and the German Research Centre for Geosciences (GFZ) installed and maintained the first broadband seismic network on the island (Fig. II.1), consisting of 30 temporary stations running for a period of 13 months. Here, we image the crustal structure of Sri Lanka using the new seismic data. We performed a joint inversion of surface wave dispersion derived from seismic ambient noise cross-correlation, together with receiver functions. A Bayesian approach (part III) allows us to compute a collection of likely models and to estimate the uncertainties of the model parameters.

Contents. The geologic and tectonic development of Sri Lanka is summarized in chapter 1. Chapter 2 provides an overview of the temporary seismic array, introduces the seismic data relevant for our study, and illuminates problems that occurred during the operational period of the stations and solutions. The continuous seismic data were processed towards ambient noise cross-correlation and the retrieval of Green's functions for Rayleigh surface waves (chapter 3). Phase velocities were measured for each of the four components that include the Rayleigh wave signal (i.e., ZZ, RR, ZR and RZ), and averaged for each period to retrieve a final dispersion curve from between station pairs. Travel time tomography was performed. For receiver function computation (chapter 4), earthquake signals were selected based on their quality (SNR) and processed to retrieve Q receiver function stacks. Moho depths and V_P/V_S ratios were estimated by $H\kappa$-stack grid search. The tomographically derived dispersion curves and receiver functions were jointly inverted for the crustal structure beneath Sri Lanka, using a Bayesian approach (chapter 5). Finally, results are discussed and interpreted in chapter 6.

Additional information can be found in appendices II.A–II.B

Geologic background

Sri Lanka is mostly composed of Precambrian crust; only the northern and north-western coasts show younger Jurassic-Quaternary sedimentary deposits (Fig. II.1). The Precambrian basement consists of three major units, namely, from west to east, the Wanni Complex (WC), the Highland Complex (HC), and the Vijayan Complex (VC). Some HC erosion remnants (Klippen) occur around Buttala, Kataragama and Kuda Oya in the southern part of the VC. The Kadugannawa

Complex (KC) is a relatively small unit located between the WC and HC. It is contentious whether it is part of the WC, part of the HC or the root zone of an island arc (Cooray, 1994, and references therein). The WC/HC represents as a combined unit a tilted section of former middle–lower crust, with the HC representing the lower level. The KC is at a crustal level between the WC and the HC (Kehelpannala, 1997; Kriegsman, 1994; Sandiford et al., 1988). The WC consists of metamorphic rocks of upper amphibolite- to granulite-facies, the HC predominately of granulite facies and the VC of amphibolite facies (Kehelpannala, 2003, and references therein).

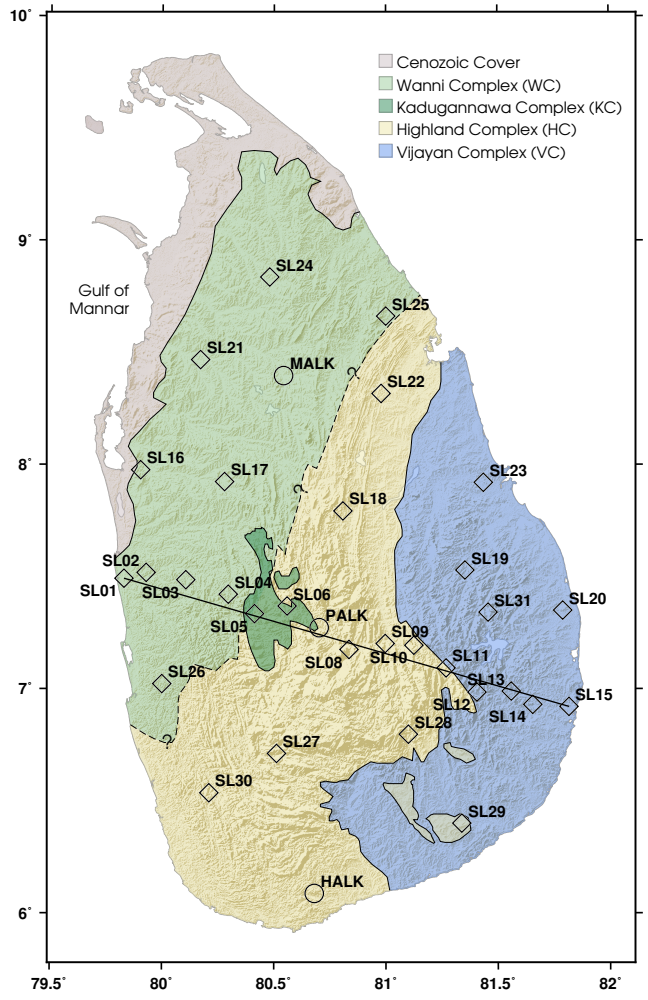

Figure II.1: Major lithotectonic units in Sri Lanka (modified after Dissanayake and Chandrajith, 1999). Diamonds represent station locations of temporary seismic array (FDSN code: 1A, 2016–2017). Circles denote three permanent stations (MALK, PALK, HALK). Black line indicates profile location for a cross section.

The contact between the WC and the HC is controversial due to the absence of a clear structural break between them (Kröner and Brown, 2005). Stretching lineations, shear sense indicators and sheath folds demonstrate that a collision has occurred in a NNW-SSE direction, i.e., the WC/KC was moving on top of the HC from NNW towards SSW (Kehelpannala, 2003, and references therein). The boundary between the WC and the KC is less clear, while that between the KC and the HC is well defined. The contact between the HC and the VC is considered to be a deep crustal, sub-horizontal ductile shear and thrust zone (Kehelpannala, 2003; Kleinschrodt, 1994, 1996, and references therein). E-W stretching lineations in the VC and N-S trending stretching lineations and shear sense indicators at and close to the shear zone suggest a nearly E-W directed transpressional collision between the combined WC/HC unit and the VC (Kehelpannala, 1997, and references therein). The general trend of subhorizontal fold envelopes suggests the thrust to underlie large parts of the HC; Klippen south of the HC prove that the thrust plane extended nearly up to the south coast (Kleinschrodt, 1994, 1996). Furthermore, Kleinschrodt (1994) suggests that the HC climbed on top of the east-VC with a ramp-flat geometry or a low-angle thrust, steepening to higher crustal levels.

The amalgamation of the Sri Lankan complexes took place within the framework of the Pan-African continental collision between West and East Gondwana. Petrological, geochemical and geochronological studies suggests that the WC, KC and VC have been formed through

arc-related events during the Early Neoproterozoic, i.e., ∼1.0 Ga (Takamura et al., 2016, and references therein). A well-established theory for the amalgamation of Sri Lanka suggests a stepwise collision of the Precambrian arcs (e.g., Kehelpannala, 2004) during the Pan-African Orogeny, whereas Santosh et al. (2014) recently interpreted the WC, KC and VC as Early to Late Neoproterozoic continental arcs, with the HC as a Neoproterozoic suture zone formed by double-sided subduction and final collision of the WC and VC.

The hypothesis of the stepwise collision of the Precambrian arcs suggests an initial collision of the WC and HC fragments. As a unified block the WC/HC has experienced six phases of ductile deformation (D1–D6 in 0.61–0.55 Ga), which are not seen for the VC (Kehelpannala, 1997). The evidence therefore suggests an early stage collision of the WC/HC unit with the VC at D5 (0.58 Ga), and the WC/HC subsequently being thrust over the VC (Kehelpannala, 2003, and references therein). Based on post-tectonic intrusion by Cambrian granites and syenites through all three units, i.e., WC, HC and VC, the fragments of Sri Lanka were united at 0.55 Ga. Most of the older structures have been obliterated by strong Pan-African non-coaxial strain, which also brought all the early planar and linear fabrics into parallelism with those formed during the Pan-African event (Kehelpannala, 1997).

Based on petrological and geochemical data, Santosh et al. (2014) recently proposed an alternate scenario, termed divergent subduction, which involves a double-sided subduction of oceanic crust beneath the WC to the west and the VC to the east. The HC is therefore the collisional suture and accretionary complex in between, where trench-fill sediments and ancient micro-continents or arcs are accreted and admixed during the final collision stage. Santosh et al. (2014) do not comment which larger lithospheric structures would be predicted by their model.

The Mannar basin (west of Sri Lanka, partly onshore, Fig. II.1) has been formed during Gondwana break-up, which initiated at approximately 165 Ma (Royer and Coffin, 1992). A great amount of rifting between India and Sri Lanka together with strike slip movement and anticlockwise rotation of Sri Lanka was responsible for significant widening and rapid subsidence in the basin (Kularathna et al., 2015), and is associated with strong crustal thinning along the west coast.

2 Seismic data

Until May 2016 the island of Sri Lanka was equipped with only three seismic stations: PALK, MALK and HALK. PALK is an IRIS/IDA station and operates since 2000 (SIO, 1986). MALK and HALK are GEOFON stations and have been operating since 2010 (GEOFON, 1993). In mid 2016 a field campaign was initiated by the GSMB of Sri Lanka and executed jointly with the GFZ (Seneviratne et al., 2016). A network of 30 three-component broadband stations was deployed (Fig. II.1), which recorded continuous data for a period of 13 months.

The array was designed for seismic ambient noise and receiver function analyses as well as local earthquake studies. Fourteen temporary stations and the permanent station PALK form a 230 km long profile across the island, from the west to the east coast, perpendicular to the

predominant geologic strike (profile in Fig. II.1). Inter-station distances are ∼15 km. Another sixteen stations were spread out on the island at a larger spacing of ∼50 km.

Figure II.2: Deployment of seismic stations (SL19, SL15, SL23) and preparation for shipping after deinstallation of the temporary network (top, left). Solar panels were installed at half of the stations, which was the preferred source of energy.

Field impressions of station installations are shown in Figure II.2. Half of the stations were equipped with solar panels, which was preferred over the usage of the power supply system. The use of solar energy offered advantages for the site selection (to reduce human noise and chance of vandalism) and a more reliable power supply. Rural areas do not always have stable and continuous power supply and failures of the power grid could result in loss of data.

Seismometers were installed with direct contact to hard rock (if possible), and insulated to avoid temperature fluctuations. Additional plastic covers protected from potential water damage, especially during the rain season. The sensor was buried (if possible) or protected by any kind of enclosure, e.g., a brick wall (Fig. II.2, bottom left). Barb wire offered additional backstop against animals. Buddhist temples were often a suitable installation site, as they are mostly isolated yet permanently inhabited and hence protected against vandalism and theft.

Most of the stations operated when recovered at deinstallation. Three stations (SL04, SL14, SL30) were operating only for a short period of time. SL14 failed after just 13 days, which was too short to record enough earthquake signals or to recover stable Green's functions; hence it was excluded from both analyses. Stations SL04 and SL30 were recording for 85 and 30 days, respectively. These stations were included for the ambient seismic noise analysis, but discarded

for receiver function computation, as too few events occurred during operational time. The stations included in this study and the time period considered for further analyses are summarized in Table II.1. Station meta data can be found in Table II.A1.

Table II.1: Seismic broadband stations and time span included in this study. The temporary network 1A is our primary data source. SR: sampling rate (Hz); SWD: Surface wave dispersion; RF: Receiver functions. See also Table II.A1.

Network*	Stations	SR	SWD | Time Span | RF	
1A	SL01–SL31	100	06/2016–06/2017	06/2016–06/2017
GE	MALK, HALK	50	05/2016–08/2017	01/2015–12/2017
II	PALK	40	05/2016–08/2017	01/2015–12/2017

* 1A–Temporary; GE–GEOFON; II–IRIS/IDA

Two major problems were recognized. (1) Sensor issues during operational hours forced us to delete several weeks of data. (2) GPS signal problems caused time drifting and shifting in the data records. Both issues were discovered through ambient noise cross-correlation, as either the surface wave signal disappeared, or the surface wave signal was lagged along the time axis (see section 3.1, Fig. II.6).

Sensor or cable malfunction and data loss. Stations SL23 and SL31 experienced a malfunction of the sensor. We analyzed frequency spectra of the raw data before and after the malfunction (Fig. II.3) and observed a drastic change of the frequency content and energy for both stations. While both stations are functional, hourly spectra are relatively similar with dominant amplitudes at frequencies between 0.2–0.3 Hz. During the failure (SL23: 24.01.2017 at 16–17 UTC; SL31: 19.11.2016 at 19–20 UTC) the hourly spectrum shows anomalous behavior with strong amplitude increase for all frequencies and an overall amplitude drop afterwards.

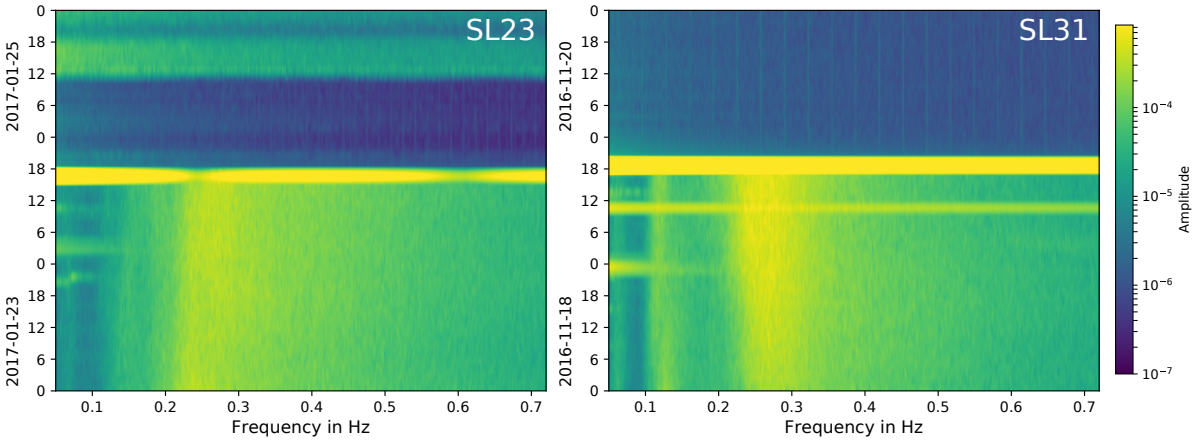

Figure II.3: Spectrogram of seismic raw data from station SL23 (left) and SL31 (right), recorded during sensor failure. Each subplot shows hourly computed spectra for 72 hours. Spectra are from decimated raw data (10 Hz). Amplitudes during sensor break are very large and exceed $8.5 \cdot 10^{-4}$ (maximum of color bar).

We recovered SL23 with a corroded pin on the sensor outlet, which likely explains the data loss from January 2017. Reasons for the malfunction of SL31 remain unclear. As the seismic

records after the failure just show noise, they were deleted; this resulted in available data of 7.5 months for SL23 and 5.5 months for SL31.

GPS signal loss and signal drift. Clock drift issues were discovered for stations SL11, SL15 and SL26 after ambient noise cross-correlation. The exact timing error of each station was computed by cross-correlating the daily Green's functions with their final stack for every station pair including the error afflicted station. For each day, the lag time of the maximum correlation was extracted, and the mode for all stations was computed. Thus, outliers and signals from the stations which also experienced clock drift were eliminated. The mode corresponds to the timing error. Figure II.4 shows the results for SL11 (left) and SL26 (right). The station pair lag times are shown in the bottom, with the mode in the top plot.

The strongest drift occurred at SL11 with a time shift from -49.8 to 69.8 s over a time period of 74 days. SL15 and SL26 show a drift period of 4 and 39 days, respectively, with maximum delay times of ±2 s. For the stations with continuous GPS reception this method results in a mode of 0 s throughout the complete time period. Note that the clock drift values cannot be more accurate than the sampling interval of 0.2 s.

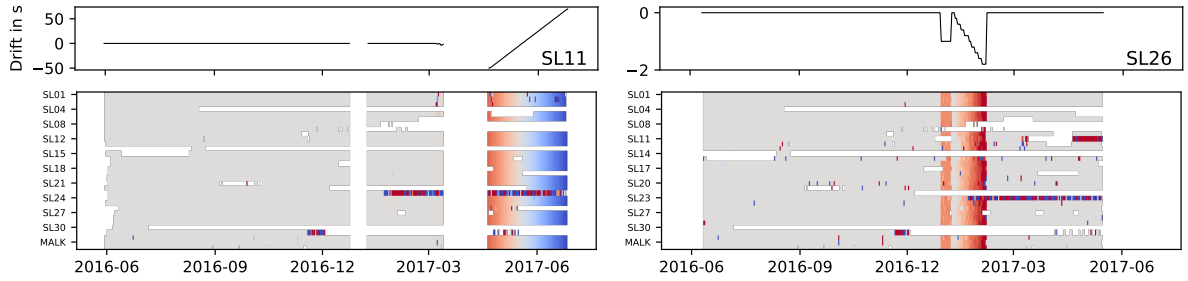

Figure II.4: Lag time of the maximum correlation (clock drift) for station pairs including SL11 (left) and SL26 (right). (bottom) The color coded area corresponds to the timing error derived from different stations. Gray areas represent times of no clock drift. Note that only every third station is labeled. (top) The clock drift for SL11 and SL26, derived from the mode of all stations.

The affected daily ambient noise correlograms were corrected for the clock drift with the daily drift value. The earthquake records within this time period were corrected with interpolated time drift.

3 Surface wave dispersion and tomography

3.1 Ambient noise Green's functions

In order to prepare the data for calculating the cross-correlation stacks, the linear trend and the mean were removed from the raw data and a lowpass filter was applied prior to decimation to prevent aliasing effects. The threshold was set to 85 % of the new Nyquist frequency (2.125 Hz). The data were down sampled to a sampling rate of 5 Hz, with subsequent removal of the instrument response.

For ambient noise cross-correlation, we applied the pre-processing procedures suggested by Bensen et al. (2007). The instrument corrected data were clipped at 3 standard deviations and bandpass filtered between 0.01–1.25 Hz. Then, spectral whitening and 1-bit normalization were applied. The cross-correlation was performed by correlating 1 hour segments of all station and component combinations and subsequent rotation of the full Green's tensor stream from the ZNE to the ZRT coordinate system. Daily stacks were computed by adding the correlograms

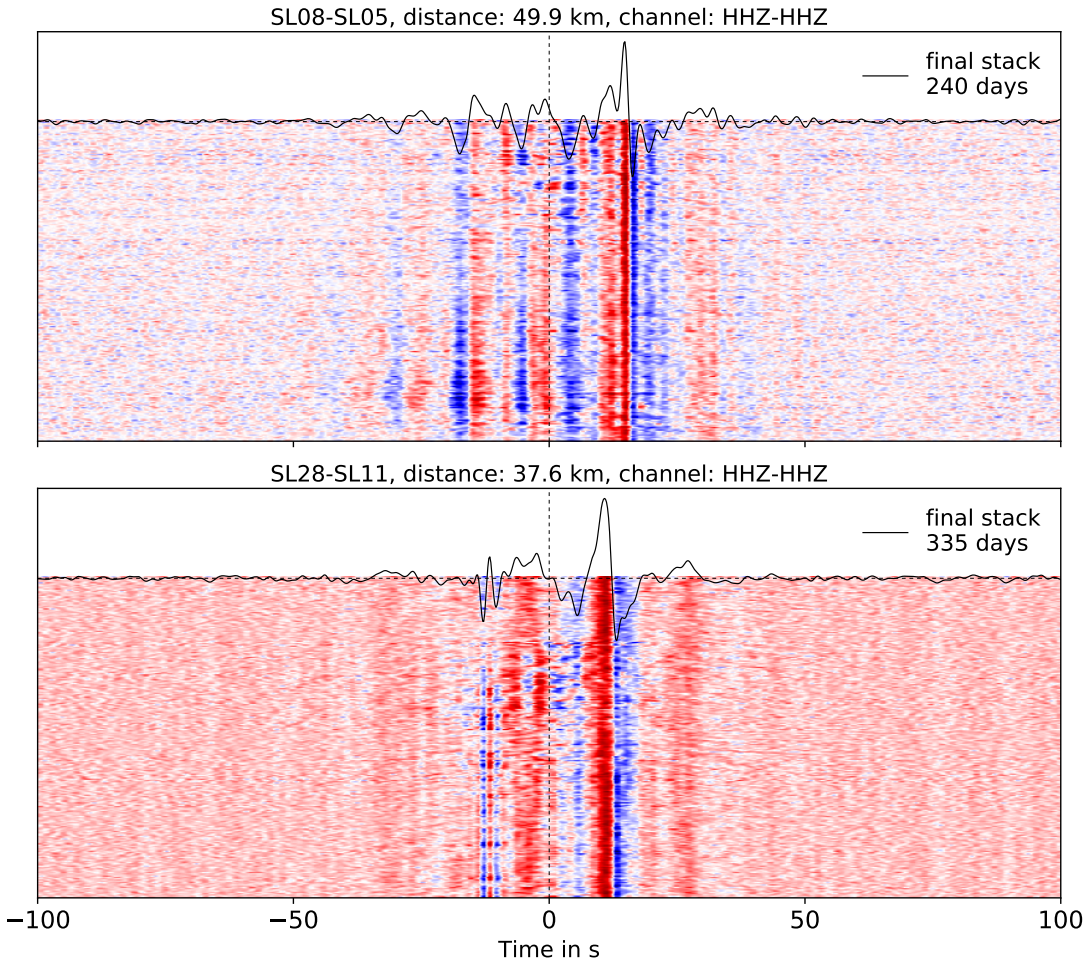

Figure II.5: Recovered Green's functions over time (colored area) and final stack (black line) for station pairs SL08-SL05 and SL28-SL11. Bandpass filtered between 2–35 s. SL11 is corrected for the clock drift; see Figure II.6 for uncorrected data.

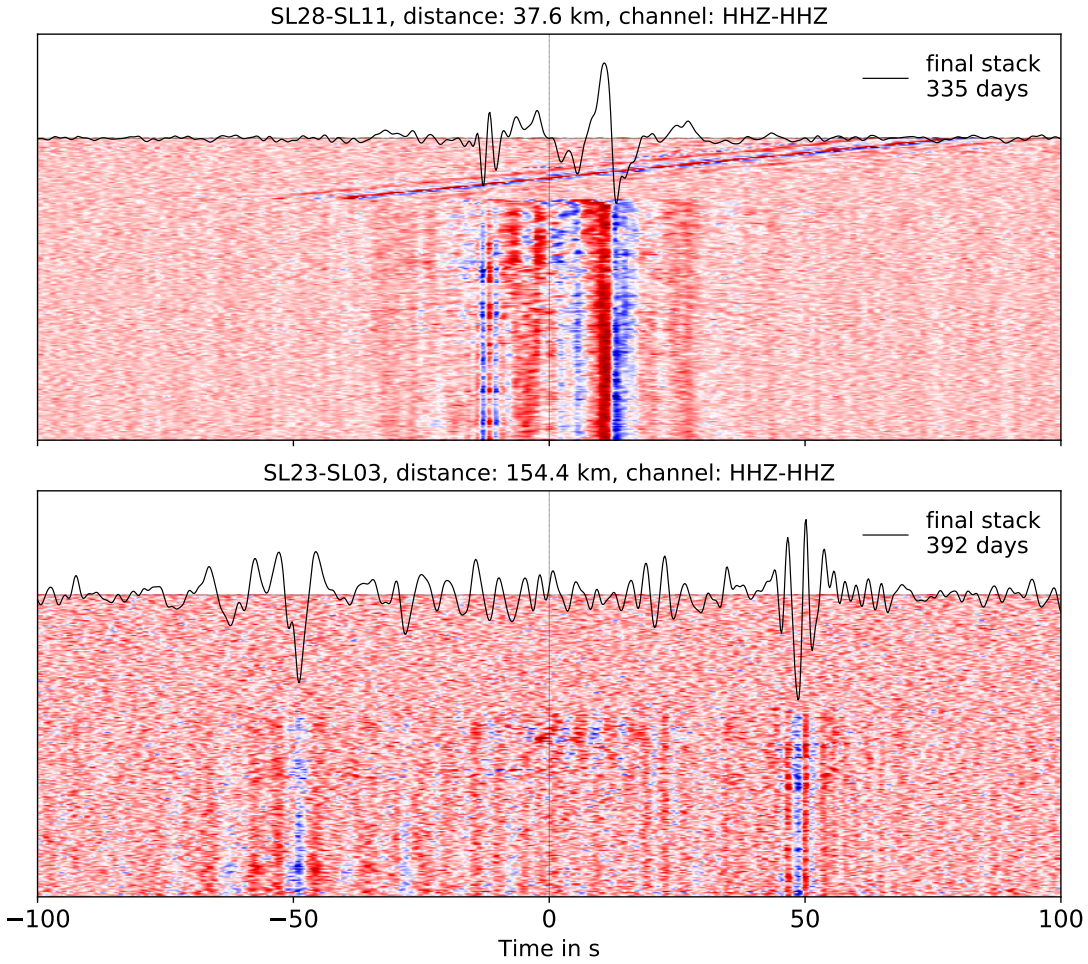

Figure II.6: Green's functions over time and final stack for two station pairs, each of which includes a station that experienced instrumental problems (chapter 2). (top) Clock drift issues contributed by SL11. The same station pair with clock drift correction is shown in Figure II.5. (bottom) Sensor failure from SL23 after 7.5 months.

resulting from one day. Stacking of the daily stacks for the available time period resulted in a final correlogram stack for each of the station pairs and components. We consider only combinations of the radial and vertical components, relevant for the Rayleigh surface wave, i.e., vertical-vertical (ZZ), radial-radial (RR), radial-vertical (RZ), and vertical-radial (ZR).

Figures II.5 and II.6 show daily correlograms over time and their final stack. Figure II.6 highlights the GPS and sensor issues of stations SL11 and SL23 (chapter 2). Figure II.5 (bottom) shows the correlograms of drift-corrected data from SL11. The Rayleigh wave shows a continuous and clear signal over the complete time period.

Data quality. Figure II.7 shows final stacks for different station pairs at two frequency bands. The signal is generally strong and cohesive for all components of a station pair. The Green's functions show stronger signals on the causal or on the acausal correlation lag, or equally strong signals on both time lags (Fig. II.7, bottom). This depends on the back azimuth of the station pair and on the period of the surface wave. The inter-station distance limits the maximum period at which surface wave signals are distinguishable from background noise (Fig. II.7 top middle).

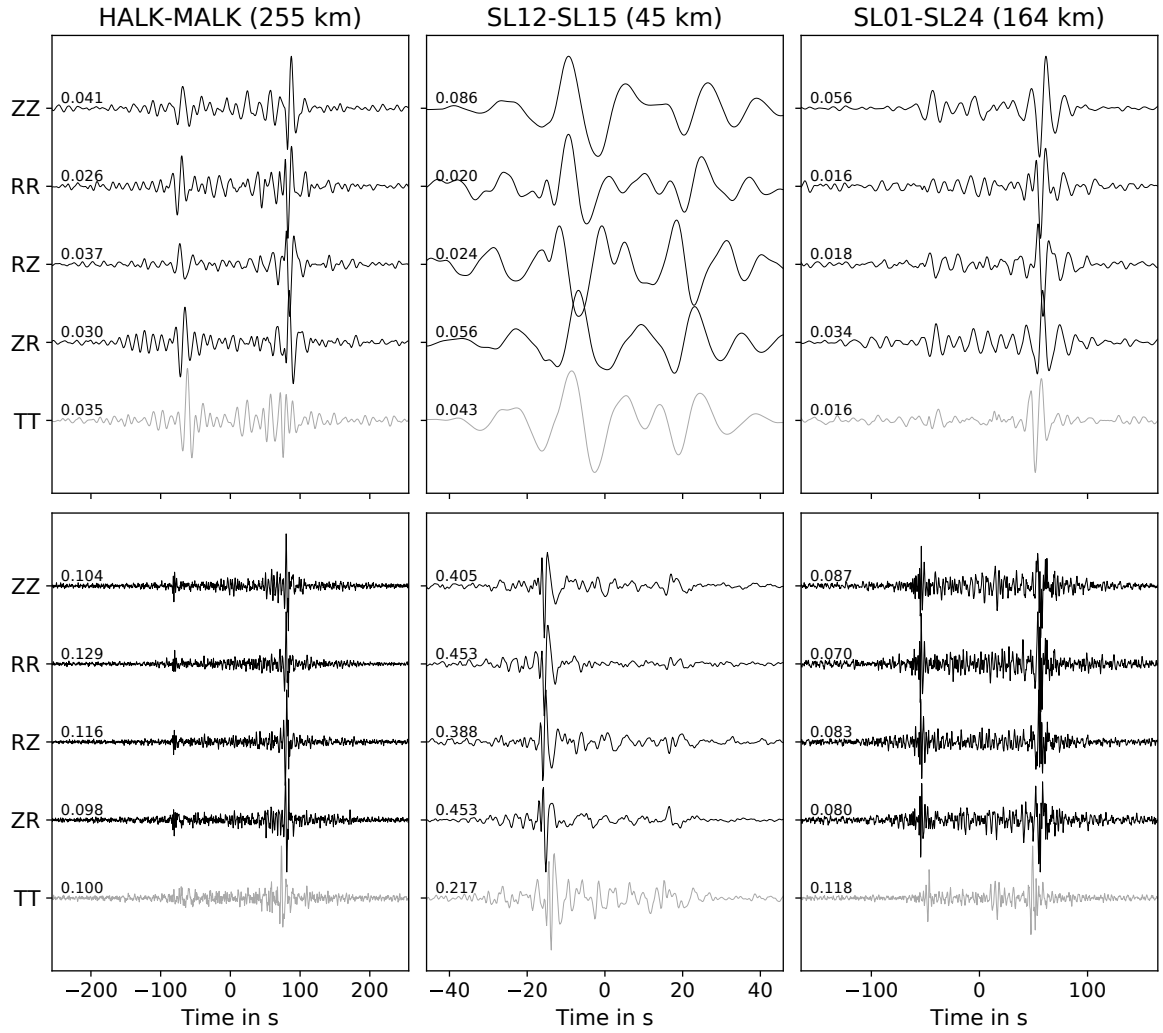

Figure II.7: Green's functions for ZZ, RR, RZ, ZR and TT components, frequency filtered between 10–40 s (top) and 1–10 s (bottom). The maximum amplitude before normalization is annotated at each time series.

We computed signal-to-noise ratios to estimate the signal strength of Green's functions. The signal is defined as the maximum amplitude within the time window at speeds between 1–4.5 km/s, and the noise by the root-mean-square of the correlogram at 300–500 s. SNRs were calculated separatly for the causal and acausal correlation lags. Figure II.8 shows SNRs dependent on inter-station distance and back azimuth for three period bands, which are representative for the short (<4 s), middle (4–14 s) and long (14–40 s) periods of this investigation.

SNRs decrease with distance, which is dominantly caused by the attenuation of wave amplitudes. At close distances, short periods show a higher signal strength than the longer periods, but they attenuate much quicker. The four Rayleigh components show comparably strong signals for the shorter periods, while the Love wave shows distinctly lower SNRs. For the longer periods, the signal strengths are highest for the ZZ and RZ components, and are similarly lower for the RR, ZR and TT components.

The relation between SNR and back azimuth depends on the azimuthal distribution of noise sources, which also can vary over time. For the short periods, the signal strengths of the Rayleigh

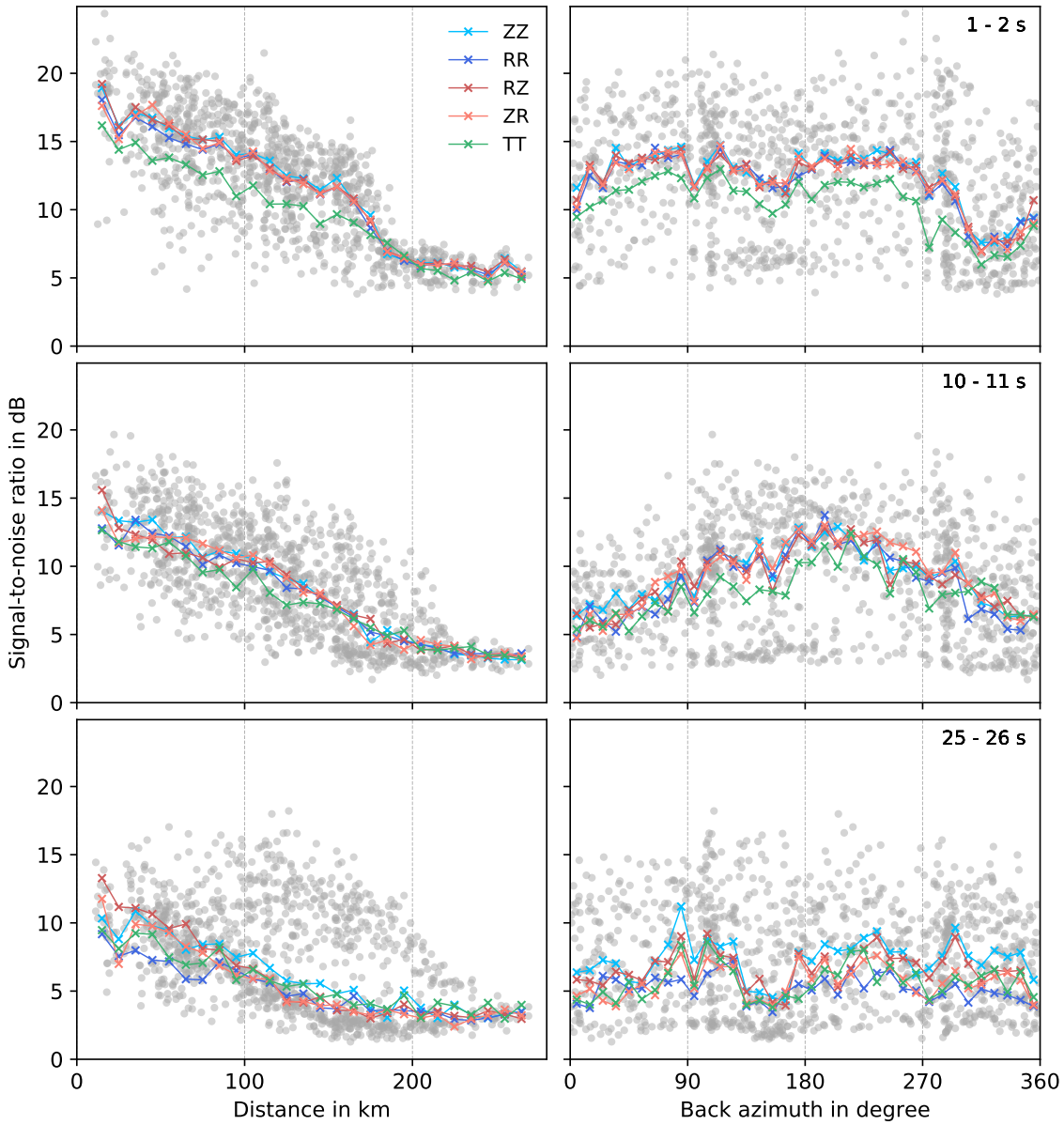

Figure II.8: Signal-to-noise ratios of Green's functions dependent on inter-station distance (left) and back azimuth (right). Illustrated are results for three period bands, representing the short (<4 s), middle (4–14 s) and long (14–40 s) periods from the complete data set. Gray dots show data for the ZZ Rayleigh component. Colored lines show the mean SNRs for each component (ZZ, RR, RZ, ZR and TT), binned in 10 km and 10° intervals.

wave components are similar, and higher compared to the Love wave component. Rayleigh and Love wave SNRs become more similar with increasing periods. The short periods show a rather bimodal distribution of SNRs with peaks at back azimuths of ∼90° and 250°, which correspond to waves traveling in W-E direction. A similar but less distinctive pattern is observable for the long periods. The middle period band shows strong amplitudes at ∼180°, corresponding to strong noise sources from the south.

Moveout velocity. Figure II.9 shows record sections of cross-correlograms from station pairs including PALK. The correlograms were bandpass filtered between 1–4, 4–8 and 8–32 s. The

Rayleigh wave moveout velocities increase towards the longer periods and are between 2.5–4 km/s. The surface waves are symmetric regarding the arrival times and show no obvious velocity dispersion.

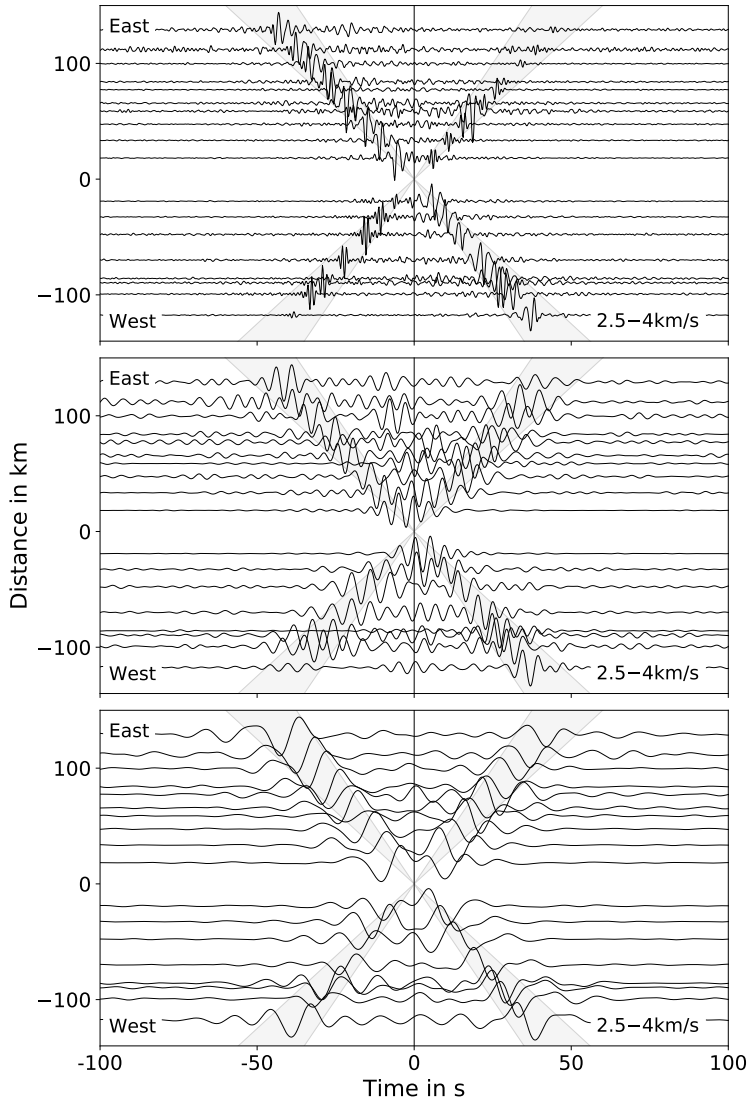

Figure II.9: Record sections of ZZ Rayleigh wave correlograms with station pairs along the main profile including the station PALK. Positive and negative distances are relative to PALK and represent the inter-station distances of stations located to the east and west, respectively. Correlograms were bandpass filtered between 1–4 and 4–8 s and 8–32 s.

3.2 Surface wave dispersion

Surface wave dispersion was determined from the phase of the fundamental mode Rayleigh wave, based on the zero crossings of the real part of the correlation spectrum (Aki, 1957; Ekström et al., 2009). The 2π ambiguity leads to a family of possible period–phase velocity relations. Therefore, the average phase velocity dispersion (Prieto et al., 2009) was computed for Sri Lanka and used as a guide for selecting the most likely branch for each station pair. To retrieve phase velocity measurements we used the tool GSpecDisp (Sadeghisorkhani et al., 2017). Advantages of phase velocities over group velocities are highlighted in section I.3.2.

Dispersion curves were determined for the ZZ, RR, RZ, and ZR components, separately, resulting in 478, 422, 440, and 454 successful measurements, respectively. For 385 station pairs, all four components were picked. To retrieve the final Rayleigh wave dispersion curve

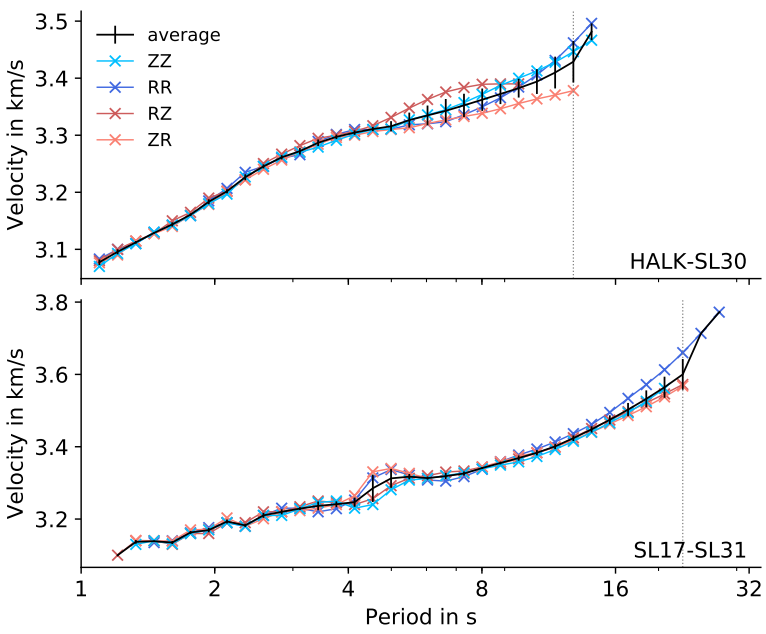

Figure II.10: Construction of average dispersion curves from the four measured Rayleigh wave components (ZZ, RR, RZ, and ZR) at two station pairs. The black line shows the average curve including standard deviations. The vertical line shows the maximum period considered. Cutting was only necessary, if the maximum period measured from each component was different from each other, and would introduce a kink in the average curve.

for each station pair, the four dispersion curves were averaged after interpolation, and cut at a maximum period. Figure II.10 shows the process for two station pairs. The final 385 phase velocity dispersion curves for Sri Lanka are illustrated in Figure II.11. The velocities increase from 2.9–3.3 km/s at the period of 1 s to 3.7–4.0 km/s at 30 s. The variations of phase velocities cover a narrow band with an average width of 0.35 km/s.

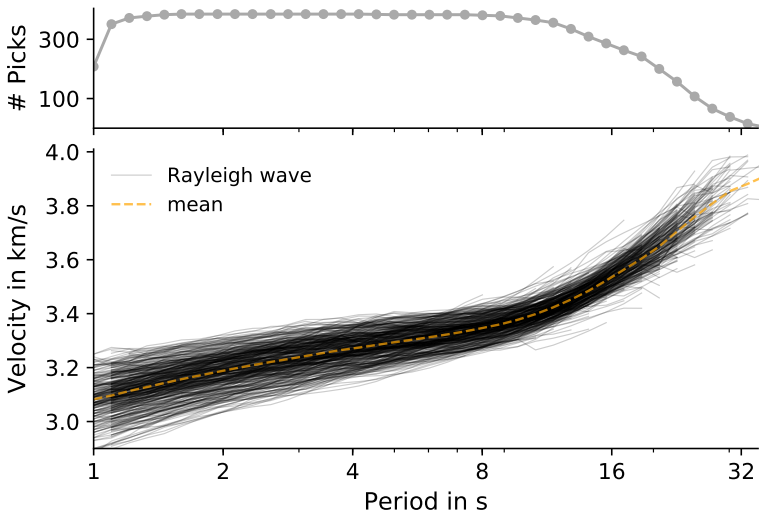

Figure II.11: (top) Number of measured phase velocities at discrete periods. For most periods, the number of picks is >300. (bottom) Rayleigh wave dispersion curves for 385 station pairs.

3.3 Travel time tomography

For travel time tomography, we used the FMST package (FMST; Rawlinson, 2005; Rawlinson and Sambridge, 2005) as described in section I.3.1. We gridded our study area into 12 x 15 cells, each having a dimension of ∼25 x 33 km. We considered 5 iterations, as the residuals rapidly

decreased and converged. We assumed 2.5 % outliers, which were removed at the 2nd iteration. As starting model, each grid node was set to the observed mean velocity at the period.

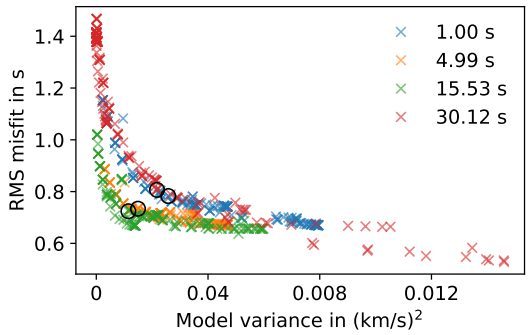

Figure II.12: Trade-off between data misfit and model roughness based on 150 parameter combinations, considering 25 damping factors (log-spaced between 0.1–10,000), and 6 smoothing factors (log-spaced between 0.01–1000). Illustrated are four periods. The optimum minimizing data misfit and model roughness is encircled.

Trade-off curves were computed to extract optimum damping and smoothing parameters that minimize data misfit and model variance (Fig. II.12). We used the standard deviations from averaging of measured phase velocities of the Rayleigh components (Fig. II.10) as uncertainties for each ray path within the tomographic inversion. The standard deviations were rounded to one decimal place (i.e., 0.1 s, 0.2 s, etc.), but any value rounding to 0 s was set to 0.1 s, as 0 s would unrealistically imply no uncertainty. Additionally, the median uncertainty was computed for each discrete period. If a ray path has an uncertainty larger than three times the median value, the station pair was excluded for the particular period. Up to 15 ray paths per period were eliminated due to this pre-selection condition.

A selection of tomography results is illustrated in Figure II.13. For shorter periods (1–8.5 s), velocity contours roughly follow the geological boundaries along a NNE-SSW direction. The highest velocities are around the WC/KC/HC contact and decrease towards the west and east. The lowest velocities are in the south-east of the island. For periods above 10 s, the pattern

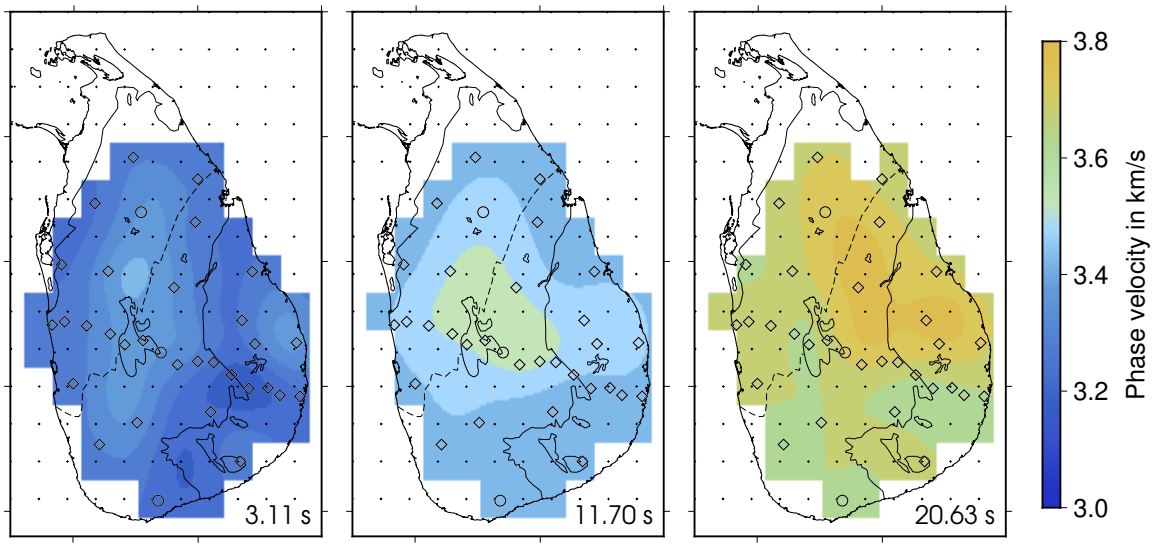

Figure II.13: Tomographic inversion results for Rayleigh wave phase velocities for three discrete periods. Black crosses indicate grid cell nodes. Grid cells are only colored if rays are propagating through. Black lines and symbols represent geologic boundaries and seismic stations, respectively (see Fig. II.1 for reference).

changes towards a north–south subdivision of velocity regions, instead of following the geologic boundaries.

Final dispersion curves were constructed from the tomography results, based on the locations of the seismic stations. These dispersion curves are smooth and stable up to a period of 30 s (see Fig. II.B1).

4 Receiver function analysis

4.1 Earthquake records

We considered earthquakes with magnitudes M>5.5 and epicentral distances of 30–90° (based on the USGS catalog). The temporary network recorded 246 events, the permanent stations 636 events. Earthquakes with magnitudes M<5.5 have low signal strengths and are barely visible on the broadband records. Event locations are illustrated in Figure II.14.

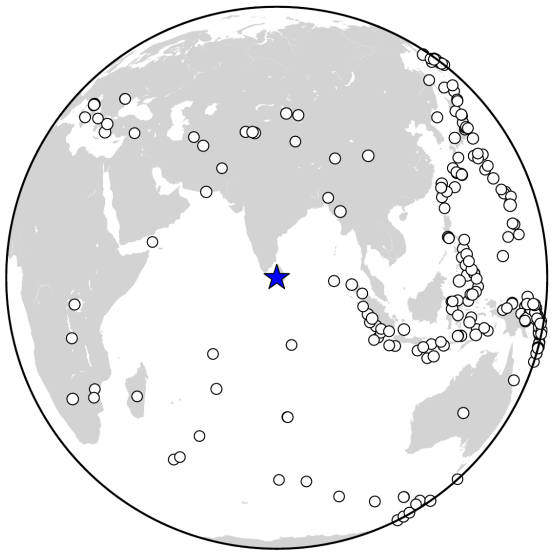

Figure II.14: Earthquake epicenters of events with M>5.5 and epicentral distances of 30–90°. Blue star marks the location of Sri Lanka.

Most of the events are located NE-SE of Sri Lanka within a back azimuthal range of 40–120°, specifically along the West-Pacific and Indonesian plate boundaries. The back azimuths of 0–30° and 120–360° show only few events and hence, sparse azimuthal ray path coverage. The rays cover a slowness range of 4.6–8.8 s/°.

Figure II.15 shows seismic record sections from the vertical component of two events. The marked P- and S-onset times of the direct waves were computed based on the reference Earth model IASP91. The middle column provides a close-up of the P-coda and shows clear phase arrivals for each trace. The right column visualizes spectral, amplitude and mean signal-to-noise ratios. To ensure good quality earthquake recordings for receiver function computation, we selected seismograms with a mean signal-to-noise ratio >2.5.

The spectral SNR displays the general detectability of an event. The signal window is defined by the theoretical P- and S-onsets (Fig. II.15, left). The noise window is defined by the time window directly before the P-onset with the same length as the signal window. The spectral SNR was computed between frequencies of 0–2 Hz and averaged to a single SNR value.

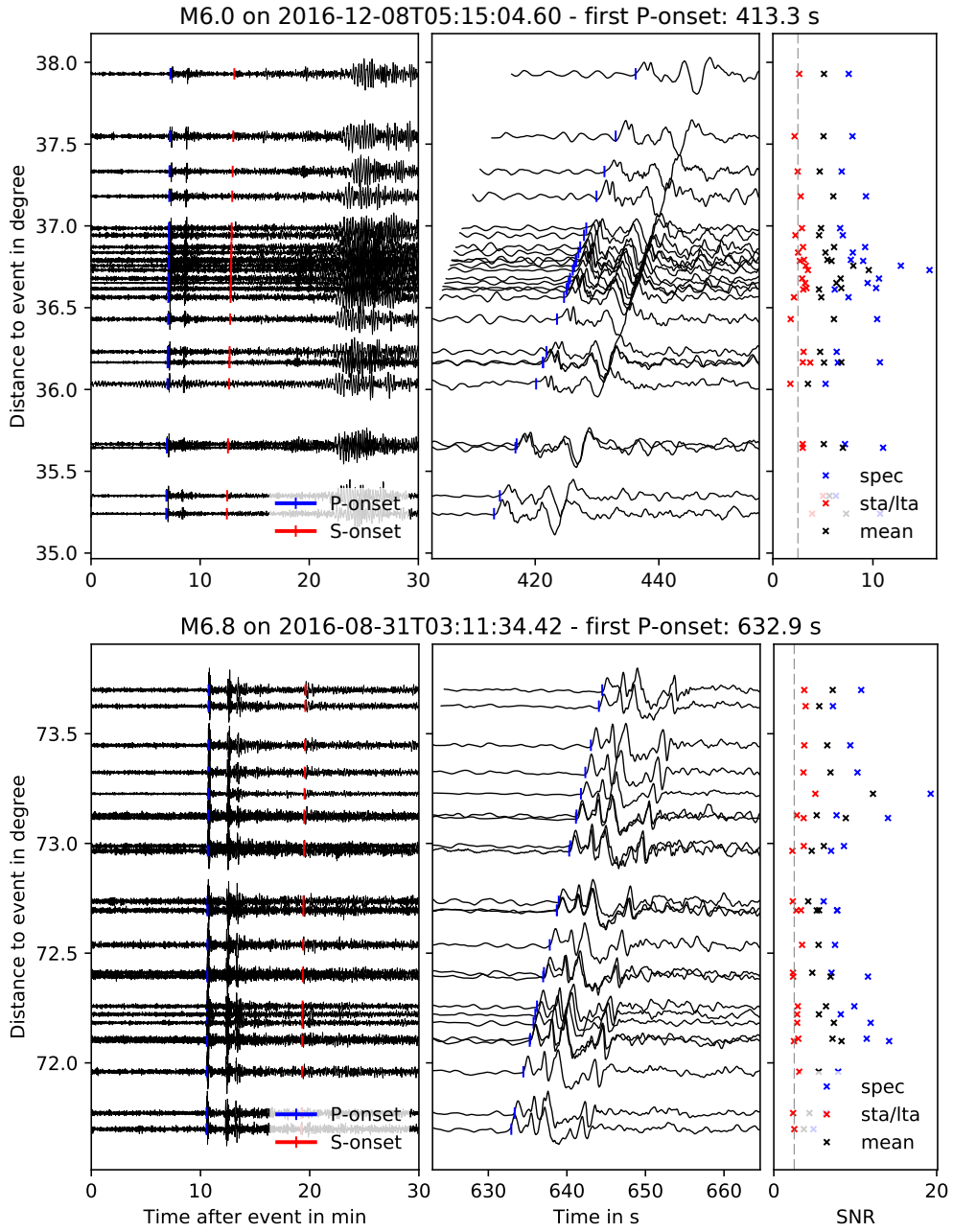

Figure II.15: Record sections of two seismic events from the vertical component, bandpass filtered 0.05–5 Hz. (left) Theoretical arrival times for direct P- and S-waves were computed based on the Earth model IASP91, and define the signal window for the spectral SNRs. (middle) A close-up to the direct P-wave arrival and P-wave coda. (right) Spectral, amplitude and mean vertical SNR for each trace. Gray dashed line at SNR=2.5 represents the threshold for trace selection.

The amplitude SNR indicates the sharpness of the P-wave coda relative to the background noise. The short time average over long time average (STA/LTA) helps to define the length of the signal window (Fig. II.16, green shaded). The start of the signal window is defined by the theoretical P-wave arrival (solid blue line). The closest STA/LTA amplitude peak after the P-wave arrival defines the start of the detection window (gray shaded). Within the 100 s long detection window, the minimum STA/LTA (solid green line) marks the end of the signal window (dashed green line). Through this approach, we are able to adjust the length of the signal window

to capture the first bundle of P-wave energy. If there is no clear P-wave signal (Fig. II.16, top left), the signal window is defined by random changes in the seismogram. The signal window has a minimum length of 30 s. The noise window (red shaded) is defined by the time window directly before the P-onset with the same length as the signal window. The amplitude SNR was computed by the root-mean-square of the data within each window.

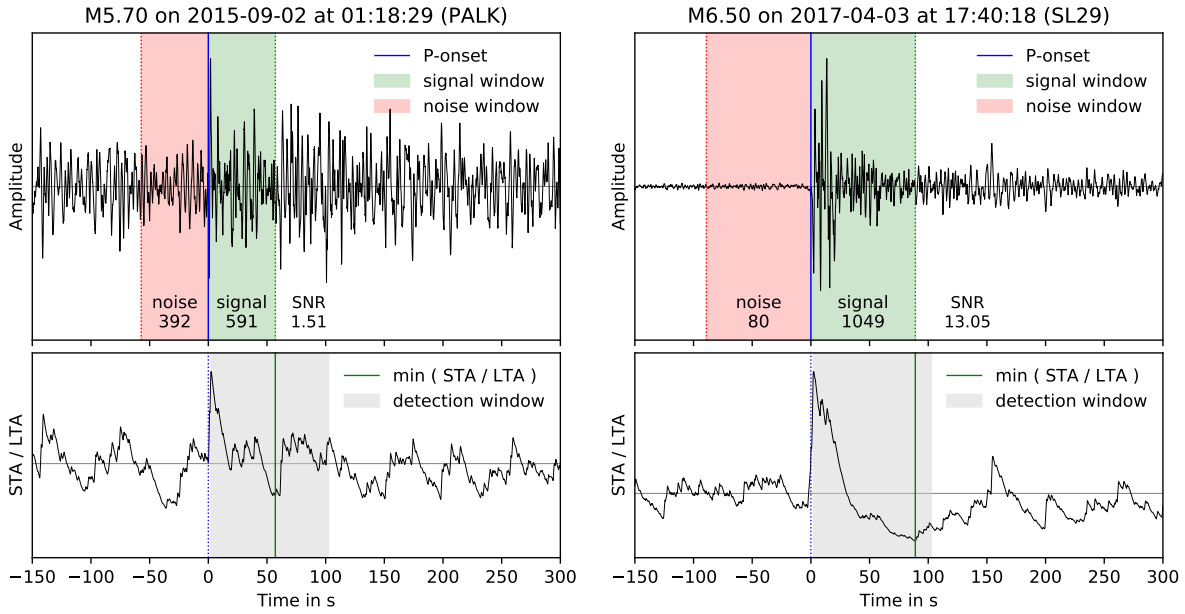

Figure II.16: Computation of amplitude SNR. Construction of the signal and noise windows based on the STA/LTA ratio with a 10:30 s window ratio. Illustrated are two event traces of the vertical component showing a weak (left) and a strong signal (right). For details see text.

Spectral and amplitude SNRs were computed for each component of an event, i.e., Z, N and E, resulting in six values for each trace. Figure II.17 displays the spectral, amplitude and mean (of spectral and amplitude) values for each component, dependent on event magnitude and P-wave travel duration between source and station. Higher event magnitudes and shorter travel times (short distances) correspond to higher SNRs. The highest SNRs can be observed on the vertical component. The spectral ratios are significantly higher than the amplitude ratios.

Table II.2: Number of traces selected for receiver function computation for each station. Mean (spectral and amplitude) signal-to-noise ratios are >2.5.

station	traces	station	traces	station	traces	station	traces	station	traces
SL01	48	SL09	32	SL16	52	SL23	35	SL30	3
SL02	63	SL10	59	SL17	63	SL24	84	SL31	25
SL03	46	SL11	43	SL18	61	SL25	78	HALK	169
SL04	8	SL12	47	SL19	65	SL26	43	MALK	193
SL05	49	SL13	59	SL20	64	SL27	48	PALK	200
SL06	53	SL14	2	SL21	68	SL28	55		
SL08	40	SL15	53	SL22	23	SL29	48		

To select high quality traces for receiver function computation, three component event traces were selected if the vertical component mean SNR is >2.5. The selection process resulted in

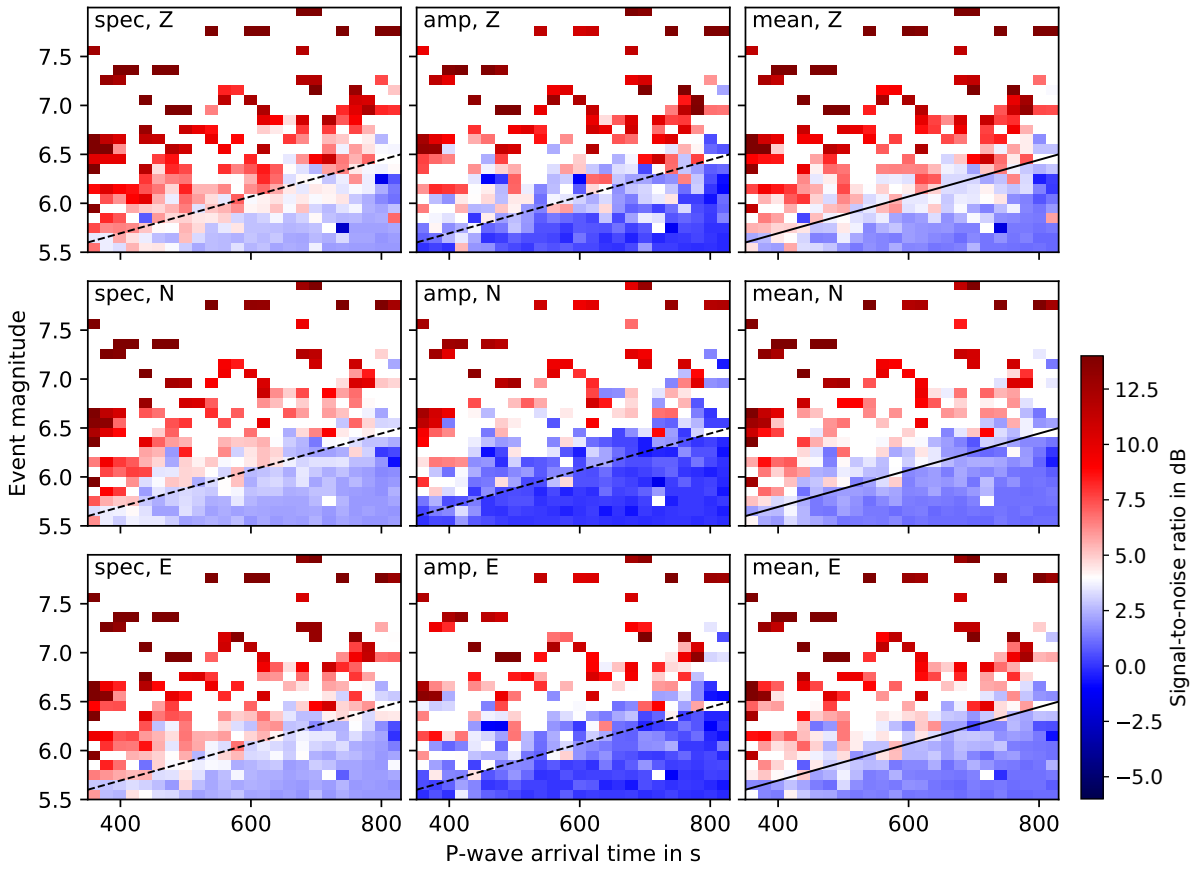

Figure II.17: Spectral (spec), amplitude (amp) and mean signal-to-noise ratios for each component (Z, N, E). The values are illustrated dependent on event magnitude and direct P-wave travel time between source and station, and averaged in bins of width 0.1 and 20 s, respectively. A SNR of 2.5 corresponds to 4 dB (white in colorbar). The 2.5 SNR threshold was estimated from the mean SNR plots (third column, solid lines), and copied to the spectral and amplitude SNR plots (dashed lines, two left columns).

1979 traces from 267 events (Tab. II.2). Stations SL04, SL14 and SL30 were excluded as they only show 8, 2 and 3 good traces, respectively.

4.2 Receiver function computation

For P receiver function computation, each trace was filtered (bandpass: 0.05–5 Hz), decimated to a sampling rate of 20 Hz, and trimmed to 5 s before and 30 s after the P-onset. Subsequently, each trace was rotated from the ZNE into the LQT ray coordinate system based on the theoretical incidence angle assuming a surface V_S of 3.5 km/s (see analysis below). The Q component was then deconvolved with the respective L component, utilizing water level stabilization (level: 0.001) and lowpass filtering with a Gaussian function (Gauss factor: 1.0). The receiver functions were sorted according to slowness and stacked in bins of 0.2 s/° without amplitude normalization. The bin-stacked RFs show a coherent signal, as can be seen in Figure II.18. The Q-RFs were not moveout corrected for the final stack, as the moveout correction has a strong effect on the multiple timing, which would result in biased interface depths in an inversion.

On each stack (Fig. II.18, tops), the Ps conversion (Moho arrival) is the clearest peak

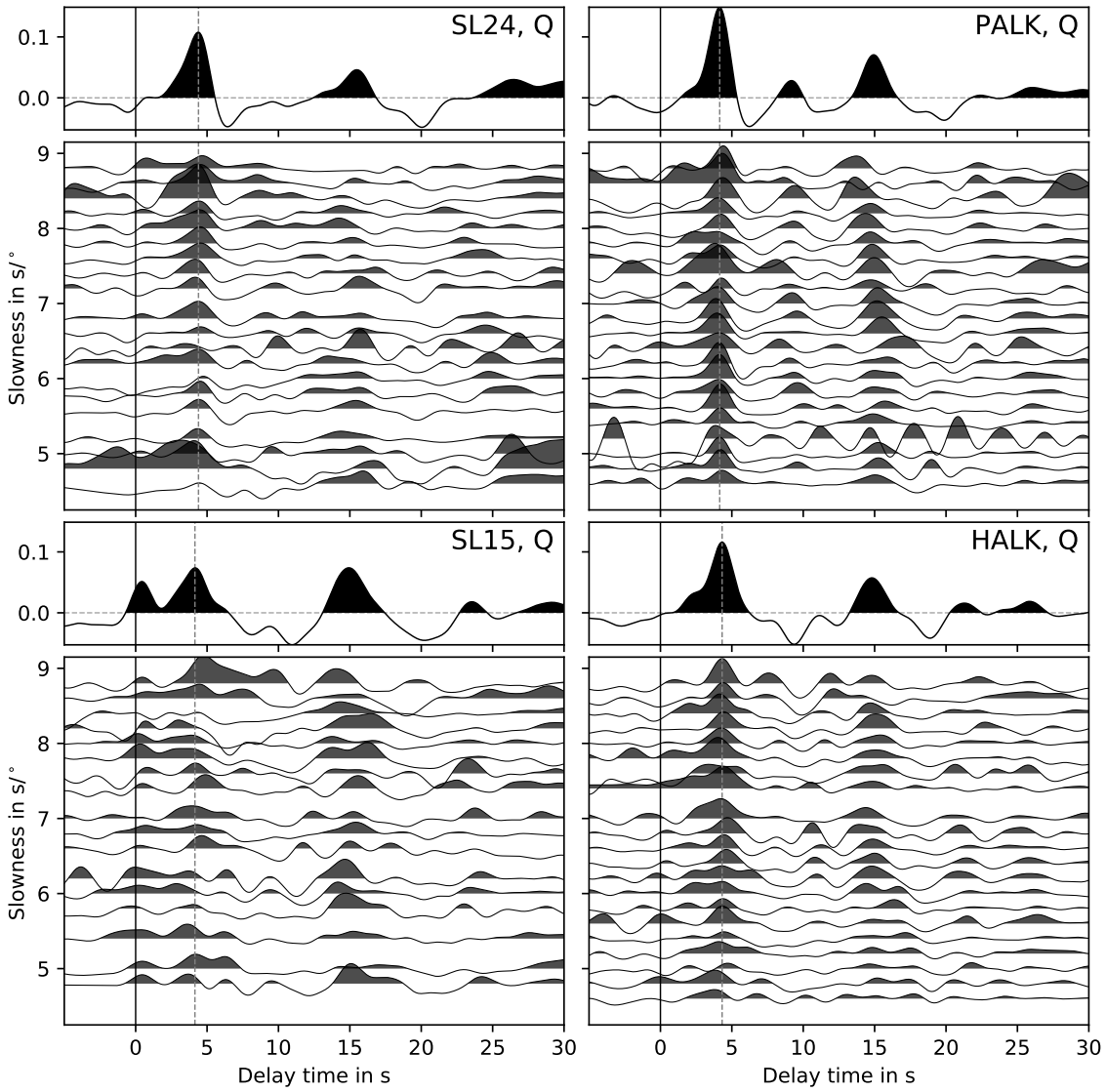

Figure II.18: Binned Q-RFs for different stations located in the north (SL24), center (PALK), east (SL15) and south (HALK) of Sri Lanka. Single event RFs were sorted for slowness and bin-stacked for 0.2 s/° intervals. The top of each subplot shows the stack derived from averaging the binned receiver functions. The dashed line indicates the Ps converted Moho phase.

(t_{Ps} ≈4.2 s), Moho multiples are visible at ∼15 and ∼20 s, respectively. No intra-crustal arrivals appear before the Ps phase, however, PALK shows a strong positive phase at 9.4 s. When applying a broader Gaussian filter, a small amplitude phase occurs before the Ps phase, which might be the direct phase of an intra-crustal conversion corresponding to the 9.4 s multiple. However, applying a broader filter includes many unwanted high-frequency phases. For SL15, the peak at close-to-zero delay time is direct P-wave energy. It was not completely eliminated by the rotation into the LQT coordinate system, because of the chosen rotation angle. This peak tells us, that the surface velocity, on which the rotation angle is based on, is higher then the assumed 3.5 km/s. Using a constant surface velocity for rotation has the advantage to minimize the number of variables for synthetic modeling in the later Bayesian inversion.

Receiver functions along the main profile are illustrated in Figure II.19. The independently

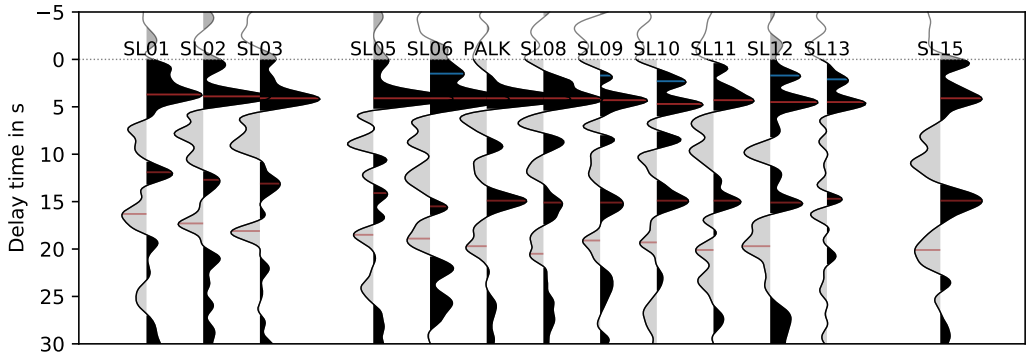

Figure II.19: Receiver function stacks along main profile from SL01 to SL15. Brown markers indicate clear Ps converted phase at the Moho and corresponding multiples. Indications for a mid-crustal converter are marked in blue.

derived station stacks show consistent phases throughout the profile, especially regarding the Ps phase and its multiples. An intra-crustal phase (including first multiple) is visible at the central stations SL06–SL10 and fades at SL11–SL13. This intra-crustal arrival indicates a discontinuity with a strong velocity contrast at about 15–25 km depth.

Surface velocity from RF rotation angle. The apparent incidence angle of a P-wave at the surface depends on the surface S-wave velocity (see general *Methodological background*). Hence, a wrongly assumed V_S for the trace rotation into the LQT coordinate system would not (perfectly) separate P-, SV- and SH-energy onto different components, and the Q component would show P-energy, especially prominent at zero delay time. Note, that also with Q⊥L the rotation itself does not perfectly separate P- and S-waves at the free surface. Here, we use the relation to quantitatively estimate the surface V_S below a receiver and assume the P-energy at zero delay time to (almost) disappear, if the V_S assumed for rotation is correct.

Table II.3: Surface V_S (km/s) derived from RF rotation analysis. Values in brackets denote unreliable measurements. We estimate an average uncertainty ±0.13 km/s (see text).

station	V_S	station	V_S	station	V_S	station	V_S	station	V_S
SL01	3.45	SL09	3.10	SL16	3.75	SL23	(4.25)	SL30	–
SL02	3.70	SL10	3.20	SL17	3.25	SL24	3.35	SL31	3.20
SL03	3.80	SL11	3.40	SL18	3.40	SL25	3.80	HALK	3.45
SL04	–	SL12	3.50	SL19	3.30	SL26	3.75	MALK	3.40
SL05	3.70	SL13	3.35	SL20	(4.05)	SL27	3.15	PALK	3.30
SL06	(4.00)	SL14	–	SL21	3.25	SL28	3.40		
SL08	3.15	SL15	3.80	SL22	3.75	SL29	3.80		

We computed receiver functions as described above, and used the theoretical incidence angles for surface velocities between 2.5–4.5 km/s (0.05 km/s steps). Figure II.20 illustrates results for two stations. Besides the amplitudes before and at the P-onset, the overall shape of the RFs is independent from the rotation angle and shows similar character with only minor amplitude differences, and edge effects at >26 s. With increasing surface V_S the P-onset energy decreases and at some point crosses the zero-energy threshold. For all stations, this relation is linear with

an average P-onset amplitude decrease of 0.115 per 1 km/s V_S increase.

The RF with the lowest P-onset energy (Fig. II.20, red) represents the best model for the station. Table II.3 summarizes the surface V_S gained for all stations. Surface V_S >4 km/s are highly unlikely and are outlier measurements. Reliable measurements of surface V_S range between 3.1–3.8 km/s and show an average of 3.5±0.2 km/s. The results show a wide scatter and do not consider noise for the RFs.

To estimate uncertainties for the surface V_S, we assumed a noise level of 15 % of the maximum RF amplitude, i.e., a noise amplitude of about ±0.015. Based on the linear relation between surface V_S and P-onset amplitude, we calculated an uncertainty for V_S of ±0.13 km/s.

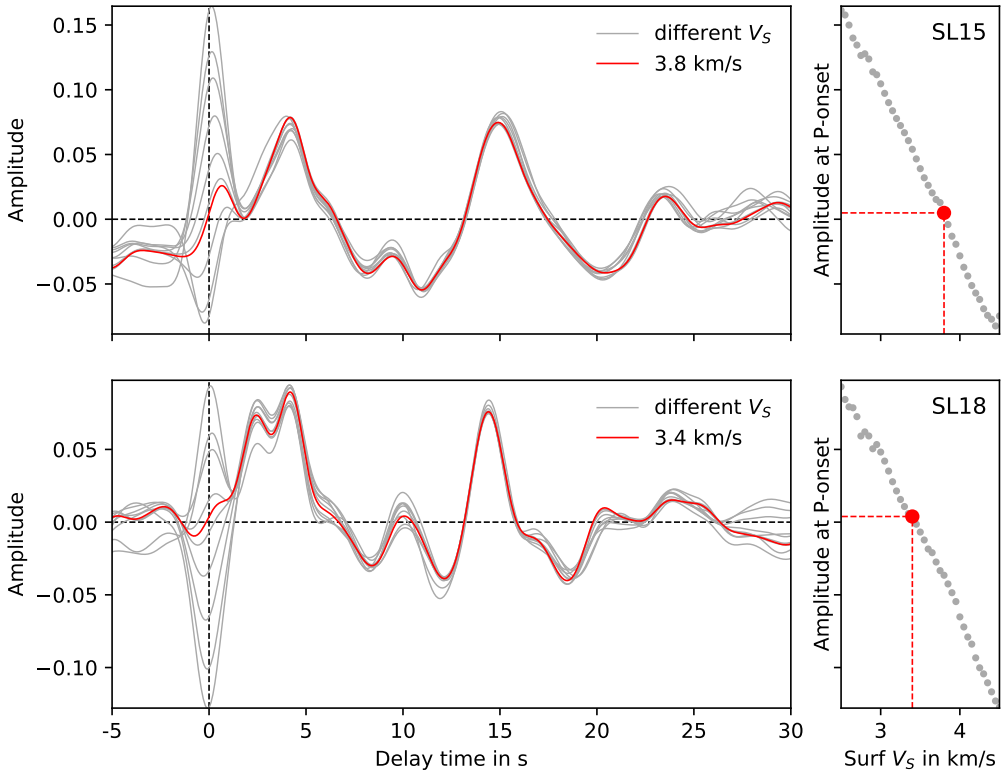

Figure II.20: (left) Q receiver function stacks (gray, red) for SL15 and SL18, respectively, using different incidence angles (surface V_S) for the rotation into the LQT system. The red RF has the lowest P-onset energy (>0). (right) P-onset energy dependent on the surface V_S (gray dots). The red dot marks the lowest P-onset energy. For details see text.

4.3 Hκ-stack grid search

The Hκ-stack grid search method following Zhu and Kanamori (2000) was applied to estimate Moho depths and V_P/V_S ratios. Hereafter, Hκ-stack values are first calculated for single events and then the grids for all events are stacked. The maximum stack value then gives the optimum combination of Moho depth and V_P/V_S ratio. After testing a larger grid search area, the grid was limited to Moho depths between 25–41 km and V_P/V_S ratios between 1.55–1.95. We assume an average crustal V_P of 6.5 km/s, which is reasonable for felsic amphibolite and granulite facies continental crust (Huang et al., 2013).

Figure II.21 shows Hκ-stack results for six stations. The theoretical arrival times for Moho phase and multiples (red lines) correspond to the best model (red +). Uncertainties are computed based on the 97.5 % contour line, and agree approximately with uncertainties estimated with Monte Carlo (drawing randomly with replacement from the event set for each station, Fig. II.21, blue dots). For SL18 and HALK, the Monte Carlo estimates are very concentrated, implying that the uncertainty is small. SL03 shows a large range of possible Moho depth and V_P/V_S ratio combinations and a large uncertainty; nevertheless, the best estimate seems reasonable when comparing theoretical model arrival times to the actual input RFs. SL31 shows estimates close to the upper and lower V_P/V_S limits. If extending the grid, the estimates (including the best

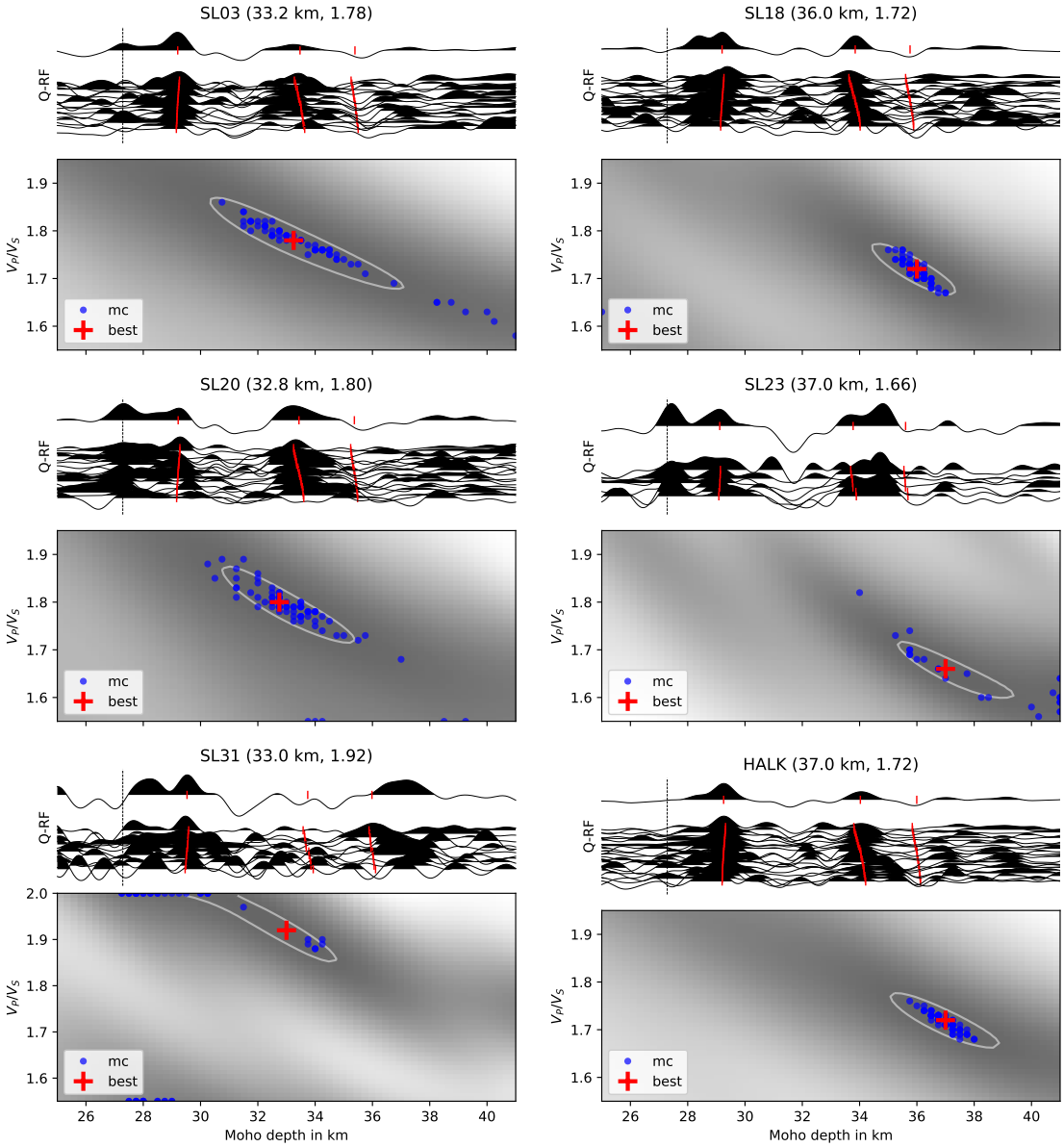

Figure II.21: Hκ-stack grid search for six stations, showing (top) input RFs and theoretical arrival times for Moho phase and multiples corresponding to the best model, and (bottom) stacked Hκ-grid from single events with Moho depth and V_P/V_S ratio estimates from Monte Carlo (mc), and the best estimate (global maximum of the search field). The white contour line corresponds to 97.5 % of the best estimate's amplitude. Assumed V_P is 6.5 km/s.

model) move to higher V_P/V_S ratios and shallower Moho depths. In addition, the arrival times of the multiples for the best model do not agree with the data; the RFs for this station seem to be influenced by scattering or multiple interfaces, so that Hκ-stacking is unreliable for SL31. Hence, we disregard the results for this station. This is the only station where such behavior occurs.

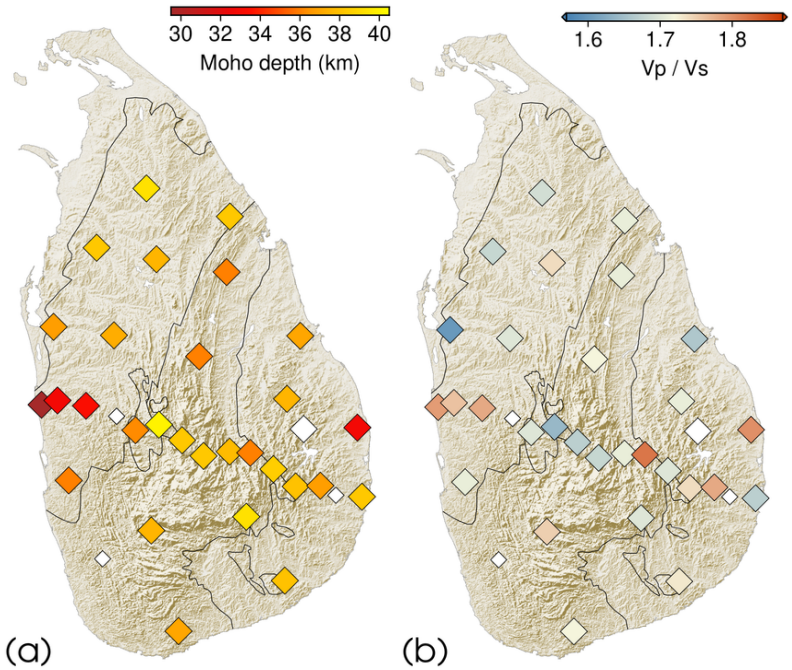

Figure II.22: Spatial distribution of (a) Moho depths and (b) V_P/V_S ratios from Hκ-stack grid search. Small and normal sized white symbols show stations with no analysis performed or no result gained, respectively.

Moho depths and V_P/V_S ratios and their uncertainties are summarized in Table II.B1. Moho depths for Sri Lanka are between 29.5–40 km with a typical uncertainty of ∼0.7 km; for V_P/V_S ratios, the range is 1.6–1.82 with an average of 1.71 and a typical uncertainty of 0.02. The Moho depth estimates strongly depend on the assumed crustal V_P; a misestimation of 0.1 km/s would result in a crustal thickness variation of about 1 km. The V_P/V_S ratios do not depend significantly on the assumed V_P. The spatial distribution of Moho depths and V_P/V_S ratios are illustrated in Figure II.22.

5 Bayesian inversion of SWD and RF

5.1 Inversion with BayHunter

As a final step, phase velocity dispersion curves and receiver functions were jointly inverted with a Markov chain Monte Carlo (McMC) transdimensional Bayesian inversion tool (BayHunter; Dreiling and Tilmann, 2019), where we solve for the V_S-depth structure, the number of layers, the noise parameters, and the crustal average V_P/V_S ratio. While other inversion methods often favor one best model based on the least misfit, an inversion after Bayes' theorem is based on the model's likelihood and results in probability distributions for each parameter of the model. The inversion result is represented by a collection of models, the posterior distributions of which ideally form Gaussian distributions if the chains have converged. For further details refer to part III of this thesis.

Table II.4: Model priors and parameters used for Bayesian inversion of each station. Model prior tuples define the limits of a uniform distribution. Detailed explanation of parameters can be found in section III.3.2.

Model priors	
vpvs	= (1.55, 2.05)
layers	= (1, 20)
vs	= (2, 5)
z	= (0, 75)
r_{RF}	= 0.96
σ_{RF}	= (1e-5, 0.05)
r_{SWD}	= 0.
σ_{SWD}	= (1e-5, 0.05)

Inversion parameters	
nchains	= 100
$iter_{burnin}$	= 1 200 000
$iter_{main}$	= 600 000
acceptance	= (55, 65)
r_{cond}	= 1e-7

The model priors (Tab. II.4) were set to a wide range, i.e., a depth range for the interfaces from the surface to 75 km, V_S between 2–5 km/s, and average crustal V_P/V_S ratios between 1.45–2.05. Additionally, a maximum of 20 layers was imposed. The noise amplitude σ_{RF} is between ∼0–0.05, and σ_{SWD} between ∼0–0.05 km/s. The correlation parameter r for the correlated noise of RFs was fixed to a value of r_{RF}=0.96. The threshold to suppress small eigenvalues to stabilize the noise correlation matrix, r_{cond}, was set to 10^{-7}. For surface wave dispersion, the noise was assumed to be uncorrelated. The model priors turn out to be sufficiently wide, relative to the values with significant probability, i.e., none of the parameters inverted for have settled on a boundary.

The inversion was performed with 100 chains to ensure a sufficient number of independent parameter search paths. Each chain performed 1.8 million iterations, with a 2:1 ratio for the burn-in and exploration phase. The probability distributions for the proposal generation were adjusted during the inversion to maintain an overall acceptance rate of ∼40 %. Some chains failed to converge, returning significantly lower likelihoods and higher misfits than most chains after the burn-in phase. Such chains were declared as outlier chains. For the complete data set, ∼5 % of the chains were declared as outlier chains, which indicates that the chosen number of iterations was sufficient enough for most chains to converge properly. The final posterior distribution gathers 100,000 models from the main inversion phase by sub-sampling all non-outlier chains.

Posterior models and their distributions. The posterior distributions of 100,000 models were sorted according to the likelihood and categorized into three groups, including the best 25 %, 50 % and all models. Figure II.23 shows an example of the inversion results for station SL21, showing V_S-depth structures and corresponding data fits from randomly selected models from each group, and the posterior distributions of likelihood, joint misfit, SWD and RF noise amplitudes, number of layers and V_P/V_S ratio for all models within a group. The grouping (colors) shows the compromises the algorithm made during an inversion, e.g., increasing the number of layers to reduce the noise level and the misfit. Each of the posterior parameters is distributed unimodal. The surface wave dispersion shows a good data fit. For the receiver functions, the majority of modeled RFs agrees very well in their signature, however, not all details of the waveform are matched. The first order features are modeled in nearly every chain and the V_S-depth models show similar structures. The median model shows a sharp interface at

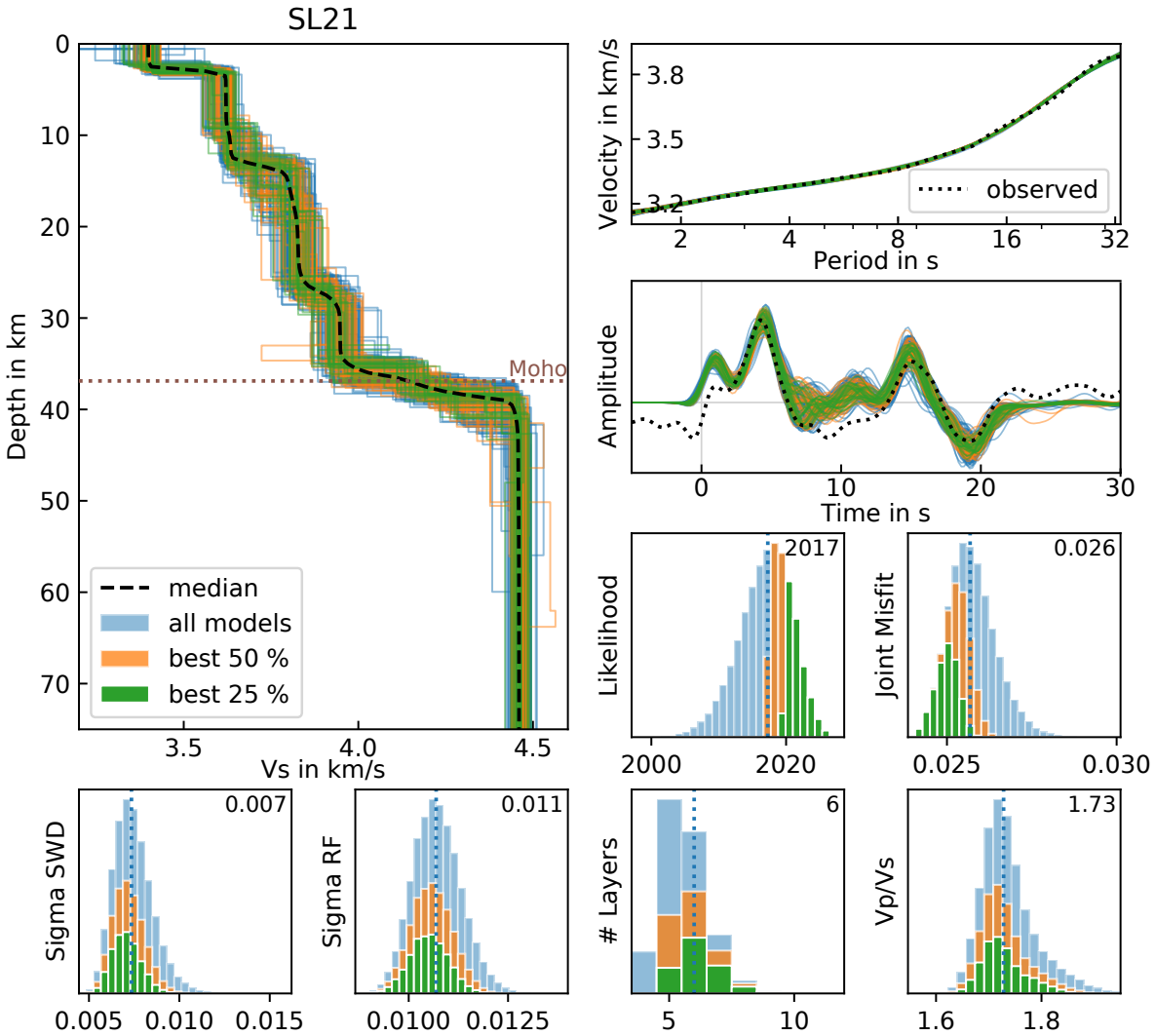

Figure II.23: Selection of V_S models and corresponding data fits for station SL21, along with posterior distributions of likelihood, joint misfit, SWD and RF noise amplitudes, number of layers and V_P/V_S ratio. The results are color coded according to the likelihood, i.e., three groups showing 25, 50 and 100 % of the best models. Dotted vertical lines illustrate the median with a value as displayed in the upper right corner of each panel.

3 km depth and more gradual transitions at 13–15, 26–29 and 35–39 km; the gradual transitions imply a higher uncertainty about the correct interface depth.

The quality of data fit for SL21 is representative for the other stations. (Data fits and average velocity-structures are shown for all stations in appendix II.B.) The posterior distributions are unimodal with the exception of the crustal V_P/V_S ratios of seven stations, which show bimodal distributions, and the V_P/V_S ratio of one station (SL31), which did not yield plausible values (i.e., they settle on a boundary, even if extending the boundary to unrealistic values). V_P/V_S is a fine-tuning parameter, meaning, that the average V_S-depth structures we derived from our data set are relatively insensitive to V_P/V_S. For the seven stations showing bimodal V_P/V_S ratio distributions, the inversion finds two optima, and therefore compromises by slight modifications of the other parameters, but still leading to Gaussian distributions for V_S. The most probable V_S-depth models corresponding to either of the V_P/V_S optima, show identical major structures. For the station not converging in V_P/V_S, we compared the results with those from an inversion assuming a fixed V_P/V_S ratio (=1.73), resulting in models that are very similar in their V_S-depth structure.

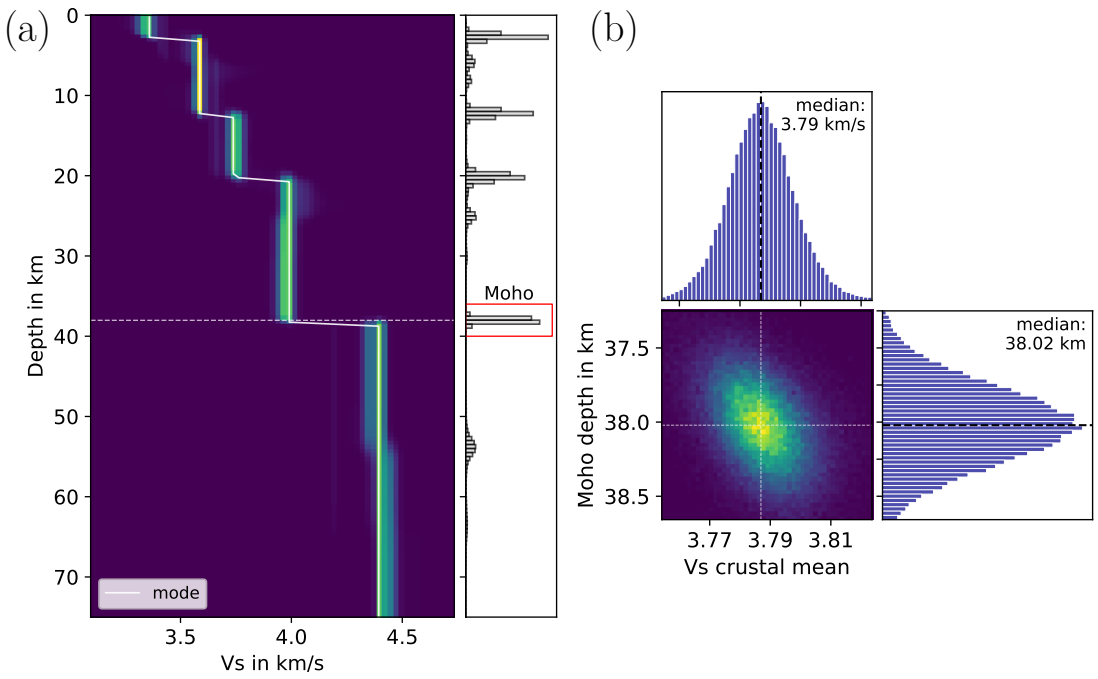

Figure II.24: (a) Posterior distributions of V_S and interface depth for station SL10. The red box marks the interface depth probability of the Moho. (b) Posterior distributions of the Moho depth and crustal average V_S. The median Moho depth is 38±0.2 km and the average crustal V_S is 3.79±0.01 km/s.

Estimation of Moho depths and corresponding V_S values. Figure II.24a shows posterior distributions for SL10 for the V_S-depth structures and interface depth probabilities. The surface velocity is ∼3.4 km/s, the interfaces are well defined at 3, 12, 20, and 38 km depth. The Moho depth is between 37–39 km, emphasized by the red box in Figure II.24a. To retrieve a robust estimate for the Moho depth, the average V_S model of each station was visually inspected to define a Moho depth search range (e.g., 37–39 km for SL10, 35–39 km for SL21). Each of the

100,000 models was then automatically analyzed to find the interfaces within that search range, with the last crustal layer having a V_S <4.2 km/s. (See Fig. II.24b for the distribution of Moho depths at SL10.) Additional parameters, e.g., V_S in the last crustal layer, average crustal V_S, V_S increase across the Moho and upper mantle V_S were extracted. Those values show a moderate trade-off with the crustal thickness, as is illustrated in Figure II.24b; although subtle, a deeper Moho estimate is accompanied by a larger average crustal Vs. This trade-off is well known for receiver functions, but reduced in its impact by the inclusion of surface wave dispersion in the inversion.

5.2 Joint inversion results

Data fits and Vs-depth structures gained from the inversion are shown in Figures II.B1–II.B3 for each station. The results are discussed in four sections, i.e., (1) seismic noise level, (2) surface V_S, (3) average crustal V_P/V_S and V_S, and (4) crustal thicknesses and features. Bayesian inversion results, i.e., crustal thicknesses, average crustal V_P/V_S and V_S, and depth of a prominent mid-crustal interface are summarized in Table II.B1.

Seismic noise level. The seismic noise levels for dispersion curves (σ_{SWD}) and receiver functions (σ_{RF}) are estimated during the inversion. Multiple sources of noise are included in σ and consider observational errors, processing errors and theory errors (Bodin et al., 2012). Below is an overview of these sources.

(1) **Observational errors** from background seismic noise (micro-seisms) and instrumental noise.
(2) **Processing errors** introduced by parameter choices and generally unstable operations (e.g., the deconvolution for receiver functions).
(3) **Theory errors** from forward modeling and inversion algorithms through physical approximations of the Earth, e.g., horizontal homogeneous isotropic layers. This noise type is coherent and reproducible, and part of the signal chosen not to explain (e.g., Gaussian filtering for receiver functions with frequency band corresponding to major scale structures).

These contributions are not simply additive and are all partly reflected in the noise amplitudes σ_{SWD} and σ_{RF}. Figure II.25 shows the spatial distribution of σ_{SWD} and σ_{RF}. σ_{SWD} ranges between 0.0043–0.0241 km/s with a median of 0.0078±0.0044 km/s. σ_{RF} ranges between 0.0048–0.0157 with a median of 0.0082±0.0021. Concrete values for all stations are annotated in Figure II.B1.

Surface velocities. We extracted surface V_S and uncertainties for each station (Tab. II.5). The values range between 3.1–3.6 with an average of 3.4±0.13 km/s. The spatial distribution of surface V_S is shown in Figure II.27a.

Figure II.26 (top) shows a comparison to the surface V_S derived from RF rotation angle analysis (section 4.2). The hollow symbols denote outliers and are discarded. Surface V_S derived

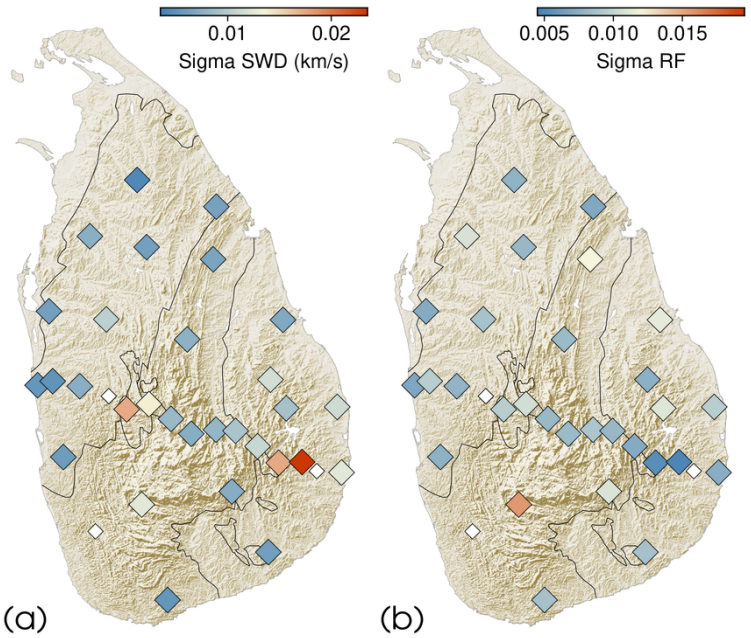

Figure II.25: Distribution of seismic noise level for (a) surface wave dispersion and (b) receiver functions, with concrete values as annotated in Figure II.B1.

Table II.5: Surface V_S and uncertainties (km/s) derived from Bayesian inversion. Average V_S for study area is 3.4±0.13 km/s.

station	V_S	station	V_S	station	V_S	station	V_S
SL01	3.36±0.03	SL11	3.25±0.04	SL20	3.05±0.33	SL29	3.43±0.04
SL02	3.33±0.05	SL12	3.32±0.06	SL21	3.40±0.06	SL30	–
SL03	3.24±0.89	SL13	3.28±0.07	SL22	3.52±0.04	SL31	3.27±0.07
SL04	–	SL14	–	SL23	3.08±0.31	HALK	3.36±0.26
SL05	3.44±0.30	SL15	3.21±0.15	SL24	3.45±0.02	MALK	3.52±0.02
SL06	3.57±0.06	SL16	3.41±0.04	SL25	3.49±0.02	PALK	3.48±0.03
SL08	3.38±0.04	SL17	3.45±0.09	SL26	3.34±0.47		
SL09	3.39±0.08	SL18	3.57±0.08	SL27	3.59±0.17		
SL10	3.35±0.03	SL19	3.40±0.03	SL28	3.36±0.02		

from the two methods mostly agree in their relative trend and show a similar mean (3.4±0.1 and 3.5±0.2 km/s). Median absolute differences are ∼0.2 km/s. Four stations (i.e., SL03, SL15, SL26, and SL27) show discrepancies larger than 0.4 km/s; two of these stations (SL15, SL27) are adjoined by large uncertainties (Bayesian results), but do not overlap with the uncertainty intervals from RF rotation. High uncertainties (Bayesian results) are also observed at the stations where the RF rotation analysis yielded outlier measurements. Most of the mentioned stations are located close to the coast. No clear correlation to σ_{SWD} or σ_{RF} is observable.

Although each method includes the same RF data set, they are constrained very differently and the Bayesian inversion includes surface wave dispersion data to constrain absolute Vs. Hence, surface V_S derived from joint inversion are more reliable and trustworthy.

Average crustal V_P/V_S ratios and V_S. Figure II.27(b,c) shows average crustal V_P/V_S ratios and V_S. The V_P/V_S ratios from joint inversion are between 1.5–1.93 (majority: 1.68–1.8).

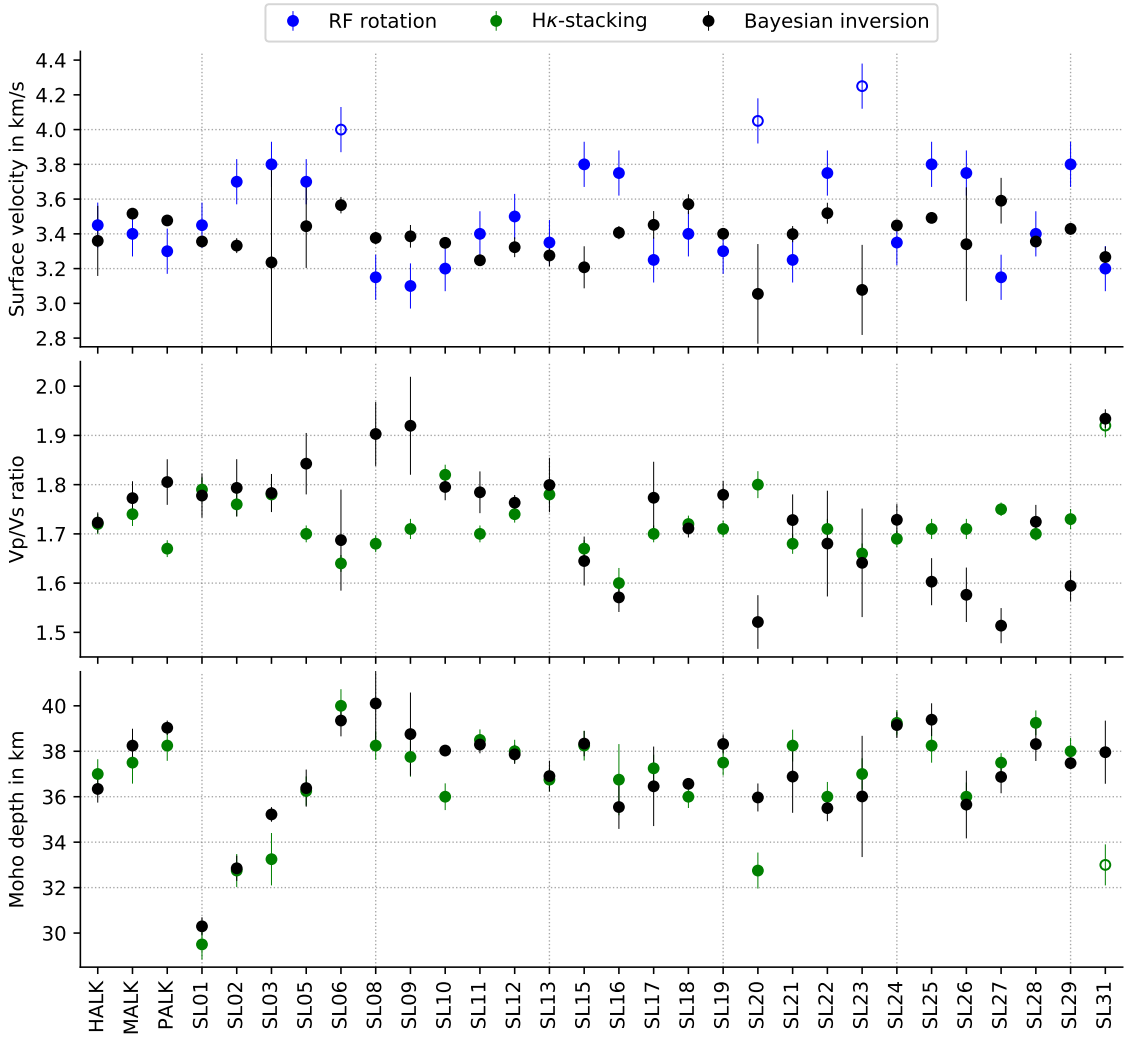

Figure II.26: Seismic properties derived from Bayesian inversion (black), RF rotation (blue) and $H\kappa$-stacking (green). The compared properties are surface V_S, V_P/V_S ratios and Moho depths. Hollow symbols mark outliers. Note that the uncertainties of surface V_S from RF rotation are equal for each station (section 4.2).

For $H\kappa$-stacking, V_P/V_S ratios are between 1.6–1.82 (majority: 1.66–1.73). The velocity ratios from both techniques agree in their general trend and show typical differences of ∼0.03, but several stations also show large discrepancies (Fig. II.26, middle). The V_P/V_S ratios from Hκ-stacking are more reliable, as they include a range of RFs and consider the arrival times of Ps conversion and multiples directly associated with the slowness. For joint inversion, we considered the RF stack with its median slowness. Hκ-stack V_P/V_S ratios (Fig. II.22b) are <1.7 in the central HC and northern Sri Lanka, correlative to larger crustal thicknesses (>38 km). Low V_P/V_S ratio anomalies are observable for SL23 and SL15 on the east coast. The west coastal stations SL01–SL03 show high V_P/V_S ratios (1.76–1.79) with thinner crustal thicknesses (<35 km).

The average crustal V_S (Fig. II.28c) is 3.7–3.9 km/s, with increased velocities in the central HC (>3.83 km/s), decreasing with distance towards the coastal regions. The western and southernmost coastal stations (SL01, SL02, HALK) show the lowest crustal V_S.

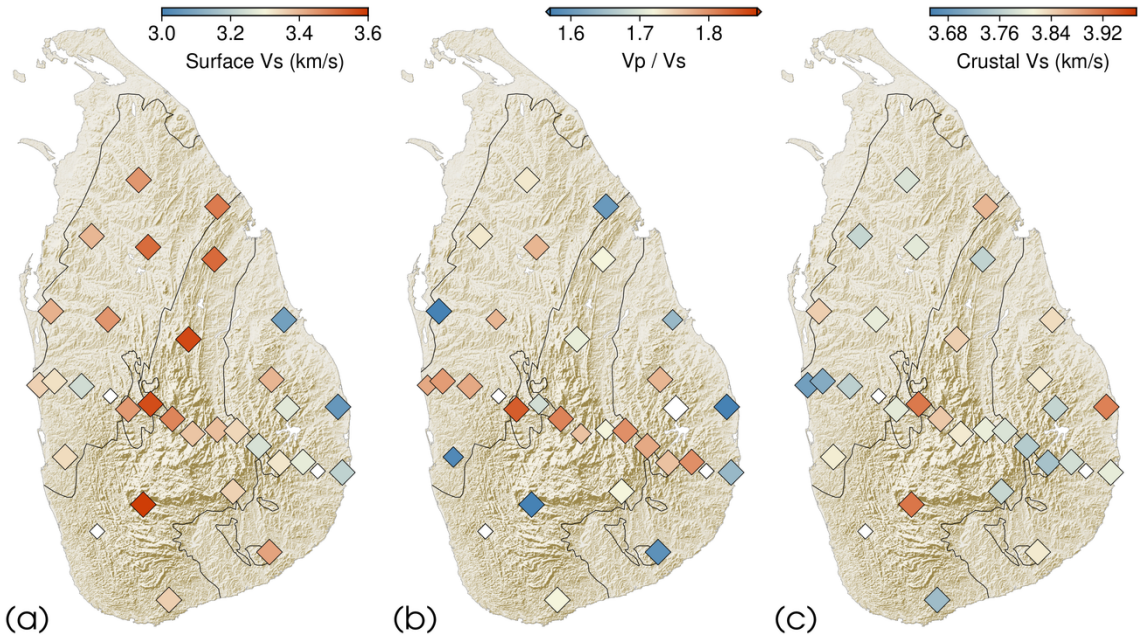

Figure II.27: Distribution of (a) surface V_S, (b) V_P/V_S ratios and (c) crustal average V_S from McMC Bayesian inversion. Small and normal sized white symbols show stations with no inversion performed or not converged V_P/V_S, respectively. The smaller colored symbol sizes in (b) illustrate that the V_P/V_S ratio posterior distributions are bimodal.

Crustal thickness and features. Figure II.28(a,b) shows Moho depths and the number of crustal layers derived by joint inversion. The crust beneath each station is approximated by 3–8 layers. SL18 is the only station with a three-layer representation. A more complex structure with 7 and 8 layers is observable for MALK, SL15, SL20, SL23 and SL13, SL25, SL26. Most of these stations are located along the eastern coast of Sri Lanka. These stations show also the largest surface V_S discrepancies as described before.

Moho depths derived from joint inversion show a depth range between 30–40 km (Fig. II.28a) and agree well with results from Hκ-stacking (Tab. II.B1, Fig. II.26, bottom). Absolute differences between both methods are between 0.1–3.2 km with a median difference of 0.7 km. The largest Moho depths (38–40 km) are found below the topographic high in the HC. The three northernmost stations in Sri Lanka (SL24, SL25, MALK) also have a deep Moho interface at >38 km depth. The west coastal stations SL01–SL03 show the thinnest crust (30–35 km). SL20 at the east coast also shows a shallow Moho depth in the Hκ-stack ($\sim$33$\pm$2 km), but not in the joint inversion ($\sim$36 km). We note that there is a strong interface at $\sim$31 km depth that might have been interpreted as the Moho interface in the Hκ-stack (Fig. II.30b, right); this station has the largest Moho deviation of 3.2 km.

Figure II.29 illustrates a V_S cross section along the main profile. The Moho interface generally mirrors the topography, i.e., higher crustal elevations correspond to larger Moho depths. The crustal thickness is continuously increasing from SL01 to SL05 (30–36 km), with a sudden increase of 3 km to 39 km at SL06, which corresponds to the topographic trend with an elevation change by a factor of 4 from SL05 to SL06. SL08 shows the deepest Moho interface.

The V_S cross section in Figure II.30a (and Fig. II.29) shows a prominent westward dipping

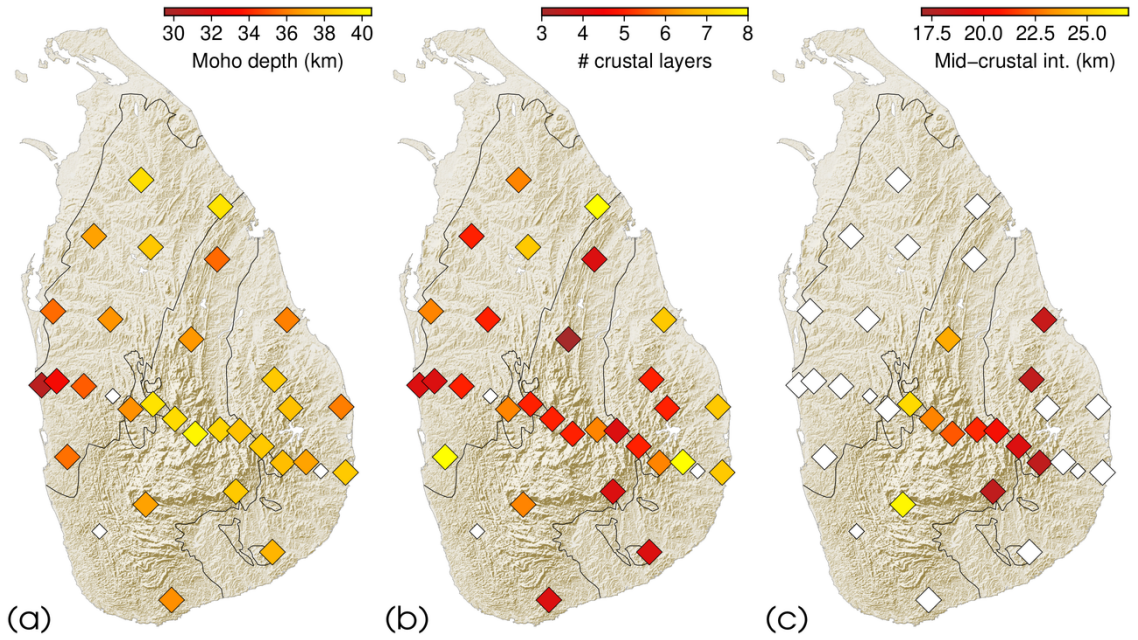

Figure II.28: Distribution of (a) Moho depths, (b) number of crustal layers, and (c) extend of mid-crustal interface from McMC Bayesian inversion. Small and normal sized white symbols show stations with no inversion performed or no mid-crustal interface, respectively.

mid-crustal interface with an apparent angle of ∼4.3° between SL06–SL12, and an average velocity increase from 3.75 to 4 km/s. These lower crustal high velocities are absent at the stations adjacent to the west (SL01–SL05), while the stations to the east (SL11–SL13) show a thinner or inter-layered section of the higher velocities. The probability of interfaces (Fig. II.29) furthermore suggest the dipping interface to be traceable across the entire profile (SL03–SL15). Figure II.30a shows our interpretation of the intra-crustal interface; it is also evident on five other stations across Sri Lanka (Fig. II.30b, left). The mid-crustal interface is observable on the central stations in the HC, and on three additional stations in the VC (Fig. II.28c). For the

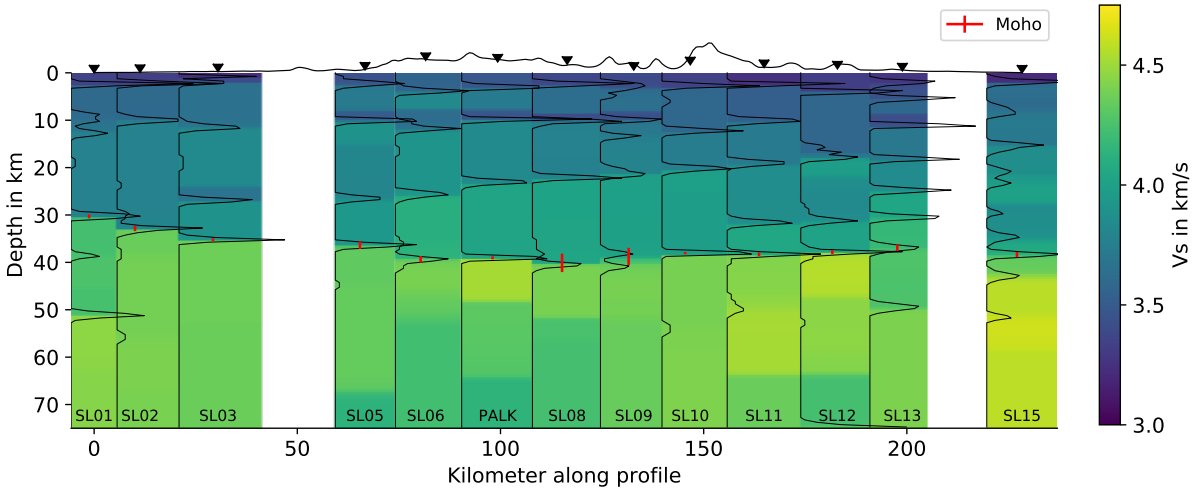

Figure II.29: V_S cross section along the main profile. Black curves indicate the interface probability (V_S increase). Red lines indicate Moho intervals. Topography is exaggerated (x5).

stations in the HC the interface depth lies between ∼18–27 km; the interface in the VC is at ∼18 km depth. The strike has an orientation similar to the general geologic strike with a dip towards WNW.

A well constrained low velocity zone is observed along SL05–SL09, and SL13 at depths of 10 km, with V_S between 3.4–3.6 km/s. Stations SL15, SL20, SL23, SL25 and SL26 show low velocity zones at mid- to lower crustal depths (20/30 km); they are located at the western and eastern coastlines.

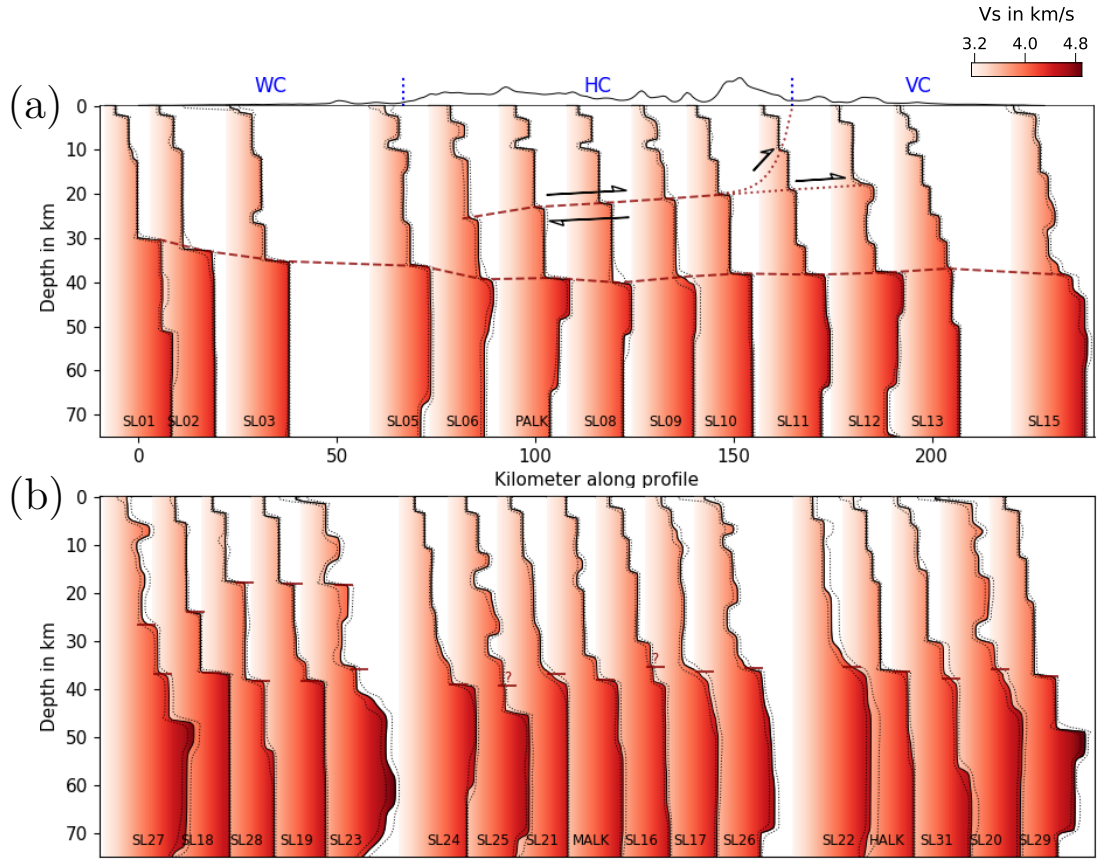

Figure II.30: V_S models at stations along the main profile (a) and at other stations away from the profile (b). The shallow and deeper red markers indicate the mid-crustal and Moho interface, respectively. The dotted lines mark an interpretation of the outcropping mid-crustal interface, and a possible continuation within the crust. Shear sense indicators denote the ancient thrust direction. The V_S models in (b) are divided into 3 groups, from left to right, with stations that include the mid-crustal interface, stations in the WC, and stations located in the HC and VC, respectively. Moho depths labeled with a question mark indicate an interpretation leaned on surrounding stations (see also SL13).

6 Interpretation and discussion

Comparison with other geophysical studies. The Hκ-stack analysis from Pathak et al. (2006) reveals a Moho depth of 34±1 km beneath PALK, much shallower compared to our results from two independent analyses, which are 38.25±0.65 km and 39±0.3 km from Hκ-stacking and Bayesian inversion, respectively. This discrepancy can (partially) be explained by the average V_P they assumed for the crust (6.0 or 6.1 km/s?), which is lower than our V_P assumption of 6.5 km/s. Rai et al. (2009) obtained a crustal thickness of 37.5±1 km and V_P/V_S ratio of 1.72±0.02 for PALK. Their estimates of Moho depth and V_P/V_S ratio agree borderline with ours. By forward and inverse modeling of RF and surface wave data they inferred a velocity-depth structure with a low velocity layer in the upper crust and a mid-crustal discontinuity at a depth of 22.5 km. We also observe a shallow low velocity zone (∼10 km) and an intra-crustal discontinuity at 23±0.4 km.

Mishra et al. (2006) used gravity data and modeled the anomalies along an E-W profile through PALK. They modeled crustal thicknesses of up to 40–41 km under the eastern part of the HC, close to our observations, and explain the central gravity high with a higher density crustal section protruding in the upper crust (10–15 km). We also observe a central anomalous higher velocity section (which can correlate to higher densities), however, situated in the lowermost crust. A fresh gravity modeling based on our results might be of interest, but would exceed the scope of this study.

Average crustal V_P/V_S ratios. The velocity ratios can be helpful to distinguish between felsic and mafic rocks as a matter of the relative proportions of quartz (V_P/V_S ∼1.49) and plagioclase (V_P/V_S ∼1.87) (Christensen, 1996). Musacchio et al. (1997) grouped crustal rocks based on V_P/V_S and V_P into three categories: felsic, anorthositic and mafic rocks.

Classifying the results from Hκ-stacking, none of the V_P/V_S ratios lies beyond 1.82, which would exclude an anorthositic rock composition. As our V_P/V_S ratios for both analyses are generally more on the lower side (1.66–1.73 and 1.68–1.8), most of Sri Lanka is represented by felsic rocks with intermediate to high silica content. However, our V_P/V_S ratio estimates are crustal averages; it is possible that sections of the crust are dominated by different compositions. The joint inversion shows average crustal Vs between 3.7–3.9 km/s (V_P: 5.9–7.3 km/s), which would predominantly still favor a felsic composition over a mafic one.

Moho depths and intra-crustal features. The Moho depths are not obviously correlated with the geologic units, which suggests that the crustal fragments have been unified through reworking and deformation through the Pan-African collision and possibly later erosive processes. The Moho interface generally mirrors the topography, except for the thicker crust in the northernmost part of the island, which might be caused by density differences through crustal composition. The thinner crust along the west coast (<36 km), including the thinnest crust at SL01–SL03 (30–35 km), can be explained by the formation of the adjacent Mannar

basin, including rifting and crustal thinning.

Our study reveals a major WNW-dipping mid-crustal interface in the central HC with an apparent dip of ∼4.3° along the profile. Stations in the VC and close to the HC/VC border (i.e., SL12, SL19, SL23, SL28) also show a discontinuity at a depth of ∼18 km. It is unclear whether the four stations see the same structure as the stations in the HC or image a separate feature within the eastern VC. The mid-crustal interface might be a feature from before the Pan-African collision; however, as the extent of the discontinuity from the HC into the eastern VC continues at the same depth and shows coherent Vs contrast, it is likely that the interface is the result of a shared event. Therefore, we are inclined to interpret this mid-crustal feature as being related to the HC/VC thrust contact.

Kleinschrodt (1994, 1996) suggested that the HC was thrust onto the eastern VC along a deep crustal, sub-horizontal to gently west-dipping thrust surface, which underlies large parts of the HC, with a ramp-flat thrust geometry or a low-angle thrust that steepens to higher crustal levels. Our results are in agreement with this hypothesis, which is supported by several other studies (see introduction). The interface might be interpreted as the HC/VC thrust contact that steepens to shallower crustal levels and the surface (Fig. II.30a). Stations SL11-SL13 show a slightly different V_S structure below the discontinuity (Fig. II.29), i.e., high V_S inter-layered with lower Vs, which could reflect the complicated contact zone between the HC and VC and might even image a buried continuation of the thrust contact within the VC, i.e., a blind thrust.

A low velocity layer as we observe at the central stations within the HC, was also observed by Rai et al. (2009) in the upper crust of other Pan-African terranes. Such intra-crustal structure is assumed to be a relic of deformation and magmatism caused by upwelling of lower crust or subcrustal melts. Low velocity zones are thought to be the consequence of an influx of CO_2-rich fluids, that are trapped at these depths or originated from retrograde metamorphism to amphibolite and greenschist facies, and were brought there through deep-seated thrusting and lateral shearing during a transpressive regime (Rai et al., 2009, and references therein).

The amalgamation of Sri Lanka. The hypothesis of the stepwise collision predicts westwards dipping thrust contacts between the WC/KC, the HC and the VC island arcs (e.g., Kehelpannala, 2004). We observe a gently westward dipping mid-crustal interface beneath the HC which shows a strong Vs increase and thus indicates a change of rock material. Our observation matches the proposed position and orientation of the HC/VC thrust contact. The velocity change is also seen within the eastern VC, which suggests that the structure might has been part of the VC crust before thrusting, or evolved alongside. We assume a steepening of the thrust contact to the surface; as the signature of the mid-crustal interface in the central HC does not disappear, but fades towards the east, we propose a buried continuation within the VC. The low velocity layer in the HC along the main profile (∼10 km depth) might be caused by influx of CO_2-rich fluids of retrograde metamorphism to amphibolite facies. The dipping mid-crustal interface and the low velocity zone, both relate to deeper thrusting and a transpressive regime, which clearly favors the stepwise collision theory as described with its details (chapter 1).

Does this exclude the possibility of an amalgamation through divergent double subduction? Santosh et al. (2014) sketch the amalgamation with processes such as slab melting and arc

magmatism, basaltic underplating, astenospheric upwelling and slab break-off; features, that are also included in the stepwise collision and we cannot asses with our data. In their study, Santosh et al. (2014) did not focus on crustal structures, which makes it impossible for us to discuss the matter based on their information.

Divergent double subduction occurs rather rarely (e.g., the Lachlan fold belt in southern Australia, the Molucca Sea collision zone in Indonesia). Also, a large scale dipping structure in the accretionary zone is not a feature seen for this type of subduction (e.g., Soesoo et al., 1997; Zhang et al., 2017); however, the crustal structure is mostly not the focus of these studies. As argued above, we prefer the stepwise collision hypothesis, although we cannot completely exclude the theory of the double-sided subduction.

Project III

BayHunter – A Python tool for transdimensional Bayesian inversion of surface wave dispersion and receiver functions

Published as Dreiling and Tilmann (2019): Dreiling, J. and Tilmann, F. BayHunter – McMC transdimensional Bayesian inversion of receiver functions and surface wave dispersion. GFZ Data Services, 2019. https://doi.org/10.5880/GFZ.2.4.2019.001. Available on GitHub: https://github.com/jenndrei/BayHunter

1 Introduction

Bayesian inversion is becoming more and more popular for several years and it has many advantages compared to conventional optimization approaches. While other methods often are more constrained and favor one best model based on the least misfit, an inversion after Bayes theorem is based on the model's likelihood and results in probability distributions for each parameter of the model. The inversion result is represented by a collection of models (posterior distribution) that are consistent with the data and with the selected model priors. They image the solution space and disclose uncertainties and trade-offs of the model parameters.

No open-source tools were available that suited our purpose of a joint inversion of SWD and RF after Bayes using a Markov chain Monte Carlo (McMC) sampling algorithm, and solve for the velocity-depth structure, the number of layers, the noise parameters, and the average crustal V_P/V_S ratio. So it was natural to take care of this. We developed BayHunter to serve that purpose, and BayWatch, a module that allows to live-stream the inversion while it is running.

Contents. Chapter 1 describes Bayes theorem and the McMC inversion approaches. They set the foundation for BayHunter, an inversion framework for transdimensional Bayesian inversion, described in chapter 2. We test the inversion code using synthetic data and provide a tutorial in chapter 3. Appendix III.A provides a minimalistic working example of the code.

Bayes theorem

Bayes theorem (Bayes, 1763) is based on the relationship between inverse conditional probabilities. Assuming observed data d_{obs} and a model m; the probability that we observe d_{obs} given m is $p(d_{obs}|m)$, and the probability for m given d_{obs} is $p(m|d_{obs})$. Both occurrences are also dependent on the probability that m or d_{obs} is given, i.e., $p(m)$ and $p(d_{obs})$.

The inverse conditional probability that both events occur, is given by:

$$p(m|d_{obs})p(d_{obs}) = p(d_{obs}|m)p(m) \tag{III.1}$$

As d_{obs} is known as the evidence, i.e., the measurements, Bayes theorem can be rewritten to:

$$p(m|d_{obs}) \propto p(d_{obs}|m)p(m) \tag{III.2}$$

$p(m|d_{obs})$ is the posterior distribution, $p(d_{obs}|m)$ is called the likelihood, and $p(m)$ is the prior probability distribution.

Markov chain Monte Carlo

Markov chain Monte Carlo describes a sampling algorithm for sampling from a probability distribution. This algorithm is a combination of Monte Carlo, a random sampling method, and

Markov chains, assuming a dependency between the current and the previous sample. The exact implementation of the algorithm is described in chapter 2.

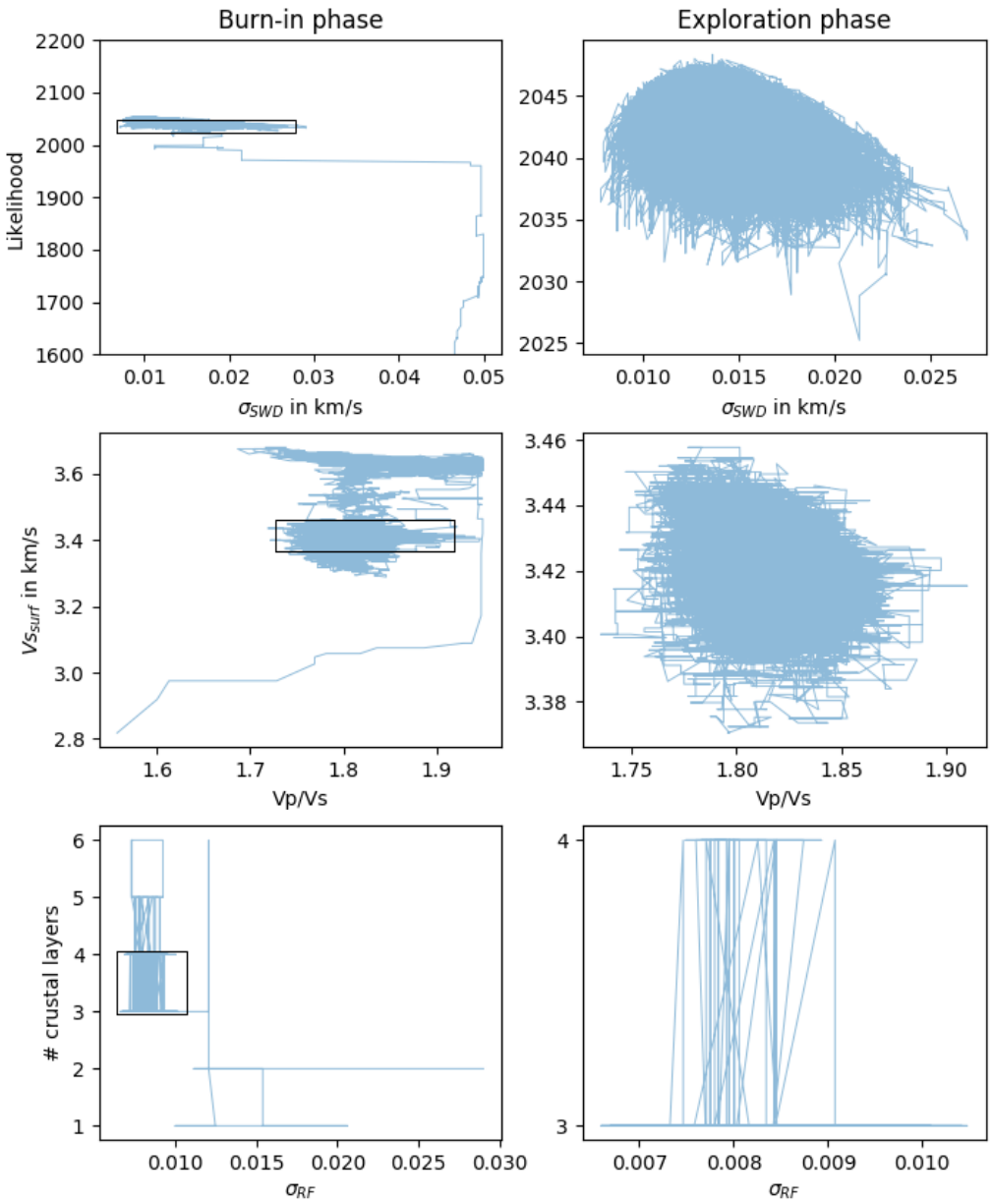

Figure III.1: McMC sampling scheme for one chain progressing through the parameter space. Left and right columns show iterations of the burn-in (first phase) and exploration phase (second phase), respectively, with the black box framing the exploration region as shown in the right column. Illustrated parameters are the likelihood and noise amplitude σ_{SWD}, surface V_S and V_P/V_S, and number of crustal layers and noise amplitude σ_{RF}. The top panels reflect the optimization process based on the likelihood, while the lower panels show the parameter trade-off. Example taken from station SL10 in Sri Lanka.

Figure III.1 shows a real data example from a station in Sri Lanka (SL10), following the evolution of one chain through the model parameter space. Parameters are shown in couples, but note that the parameter space is multidimensional. In the burn-in phase (left column) the chain starts at a random parameter combination in the solution space and progresses with ongoing

iterations towards an optimum, based on the likelihood. In the second phase (right column) the chain has already reached its exploration region and samples the posterior distribution.

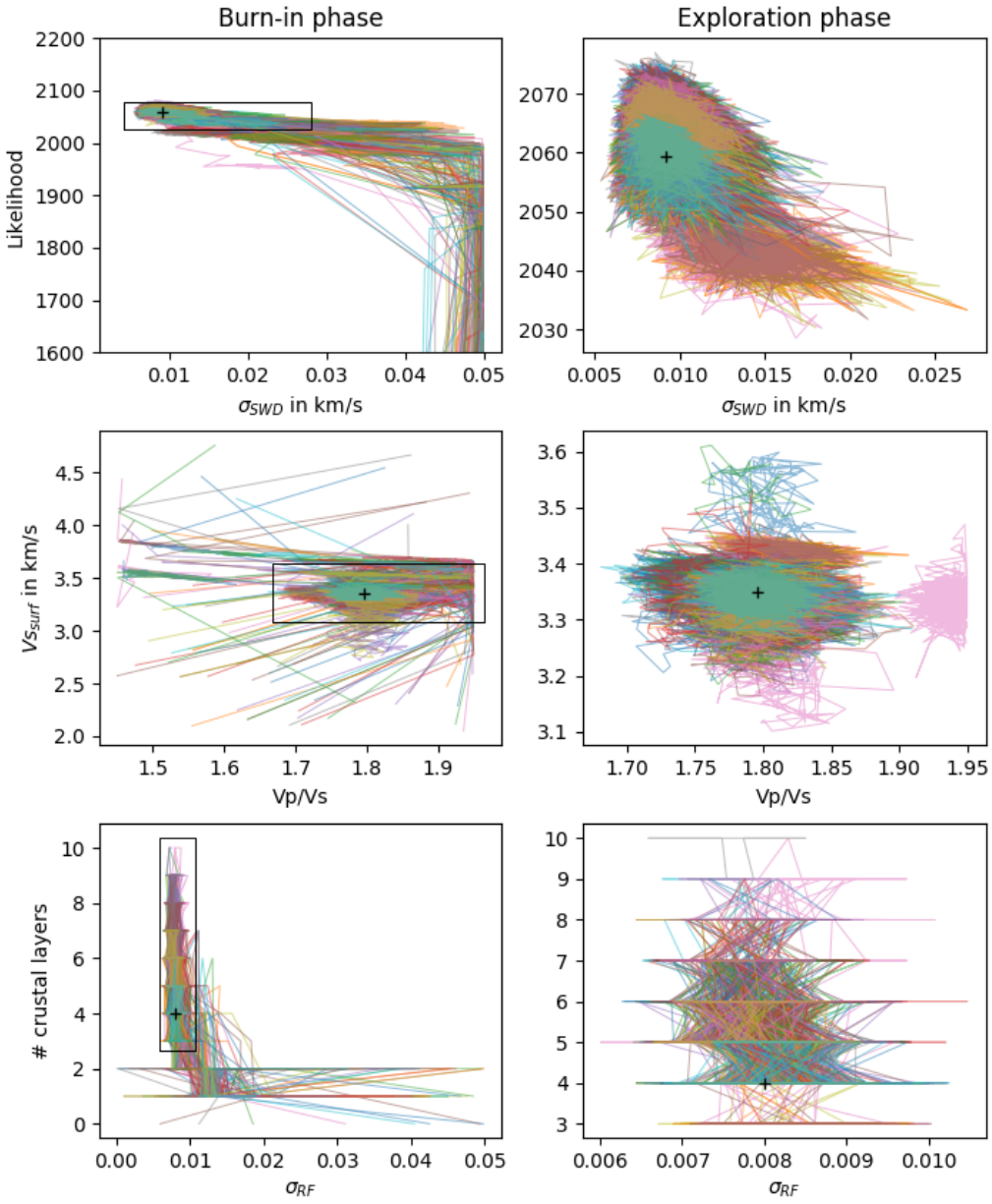

Figure III.2: McMC sampling scheme for one hundred chains progressing independently through the parameter space. Same parameters and parameter space as illustrated in Figure III.1. Black cross shows the median from the complete posterior distribution (exploration phase). Example taken from station SL10 in Sri Lanka.

Figure III.2 shows one hundred independent chains exploring the same parameter space. Each chain starts with a different random model, yet most chains converge to the same exploration region for sampling the posterior distribution. There are still chains (e.g., the two rose colored ones in the middle panel) that have not converged into the optimum zone when entering the exploration phase. If those chains do not converge to that optimum zone within the second phase, they probably represent outlier chains (or secondary minima) and should not be considered for the posterior distribution.

2 Development of BayHunter

BayHunter is a tool to perform McMC transdimensional Bayesian inversion of SWD and RF, solving for the velocity-depth structure, the number of layers, noise scaling parameters (correlation, sigma), and average crustal V_P/V_S. The inversion algorithm uses multiple independent Markov chains and a random Monte Carlo sampling to find models with the highest likelihood.

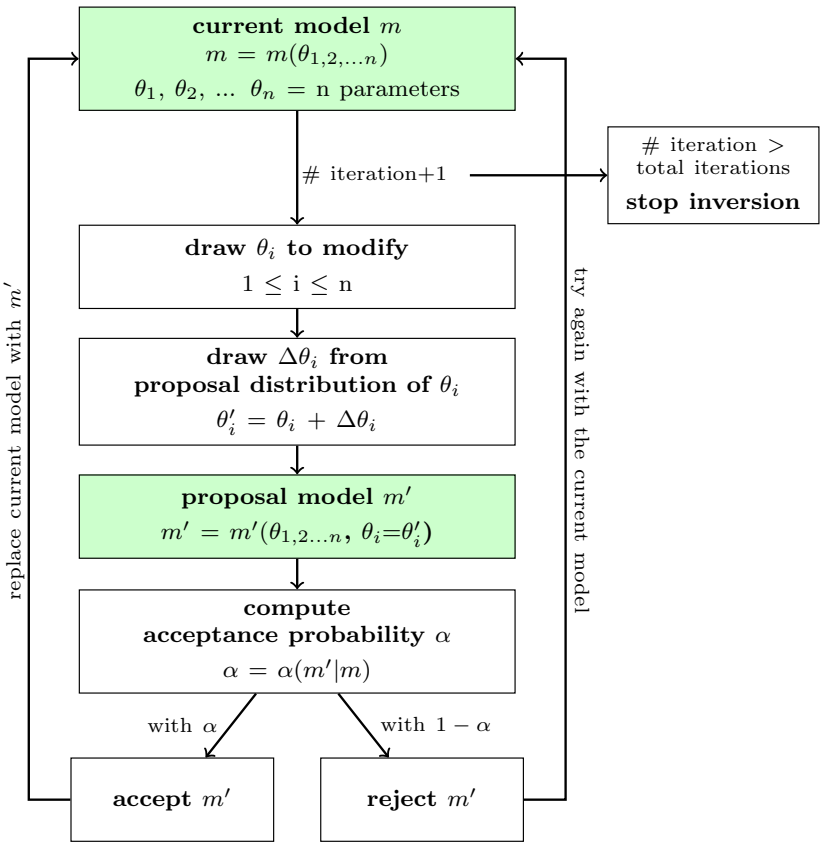

Figure III.3: Schematic workflow of an McMC chain sampling the parameter space. The posterior distribution includes all accepted models of a chain after a chosen number of iterations.

How each chain is progressing through the parameter space is schematically illustrated in Figure III.3. Each chain contains a current model. In each iteration a new model will be proposed, considering a proposal distribution, by modification of the current model. The acceptance probability is computed based on the prior, proposal and posterior ratios from proposal to current model. A proposed model gets accepted with a probability equal to the acceptance probability, i.e., if the likelihood of the proposed model is larger than the one of the current model, it gets accepted; but also models that are less likely than the current model get accepted with a small probability, which prevents the chain to get stuck in a local maximum. If a proposal model gets accepted, it will replace the current model; if not, the proposal model gets rejected and the current model stays unmodified. This process will be repeated for a defined number of iterations. Each accepted model of the exploration phase contributes to the posterior distribution of the parameters.

Equations given in section 2.1 are reduced to the number of those required in BayHunter, and will not be fully deduced. For mathematical derivations and details be referred to Bodin (2010) and Bodin et al. (2012), which inspired the idea of BayHunter and on which our algorithm is based on.

2.1 The Optimizer and Chain modules

The *BayHunter.mcmcOptimizer* manages the chains in an overarching module. It starts each single chain's inversion and schedules the parallel computing. Each chain and its complete model data can be accessed (in the Python environment) after the inversion has finished. Before the optimizer initializes the chains, a configuration file will automatically be saved, which simplifies the process of illustrating results after an inversion.

Each *BayHunter.SingleChain* explores the parameter space independently and collects samples by following Bayes theorem (Eq. III.2). A chain has multiple tasks, which are described below in detail and begin with the random initialization of a starting model.

Initialize the targets. The first step towards an inversion is to define the target(s). Therefore, the user needs to pass the observed data to the designated BayHunter target type. For surface wave dispersion, period-velocity observables must be assigned to the class that handles the corresponding data (*RayleighDispersionPhase*, *RayleighDispersionGroup*, *LoveDispersionPhase*, *LoveDispersionGroup*). They default into the fundamental wave mode. For receiver functions, observed time-amplitude data must be assigned to the *PReceiverFunction* (or *SReceiverFunction*) class from *BayHunter.Targets*. Parameters (Gauss filter width, slowness, water level, near surface velocity) for forward modeling should be updated, if the default values differ from the values used for RF computation.

Each of the target classes comes with a forward modeling plugin, which is easily exchangeable. For surface waves, a quick Fortran routine based on `CPS/surf96` (Herrmann and Ammon, 2002) is pre-installed. For receiver functions, the plugin is based on `rfmini` (Joachim Saul, GFZ). Also other targets can be defined.

Parametrization of the model. The model includes the velocity-depth structure and the noise parameters of the observed data.

- **Velocity-depth structure.** The velocity-depth model is parametrized through a variable number of Voronoi nuclei, the position of each is given by a depth and a seismic shear wave velocity (V_S). A model containing only one nucleus represents a half-space model, two nuclei define a model with one layer over a half-space and so on. The layer boundary (depth of an interface) lies equidistant between two nuclei. The advantage to use Voronoi nuclei over a simple thickness-velocity representation is, that one model can be parametrized in many different ways. However, a set of Voronoi nuclei defines only one model. The number of layers in a model is undefined and will be inverted for (transdimensional). V_P is computed from V_S through V_P/V_S, which is chosen by the user to be constant, or an additional parameter to solve for.

• **Covariance matrix of data noise.** The noise level is defined by two parameters, the correlation r (i.e., the correlation of adjacent data points) and the noise amplitude σ. Both r and σ are treated as unknown and can be estimated during the inversion. They are the part of the observed data that can not be fitted. Hence, the observed data vector can be described as

$$d_{obs}(i) = d_{True}(i) + \epsilon(i) \qquad i = [1, n] \tag{III.3}$$

where n is the size of the vector and $\epsilon(i)$ represents errors that are distributed according to a multivariate normal distribution with zero mean and covariance C_e.

$$C_e = \sigma^2 R \tag{III.4}$$

The covariance matrix C_e is dependent on σ and R, which is the symmetric diagonal-constant or Toeplitz matrix.

$$R = \begin{bmatrix} 1 & c_1 & c_2 & \dots & c_{n-1} \\ c_1 & 1 & c_1 & \dots & c_{n-2} \\ c_2 & c_1 & 1 & \dots & c_{n-3} \\ & & & \vdots & \\ c_{n-1} & c_{n-2} & c_{n-3} & \dots & 1 \end{bmatrix} \tag{III.5}$$

We consider two correlation laws for the correlation matrix R. The exponential law is given by

$$c_i = r^i \tag{III.6}$$

and the Gaussian law by

$$c_i = r^{(i^2)} \tag{III.7}$$

where $r = c_1$ is a constant number between 0 and 1. In BayHunter we consider the exponential correlation law for surface wave dispersion, and both the exponential and the Gaussian law for receiver functions.

Initialize a model. For each chain, the initial model parameters (starting model) are drawn from the uniform prior distributions. These are, for the velocity-depth structure, the distributions of V_S, depth, the number of layers and the average crustal V_P/V_S. The initial model has a number of layers equal to the minimum value of the corresponding prior distribution. If set to 0, a half-space model will be drawn, if set to 1 a one layer over a half-space model represents the initial model and so on. The initial number of layers determines how many Voronoi nuclei will be drawn, i.e., how many pairs of V_S and depth. If a velocity-depth model was drawn, V_P will be computed from V_P/V_S, which was either drawn hitherto or given as constant by the user. If appropriate, the user may wish to select a mantle specific V_P/V_S, by also assuming a V_S to distinguish the mantle from the crust. The density is computed by $\rho = 0.77 + 0.32V_P$ (Berteussen, 1977).

It is possible to give a single interface depth estimate (it can be any interface, e.g., the Moho). The estimate includes a mean and a standard deviation of the interface depth. When initializing a model - and only if an estimate was given - an interface depth is drawn from the given normal distribution and two nuclei will be placed equidistant to the interface. If the initial model only consists of a half-space, the interface estimate will be ignored. Giving an estimate can help the chains to converge more quickly, e.g., if computation capacity is limited, but might generate biased posterior distributions.

Each target has two noise scaling parameters (r, σ). The user needs to define the prior distributions for the overarching target type, i.e., SWD and RF, nevertheless, each target will sample an own posterior distribution. Single noise parameters can also be set constant during an inversion by giving a single digit, instead of a range. Initial values are then the given digits, and/or will be drawn from the prior range.

The drawn starting model automatically is assigned as the current model of the chain. The corresponding likelihood is computed. This model is also the first model in the model chain that gets collected for the burn-in phase.

Computation of model likelihood. The likelihood is an estimate of the probability of observing the measured data given a particular model m. It is an important measure for accepting and declining proposal models. The likelihood function is

$$p(d_{obs}|m) = \frac{1}{\sqrt{(2\pi)^n |C_e|}} \times exp\left\{\frac{-\Phi(m)}{2}\right\} \tag{III.8}$$

where $\Phi(m)$ is the Mahalanobis distance (Mahalanobis, 1936), i.e., the multidimensional distance between observed d_{obs} and estimated $g(m)$ data vectors.

$$\Phi(m) = (g(m) - d_{obs})^T C_e^{-1} (g(m) - d_{obs}) \tag{III.9}$$

As the likelihood often results in very small numbers, the log-likelihood is preferred.

$$\log p(d_{obs}|m) = -\frac{n}{2}\log(2\pi) - \frac{1}{2}\log(|C_e|) - \frac{\Phi(m)}{2} \tag{III.10}$$

The computation of the likelihood needs the inverse C_e^{-1} and determinant $|C_e|$ of the covariance matrix. For the exponential correlation law (Eq. III.6), the covariance matrix is described by

$$C_e = \sigma^2 \begin{bmatrix} 1 & r & r^2 & \dots & r^{n-1} \\ r & 1 & r & \dots & r^{n-2} \\ r^2 & r & 1 & \dots & r^{n-3} \\ & & & \vdots & \\ r^{n-1} & r^{n-2} & r^{n-3} & \dots & 1 \end{bmatrix} \tag{III.11}$$

C_e^{-1} and $|C_e|$ can be solved through linear algebra, and are given by the analytical forms

$$C_e^{-1} = \frac{1}{\sigma^2(1-r^2)} \begin{bmatrix} 1 & -r & 0 & \dots & 0 & 0 \\ -r & 1+r^2 & -r & \dots & 0 & 0 \\ 0 & -r & 1+r^2 & \dots & 0 & 0 \\ & & & \vdots & & \\ 0 & 0 & 0 & \dots & 1+r^2 & -r \\ 0 & 0 & 0 & \dots & -r & 1 \end{bmatrix} \tag{III.12}$$

and

$$|C_e| = \sigma^{2n}(1-r^2)^{n-1} \tag{III.13}$$

These can be easily constructed and quickly computed in the Python language. Obviously, if the correlation of noise $r = 0$, the matrices R (Eq. III.5) and R^{-1} are simply formed by the diagonal matrix, and the determinant is given by σ^{2n}. This is the default case for surface wave dispersion.

For receiver functions, unless they are computed utilizing an exponential filter, the Gaussian correlation law (Eq. III.7) should be considered. In this case C_e^{-1} and $|C_e|$ cannot be solved analytically and the numerical computation of these is necessary. Considering a numerical computation each time a noise parameter is perturbed will increase the computation time tremendously. A trick to speed up the computation is accompanied by estimating r priorly and keeping it constant during the inversion. The equations

$$C_e^{-1} = (\sigma^2 R)^{-1} = \frac{1}{\sigma^2} R^{-1} \tag{III.14}$$

and

$$|C_e| = |\sigma^2 R| = \sigma^{2n}|R| \tag{III.15}$$

show, that R^{-1} and $|R|$ can be isolated from σ. Therefore, the numerical computations of R, R^{-1} and $|R|$ will be executed only once at the beginning of the inversion. R^{-1} and $|R|$ will be multiplied by the σ-terms and used in equations III.9 and III.10 to compute the likelihood. The correlation parameter r in R needs to be chosen by the user, but can be estimated by $r = f_s/a$ with RF sampling rate f_s and the applied Gaussian filter width a (Bodin et al., 2012). If r is set too large, R^{-1} becomes instable and small eigenvalues need to be suppressed.

The likelihood for inversions of multiple data sets is computed by the sum of the log-likelihoods from different targets.

Propose a model. At each iteration a new model is proposed using one of six modification methods. The method is drawn randomly and the current model will be modified according to the method's proposal distribution. Either a parameter is modified (V_S or depth of Voronoi nucleus, V_P/V_S, r, σ) or the dimension of parameters, i.e., the number of layers in the velocity-depth structure (layer birth, death). The methods are summarized below.

(1) Modification of V_S (Voronoi nucleus)
(2) Modification of depth (Voronoi nucleus)
(3) Modification of crustal V_P/V_S
(4) Modification of a noise parameter (r, σ)
(5) Modification of dimension (layer birth)
(6) Modification of dimension (layer death)

Each method except (4) is altering the velocity-depth structure. For (1) and (2), a random Voronoi nucleus from the current model is selected. For (1), the V_S of the nucleus is modified according to the proposal distribution of V_S. Therefore, a sample from this normal distribution (centered at zero) is drawn and added to the current V_S value of the nucleus. For (2), a sample from the depth proposal distribution is drawn and added to the depth-coordinate of the nucleus. For (3), if not constant, a sample from the V_P/V_S proposal distribution is drawn and added to the V_P/V_S value of the current model. For (4), one random noise parameter from one target is selected (r or σ). This parameter, if not constant, is modified according to the procedure before and according to its own proposal distribution. C_e assumed for surface wave dispersion is based on the exponential law. For receiver functions, the exponential law is only assumed, if the user wants to invert for r. If r is given by a constant, automatically the Gaussian correlation law is considered.

For (5) and (6), the proposal distributions are equal. For (5), a random depth-value will be drawn from the uniform depth prior distribution, where a new Voronoi nucleus will be born. The new velocity of this nucleus will be computed by the current model velocity at the drawn depth, modified by the proposal distribution. For (6), a random nucleus from the nuclei ensemble of the current model is chosen and removed. Here, the proposal distribution is only relevant for the computation of the acceptance probability, not for the actual modification of the model. Note that the proposal distributions for (5) and (6) relate to V_S.

For the six modification methods, the user must define five normal distributions as initial proposal distributions by giving their standard deviations. For the model modification methods (1)-(4), it is obvious, that small standard deviations of the distributions cause a high chance of only small parameter changes. So, the proposal models are very similar to the current model. On the other hand, if the proposal distribution width is large, the modifications tend to be larger and the proposal models are likely to be more different from the current model. For (5) and (6) however, the proposal distribution only plays a subordinate role. If a random nucleus is added or removed, the complete model structure between the adjacent nuclei is modified, which can cause large interface depth shifts – dependent on the proximity of the adjacent nuclei. A nucleus birth with a V_S modification of zero would still result in a shift of the layer interface.

The initial width of the proposal distribution, however, will be adjusted during the inversion to reach and maintain a specific acceptance rate of proposal models (see section 3.2).

Accept a model. After a model is proposed, it needs to be evaluated in comparison to the current model. Therefore, the acceptance probability α is computed. If any parameter of the proposed model does not lie within its prior distribution, the acceptance probability drops to

zero and the model will automatically be declined. A model parameter can only lie outside the prior if the current value of it is very close to the prior limits or its proposal distribution width is very large. Further criteria that will force a refusal of the proposal model by setting $\alpha = 0$:

- a layer thickness is smaller than *thickmin*
- a low / high velocity zone does not fulfill the user defined constraint

If a model proposal clears the above criteria, the actual acceptance probability α is computed. The acceptance probability is a combined probability and will be computed from the prior, proposal and likelihood ratios of the proposal model m' and the current model m.

$$\alpha = \text{prior ratio x likelihood ratio x proposal ratio x Jacobian}$$

$$\alpha(m'|m) = \frac{p(m')}{p(m)} \times \frac{p(d_{obs}|m')}{p(d_{obs}|m)} \times \frac{q(m|m')}{q(m'|m)} \times |J| \tag{III.16}$$

The determinant of the Jacobian matrix equals 1 in any case of modification. Furthermore, the acceptance term can be rearranged dependent on the type of model modification.

- **Voronoi nucleus position, V_P/V_S, and covariance matrix.** The modification of the nucleus position (i.e., V_S and depth), V_P/V_S and the covariance matrix (i.e., r and σ) do not involve a change of dimension. For these model proposals, the prior ratio equals 1 and the proposal distributions are symmetrical, i.e., the probability to go from m to m' is equal to the probability to go from m' to m. Hence, the proposal ratio also equals 1. We can shorten the acceptance probability to the likelihood ratio:

$$\alpha(m'|m) = \frac{p(d_{obs}|m')}{p(d_{obs}|m)} \tag{III.17}$$

If the Voronoi nucleus position or V_P/V_S was modified, the factor $\frac{1}{\sqrt{(2\pi)^n |C_e|}}$ in the likelihood function (Eq. III.8) is equal for proposed and current model and cancels out. Thus, α is only dependent on the Mahalanobis distance and is defined as:

$$\alpha(m'|m) = exp\left\{-\frac{\Phi(m') - \Phi(m)}{2}\right\} \tag{III.18}$$

If a noise parameter was modified, C_e are different for proposal and current model; therefore the mentioned factor in the likelihood function must be included in the computation of α. Note that the Mahalanobis distance also includes the covariance matrix C_e. The acceptance probability computes as follows:

$$\alpha(m'|m) = \left(\frac{|C_e|}{|C_e'|}\right)^{\frac{1}{2}} \times exp\left\{-\frac{\Phi(m') - \Phi(m)}{2}\right\} \tag{III.19}$$

- **Dimension change of velocity-depth model.** A dimension change of a model implies the birth or death of a Voronoi nucleus, which corresponds to a layer birth or death. In this case, the prior and proposal ratios are no longer unity. For a birth step, the acceptance probability

equals:

$$\alpha(m'|m) = \frac{\theta\sqrt{2\pi}}{\Delta v} \times exp\left\{\frac{(v'_{k+1} - v_i)^2}{2\theta^2} - \frac{\Phi(m') - \Phi(m)}{2}\right\} \tag{III.20}$$

where i indicates the layer in the current Voronoi tessellation c that contains the depth c'_{k+1} where the birth takes place. v_i and v'_{k+1} are the velocities at given depth of the current and the proposal model, i.e., before and after the birth. θ is the standard deviation of the proposal distribution for a dimension change. The acceptance probability of the birth step is a balance between the proposal probability (which encourages velocities to change) and the difference in data misfit which penalizes velocities if they change so much that they degrade the fit to the data.

The acceptance probability for a death of a Voronoi nucleus is:

$$\alpha(m'|m) = \frac{\Delta v}{\theta\sqrt{2\pi}} \times exp\left\{-\frac{(v'_j - v_i)^2}{2\theta^2} - \frac{\Phi(m') - \Phi(m)}{2}\right\} \tag{III.21}$$

where i indicates the layer that was removed from the current tessellation c and j indicates the cell in the proposed Voronoi tessellation c' that contains the deleted point c_i. v_i and v'_j are corresponding velocities.

The proposal candidate will be accepted with a probability of α, or rejected with a probability of $1 - \alpha$. The computational implementation is a comparison of α to a number u, which is randomly drawn from a uniform distribution between 0–1. The model is accepted if $\alpha > u$, which is always the case if $\alpha > 1$. As we consider the log-space for our computations, we use $\log(\alpha)$ and $\log(u)$.

When a proposal model is accepted, it will replace the current model. On the other hand, when a model is rejected, the current model stays unmodified. In the next iteration, a new model is proposed. This process will be repeated until the defined number of iterations is reached. The accepted models form the Markov chain and define the posterior distribution of the parameters after the burn-in phase.

The posterior distribution. After a chain has finished its iterations, it automatically saves ten output files in `.npy` format (NumPy binary file), holding V_S-depth models, noise parameters, V_P/V_S ratios, likelihoods and misfits for the burn-in (p1) and the posterior sampling phase (p2), respectively. Every i-th chain model is saved to receive a p2-model collection of $\sim$ *maxmodels*, a constraint given by the user. The files are saved in *savepath/data* as follows:

`c*_p1models.npy`	`c*_p2models.npy`	
`c*_p1noise.npy`	`c*_p2noise.npy`	
`c*_p1vpvs.npy`	`c*_p2vpvs.npy`	
`c*_p1likes.npy`	`c*_p2likes.npy`	*three-digit chain identifier number
`c*_p1misfits.npy`	`c*_p2misfits.npy`	

While V_P/V_S and the likelihood are vectors with the lengths defined by *maxmodels*, the models, noise and misfit values are represented by matrices, additionally dependent on the

maximum number of model layers and the number of targets, both also defined by the user. The models are saved as Voronoi nuclei representation. For noise parameters, the matrix contains r and σ of each target. For the RMS data misfit, the matrix is composed of the misfit from each target and the joint misfit.

2.2 The Saving and Plotting modules

The *BayHunter.Plotting* module cannot only be utilized for data illustration, but also for outlier detection and re-saving of *BayHunter.SingleChain* results.

Outlier detection. Not every chain converges to the optimum solution space. BayHunter provides a method for outlier chain detection based on the median likelihood. For each chain, the median likelihood of the exploration phase is computed. A threshold is computed below which chains are declared as outliers. The threshold is a percentage of the maximum reached median likelihood from the chain ensemble. The percentage is defined by the user in terms of deviation from the maximum likelihood. For instance, if the deviation *dev*=0.05 (5 %), all chains not reaching a median likelihood of 95 % of the maximum median likelihood, are declared as outlier chains. If no or another outlier detection method is preferred, the user may chose a large value for *dev*, e.g., *dev*=5. The chain identifiers of the outlier chains will be saved to a file, which will be overwritten when repeating outlier detection.

Final posterior distribution. The *BayHunter.PlotFromStorage* class provides a method called *save_final_distribution*, which can be used to combine *BayHunter.SingleChain* results and store final posterior distribution files. Therefore, two arguments need to be chosen. The deviation *dev* is considered for outlier detection. *maxmodels* is the number of models that define the final posterior distribution. An equal number of p2-models per chain (except outlier chains) is chosen to assemble the posterior distribution of the inversion. Five files will be saved in `savepath/data` and represent the V_S-depth models, noise parameters, V_P/V_S ratios, likelihoods and misfits, respectively. The filename contains neither a chain identifier nor a phase tag and is e.g., for the V_P/V_S ratios: `c_vpvs.npy`.

Plotting methods. The plotting methods utilize the configuration file that was stored by the Optimizer module after initiation of the inversion. A list of plotting methods is presented below. Plots generated by these methods can be found in section 3.3.

plot_iiter*	* likes, nlayers, noise, vpvs, misfits	parameter with iterations (Fig. III.5)
plot_posterior_*	* likes, nlayers, noise, vpvs, misfits, models1d, models2d	parameter posterior distribution or V_S-depth models (Fig. III.7)
plot_current*, plot_best*	* datafits, models	data fits or V_S-depth models from current or likeliest models (Fig. III.6)
plot_refmodel	add reference model to posterior distributions (Figs. III.6, III.7)	

2.3 The BayWatch module

During a BayHunter inversion the user can live-stream progress and results with the BayWatch graphical interface. This makes it easy to see how chains explore the parameter space, how the data fits and models change, in which direction the inversion progresses and if it is necessary to adjust parameters or prior settings. If the user sets *baywatch=True* in the inversion start command, BayHunter spawns a process only for streaming out the latest chain models. When starting BayWatch, those models are received and temporarily stored in memory, and will be visualized as shown in the screen shot (Fig. III.4).

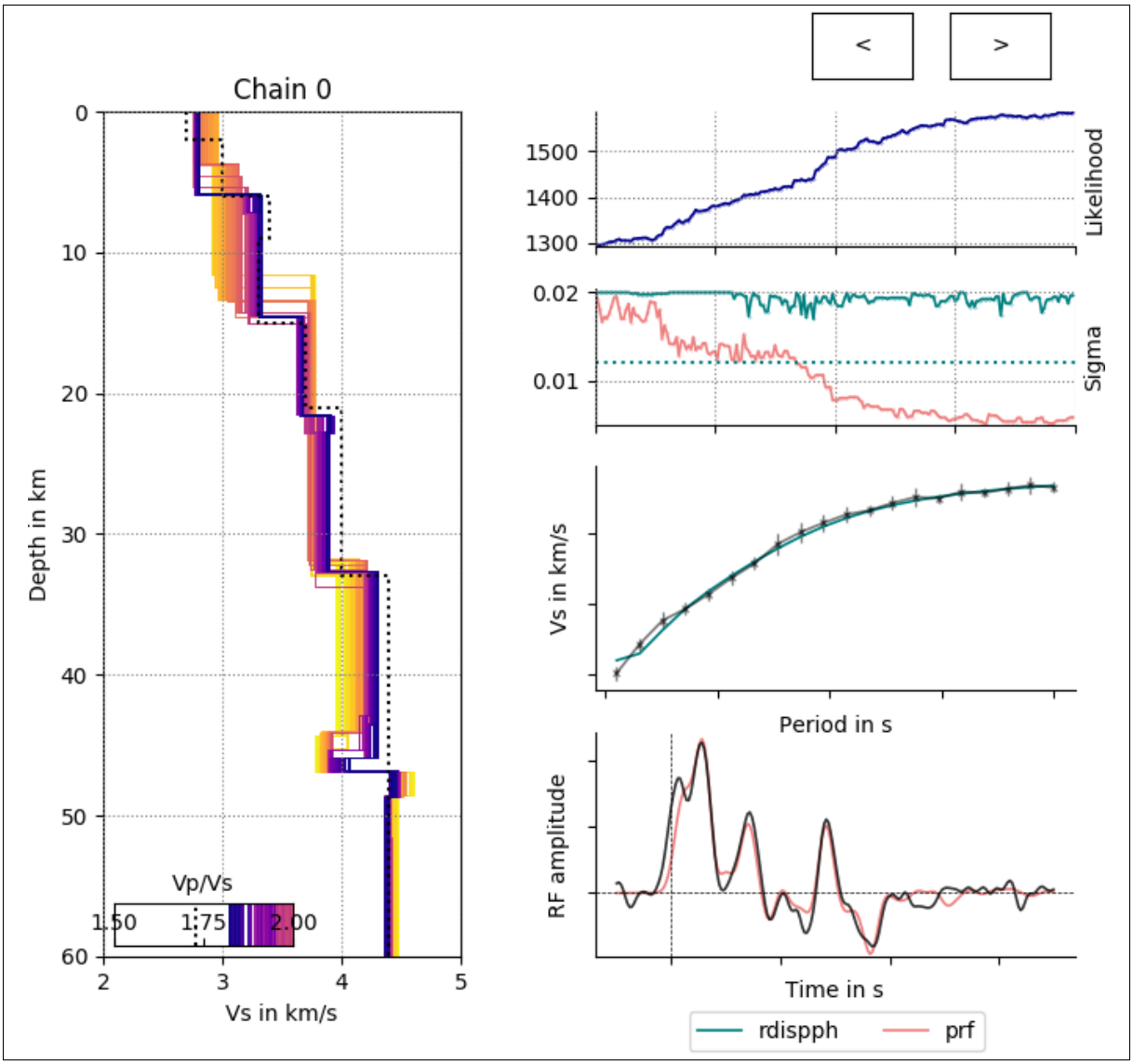

Figure III.4: Screen shot of BayWatch live-stream showing the evolution of chain models with likelihood, i.e., the evolution of the V_S-depth structure, V_P/V_S (with the darkest colored model being the current model) and σ (sigma) for the two targets. The live-stream shows an inversion of synthetic data from a six-layer velocity-depth model as described in section 3.3. The Colored dotted lines represent the "true" model values.

3 Tutorial

This chapter contains the installation instructions of BayHunter, followed by an example of how to set up and run an inversion. A minimalistic working example is shown in appendix III.A. Furthermore, results from an inversion using synthetic data are shown and discussed. For the full tutorial including data files be referred to the GitHub repository[1].

3.1 Requirements and installation

BayHunter is currently for a Python 2 environment (as of October, 2019). After installation of the required Python-modules, simply type the following to install BayHunter:

```
sudo python setup.py install
```

Required Python-modules and usage	
`numpy`	numerical computations
`matplotlib`	plotting library
`pyPdf`	merging PDFs
`configobj`	configuration file
`zmq`	BayWatch, inversion live-streaming
`rfmini`	receiver function forward modeling

The Fortran forward modeling code for surface wave dispersion is already included in the BayHunter package and will be compiled when installing BayHunter. BayHunter uses a Python wrapper interfacing the `CPS/surf96` routine from Herrmann and Ammon (2002). The code to forward model receiver functions, however, must be installed (only if wished to invert for receiver functions). A copy of rfmini and installation instructions can be found in the BayHunter package (`rfmini.tar.gz`). The code `rfmini` was developed for BayHunter by Joachim Saul (GFZ).

3.2 Setting up and running an inversion

Setting up the targets. As mentioned in section 2.1 (Initialize the targets), BayHunter provides six target classes (four SWD and two RF), which use two types of forward modeling plugins (`CPS/surf96`, `rfmini`). For both targets, the user may update the default forward modeling parameters with *set_modelparams* (appendix III.A). Parameters and default values are given in Table III.1.

If the user wants to implement own forward modeling code, a new forward modeling class for it is needed. After normally initializing a target with BayHunter, an instance of the new forward modeling class must be initialized and passed to the *update_plugin* method of the target. If an additional data set is wished to be included in the inversion, i.e., from a non pre-defined

[1] `https://github.com/jenndrei/BayHunter`

Table III.1: Default forward modeling parameters for SWD and RF.

SWD	mode = 1	1=fundamental mode, 2= 1st higher mode, etc.
RF	gauss = 1.0	Gauss factor, low pass filter
	water = 0.001	water level stabilization
	p = 6.4	slowness in deg/s
	nsv = None	near surface velocity in km/s for computation of incident angle (trace rotation). If `None`, nsv is taken from velocity-model.

target class, a new target class needs to be implemented, additionally to the forward modeling class that handles the synthetic data computation. For both, the forward modeling class and the new target class, a template is stored on the GitHub repository. It is important that the classes implement specifically named methods and parameters to ensure the correct interface with BayHunter.

Setting up parameters. Each chain will be initialized with the targets and with parameter dictionaries. The model priors and inversion parameters that need to be defined are listed with default values in Table III.2, and are explained below in detail.

Table III.2: Default model priors and inversion parameters. Model prior tuples define the limits (min, max) of a uniform distribution. `None` implies that the constraint is not used. SI indicates corresponding units of the international system. Abbreviations and constraints are explained in the text.

Model priors			**Further parameters**		
vs	= (1, 5)	km/s	nchains	= 3	
z	= (0, 60)	km	$iter_{burnin}$	= 4096	
layers	= (1, 20)		$iter_{main}$	= 2048	
vpvs	= (1.5, 2.1)		acceptance	= (40, 45)	%
mantle[1]	= `None`	(km/s, -)	propdist[3]	= (0.015, 0.015, 0.015,	
mohoest[2]	= `None`	(km, km)		0.005, 0.005)	SI
r_{RF}	= (0.35, 0.75)		thickmin	= 0.	km
σ_{RF}	= (1e-5, 0.05)		lvz	= `None`	
r_{SWD}	= 0.		hvz	= `None`	
σ_{SWD}	= (1e-5, 0.1)	km/s	rcond	= `None`	
[1]i.e., (vs_m, $vpvs_m$), e.g., (4.2, 1.8)			station	= 'test'	
[2]i.e., (z_{mean}, z_{std}), e.g., (40, 4)			savepath	= 'results/'	
[3]i.e., (vs, z_{move}, $vs_{birth/death}$, noise, vpvs)			maxmodels	= 50 000	

The priors for the velocity-depth structure include V_S and depth, the number of layers, and average crustal V_P/V_S. The ranges as given in Table III.2 indicate the bounds of uniform distributions. V_P/V_S can also be given as a float digit (e.g., 1.73), indicating a constant value during the inversion. The parameter *layers* does not include the underlying half space, which is always added to the model. A mantle condition (vs_m, $vpvs_m$), i.e., a vs_m threshold beyond

which V_P is computed from $vpvs_m$, can be chosen if appropriate. There is also the option to give a single interface depth estimate through *mohoest*. It can be any interface, but the initial idea behind was to give a Moho estimate. As explained in section 2.1 (Initialize a model), this should only be considered for testing purposes. Each noise scaling parameter (r, σ) can be given by a range or a digit, corresponding to the bounds of a uniform distribution (the parameter is inverted for) or a constant value (unaltered during the inversion), repectively.

For surface waves, the exponential correlation law (Eq. III.6) is a realistic estimate of the correlation between data points and is automatically applied. For receiver functions, the assumed correlation law should be Gaussian (Eq. III.7), if the RFs are computed using a Gaussian filter, and exponential, if the RFs are computed applying an exponential filter. The inversion for r_{RF} is viable for the latter, however, not for the Gaussian correlation law as of computational reasons (section 2.1, Computation of model likelihood). Only if r_{RF} is estimated by giving a single digit, the Gaussian correlation law is considered. Otherwise, if given a range for r_{RF}, the exponential correlation law is used. Note that the estimation of r_{RF} using the exponential law during an inversion, may not lead to correct results if the input RF was Gaussian filtered.

Nevertheless, r_{RF} can be estimated, as it is dependent on the sampling rate and the applied Gaussian filter width. However, if r_{RF} is too large (i.e., very close to 1), R^{-1} becomes instable and small eigenvalues need to be suppressed. The user can define the cutoff for small singular values by defining *rcond*. Singular values smaller than *rcond* x the largest singular value (both in modulus) are set to zero. *rcond* is not ascribed to the prior dictionary, but to the inversion parameter dictionary (see configuration file).

The inversion parameters can be subdivided into three categories: (1) actual inversion parameters, (2) model constraints and (3) saving options. Parameters to constrain the inversion are the number of chains, the number of iterations for the burn-in and the main phase, the initial proposal distribution widths, and the acceptance rate. A large number of chains is preferable and assures good coverage of the solution space sampling, as each chain starts with a randomly drawn model only bound by the priors. The number of iterations should also be set high, as it can benefit, but not guarantee, the convergence of the chain towards the global likelihood maximum. The total amount of iterations is $iter_{total} = iter_{burnin} + iter_{main}$. We recommend to increase the ratio towards the iterations in the burn-in phase (i.e., $iter_{burnin} > iter_{main}$), so a chain is more likely to have converged when entering the exploration phase for the posterior distribution.

The initial proposal distributions, i.e., Gaussian distributions centered at zero, for model modifications, must be given as standard deviations according to each of the model modification methods (section 2.1, Propose a model). The values must be given as a vector of size five, the order representing following modifications: (1) V_S, (2) depth, (3) birth/death, (4) noise, and (5) V_P/V_S. The first three distributions represent V_S-depth model modifications referring to alterations of V_S (1,3) and z (2) of a Voronoi nucleus. There is one proposal distribution for both noise parameters r and σ (4) and one for V_P/V_S (5).

If the proposal distributions were constant, the percentage of accepted proposal models would decrease with ongoing inversion progress, i.e., the acceptance rate decreases at the expense of an

efficient sampling. To efficiently sample the parameter space, an acceptance rate of ∼40–45 % is forced for each proposal method by dynamically adapting the width of each proposal distribution. We implemented a minimum standard deviation of 0.001 for each proposal distribution.

The most accepted model modifications are (1) and (2); their acceptance rates get easily forced to the desired percentage without even coming close to the defined minimum width of a proposal distribution. Birth and death steps, however, barely get accepted after an initial phase of high acceptance; if not limiting the proposal distribution width to a minimum, the standard deviations for (3) will get as small as 10^{-10} km/s and smaller to try to keep the acceptance rate up. However, as discussed in 2.1 (Propose a model), the distribution width does not in the first place influence the model-modification, but the added or removed Voronoi nucleus. Models modified by birth and death steps will naturally not be accepted very often and even less the further the inversion progresses. Therefore, the overall acceptance rate is stuck with a specific level below the forced rate. An estimate of the actual overall acceptance rate can be made, assuming a realistic acceptance for the birth and death steps, e.g., 1 %. A user given target rate of 40 % for each method would give an actual overall acceptance rate of ∼3 %. (→ 6 methods, 4 reach 40 %, 2 only 1 % = 30 % over all.) The target acceptance rate must be given as an interval.

There are three additional conditions, which might be worthwhile to use to constrain the velocity-depth model. However, using any of them could bias the posterior distribution. The user is allowed to set a minimum thickness of layers. Furthermore low and high velocity zones can be suppressed. If not `None`, the value for *lvz* (or *hvz*) indicates the percentage of allowed V_S decrease (or increase) from each layer of a model relative to the underlying layer. For instance, if *lvz*=0.1, then a drop of V_S by 10 %, but not more, to the underlying layer is allowed. As V_S naturally increases with depth, and the algorithm only compares each layer with the layer underneath, the *hvz* criteria should only be used if observing extreme high velocity zones in the output. Otherwise sharp (but real) discontinuities could be smoothed out, if chosen too small. The *lvz* and *hvz* criteria will be checked every time a velocity-depth model is proposed and the model will be rejected if the constraints are not fulfilled.

The saving parameters include the *station*, *savepath* and *maxmodels*. The *station* name is optional and is only used as a reference for the user, for the automatically saved configuration file after initiation of an inversion. *savepath* represents the path where all the result files will be stored. A subfolder *data* will contain the configuration file and all the *SingleChain* output files, the combined posterior distribution files and an outlier information file. *savepath* also serves as figure directory. *maxmodels* is the number of p2-models that will be stored from each chain.

Running an inversion. The inversion will start through the *optimizer.mp_inversion* command with the option to chose the number of threads, *nthreads*, for parallel computing. By default, *nthreads* is equal to the number of CPUs of the user's PC. One thread is occupied if using BayWatch. Ideally, one chain is working on one thread. If fully exhausting the capacity of a 8 CPUs PC, give *nthreads*=8 and *nchains*=multiple of *nthreads* or (*nthreads*-1) if using BayWatch. This would cause *nthreads*(-1) chains to run parallel at all times, until *nchains* are worked off.

The speed of the inversion will not increase by choosing a larger *nthreads*. In fact, the speed is determined by the number of CPUs. If, for instance, the user doubles *nthreads*, the number of chains running parallel at once is also double, but the chains queue for some non-threadable computations blocking one CPU at a time, so each chain runs half the speed. To decrease *nthreads* offers a possibility to minimize the workload for a PC and that it is still accessible for other tasks during an inversion.

Although having access to a cluster, inversions were also performed on a single work station to determine the duration of an inversion with standard PC equipment (e.g., Memory: 16 GB, Processor model: 3.60 GHz x 8 cores). The runtime is not only dependent on the PC model, but also on the number of chains and iterations, and the number of layers of the actual velocity-depth structures, which directly influences the computational time of the forward modeling. The inversion for the example given in section 3.3 with 21 chains, 150,000 iterations and models with 3–10 layers, took 20.4 minutes; so each batch of 7 chains took 7 minutes.

Another argument to set when starting an inversion is *baywatch*. If set to True, model data will be send out with an interval of *dtsend*=0.5 s and can be received by BayWatch until the inversion has finished.

3.3 Testing with synthetic data

A set of test data was computed with the *BayHunter.SynthObs* module, which provides methods for computing receiver functions (P, S), surface wave dispersion curves (Love, Rayleigh, phase, group), and synthetic noise following the exponential or the Gaussian correlation law. We computed the P-RF and the fundamental mode SWD of the Rayleigh wave phase velocity from a six-layer model including a low velocity zone. We computed non-correlated noise for SWD and Gaussian correlated noise for the RF with values for r and σ as given in Table III.3 (*true*). Noise and synthetic data were then added to create observed data. An example script, including these steps, can be found in appendix III.A and the online repository.

Table III.3: Model priors and inversion parameters for synthetic test inversion and *true* values used for modeling of the observed data. Model prior tuples define the limits (min, max) of a uniform distribution.

Model priors		true	**Further parameters**	
vs	= (2, 5)	see plots	nchains	= 21
z	= (0, 60)	see plots	$iter_{burnin}$	= 100,000
layers	= (1, 20)	6	$iter_{main}$	= 50,000
vpvs	= (1.5, 2.1)	1.73	acceptance	= (50, 55)
r_{RF}	= 0.92	0.92	propdist	= (0.005, 0.005, 0.005,
σ_{RF}	= (1e-5, 0.05)	0.0052		0.005, 0.005)
r_{SWD}	= 0.	0.	rcond	= 1e-6
σ_{SWD}	= (1e-5, 0.1)	0.01	station	= 'st6'

Two targets (*PReceiverFunction*, *RayleighDispersionPhase*) were initialized with the "ob-

served" data and combined to a *BayHunter.JointTarget* object. The latter and the two parameter dictionaries of model priors and inversion parameters (Tab. III.3) were passed to the Optimizer. Parameters that were not defined fall back to the default values. We purposely show a run with only 150,000 iterations to visualize the convergence of different chains and the outlier detection method. The inversion finished after 20 minutes, saving and plotting methods were applied afterwards.

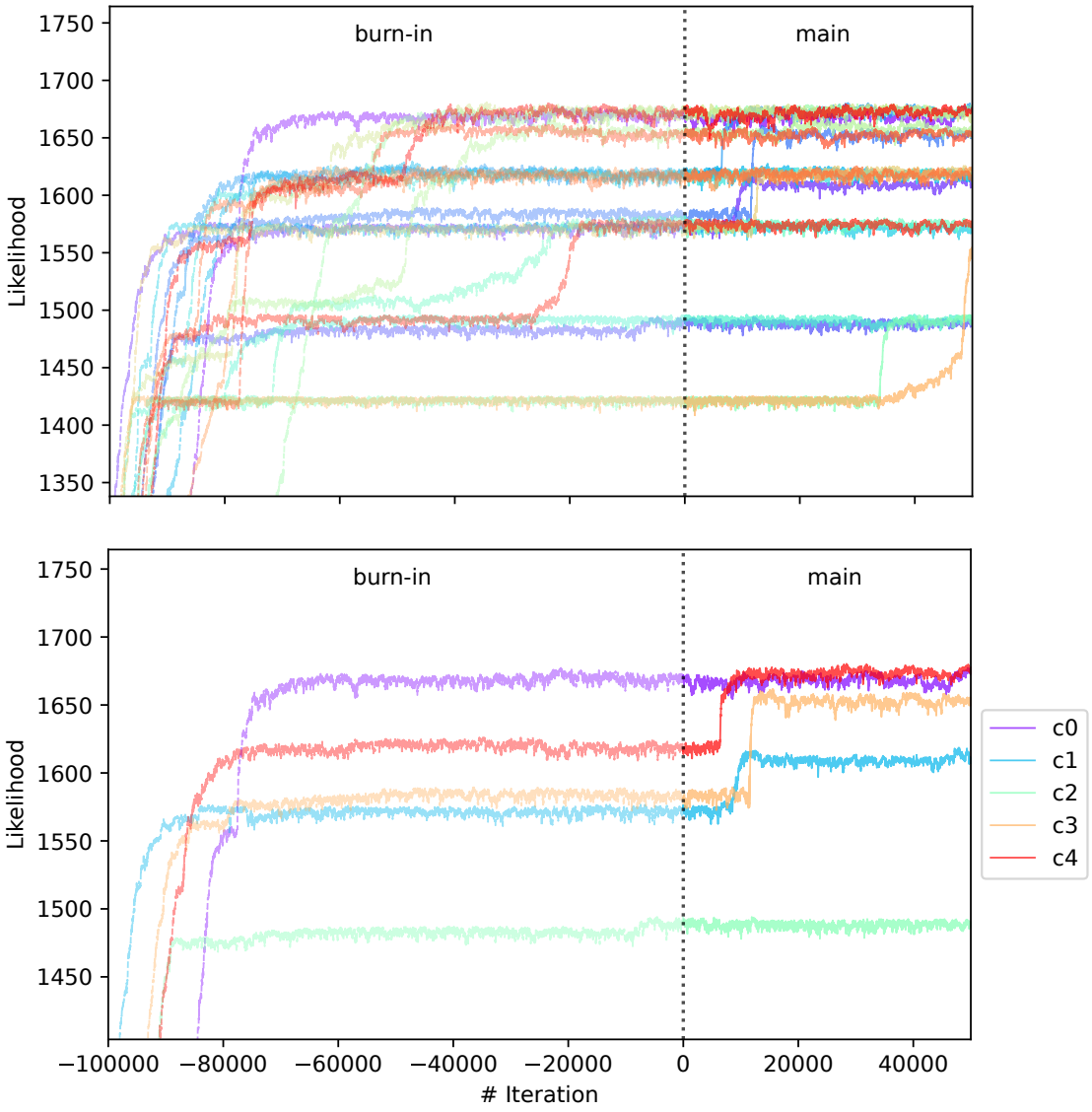

Figure III.5: Development of likelihood over iteration for all 21 chains (top) and a small selection of chains (bottom).

Figure III.5 shows the likelihood development over the iterations for all and for a selection of chains. A strong increase of likelihood can be observed at the first iterations in the burn-in phase, converging towards a stable value with increasing number of iteration. Some chains reached the final likelihood plateau in the burn-in phase (e.g., $c0$), some within the posterior sampling phase (e.g., $c4$), and some did not converge at all ($c2$). The chain $c2$ (also $c1$ and $c3$) had a good chance of reaching the maximum likelihood, if the small number of iterations would

not have stopped the exploration at this early stage. However, the number of iterations cannot be eternal; in any case it is necessary to compare the convergence level of the chains.

Here, we defined a 0.02 deviation condition for outliers. With a maximum median posterior likelihood of 1674 ($c13$), the likelihood threshold is 1640, which declared 13 chains with deviations of 0.032–0.159 as outliers (see Tab. III.4). In a real case inversion, the number of iterations should be much higher, and the number of outlier chains is small. The detected outlier chains will be excluded from the posterior distribution.

Table III.4: Deviations of each chain's median likelihood from the maximum median likelihood of the chain ensemble. Only outlier chains with deviations >0.02 (2 %) are listed.

c1	0.039	c6	0.061	c9	0.059	c15	0.150	c19	0.059
c2	0.111	c7	0.033	c10	0.150	c16	0.033		
c5	0.032	c8	0.109	c14	0.033	c17	0.033		

Figure III.6 shows the current V_S-depth models from different chains and corresponding data fits (same chains as in Fig. III.5, bottom). Chains $c1$ and $c2$ show the worst data fits; they were declared as outliers. The other chains ($c0$, $c3$, $c4$) show a reasonably good data fit with very similar velocity models. Chains $c0$ and $c4$ already found a six-layer model, $c3$ found a five-layer model averaging the low velocity zone.

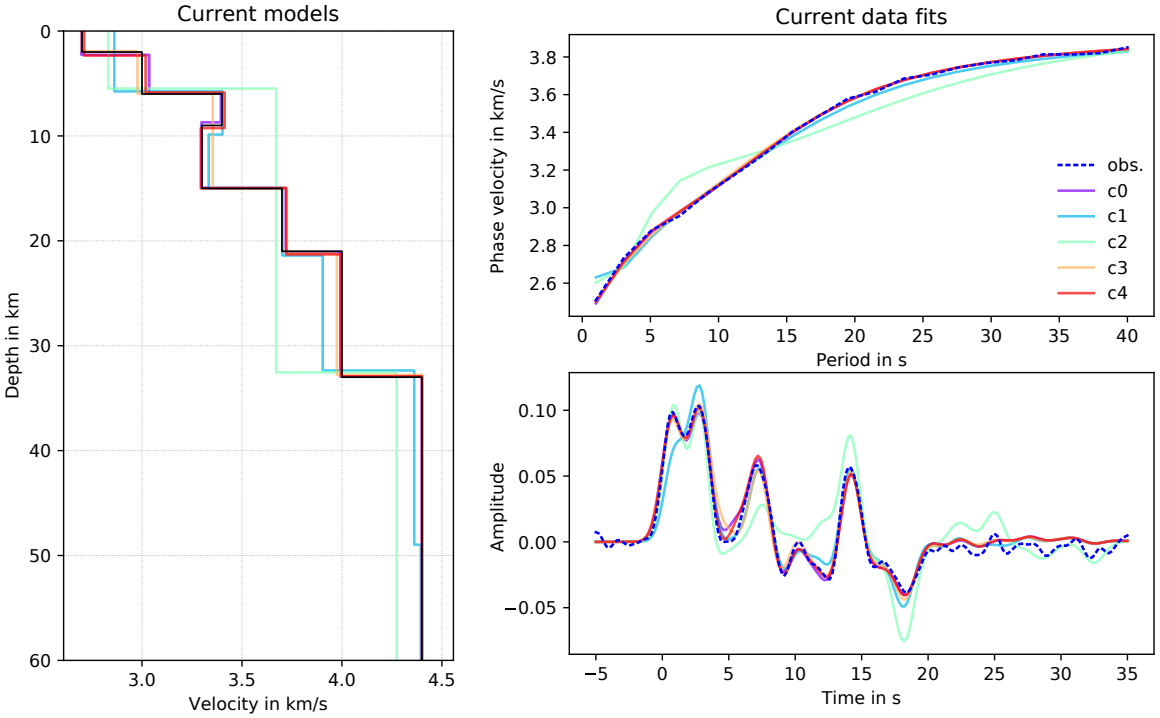

Figure III.6: Current velocity-depth models and data fits of corresponding SWD and RF data from different chains with likelihoods as illustrated in Figure III.5 (bottom). The black line (left) is the synthetic V_S-depth structure.

The posterior distribution of the eight converged chains, containing 100,000 models, are illustrated in Figure III.7. The mean (and mode) posterior V_S-depth structure images the true model very well, including the low velocity zone. The number of layers is determined to be

most likely six. The σ distributions of both, RF and SWD show a Gaussian shape, inhering a tail of higher values from models of chains that only converged within the exploration phase of the inversion (e.g., $c3$ and $c4$). The distribution of σ_{SWD} already represents a good estimate, slightly overestimated, which falls back to the number of iterations. Tests with more iterations show that the median of σ_{SWD} is in perfect agreement with the true value.

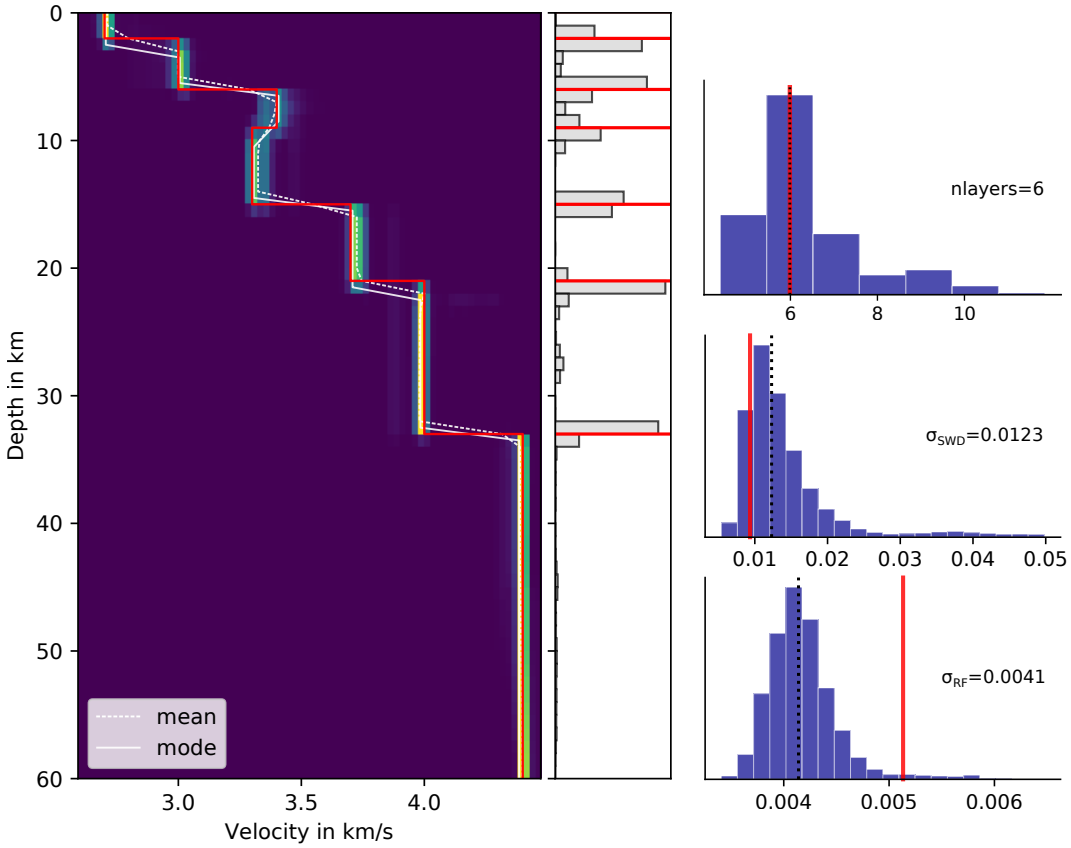

Figure III.7: Recovered posterior distributions of V_S, interface depth, number of layers, and noise level for synthetic data. Red lines indicate the true model, as given in Table III.3. The posterior distribution is assembled by 100,000 models collected by 8 chains.

σ_{RF} is underestimated, which theoretically means that noise was interpreted as signal and receiver function data is overfitted. The difference to SWD is the type of noise correlation (= Gaussian) and the assumption of the correlation r of data noise ($r \neq 0$). We computed synthetic RF data applying a Gaussian lowpass filter with a Gaussian factor of 1. Separately, noise was generated randomly with a correlation r estimated to represent the applied Gauss filter, and added to the synthetic data. The random process of generating noise does not output a noise vector which exactly matches the given values of r and σ. If only drawing one single realization with a determined amount of samples from the multivariate normal distribution may produce deviations from the targeted r and σ. From the generated noise the true σ can be computed by the standard deviation. However, the true r is not easy to reconstruct. Assuming a wrong r for the covariance matrix of noise cannot lead to the correct σ.

It is possible to clarify whether the assumed correlation parameter r is in tendency correct.

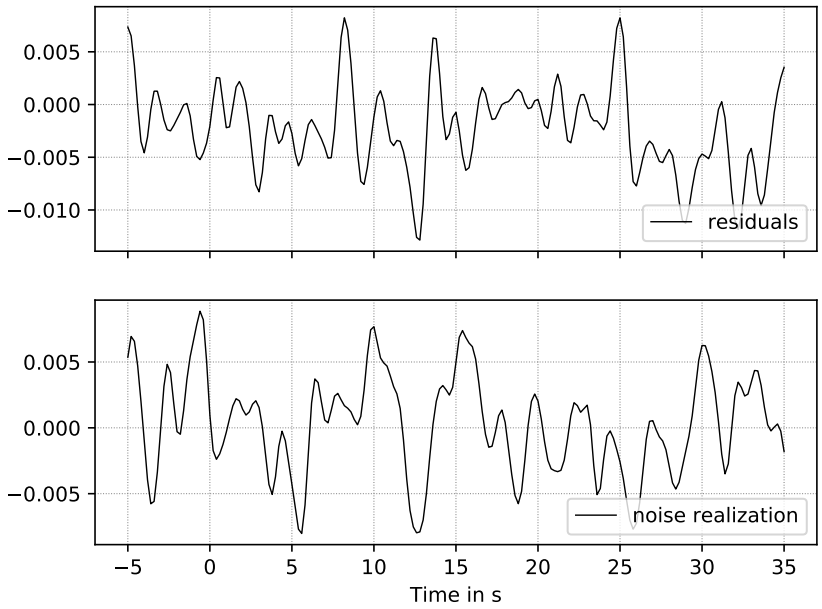

Figure III.8: Comparison of residuals of the best fitting RF model and one realization of noise through C_e^{RF} for receiver functions. Both noise vectors are of coherent appearance in frequency and amplitude, hence, the estimate of r_{RF} is appropriate.

Figure III.8 shows a comparison of (1) the RF data residuals of the best fitting model and (2) one realization of noise with the given correlation r and the estimated σ_{RF}; both noise vectors should be of coherent appearance in frequency and amplitude, if the estimate of r_{RF} is appropriate.

Conclusion and outlook

The Pan-African Orogeny (750–490 Ma) was the key event for the amalgamation of West and East Gondwana, and also for the assembly of Madagascar and Sri Lanka. Both islands occupied central positions in Gondwana and the Pan-African Orogen. We investigated seismic crustal properties and imaged the V_S-depth structure in Sri Lanka, and radial anisotropy in southern Madagascar. Our findings are valuable for an interpretation in the greater context of the assembly and break-up of Gondwana. We want to compare seismic properties derived in our study to results of other Gondwana studies, in particular located in Madagascar, southern India and East Antarctica.

Comparison of seismic properties in East Gondwana terranes

A mixing and joint-reworking of crustal material from different terranes during an orogeny can lead to an increasing unification across the regions (e.g., through metamorphosis), and therefore to similar crustal properties. However, similar seismic properties do by implication not necessarily tell the same story. We will compare crustal properties of Pan-African terranes, but must first clarify which properties can be compared under which conditions.

Moho depths: Before the collision, each fragment inherited own crustal thicknesses, that were overformed during the Pan-African Orogeny. Large parts of the original thicknesses were unified by crustal thickening (∼60–75 km) and subsequent post-orogenic collapse. Processes during and after Gondwana's break-up lead to regional differences of crustal thicknesses, hence Moho depths are only comparable in undisturbed regions. Processes responsible for regional differences include rifting accompanied by crustal thinning (e.g., Morondava basin of Madagascar, Mannar basin of Sri Lanka) and collisional events leading to crustal thickening (e.g., Himalayan Orogeny of northern Indian subcontinent). Also, erosional processes, magmatic intrusions and isostatic compensation among others influenced the thickness of the crust until today.

V_P/V_S ratios: Seismic velocity ratios in the crust are mostly influenced by mineral composition, particularly the relative ratio of quartz and plagioclase (silica content) (Christensen, 1996). Each terrane brought its lithic composition into the collision, however, the mineral composition can change significantly through changing P-T conditions and metamorphosis. The Pan-African rocks experienced similar P-T conditions and metamorphosis to amphibolite and granulite facies rocks (Madagascar and Sri Lanka). Changes in V_P/V_S ratios with increasing metamorphic grade are related to complex mineral reactions; the most impact on seismic properties derives from changes in the abundances and composition of plagioclase feldspar (Christensen, 1996). V_P/V_S ratios are comparable for rocks undisturbed after the Pan-African Orogeny, but can show strong variations, especially if the original composition of an accreted terrane was different, or heterogeneous throughout the crust (and lithosphere). Also the migration of enriched fluids through the

crust during the orogeny can alter petrologic compositions regionally. Average crustal V_P/V_S ratios can refer to the unification-level, but do not consider pre-orogenetic conditions.

Crustal velocities: Average seismic velocities (V_P and V_S) and the density of crystalline rocks increase as the rocks become more mafic or increase in metamorphic grade (Eaton et al., 2003). Fragments within the orogeny experienced similar P-T conditions, resulting in similar metamorphic facies, and seismic velocity ranges. Seismic velocities can be correlated to metamorphic facies (Huang et al., 2013), but also show large overlaps in their values. Here, as laid out for the V_P/V_S ratios, (initial) rock composition and density (depth) must be considered. The surface rocks exposed today in each terrane were buried at different depths and have experienced different grades of metamorphism. Precambrian outcrops in Madagascar were buried to a depth of 25–35 km (Androyen domain; Jöns and Schenk, 2011) and 18–30 km (Anosyen domain; Horton et al., 2016, and references therein). Exposed Neoproterozoic high-grade metamorphic rocks found in Sri Lanka and southern India are from middle-to-deep crust of the Pan-African Orogen (Kehelpannala, 2004), with burial depths of 30 km or more (Kröner and Brown, 2005). Surface rocks of the southern Indian West Dharwar Craton (WDC, Fig. 14) were buried to a depth of only ∼15 km (Rai et al., 2013) and the northern Southern Granulite Terrain (SGT) to 15–25 km (Das et al., 2015).

Crustal features and radial anisotropy: Crustal features such as low velocity zones and mafic underplates, and radial anisotropy of undisturbed crustal regions are comparable, if they were generated during the Pan-African Orogeny. Features that were existent in the crust before the terrane accretion are not comparable in the sense of this study. However, those that evolved through the orogeny (e.g., shear zones) do not necessarily need to exist across Gondwana terranes, if they are regional observations caused by regional crustal processes and characteristics. Anisotropic structures are highly suited for a comparison, however, most studies in Pan-African terranes highlight azimuthal anisotropy (e.g., Kumar et al., 2015; Ramirez et al., 2018; Reiss et al., 2016) and also often focus on the upper mantle structure. No studies on radial anisotropy were conducted in undisturbed Pan-African regions.

Seismic properties and features derived from our study: The following list summarizes seismic properties that are selected for a comparison and were retrieved in the frame of this study. Most of those properties represent Sri Lanka. For southern Madagascar, only V_S and RA down to 30 km depth were derived.

Sri Lanka

- Crustal thickness is between 30–40 km, whereby the crust undisturbed from Mannar basin rifting shows a thickness of 35.5–40 km; mean is 37.6±1.3 km.
- Average crustal V_S shows a range of 3.7–3.9 km/s; mean is 3.8±0.05 km/s.
- Majority of V_P/V_S ratios are between 1.66–1.73; mean is 1.71±0.05 for Hκ-stacking (joint inversion: 1.71±0.1), which represents a felsic crustal composition with intermediate to high silica content.
- Surface V_S (uppermost layer) are between 3.1–3.6 km/s; mean is 3.4±0.1 km/s.

- Mantle V_S (down to 75 km) are between 4.3–4.7 km/s; mean is 4.45±0.1 km/s.
- Isostatic compensation: crustal thickness and topography correlate, except for the northernmost part of the island (density compensation).
- Low V_S zone (3.4–3.6 km/s) at ∼10 km depth at five neighboring stations in HC.
- Mafic layer per definition of V_S (4.0–4.3 km/s): V_S of the lowest crustal layer are less or only borderline 4.0 km/s for most of the stations. For single stations (i.e., MALK, SL06, SL11, SL13, SL16, SL20, SL27) V_S reaches values of ∼4.05–4.15 km/s, but show no spatial correlation.

Southern Madagascar

- Surface V_S are between 3.2–3.4 km/s.
- Upper crust (3–3.5 km/s) extends to depths of 10 km (undisturbed crust), middle crust (3.5–3.8 km/s) down to 20–25 km; generally lower V_S along the east coast.
- *RA* from surface to depth beneath Precambrian units shows a positive/negative/positive signature, corresponding to (+) layering and nappe stacking at the uppermost layers, (–) fossilized shear zones and vertically folded fabrics in the middle crust, and (+) gravitational extension and crustal flow in the lower layers.

East Gondwana related studies and comparison

We bring together seismic properties from the once adjoined terranes of East Gondwana (Fig. 14). The terranes in close juxtaposition to our study regions are the Mozambique-Tanzanian belt, India, and East Antarctica. For abbreviations in the text be referred to Figure 14.

Pan-African terranes: Rai et al. (2009) analyzed data from eight stations (Fig. 14) located in the Mozambique-Tanzanian belt (MBWE, KOND, KIBE), Madagascar (ABPO), Sri Lanka (PALK), southern Indian high-grade terranes (TRV, KOD), and East Antarctica (SYO). The majority of stations show crustal thicknesses of 37±0.8 km, a felsic bulk composition of rocks, a low V_S layer (∼3.6 km/s) in the upper crust, and a strong V_S increase at mid-crustal depths. Four stations (SYO, PALK, TRV and ABPO) show strong conformance of crustal thicknesses (37.8±0.8 km) and V_P/V_S ratios (1.7±0.03), which Rai et al. (2009) attribute to region spanning unification of crustal structures through extensive overprinting during the Pan-African Orogeny.

Southern Madagascar: Rindraharisaona et al. (2017) revealed major differences of seismic properties between Archean and Proterozoic crust (Fig. 14). The Archean domains show thicknesses of 38–43 km with a high V_S lower crust (3.8–4.0 km/s) and a thin layer of mafic lithologies beneath (4.0–4.3 km/s), which together with a gradational Moho discontinuity suggest mafic underplating below the Antananarivo domain. Low crustal V_P/V_S ratios of 1.75±0.04 in the Antananarivo domain indicate a felsic to intermediate crustal composition and seem uninfluenced by the underplated mafic layer. The Proterozoic crust shows thicknesses of 35–38 km. Crustal average V_P/V_S ratios (dominantly 1.76–1.78) and V_S in the lower crust (∼3.9 km/s) indicate a felsic to intermediate lower crust. A mafic component is either missing or has only minor contribution in the Proterozoic lower crust.

The formation of the Phanerozoic Morondava basin in the west and the Cretaceous volcanism along the east coast, influenced crustal thicknesses and V_P/V_S ratios after the Pan-African

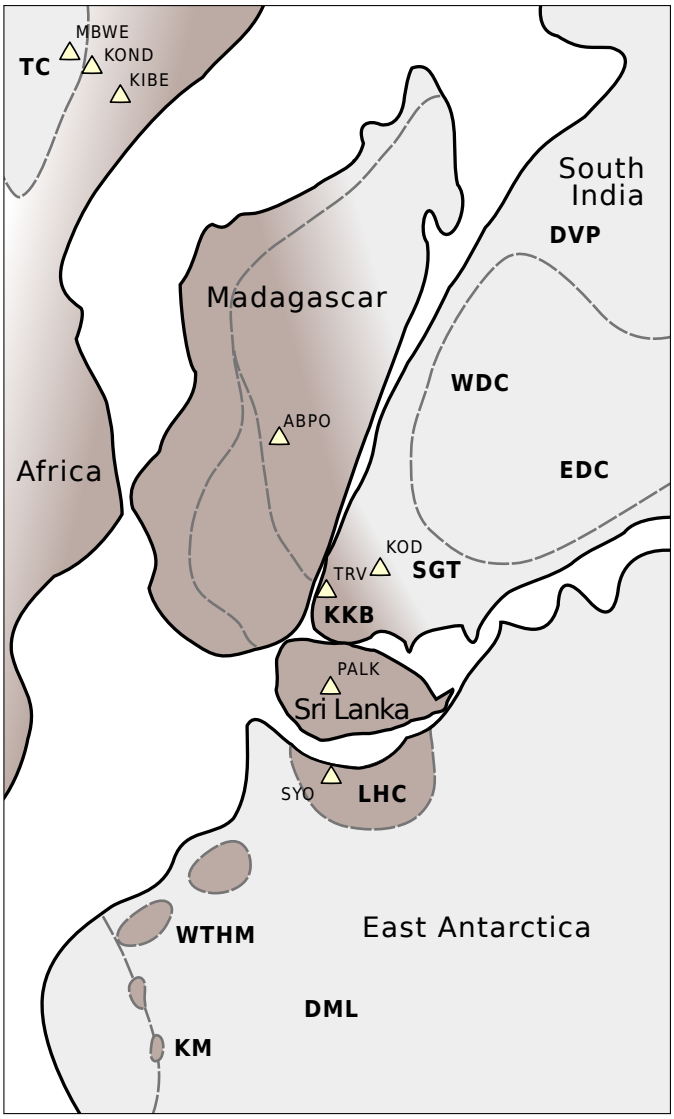

Figure 14: Reconstruction of Pan-African terranes before Gondwana break-up. Terranes include Mozambique-Tanzanian belt, Madagascar, southern India, Sri Lanka, and East Antarctica. Shaded areas represent regions affected by the Pan-African Orogeny. Marked are relevant tectonic regions and seismic stations (triangles). Dashed lines mark craton boundaries; for Madagascar dashed lines indicate basin, Proterozoic and Archean unit boundaries. TC: Tanzania Craton, DVP: Deccan Volcanic Province, WDC: West Dharwar Craton, EDC: East Dharwar Craton, SGT: Southern Granulite Terrain, KBB: Kerala Khondalite Belt, DML: Dronning Maud Land, WTHM: Wohlthat Massif, KM: Kottas Mountains, LHC: Lützow-Holm Complex at Lützow-Holm Bay (LHB). Map after Bayer et al. (2009); Das et al. (2019); Dissanayake and Chandrajith (1999).

Orogeny. The basin shows thin crust (23–31 km) with 4–10 km thick sedimentary deposits, and higher V_P/V_S ratios mostly between 1.8–1.85. The volcanic province shows crustal thicknesses of ∼30 km, generally lower V_S, mid-crustal low velocity zones at few stations, and high V_P/V_S ratios of 1.8–1.98, indicating a pervasive presence of mafic rocks.

Southern India: Das et al. (2019) highlighted seismic properties in multiple terrains of the southern Indian shield (Fig. 14). Crustal thicknesses are 34–52 km and vary significantly between provinces. Thereby, Archean terrains (WDC, SGT) and the Pan-African metamorphic terrain (KKB) show distinct differences: The Archean regions show thick crust (40–52 km) with a mafic layer underneath, and KBB shows a thin crust (34–38 km) with a more homogeneous and felsic composition. Mafic underplates with thicknesses of 4–18 km are observed in several terrains (KKB<5 km). The average crustal V_S for the terrains are between 3.65–3.9 km/s (KKB=3.75 km/s). Average surface V_S (at 2 km depth) for southern India is 3.2 km/s. The shallow mantle (down to 130 km depth) is stratified with V_S of 4.3–4.5 km/s for all terrains, except EDC.

Rai et al. (2013) found crustal thicknesses for southern India between 32–54 km, with shal-

lower Moho depths (32–38 km) in the EDC and KKB, and a deeper Moho discontinuity (38–54 km) within the other domains. V_P/V_S ratios for southern India range between 1.65–1.76 (see Rai et al., 2013, and references therein) and indicate a felsic to intermediate crustal composition, except for the mid-Archean block in the southern WDC (greenstone belt) with V_P/V_S >1.81, suggesting a mafic layer underneath. Some parts of southern India (e.g., EDC) show a flat Moho interface, which together with the felsic crustal composition could be caused by delamination of mafic lower crust. Also, as there is no correlation between topography and Moho depths, the crustal composition and lateral variation of density are interpreted to have a significant influence on regional topography and control isostatic uplift.

East Antarctica: Kanao et al. (2012) observed crustal thicknesses of 38–40 km at the LHB, which increase to 48–50 km towards the inland plateau. Bayer et al. (2009) observed crustal thicknesses of ∼42 km in the central DML (CDML) at the coast; beneath the WTHM and KM crustal thicknesses are 47–51 km and 44–52 km, respectively, both indicative of an orogenic root. The Moho discontinuity has a sharp nature. V_P/V_S ratios of ∼1.67 were found in CDML, and 1.72 in KM (Bayer et al., 2007). These low V_P/V_S ratios are predominantly found for quartz-rich, felsic bulk crustal compositions (Zandt and Ammon, 1995).

By analysis of the V_S-structure in azimuthal dependence around SYO, Kanao (1997) found average crustal V_S between 3.0–3.8 km/s and uppermost mantle V_S between 4.1–4.8 km/s. The large variations are caused by complex crust-to-mantle structures. For backazimuths directed towards the coast (210–360°, present-day), Moho depths of ∼35 km are observed with broad-transitional crust-to-mantle zone down to 45 km depth. Smooth gradual V_S increase with depth together with the broad transitional Moho may be associated with extensional stresses at Gondwana break-up. Backazimuths directed inland (50–160°, present-day) show a sharp Moho discontinuity at 36–38 km depth beneath thin-transitional lower crust. Different crustal V_S are recognized for regions of granulite facies (120–160°) and the granulite-amphibolite transitional zone (50–100°). These backazimuths show pattern of high-, low- and high-velocity lamination at surface, upper and middle crust, respectively. Lower crustal reflectivity (∼23–34 km depths) might be caused by multi-genetic features such as igneous intrusions, lithologic and metamorphic layering, mylonite zones, anastomosing shear zones, seismic anisotropy and fluid layers (Kanao, 1997, and references therein). The predominant cause for the reflectivity may be layered sequences of mafic and felsic rocks, the signals of which got enhanced through ductile stretching during the extensional period of Gondwana break-up.

Comparison to our studies: There are many similarities between the seismic properties found in Sri Lanka and other East Gondwanan terranes (Fig. 15). (Undisturbed) Moho depths for Sri Lanka are between 35.5–40 km, and fit to the crustal thicknesses of 37±0.8 km observed by Rai et al. (2009), 35–38 km in the Proterozoic domains of southern Madagascar, 32–38 km in KKB of southern India, and 38–40 km (LHB) and 35–38 km (SYO) in East Antarctica. Pan-African crust of all studies agree to average crustal V_P/V_S ratios on the lower side (1.65–1.78), as does Sri Lanka (1.66–1.73), indicating felsic to intermediate bulk crustal compositions.

Average crustal V_S for the KKB in southern India is 3.75 km/s, which is in line with our observations of 3.8±0.05 km/s for Sri Lanka. However, other regions in southern India show

similar values (e.g., 3.8 km/s for WDC-N and SGT; Das et al., 2019), but were not reworked during the Pan-African Orogeny. Sri Lanka shows relatively high surface V_S (3.1–3.6 with mean 3.4±0.1 km/s) compared to average values in southern Madagascar (3.2–3.4 km/s, this study; ∼3.3 km/s, Rindraharisaona et al., 2017), and southern India (3.2 km/s at 2 km depth), which might be due to different burial depths of surface rocks during the Pan-African Orogeny or a different petrological composition. Upper mantle V_S in Sri Lanka (4.3–4.7 km/s) show good agreement with general ranges of 4.3–4.5 km/s derived for southern India by Das et al. (2019). Our results represent averages down to 75 km depth, while Das et al. (2019) resolved the mantle structure down to a depth of 130 km.

Rai et al. (2013) explained uncorrelated crustal thicknesses and topography in southern India through effects of crustal composition and lateral variation of density, which we also considered for the northernmost part of Sri Lanka. A low velocity layer as we revealed in central Sri Lanka was also observed by Rai et al. (2009) in the upper crust of most Pan-African terranes and could have been generated by retrograde metamorphic processes and fluid migration during the transpressive regime. A mafic underplate as seen for some East Gondwanan domains is not observed in Sri Lanka.

The laminated crust observed in LHB, East Antarctica, with strong lower crustal reflectivity (∼23–34 km; Kanao, 1997) is interpreted as layered sequences of mafic and felsic rocks enhanced through ductile stretching during the extensional process of Gondwana's break-up. For Madagascar, we observe positive radial seismic anisotropy (horizontal structures) in the upper (<5 km) and lower crustal layers (>20 km), which we interpret for the lower crust as gravitational extension structures caused by crustal flow during orogenic collapse.

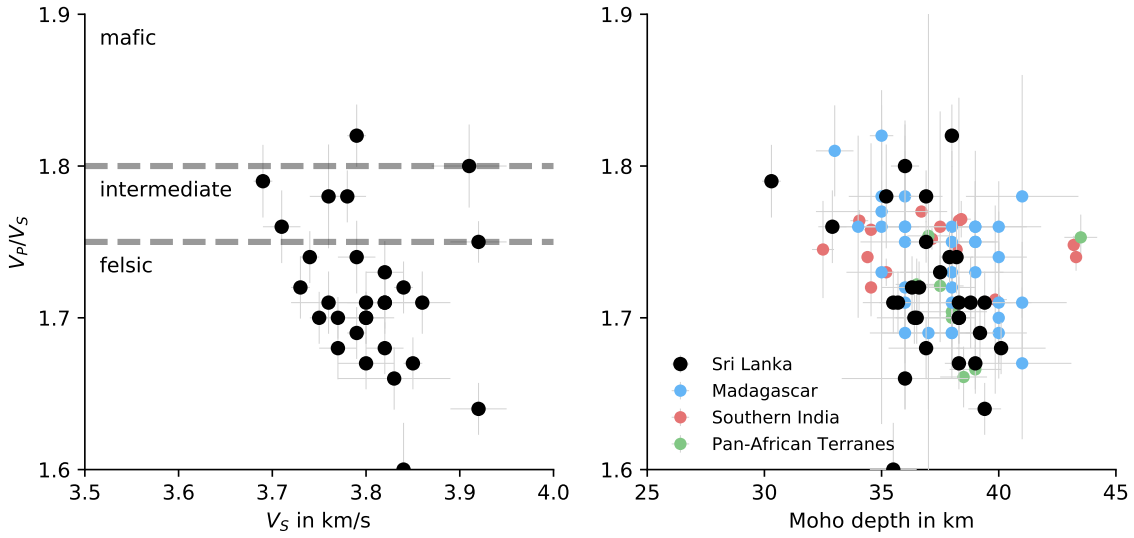

Figure 15: (left) Average crustal V_S and V_P/V_S ratios derived in Sri Lanka. Dashed lines indicate the bounds between felsic, intermediate and mafic rock compositions (Christensen, 1996). (right) Average crustal V_P/V_S and crustal thicknesses from our study compared to other Pan-African terranes. Estimates are from the Precambrian domains in southern Madagascar (blue; Rindraharisaona et al., 2017), KKB in southern India (red; Das et al., 2015; Rai et al., 2013), and from single stations in Africa, Madagascar, southern India, Sri Lanka and East Antarctica (green; Rai et al., 2009). Measurements are derived from $H\kappa$-stacking.

The strong similarities of seismic crustal properties between the Pan-African terranes might be attributed to region spanning unification of crustal structures through extensive common overprinting during the Pan-African Orogeny. Differences might be seen as consequence of autochtone terrane compositions, positions within the orogen, and individual reworking processes after the orogeny.

Summary

We determined radial seismic anisotropy (*RA*) in the crust in southern Madagascar. Radial anisotropy describes the velocity differences between V_{SV} and V_{SH}, which we derived by inversion of Rayleigh and Love surface waves dispersion. The amalgamated Precambrian units in the east and the Phanerozoic Morondava basin in the west of southern Madagascar were shaped by different geodynamic processes. The crystalline basement was strongly deformed and experienced metamorphosis to varying degrees during the assembly of Gondwana and the Pan-African Orogeny, whereas the Morondava basin was formed post-collisional with the separation of Africa and Madagascar. These different developments are reflected in first order differences in the radial anisotropy structure of the crust.

Positive *RA* (horizontal structures) is predominantly associated with an extensional regime which was likely responsible for (1) horizontal crustal stretching, thinning and sedimentary layering in the Morondava basin, and (2) shallowly dipping layering and imbricated nappe stacks in the upper crust, and gravitational extension structures through crustal flow during syn- or post-orogenic collapse in the deep crust of the Precambrian domains. Negative *RA* (vertical structures) we interpret to originate from magmatic dike intrusions and steep normal faults in the upper Morondava basin, and strongly vertical folded fabrics and fossilized late Pan-African shear zones in the mid-crust of the Precambrian domains.

We imaged the crustal velocity structure in Sri Lanka through joint inversion of surface wave dispersion and receiver functions. Vertical and lateral changes of seismic velocity indicate differences of density or rock composition and can reveal discontinuities, such as the crust-mantle boundary. For Sri Lanka, the Moho interface depth is between 30–40 km, with the thickest crust (38–40 km) beneath the central Highland Complex. The thinnest crust (30–35 km) is along the west coast, which experienced crustal thinning during the formation of the Mannar basin. The majority of V_P/V_S ratios are between 1.66–1.73 and predominantly favor a felsic composition with intermediate to high silica content of the crust.

A major intra-crustal (18–27 km), westward dipping (∼4°) interface with high V_S (∼4 km/s) underneath is prominent in the central Highland Complex, and continues to the eastern Vijayan Complex. The dipping discontinuity and a low velocity zone in the central Highlands can be related to the HC/VC contact zone and is in agreement with the well-established amalgamation theory of a stepwise collision of the arc fragments (Kehelpannala, 2004; Kleinschrodt, 1994), including deep crustal thrusting processes and a transpressional regime along the eastern suture between HC and VC.

We found striking similarities of seismic properties between southern Madagascar and Sri Lanka, and southern India and East Antarctica as once juxtaposed Pan-African terranes. Crustal thicknesses range between 35–40 km in regions with little to no influence of post-orogenic processes such as rifting or younger orogeny (Fig. 16). Pan-African crust of all comparison studies agree to average crustal V_P/V_S ratios on the lower side (1.65–1.78), indicating felsic to intermediate bulk crustal compositions. Sri Lanka shows higher surface V_S (3.1–3.6 km/s) compared to average values in southern Madagascar (3.2–3.4 km/s) and southern India (3.2 km/s), which might be due to different burial depths and metamorphic grade of surface rocks during the Pan-African Orogeny, or different petrological compositions. A low velocity layer in the upper crust as revealed in central Sri Lanka was observed by Rai et al. (2009) for most Pan-African terranes and possibly was generated through retrograde metamorphic processes and fluid migration during the transpressive regime. The strong similarities of seismic crustal properties between these regions might be attributed to the region spanning unification of crustal structures through extensive common overprinting during the Pan-African Orogeny. Differences might be seen as consequence of autochtone terrane compositions, positions within the orogen, and individual reworking processes after the orogeny.

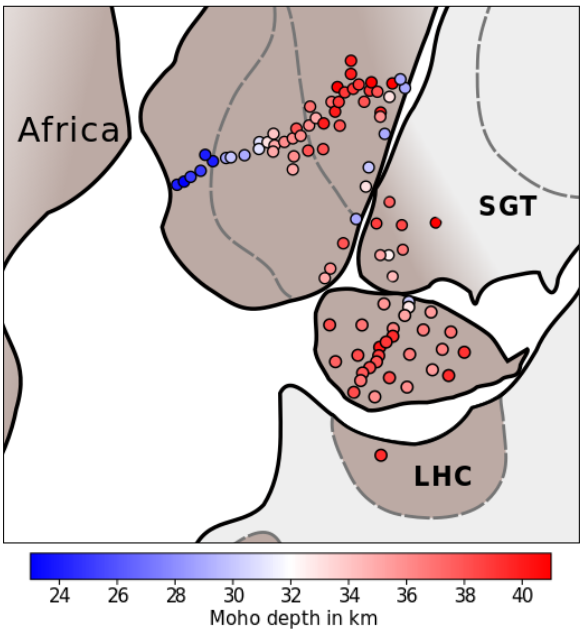

Figure 16: Reconstruction of Pan-African terranes before Gondwana break-up. Illustrated are present-day crustal thicknesses at seismic stations (symbols) in Sri Lanka (this study), southern Madagascar (Rindraharisaona et al., 2017), southern India (Rai et al., 2013) and East Antarctica (Kanao et al., 2012). Station locations are approximations. The shallow Moho depths (<30 km) beneath the Morondava basin in Madagascar are of post-collisional origin. (See Figure 14 for reference.)

Outlook and lessons learned

Especially for the early research in Madagascar I would liked to have known more about the principles of Bayes and Bayesian inversion. Starting with the tomography, but more relevant the velocity-depth inversion. Thereby, meaningful uncertainties for V_{SV} and V_{SH} could have been quantified and used, to better define the significance of the difference in V_{SV} and V_{SH}, and thus the significance and uncertainty of radial anisotropy. A Bayesian inversion directly for radial anisotropy and its uncertainty by jointly inverting Rayleigh and Love surface wave dispersion, might have been a favored solution. Another advantage of the Bayesian approach, as implemented in BayHunter, is the reduction of the influence of the starting model parametrization. We verified that the effect of the starting model on our inversion results is minor, however, we

did not compare different parameterizations with, e.g., a different number of layers. The advantage of solving for the number of layers and their thicknesses is thereby, that this approach is data-driven, and unconstrained by the user. When only inverting surface wave dispersion curves, the trade-off between velocity and interface depth is large and the models that fit the data are diverse, however, the trade-off is reflected in the uncertainty estimation. Our inversion results are robust as confirmed by several tests, but using a Bayesian approach for the inversion of the velocity-depth and radial anisotropy structure could have delivered a better estimation of uncertainties and placement of the results.

The inclusion of long period surface wave dispersion (from earthquakes) in the velocity-depth inversion increases the depth resolution and could provide valuable information about anisotropic features in the upper mantle. Radial anisotropy seems so far an unrevealed seismic property in the crust of other Pan-African terranes, and no direct measurements were available to compare our results to. This property could be determined, e.g., for Sri Lanka.

The new seismic data recorded by the temporary network in Sri Lanka was a chance to image the variation of the crustal structure beneath the island and to set a foundation for future studies not only based on seismic data. Potentially, gravity modeling is a good method to verify our determined Moho interface depths.

Last but not least, the development of BayHunter turned out to be one of my favorite projects. The development helped me to understand the workings of Bayesian inference and inversion and how our results are assembled, logically over the course of randomness. It also taught me that to provide open-source software/code is accompanied by large responsibility. The code was created most flexible to be able to incorporate additional data sets besides surface wave dispersion and receiver functions. (Radial) anisotropy could be implemented as an additional parameter to solve for.

Bibliography

Aki, K. Space and time spectra of stationary stochastic waves, with special reference to microtremors. *Bulletin of the Earthquake Research Institute, University Tokyo*, pages 415–456, 1957.

Aki, K. and Richards, P. G. *Quantitative seismology.* University Science Books, Sausalito, California, 2nd edition, 2002. ISBN 978-0-935702-96-5.

Altindag, R. Correlation between P-wave velocity and some mechanical properties for sedimentary rocks. *The Journal of The Southern African Institute of Mining and Metallurgy*, 112: 229–237, 2012.

Amante, C. and Eakins, B. W. ETOPO1 - 1 arc-minute global relief model: procedures, data sources and analysis. Technical report, National Oceanic and Atmospheric Administration. Technical Memorandum, 2009.

Anderson, D. L. Elastic wave propagation in layered anisotropic media. *Journal of Geophysical Research*, 66(9):2953–2963, 1961. doi: 10.1029/JZ066i009p02953.

Anderson, D. L. *New theory of the Earth.* Cambridge University Press, Cambridge, UK; New York, 2007. ISBN 978-0-521-84959-3. OCLC: ocm69020892.

Andriampenomanana, F., Nyblade, A. A., Wysession, M. E., Durrheim, R. J., Tilmann, F., Julià, J., Pratt, M. J., Rambolamanana, G., Aleqabi, G., Shore, P. J., and Rakotondraibe, T. The structure of the crust and uppermost mantle beneath Madagascar. *Geophysical Journal International*, 210(3):1525–1544, 2017. doi: 10.1093/gji/ggx243.

Bardintzeff, J.-M., Liégeois, J.-P., Bonin, B., Bellon, H., and Rasamimanana, G. Madagascar volcanic provinces linked to the Gondwana break-up: Geochemical and isotopic evidences for contrasting mantle sources. *Gondwana Research*, 2010.

Barruol, G., Sigloch, K., and RHUM-RUM group. RHUM-RUM experiment, 2011-2015, code YV (Réunion Hotspot and Upper Mantle – Réunion's Unterer Mantel) funded by ANR, DFG, CNRS-INSU, IPEV, TAAF, instrumented by DEPAS, INSU-OBS, AWI and the Universities of Muenster, Bonn, La Réunion. 2017. doi: 10.15778/RESIF.YV2011.

Bayer, B., Müller, C., Geissler, W., Eaton, D., Eckstaller, A., and Jokat, W. Crust and upper mantle in Dronning Maud Land, Antarctica, retrieved from shear-wave splitting, receiver functions, seismic refraction and 3-D gravity modelling. *in Antarctica: A Keystone in a Changing World - Online Proceedings of the 10 th ISAES X, edited by A. K. Cooper and C. R. Raymond et al., USGS Open-File Report 2007-1047, Extended Abstract 036, 3 p.*, 2007.

Bayer, B., Geissler, W. H., Eckstaller, A., and Jokat, W. Seismic imaging of the crust beneath Dronning Maud Land, East Antarctica. *Geophysical Journal International*, 178(2):860–876, 2009. doi: 10.1111/j.1365-246X.2009.04196.x.

Bayes, T. An Essay Towards Solving a Problem in the Doctrine of Chances. By the late Rev. Mr. Bayes, F. R. S. communicated by Mr. Price, in a letter to John Canton, A. M. F. R. S. 1763. doi: 10.1098/rstl.1763.0053.

Bensen, G. D., Ritzwoller, M. H., Barmin, M. P., Levshin, A. L., Lin, F., Moschetti, M. P., Shapiro, N. M., and Yang, Y. Processing seismic ambient noise data to obtain reliable broad-band surface wave dispersion measurements. *Geophysical Journal International*, 169(3):1239–1260, 2007. doi: 10.1111/j.1365-246X.2007.03374.x.

Berteussen, K.-A. Moho depth determinations based on spectral-ratio analysis of NORSAR long-period P waves. *Physics of the Earth and Planetary Interiors*, 15(1):13–27, 1977. doi: 10.1016/0031-9201(77)90006-1.

Bodin, T. *Transdimensional Approaches to Geophysical Inverse Problems*. PhD thesis, The Australian National University, 2010.

Bodin, T., Sambridge, M., Tkalčić, H., Arroucau, P., Gallagher, K., and Rawlinson, N. Transdimensional inversion of receiver functions and surface wave dispersion. *Journal of Geophysical Research: Solid Earth*, 117(B2):B02301, 2012. doi: 10.1029/2011JB008560.

Boger, S. D., Ferreira, C., Hirdes, W., Schulte, B., Jenett, T., and Dallwig, R. Carte geologique de Madagascar 1: 500 000, feuilles No 7 - Morondava, 2008a.

Boger, S. D., Ferreira, C., Hirdes, W., Schulte, B., Jenett, T., and Dallwig, R. Carte geologique de Madagascar 1: 500 000, feuilles No 11 - Ampanihy, 12-Tôlanaro, 2008b.

Boger, S. D., Ferreira, C., Hirdes, W., Schulte, B., Jenett, T., and Dallwig, R. Carte geologique de Madagascar 1: 500 000, feuilles No 10 - Fianarantsoa, 2008c.

Boger, S. D., Hirdes, W., Ferreira, C. A. M., Schulte, B., Jenett, T., and Fanning, C. M. From passive margin to volcano–sedimentary forearc: The Tonian to Cryogenian evolution of the Anosyen Domain of southeastern Madagascar. *Precambrian Research*, 247:159–186, 2014. doi: 10.1016/j.precamres.2014.04.004.

Boger, S. D., Hirdes, W., Ferreira, C. A. M., Jenett, T., Dallwig, R., and Fanning, C. M. The 580-520 Ma Gondwana suture of Madagascar and its continuation into Antarctica and Africa. *Gondwana Research*, 28(3):1048–1060, 2015. doi: 10.1016/j.gr.2014.08.017.

Bormann, P. and Wielandt, E. Seismic Signals and Noise. *New Manual of Seismological Observatory Practice 2 (NMSOP2)*, 2013. doi: 10.2312/gfz.nmsop-2_ch4.

Bormann, P., Storchak, D. A., and Schweitzer, J. The IASPEI standard nomenclature of seismic phases. *New Manual of Seismological Observatory Practice 2 (NMSOP2)*, 2013a. doi: 10.2312/gfz.nmsop-2_is_2.1.

Bormann, P., Wendt, S., and DiGiacomo, D. Seismic Sources and Source Parameters. *New Manual of Seismological Observatory Practice 2 (NMSOP2)*, 2013b. doi: 10.2312/gfz.nmsop-2_ch3.

Boschi, L., Weemstra, C., Verbeke, J., Ekström, G., Zunino, A., and Giardini, D. On measuring surface wave phase velocity from station–station cross-correlation of ambient signal. *Geophysical Journal International*, 2012.

Bostock, M. G. Mantle stratigraphy and evolution of the Slave province. *Journal of Geophysical Research: Solid Earth*, 103(B9):21183–21200, 1998. doi: 10.1029/98JB01069.

Chen, Y., Badal, J., and Zhang, Z. Radial anisotropy in the crust and upper mantle beneath the Qinghai-Tibet Plateau and surrounding regions. *Journal of Asian Earth Sciences*, 36(4-5): 289–302, 2009. doi: 10.1016/j.jseaes.2009.06.011.

Christensen, N. I. Poisson's ratio and crustal seismology. *Journal of Geophysical Research: Solid Earth*, 101(B2):3139–3156, 1996. doi: 10.1029/95JB03446.

Coffin, M. and Rabinowitz, P. Evolution of the conjugate East African - Madagascan margins and the Western Somali Basin. *Special Paper of the Geological Society of America*, 1988.

Collins, A., Razakamanana, T., and Windley, B. Neoproterozoic extensional detachment in central Madagascar: implications for the collapse of the East African Orogen. *Geological Magazine*, 137(01):39–51, 2000.

Cooray, P. G. The precambrian of Sri Lanka: a historical review. *Precambrian Research*, 66(1): 3–18, 1994. doi: 10.1016/0301-9268(94)90041-8.

Cotte, N. and Laske, G. Testing group velocity maps for Eurasia. *Geophysical Journal International*, 150(3):639–650, 2002.

Das, R., Saikia, U., and Rai, S. The deep geology of South India inferred from Moho depth and Vp/Vs ratio. *Geophysical Journal International*, 203(2):910–926, 2015. doi: 10.1093/gji/ggv351.

Das, R., Ashish, and Saha, G. K. Crust and shallow mantle structure of south India by inverting interpolated receiver function with surface wave dispersion. *Journal of Asian Earth Sciences*, 2019.

de Wit, M. J., Bowring, S. A., Ashwal, L. D., Randrianasolo, L. G., Morel, V. P. I., and Rambeloson, R. A. Age and tectonic evolution of Neoproterozoic ductile shear zones in southwestern Madagascar, with implications for Gondwana studies. *Tectonics*, 20(1):1–45, 2001. doi: 10.1029/2000TC900026.

Dissanayake, C. B. and Chandrajith, R. Sri Lanka-Madagasca Gondwana Linkage: Evidence for a Pan-African Mineral Belt. *The Journal of Geology*, 107(2):223–235, 1999. doi: 10.1086/314342.

Dreiling, J. and Tilmann, F. BayHunter - McMC transdimensional Bayesian inversion of receiver functions and surface wave dispersion. *GFZ Data Services*, 2019. doi: 10.5880/GFZ.2.4.2019.001.

Dreiling, J., Tilmann, F., Yuan, X., Giese, J., Rindraharisaona, E. J., Rümpker, G., and Wysession, M. E. Crustal radial anisotropy and linkage to geodynamic processes: A study based on seismic ambient noise in southern Madagascar. *Journal of Geophysical Research: Solid Earth*, 2018. doi: 10.1029/2017JB015273.

Dreiling, J., Tilmann, F., Yuan, X., Haberland, C., and Seneviratne, S. Crustal structure of Sri Lanka derived from joint inversion of surface wave dispersion and receiver functions using a Bayesian approach. *Journal of Geophysical Research: Solid Earth (submission in 2019)*, n.a.

Duret, F., Shapiro, N. M., Cao, Z., Levin, V., Molnar, P., and Roecker, S. Surface wave dispersion across Tibet: Direct evidence for radial anisotropy in the crust. *Geophysical Research Letters*, 37(16), 2010. doi: 10.1029/2010GL043811.

Dziewonski, A., Bloch, S., and Landisman, M. A technique for the analysis of transient seismic signals. *Bulletin of the Seismological Society of America*, 1969.

Eaton, D., Milkereit, B., and Salisbury, M. *Hardrock Seismic Exploration*. Geophysical development series. Society of Exploration Geophysicists, 2003. ISBN 978-1-56080-114-6.

Ekström, G., Abers, G. A., and Webb, S. C. Determination of surface-wave phase velocities across USArray from noise and Aki's spectral formulation. *Geophysical Research Letters*, 36 (18), 2009. doi: 10.1029/2009GL039131.

Emmel, B., Jöns, N., Kröner, A., Jacobs, J., Wartho, J., Schenk, V., Razakamanana, T., and Austegard, A. From Closure of the Mozambique Ocean to Gondwana Breakup: New Evidence from Geochronological Data of the Vohibory Terrane, Southwest Madagascar. *The Journal of Geology*, 116(1):21–38, 2008. doi: 10.1086/524121.

Fitzsimons, I. C. W. Pan–African granulites of Madagascar and southern India: Gondwana assembly and parallels with modern Tibet. *Journal of Mineralogical and Petrological Sciences*, 111(2):73–88, 2016. doi: 10.2465/jmps.151117.

Fritz, H., Abdelsalam, M., Ali, K., Bingen, B., Collins, A., Fowler, A., Ghebreab, W., Hauzenberger, C., Johnson, P., Kusky, T., Macey, P., Muhongo, S., Stern, R., and Viola, G. Orogen styles in the East African Orogen: A review of the Neoproterozoic to Cambrian tectonic evolution. *Journal of African Earth Sciences*, 86:65–106, 2013. doi: 10.1016/j.jafrearsci.2013.06.004.

GAF-BGR. Carte structurale de Madagascar 1:500 000, 2008.

Geiger, M., Clark, D. N., and Mette, W. Reappraisal of the timing of the breakup of Gondwana based on sedimentological and seismic evidence from the Morondava Basin, Madagascar. *Journal of African Earth Sciences*, 38(4):363–381, 2004. doi: 10.1016/j.jafrearsci.2004.02.003.

GEOFON. GEOFON Data Centre. GEOFON Seismic Network. Deutsches GeoForschungsZentrum GFZ. Other/Seismic Network. 1993. doi: 10.14470/TR560404.

GEOSCOPE. French Global Network of broadband seismic stations. *Institut de Physique du Globe de Paris & Ecole et Observatoire des Sciences de la Terre de Strasbourg (EOST)*, 1982. doi: 10.18715/GEOSCOPE.G.

Gibbons, A. D., Whittaker, J. M., and Müller, R. D. The breakup of East Gondwana: Assimilating constraints from Cretaceous ocean basins around India into a best-fit tectonic model. *Journal of Geophysical Research: Solid Earth*, 118(3):808–822, 2013. doi: 10.1002/jgrb.50079.

Giese, J., Berger, A., Schreurs, G., and Gnos, E. The timing of the tectono-metamorphic evolution at the Neoproterozoic–Phanerozoic boundary in central southern Madagascar. *Precambrian Research*, 185(3–4):131–148, 2011. doi: 10.1016/j.precamres.2011.01.002.

Giese, J., Schreurs, G., Berger, A., and Herwegh, M. Kinematics and significance of a poly-deformed crustal-scale shear zone in central to south-eastern Madagascar: the Itremo–Ikalamavony thrust. *International Journal of Earth Sciences*, 106(6):2091–2108, 2017. doi: 10.1007/s00531-016-1415-z.

Gray, D. R., Foster, D., Meert, J. G., Goscombe, B., Armstrong, R., Trouw, R., and Passchier, C. A Damara orogen perspective on the assembly of Southwestern Gondwana. *Geological Society, London, Special Publications*, 2008. doi: 10.1144/SP294.14.

Guo, Z., Gao, X., Wang, W., and Yao, Z. Upper- and mid-crustal radial anisotropy beneath the central Himalaya and southern Tibet from seismic ambient noise tomography. *Geophysical Journal International*, 189(2):1169–1182, 2012. doi: 10.1111/j.1365-246X.2012.05425.x.

Haney, M. M., Mikesell, T. D., van Wijk, K., and Nakahara, H. Extension of the spatial autocorrelation (SPAC) method to mixed-component correlations of surface waves: Mixed-component correlations in SPAC. *Geophysical Journal International*, 191(1):189–206, 2012. doi: 10.1111/j.1365-246X.2012.05597.x.

Harmon, N., Forsyth, D., and Webb, S. Using Ambient Seismic Noise to Determine Short-Period Phase Velocities and Shallow Shear Velocities in Young Oceanic Lithosphere. *Bulletin of the Seismological Society of America*, 97(6):2009–2023, 2007. doi: 10.1785/0120070050.

Herrmann, R. B. Computer Programs in Seismology: An Evolving Tool for Instruction and Research. *Seismological Research Letters*, 84(6):1081–1088, 2013. doi: 10.1785/0220110096.

Herrmann, R. B. and Ammon, C. J. Computer Programs in Seismology: Surface waves, receiver functions and crustal structure, 2002.

Horton, F., Hacker, B., Kylander-Clark, A., Holder, R., and Jöns, N. Focused radiogenic heating of middle crust caused ultrahigh temperatures in southern Madagascar. *Tectonics*, 35(2):293–314, 2016. doi: 10.1002/2015TC004040.

Hu, X., Garzanti, E., Wang, J., Huang, W., An, W., and Webb, A. The timing of India-Asia collision onset – Facts, theories, controversies. *Earth-Science Reviews*, 160:264–299, 2016. doi: 10.1016/j.earscirev.2016.07.014.

Huang, H. *Ambient noise tomography for wavespeed and anisotropy in the crust of southwestern China*. PhD thesis, Massachusetts Institute of Technology, 2014.

Huang, Y., Chubakov, V., Mantovani, F., Rudnick, R. L., and McDonough, W. F. A reference Earth model for the heat-producing elements and associated geoneutrino flux. *Geochemistry, Geophysics, Geosystems*, (6):2003–2029, 2013. doi: doi:10.1002/ggge.20129.

Jaxybulatov, K., Shapiro, N. M., Koulakov, I., Mordret, A., Landes, M., and Sens-Schönfelder, C. A large magmatic sill complex beneath the Toba caldera. *Science*, 346(6209):617–619, 2014. doi: 10.1126/science.1258582.

Jokat, W., Boebel, T., König, M., and Meyer, U. Timing and geometry of early Gondwana breakup. *Journal of Geophysical Research: Solid Earth*, 108(B9), 2003. doi: 10.1029/2002JB001802.

Jöns, N. and Schenk, V. The ultrahigh temperature granulites of southern Madagascar in a polymetamorphic context: implications for the amalgamation of the Gondwana supercontinent. *European Journal of Mineralogy*, 23(2):127–156, 2011. doi: 10.1127/0935-1221/2011/0023-2087.

Kanao, M. Variations in the crustal structure of the Lützow–Holm Bay region, East Antarctica using shear wave velocity. *Tectonophysics*, 270(1):43–72, 1997. doi: 10.1016/S0040-1951(96)00207-7.

Kanao, M., Hansen, S. E., Kamiyama, K., Wiens, D., Higashi, T., Nyblade, A. A., and Watanabe, A. Crustal structure from the Lützow-Holm Bay to the inland plateau of East Antarctica, based on onshore gravity surveys and broadband seismic deployments. *Tectonophysics*, 572-573:100–110, 2012. doi: 10.1016/j.tecto.2012.01.014.

Kanasewich, E. *Time sequence analysis in geophysics*. Canadian electronic library: Books collection, University of Alberta Press, 1981. ISBN 978-0-88864-074-1.

Karato, S.-i. and Wu, P. Rheology of the upper mantle: A synthesis. *Science*, 260, 1993.

Kayal, J. J. Seismic waves and earthquake location, 2006.

Kearey, P., Brooks, M., and Hill, I. *An introduction to geophysical exploration*. Blackwell Science, Malden, MA, 3rd edition, 2002. ISBN 978-0-632-04929-5.

Kehelpannala, K. . V. W. Deformation of a High-Grade Gondwana Fragment, Sri Lanka. *Gondwana Research*, 1(1):47–68, 1997. doi: 10.1016/S1342-937X(05)70005-8.

Kehelpannala, K. V. W. Structural evolution of the middle to lower crust in Sri Lanka - a review. *Journal of the Geological Society of Sri Lanka*, 11, 2003.

Kehelpannala, K. V. W. Arc Accretion Around Sri Lanka During the Assembly of Gondwana. *Gondwana Research*, 7(4):7, 2004.

Kind, R. and Yuan, X. Seismic, Receiver Function Technique. In Gupta, H. K., editor, *Encyclopedia of Solid Earth Geophysics*, pages 1258–1269. Springer Netherlands, Dordrecht, 2011. ISBN 978-90-481-8701-0. doi: 10.1007/978-90-481-8702-7_12.

Kitamura, K. Constraint of lattice-preferred orientation (LPO) on *Vp* anisotropy of amphibole-rich rocks. *Geophysical Journal International*, 165(3):1058–1065, 2006. doi: 10.1111/j.1365-246X.2006.02961.x.

Kleinschrodt, R. Large-scale thrusting in the lower crustal basement of Sri Lanka. *Precambrian Research*, 66(1-4):39–57, 1994.

Kleinschrodt, R. Strain localization and large-scale block rotation in the lower continental crust, Kataragama area, Sri Lanka. *Terra Nova*, 8(3):236–244, 1996. doi: 10.1111/j.1365-3121.1996.tb00752.x.

Kriegsman, L. M. Evidence for a fold nappe in the high-grade basement of central Sri Lanka: Terrane assembly in the Pan-African lower crust? *Precambrian Research*, 66(1-4):59–76, 1994. doi: 10.1016/0301-9268(94)90044-2.

Kröner, A. and Brown, L. Structure, composition and evolution of the south Indian and Sri Lankan granulite terrains from deep seismic profiling and other geophysical and geological investigations: A LEGENDS initiative. *Gondwana Research*, 8(3):317–335, 2005.

Kularathna, E., Pitawala, H., Senaratne, A., Senevirathne, B., and Weerasinghe, D. Forced-fold structures in the Mannar Basin, Sri Lanka: Modes of occurrence, development mechanism and contribution for the petroleum system. *Journal of the National Science Foundation of Sri Lanka*, 17:12, 2015.

Kumar, V. P., Prakasam, K. S., Rai, S. S., and Gupta, S. Upper-mantle anisotropy beneath the south Indian Shield: Influenced by ancient and recent Earth processes. *Lithosphere*, 7(2):108–116, 2015. doi: 10.1130/L405.1.

LaBrecque, J. L. and Barker, P. The age of the Weddell Basin. *Nature*, 290(5806):489–492, 1981. doi: 10.1038/290489a0.

Langston, C. A. Structure under Mount Rainier, Washington, inferred from teleseismic body waves. *Journal of Geophysical Research*, 84(B9):4749, 1979. doi: 10.1029/JB084iB09p04749.

Lardeaux, J.-M., Martelat, J.-E., Nicollet, C., Pili, E., Rakotondrazafy, R., and Cardon, H. Metamorphism and tectonics in southern Madagascar: an overview. *Gondwana Research*, 2 (3):355–362, 1999.

Lawver, L., Royer, J., Sandwell, D., and Scotese, C. Evolution of the Antarctic Continental Margins. *Geological evolution of Antarctica. Proceedings of the Fifth International Symposium on Antarctic Earth Sciences, Cambridge, 1987, Cambridge University Press*, pages 533–539, 1991.

Lin, F.-C., Moschetti, M. P., and Ritzwoller, M. H. Surface wave tomography of the western United States from ambient seismic noise: Rayleigh and Love wave phase velocity maps. *Geophysical Journal International*, 173(1):281–298, 2008. doi: 10.1111/j.1365-246X.2008.03720.x.

Love, A. The mathematical theory of elasticity. 1927.

Lowrie, W. *Fundamentals of geophysics*. Cambridge University Press, Cambridge; New York, 2nd edition, 2007. ISBN 978-0-521-85902-8. OCLC: ocn124025605.

Lubarda, V. and Chen, M. On the elastic moduli and compliances of transversely isotropic and orthotropic materials. *Journal of Mechanics of Materials and Structures*, 3(1):153–171, 2008. doi: 10.2140/jomms.2008.3.153.

Luo, Y., Xu, Y., and Yang, Y. Crustal radial anisotropy beneath the Dabie orogenic belt from ambient noise tomography. *Geophysical Journal International*, 195(2):1149–1164, 2013. doi: 10.1093/gji/ggt281.

Mahalanobis, P. C. On the generalized distance in statistics. 1936.

Martelat, J.-E., Lardeaux, J.-M., Nicollet, C., and Rakotondrazafy, R. Strain pattern and late Precambrian deformation history in southern Madagascar. *Precambrian Research*, 102(1–2): 1–20, 2000. doi: 10.1016/S0301-9268(99)00083-2.

Martelat, J.-E., Randrianasolo, B., Schulmann, K., Lardeaux, J.-M., and Devidal, J.-L. Airborne magnetic data compared to petrology of crustal scale shear zones from southern Madagascar: A tool for deciphering magma and fluid transfer in orogenic crust. *Journal of African Earth Sciences*, 94:74–85, 2014. doi: 10.1016/j.jafrearsci.2013.07.003.

Meert, J. G. A synopsis of events related to the assembly of eastern Gondwana. *Tectonophysics*, 362(1):1–40, 2003. doi: 10.1016/S0040-1951(02)00629-7.

Meert, J. G. and Lieberman, B. S. The Neoproterozoic assembly of Gondwana and its relationship to the Ediacaran–Cambrian radiation. *Gondwana Research*, 14(1-2):5–21, 2008. doi: 10.1016/j.gr.2007.06.007.

Meert, J. G. and Van der Voo, R. The assembly of Gondwana 800–550 Ma. *Journal of Geodynamics*, 1997.

Mishra, D. C., Vijaya Kumar, V., and Rajasekhar, R. P. Analysis of airborne magnetic and gravity anomalies of peninsular shield, India integrated with seismic and magnetotelluric results and gravity anomalies of Madagascar, Sri Lanka and East Antarctica. *Gondwana Research*, 10(1-2):6–17, 2006. doi: 10.1016/j.gr.2005.11.014.

Musacchio, G., Mooney, W. D., Luetgert, J. H., and Christensen, N. I. Composition of the crust in the Grenville and Appalachian Provinces of North America inferred from Vp/Vs ratios. *Journal of Geophysical Research*, 102, 1997.

Müller, G. Theory of elastic waves. Scientific Technical Report STR 07/03. *GeoForschungsZentrum Potsdam*, 2007. doi: 10.2312/GFZ.b103-07037.

Nishizawa, O. and Yoshino, T. Seismic velocity anisotropy in mica-rich rocks: an inclusion model. *Geophysical Journal International*, 145(1):19–32, 2001. doi: 10.1111/j.1365-246X.2001.00331.x.

Pathak, A., Ravi Kumar, M., and Sarkar, D. Seismic structure of Sri Lanka using receiver function analysis: A comparison with other high-grade Gondwana terrains. *Gondwana Research*, 10(1):198–202, 2006. doi: 10.1016/j.gr.2005.10.006.

Peterson, J. Observations and modeling of seismic background noise. Open-file Report 93-322, U.S. Department of Interior Geological Survey, 1993.

Pratt, M. J., Wysession, M. E., Aleqabi, G., Wiens, D. A., Nyblade, A. A., Shore, P., Rambolamanana, G., Andriampenomanana, F., Rakotondraibe, T., Tucker, R. D., Barruol, G., and Rindraharisaona, E. J. Shear velocity structure of the crust and upper mantle of Madagascar derived from surface wave tomography. *Earth and Planetary Science Letters*, 458:405–417, 2017. doi: 10.1016/j.epsl.2016.10.041.

Prieto, G. A., Lawrence, J. F., and Beroza, G. C. Anelastic Earth structure from the coherency of the ambient seismic field. *Journal of Geophysical Research*, 114(B7), 2009. doi: 10.1029/2008JB006067.

Rabbel, W., Siegesmund, S., Weiss, T., Pohl, M., and Bohlen, T. Shear wave anisotropy of laminated lower crust beneath Urach (SW Germany): a comparison with xenoliths and with exposed lower crustal sections. *Tectonophysics*, 298(4):337–356, 1998. doi: 10.1016/S0040-1951(98)00174-7.

Rai, A., Gaur, V. K., Rai, S. S., and Priestley, K. Seismic signatures of the Pan-African orogeny: implications for southern Indian high-grade terranes. *Geophysical Journal International*, 176 (2):518–528, 2009. doi: 10.1111/j.1365-246X.2008.03965.x.

Rai, S. S., Borah, K., Das, R., Gupta, S., Srivastava, S., Prakasam, K. S., Sivaram, K., Kumar, S., and Meena, R. The South India Precambrian crust and shallow lithospheric mantle: Initial results from the India Deep Earth Imaging Experiment (INDEX). *Journal of Earth System Science*, 122(6):1435–1453, 2013. doi: 10.1007/s12040-013-0357-0.

Rambolamanana, G., Suhadolc, P., and Panza, G. F. Simultaneous inversion of hypocentral parameters and structure velocity of the central region of Madagascar as a premise for the mitigation of seismic hazard in Antananarivo. *Pure and Applied Geophysics*, 149(4):707–730, 1997.

Ramirez, C., Nyblade, A., Wysession, M. E., Pratt, M., Andriampenomanana, F., and Rakotondraibe, T. Complex seismic anisotropy in Madagascar revealed by shear-wave splitting measurements. *Geophysical Journal International*, 2018. doi: 10.1093/gji/ggy367.

Rawlinson, N. FMST: Fast Marching Surface Tomography Package - Instructions, 2005.

Rawlinson, N. and Sambridge, M. The fast marching method: an effective tool for tomographic imaging and tracking multiple phases in complex layered media. *Exploration Geophysics*, 36 (4):341, 2005. doi: 10.1071/EG05341.

Reiss, M. C., Rümpker, G., Tilmann, F., Yuan, X., Giese, J., and Rindraharisaona, E. J. Seismic anisotropy of the lithosphere and asthenosphere beneath southern Madagascar from

teleseismic shear wave splitting analysis and waveform modeling. *Journal of Geophysical Research: Solid Earth*, 121(9), 2016. doi: 10.1002/2016JB013020.

Rey, P., Vanderhaeghe, O., and Teyssier, C. Gravitational collapse of the continental crust: definition, regimes and modes. *Tectonophysics*, 342(3):435–449, 2001.

Rindraharisaona, E. J., Guidarelli, M., Aoudia, A., and Rambolamanana, G. Earth structure and instrumental seismicity of Madagascar: Implications on the seismotectonics. *Tectonophysics*, 594:165–181, 2013. doi: 10.1016/j.tecto.2013.03.033.

Rindraharisaona, E. J., Tilmann, F., Yuan, X., Rümpker, G., Giese, J., Rambolamanana, G., and Barruol, G. Crustal structure of southern Madagascar from receiver functions and ambient noise correlation: Implications for crustal evolution. *Journal of Geophysical Research: Solid Earth*, 122(2):2016JB013565, 2017. doi: 10.1002/2016JB013565.

Roberts, G. G., Paul, J. D., White, N., and Winterbourne, J. Temporal and spatial evolution of dynamic support from river profiles: A framework for Madagascar. *Geochemistry, Geophysics, Geosystems*, 13(4):n/a–n/a, 2012. doi: 10.1029/2012GC004040.

Roig, J., Tucker, R. D., Peters, S., Delor, C., and Théveniaut, H. Carte Gèologique de la Rèpublique de Madagascar à 1 / 1 000 000, 2012.

Royer, J. and Coffin, M. F. Jurassic to Eocene plate tectonic reconstructions in the Kerguelen Plateau region. In Proceedings of the Ocean Drilling Program, Scientific Results. 1992.

Sadeghisorkhani, H., Gudmundsson, O., and Tryggvason, A. GSpecDisp: A matlab GUI package for phase-velocity dispersion measurements from ambient-noise correlations. *Computers & Geosciences*, 2017. doi: 10.1016/j.cageo.2017.09.006.

Sandiford, M., Powell, R., Martin, S. F., and Perera, L. R. K. Thermal and baric evolution of garnet granulites from Sri Lanka. *Journal of Metamorphic Geology*, 6(3):351–364, 1988. doi: 10.1111/j.1525-1314.1988.tb00425.x.

Santosh, M., Tsunogae, T., Malaviarachchi, S. P., Zhang, Z., Ding, H., Tang, L., and Dharmapriya, P. Neoproterozoic crustal evolution in Sri Lanka: Insights from petrologic, geochemical and zircon U–Pb and Lu–Hf isotopic data and implications for Gondwana assembly. *Precambrian Research*, 255:1–29, 2014. doi: 10.1016/j.precamres.2014.09.017.

Schandelmeier, H., Bremer, F., and Holl, H. G. Kinematic evolution of the Morondava rift basin of SW Madagascar—from wrench tectonics to normal extension. *Journal of African Earth Sciences*, 38(4):321–330, 2004. doi: 10.1016/j.jafrearsci.2003.11.002.

Schreurs, G., Giese, J., Berger, A., and Gnos, E. A new perspective on the significance of the Ranotsara shear zone in Madagascar. *International Journal of Earth Sciences*, 99(8): 1827–1847, 2010. doi: 10.1007/s00531-009-0490-9.

Seneviratne, S. W. M., Haberland, C., and Dreiling, J. Sri Lanka temporary broadband network. GFZ Data Services. Other/Seismic Network, 2016.

Seward, D., Grujic, D., and Schreurs, G. An insight into the breakup of Gondwana: Identifying events through low-temperature thermochronology from the basement rocks of Madagascar. *Tectonics*, 23(3):TC3007, 2004. doi: 10.1029/2003TC001556.

Shapiro, N. M. and Campillo, M. Emergence of broadband Rayleigh waves from correlations of the ambient seismic noise. *Geophysical Research Letters*, 31(7), 2004. doi: 10.1029/2004GL019491.

Shapiro, N. M., Ritzwoller, M. H., Molnar, P., and Levin, V. Thinning and flow of Tibetan crust constrained by seismic anisotropy. *Science*, 305(5681):233–236, 2004.

Shirzad, T. and Shomali, Z. H. Shallow crustal radial anisotropy beneath the Tehran basin of Iran from seismic ambient noise tomography. *Physics of the Earth and Planetary Interiors*, 231:16–29, 2014. doi: 10.1016/j.pepi.2014.04.001.

SIO. Scripps Institution Of Oceanography. Global Seismograph Network - IRIS/IDA. International Federation of Digital Seismograph Networks. Dataset/Seismic Network. 1986. doi: 10.7914/SN/II.

Sleeman, R. Ambient Earth noise and instrumental noise. Koninkliijk Nederlands Meterologisch Instituut, 2006.

Soesoo, A., Bons, P. D., Gray, D. R., and Foster, D. A. Divergent double subduction: Tectonic and petrologic consequences. *Geology*, (8):755, 1997. doi: 10.1130/0091-7613(1997)025<0755:DDSTAP>2.3.CO;2.

Stein, S. and Wysession, M. *An introduction to seismology, earthquakes, and earth structure.* Blackwell Pub, Malden, MA, 2003. ISBN 978-0-86542-078-6.

Stern, R. J. Arc Assembly and Continental Collision in the Neoproterozoic East African Orogen: Implications for the Consolidation of Gondwanaland. *Annual Review of Earth and Planetary Sciences*, 22(1):319–351, 1994. doi: 10.1146/annurev.ea.22.050194.001535.

Storey, M., Mahoney, J. J., Saunders, A. D., Duncan, R. A., Kelley, S. P., and Coffin, M. F. Timing of Hot Spot–Related Volcanism and the Breakup of Madagascar and India. *Science*, 267(5199):852–855, 1995. doi: 10.1126/science.267.5199.852.

Storey, M., Mahoney, J. J., and Saunders, A. D. Cretaceous basalts in Madagascar and the transition between plume and continental lithosphere mantle sources. *Large Igneous Provinces: Continental, Oceanic, and Planetary Flood Volcanism. Geophysical Monograph Series*, 1997. doi: 10.1029/GM100p0095.

Takamura, Y., Tsunogae, T., Santosh, M., Malaviarachchi, S. P. K., and Tsutsumi, Y. U–Pb geochronology of detrital zircon in metasediments from Sri Lanka: Implications for the regional correlation of Gondwana fragments. *Precambrian Research*, 281:434–452, 2016. doi: 10.1016/j.precamres.2016.06.015.

Tatham, D. J., Lloyd, G. E., Butler, R. W. H., and Casey, M. Amphibole and lower crustal seismic properties. *Earth and Planetary Science Letters*, 267(1):118–128, 2008. doi: 10.1016/j.epsl.2007.11.042.

Tilmann, F., Yuan, X., Rümpker, G., and Rindraharisaona, E. SELASOMA Project, Madagascar 2012-2014. 2012. doi: 10.14470/MR7567431421.

Tucker, R., Kusky, T., Buchwaldt, R., and Handke, M. Neoproterozoic nappes and superposed folding of the Itremo Group, west-central Madagascar. *Gondwana Research*, 2007.

Tucker, R., Roig, J., Macey, P., Delor, C., Amelin, Y., Armstrong, R., Rabarimanana, M., and Ralison, A. A new geological framework for south-central Madagascar, and its relevance to the "out-of-Africa" hypothesis. *Precambrian Research*, 185(3-4):109–130, 2011. doi: 10.1016/j.precamres.2010.12.008.

Tucker, R., Roig, J., Moine, B., Delor, C., and Peters, S. A geological synthesis of the Precambrian shield in Madagascar. *Journal of African Earth Sciences*, 94:9–30, 2014. doi: 10.1016/j.jafrearsci.2014.02.001.

Veevers, J. J. Gondwanaland from 650–500 Ma assembly through 320 Ma merger in Pangea to 185–100 Ma breakup: supercontinental tectonics via stratigraphy and radiometric dating. *Earth-Science Reviews*, 68(1):1–132, 2004. doi: 10.1016/j.earscirev.2004.05.002.

Walker, K. T., Nyblade, A. A., Klemperer, S. L., Bokelmann, G. H. R., and Owens, T. J. On the relationship between extension and anisotropy: Constraints from shear wave splitting across the East African Plateau. *Journal of Geophysical Research: Solid Earth*, 109(B8), 2004. doi: 10.1029/2003JB002866.

Wang, N., Montagner, J.-P., Fichtner, A., and Capdeville, Y. Intrinsic versus extrinsic seismic anisotropy: The radial anisotropy in reference Earth models. *Geophysical Research Letters*, 40(16):4284–4288, 2013. doi: 10.1002/grl.50873.

Weiss, T., Siegesmund, S., Rabbel, W., Bohlen, T., and Pohl, M. Seismic Velocities and Anisotropy of the Lower Continental Crust: A Review. *Pure and Applied Geophysics*, 156 (1-2):97–122, 1999. doi: 10.1007/s000240050291.

Wescott, W. A. and Diggens, J. N. Depositional history and stratigraphical evolution of the Sakoa Group (Lower Karoo Supergroup) in the southern Morondava Basin, Madagascar. *Journal of African Earth Sciences*, 24(4):585–601, 1997. doi: 10.1016/S0899-5362(97)00082-1.

Wescott, W. A. and Diggens, J. N. Depositional history and stratigraphical evolution of the Sakamena group (Middle Karoo Supergroup) in the southern Morondava Basin, Madagascar. *Journal of African Earth Sciences*, 27(3):461–479, 1998. doi: 10.1016/S0899-5362(98)00073-6.

Wong, R. C. K., Schmitt, D. R., Collis, D., and Gautam, R. Inherent transversely isotropic elastic parameters of over-consolidated shale measured by ultrasonic waves and their comparison with static and acoustic *in situ* log measurements. *Journal of Geophysics and Engineering*, 5(1): 103–117, 2008. doi: 10.1088/1742-2132/5/1/011.

Wysession, M. E., Wiens, D. A., and Nyblade, A. A. Investigation of Sources of Intraplate Volcanism Using Passcal Broadband Instruments in MAdagascar, the COmores, and MOzambique. 2011. doi: 10.7914/SN/XV_2011.

Xie, J., Ritzwoller, M. H., Shen, W., Yang, Y., Zheng, Y., and Zhou, L. Crustal radial anisotropy across eastern Tibet and the western Yangtze craton. *Journal of Geophysical Research: Solid Earth*, 118(8):4226–4252, 2013.

Yao, H., van der Hilst, R. D., and de Hoop, M. V. Surface-wave array tomography in SE Tibet from ambient seismic noise and two-station analysis - I. Phase velocity maps. *Geophysical Journal International*, 166(2):732–744, 2006. doi: 10.1111/j.1365-246X.2006.03028.x.

Zandt, G. and Ammon, C. J. Continental crust composition constrained by measurements of crustal Poisson's ratio. *Nature*, pages 152–154, 1995.

Zhang, Q., Guo, F., Zhao, L., and Wu, Y. Geodynamics of divergent double subduction: 3-D numerical modeling of a Cenozoic example in the Molucca Sea region, Indonesia. *Journal of Geophysical Research: Solid Earth*, 2017. doi: DOI:10.1002/2017JB013991.

Zhu, L. and Kanamori, H. Moho depth variation in southern California from teleseismic receiver functions. *Journal of Geophysical Research*, 2000.

Appendices

I.A Station meta data

Table I.A1: Meta data for seismic stations included in part I. NW: Network, Lat: Latitude, Long: longitude, Alt: Altitude (m), SR: sampling rate (Hz).

NW	Station	Lat	Long	Alt	SR	Sensor type	Start time	End time
ZE	AM01	-21.0772	48.2392	43	50	L4-3D	2013-04-29	2014-12-31
ZE	AM02	-21.2441	48.3472	11	50	L4-3D	2013-05-08	2014-12-31
ZE	AM04	-21.1811	47.6382	454	50	L4-3D	2013-05-07	2014-12-31
ZE	AM05	-21.1729	48.0765	45	50	L4-3D	2013-05-08	2014-12-31
ZE	AM06	-21.0461	47.2004	1236	50	L4-3D	2013-05-06	2014-12-31
ZE	AM07	-20.7958	47.1776	1817	50	L4-3D	2013-05-06	2014-12-31
ZE	AM08	-21.3247	46.9385	1118	50	L4-3D	2013-05-04	2014-12-31
ZE	AM09	-21.5598	47.5170	402	50	L4-3D	2013-05-06	2014-12-31
ZE	AM10	-21.5866	47.9659	63	50	L4-3D	2013-05-07	2014-12-31
ZE	AM11	-21.7431	47.4937	230	50	L4-3D	2013-05-06	2014-12-31
ZE	AM12	-21.8170	47.8793	32	50	L4-3D	2013-05-07	2014-12-31
ZE	AM13	-21.6140	46.8444	1010	50	L4-3D	2013-05-04	2014-12-31
ZE	AM14	-22.5242	46.7370	647	50	L4-3D	2013-05-02	2014-12-31
ZE	AM15	-22.0545	47.0516	1056	50	L4-3D	2013-05-04	2014-12-31
ZE	AM16	-21.7262	46.3964	755	50	L4-3D	2013-05-03	2013-11-13
ZE	AM16A	-21.7191	46.3788	733	50	L4-3D	2013-11-14	2014-12-31
ZE	AM17	-22.1667	46.1525	726	50	L4-3D	2013-05-03	2014-12-31
ZE	AM18	-22.5707	46.4273	638	50	L4-3D	2013-05-02	2014-12-31
ZE	AM19	-22.6999	46.1438	1038	50	L4-3D	2013-05-02	2014-12-31
ZE	AM20	-22.3028	45.6823	1088	50	L4-3D	2013-04-30	2014-12-31
ZE	AM21	-22.6137	45.3959	800	50	L4-3D	2013-04-29	2014-12-31
ZE	AM22	-22.6438	45.7011	929	50	L4-3D	2013-04-30	2014-12-31

ZE	AM23	-22.9496	46.1397	1030	50	L4-3D	2013-05-02	2014-12-31
ZE	MS01	-23.4139	43.7546	12	100	CMG-3ESP/60	2012-04-30	2014-12-31
ZE	MS02	-23.3434	43.8945	166	50	L4-3D	2012-04-30	2014-12-31
ZE	MS03	-23.2382	44.0240	326	50	L4-3D	2012-04-29	2014-12-31
ZE	MS04	-23.1050	44.2199	439	100	CMG-3ESP/60	2012-05-03	2014-12-31
ZE	MS05	-22.9061	44.4639	421	50	L4-3D	2012-05-04	2014-12-31
ZE	MS06	-22.8862	44.6913	820	100	CMG-3ESP/60	2012-05-05	2014-12-31
ZE	MS06A	-22.8271	44.7327	970	100	Trillium-240	2013-04-26	2014-12-31
ZE	MS07	-22.8124	44.8289	663	100	CMG-3ESP/60	2012-04-28	2014-12-31
ZE	MS08	-22.7548	45.1131	855	100	CMG-3ESP/60	2012-05-02	2014-12-31
ZE	MS09	-22.4826	45.3982	723	100	CMG-3ESP/60	2012-05-04	2014-12-31
ZE	MS10	-22.4735	45.5668	972	100	CMG-3ESP/60	2012-05-04	2014-12-31
ZE	MS11	-22.5197	45.7215	961	100	CMG-3ESP/60	2012-05-03	2014-12-31
ZE	MS12	-22.4374	45.9150	1038	100	Trillium-240	2012-05-03	2014-12-31
ZE	MS13	-22.3575	46.0879	732	100	CMG-3ESP/60	2012-05-01	2014-12-31
ZE	MS14	-22.2995	46.2516	721	100	CMG-3ESP/60	2012-05-01	2014-12-31
ZE	MS15	-22.0855	46.4091	965	100	CMG-3ESP/60	2012-04-30	2014-12-31
ZE	MS16	-21.9357	46.5430	772	100	Trillium-240	2012-05-01	2014-12-31
ZE	MS17	-21.7900	46.9260	963	100	CMG-3ESP/60	2012-04-30	2014-12-31
ZE	MS18	-21.5976	46.9949	1200	100	CMG-3ESP/60	2012-04-30	2014-12-31
ZE	MS18A	-21.5975	46.9948	1200	100	CMG-3ESP/60	2013-05-04	2014-12-31
ZE	MS19	-21.4093	47.1028	1140	100	CMG-3ESP/60	2012-05-07	2014-12-31
ZE	MS20	-21.3316	47.2715	1126	100	CMG-3ESP/60	2012-05-08	2014-12-31
ZE	MS21	-21.2389	47.3825	1135	100	CMG-3ESP/60	2012-05-08	2014-12-31
ZE	MS22	-21.3382	47.6161	463	50	L4-3D	2012-04-26	2014-12-31
ZE	MS23	-21.3542	47.7780	254	100	CMG-3ESP/60	2012-04-27	2014-12-31
ZE	MS24	-21.4254	48.0393	197	100	CMG-3ESP/60	2012-04-28	2014-12-31
ZE	MS25	-21.2767	48.1710	76	100	CMG-3ESP/60	2012-04-28	2014-12-31
ZE	MS25A	-21.2876	48.1858	109	100	CMG-3ESP/60	2013-05-08	2014-12-31
XV	MMBE	-21.7500	43.3721	32	40		2011-09-28	2013-06-11
XV	LONA	-22.8057	44.2958	416	40		2011-09-25	2013-12-31
XV	AMPY	-24.7033	44.7435	252	40		2012-08-15	2013-12-31
XV	CPSM	-25.5358	45.1500	172	40		2012-08-13	2013-12-31
XV	BKTA	-24.1821	45.6730	576	40		2012-08-11	2013-12-31
XV	MAHA	-23.1714	47.6898	31	40		2011-10-04	2013-12-31
YV	RUM1	-22.8022	47.7175	45	100	STS2	2012-09-25	2014-08-31
YV	RUM2	-22.1367	48.0022	11	50/100	STS2	2012-09-23	2014-08-31
YV	RUM3	-23.7988	47.5459	8	100	STS2	2012-09-27	2014-08-30
YV	RUM4	-24.2767	47.3157	15	100	STS2	2012-09-28	2014-08-29
YV	RUM5	-24.7852	47.0851	21	100	STS2	2012-09-30	2014-08-27
G	FOMA	-24.9756	46.9788	28	20	STS2	2008-09-01	2017-01-31
GE	VOI	-21.9064	46.7932	1158	20		2009-11-26	

I.B Travel time tomography

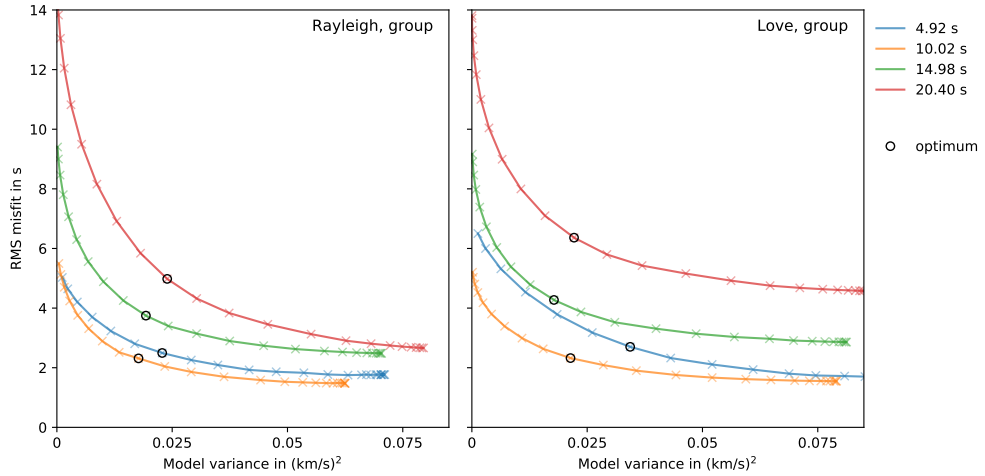

Figure I.B1: Damping factor trade-off curves for different periods for Rayleigh and Love group velocities. The crosses are computed values for 25 discrete damping factors (log-spaced between 0.01–1000). Optimum damping factors are encircled. Because of the similarity of the optimum value for the Rayleigh and Love wave, we used their mean value (per period).

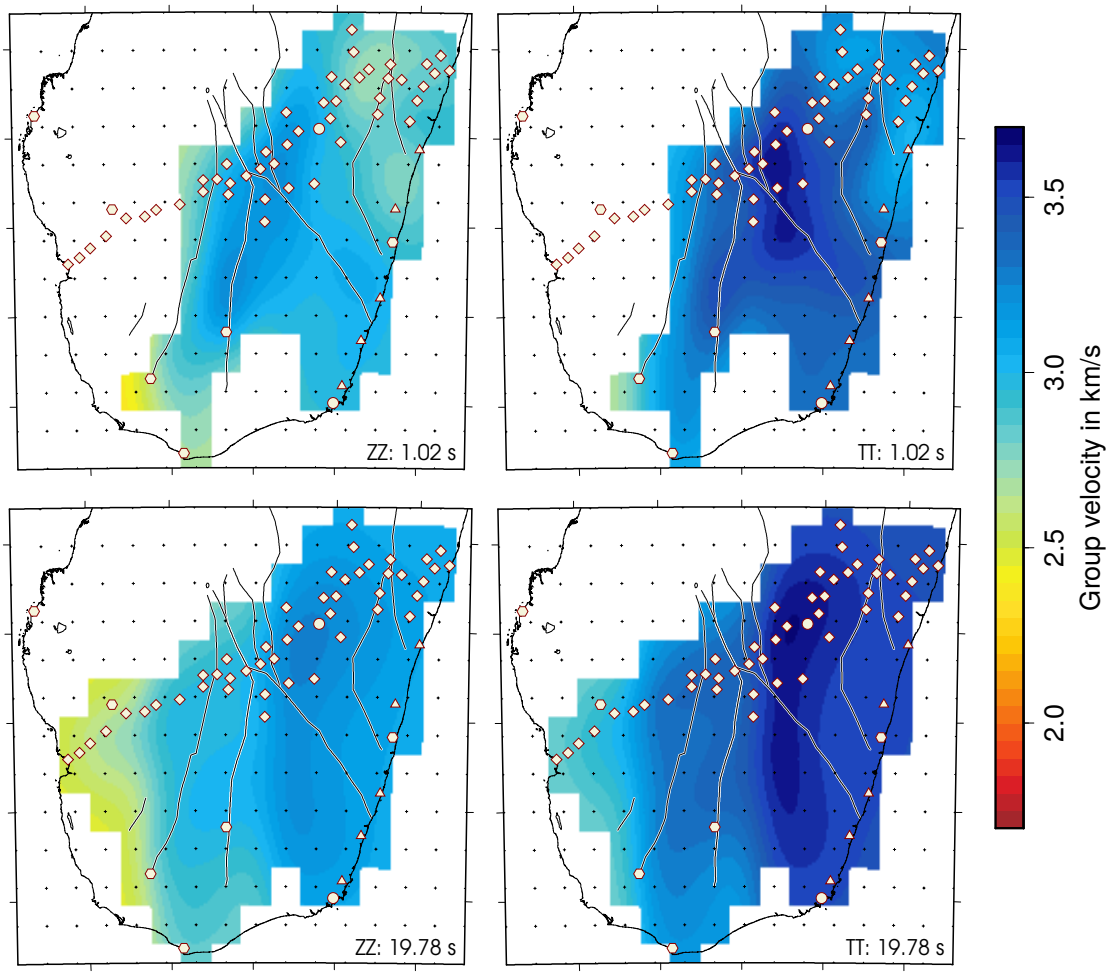

Figure I.B2: Tomographic results for Rayleigh and Love wave group velocities for different periods. Black crosses indicate grid cell nodes. Grid cells are only colored if rays are propagating through. Black lines correspond to shear zones, red symbols to seismic stations (as in Fig. I.1).

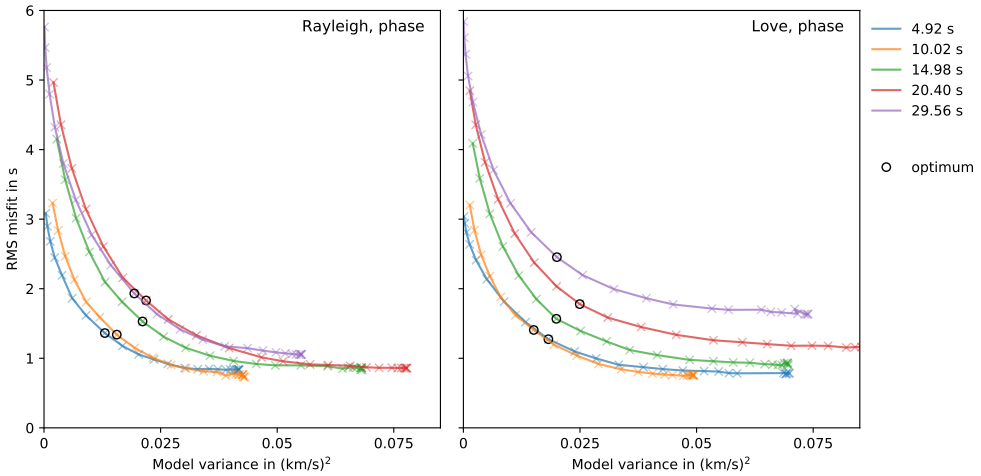

Figure I.B3: Damping factor trade-off curves for different periods for Rayleigh and Love phase velocities. The crosses are computed values for 25 discrete damping factors (log-spaced between 0.01–1000). Optimum damping factors are encircled. Because of the similarity of the optimum value for the Rayleigh and Love wave, we used their mean value (per period) for the final tomographies.

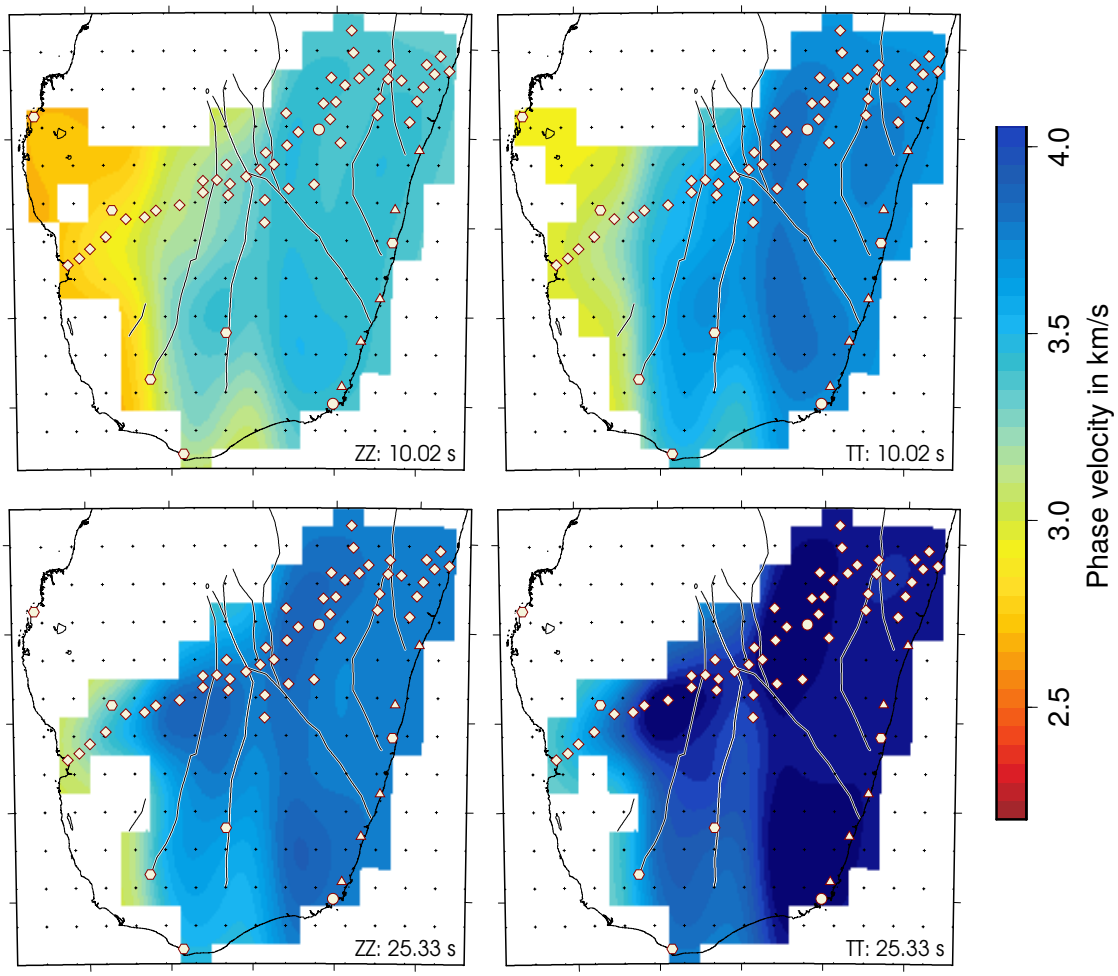

Figure I.B4: Tomographic results for Rayleigh and Love wave phase velocities for different periods. See caption of Fig. I.B2.

I.C Velocity-depth inversion

Group velocity inversion

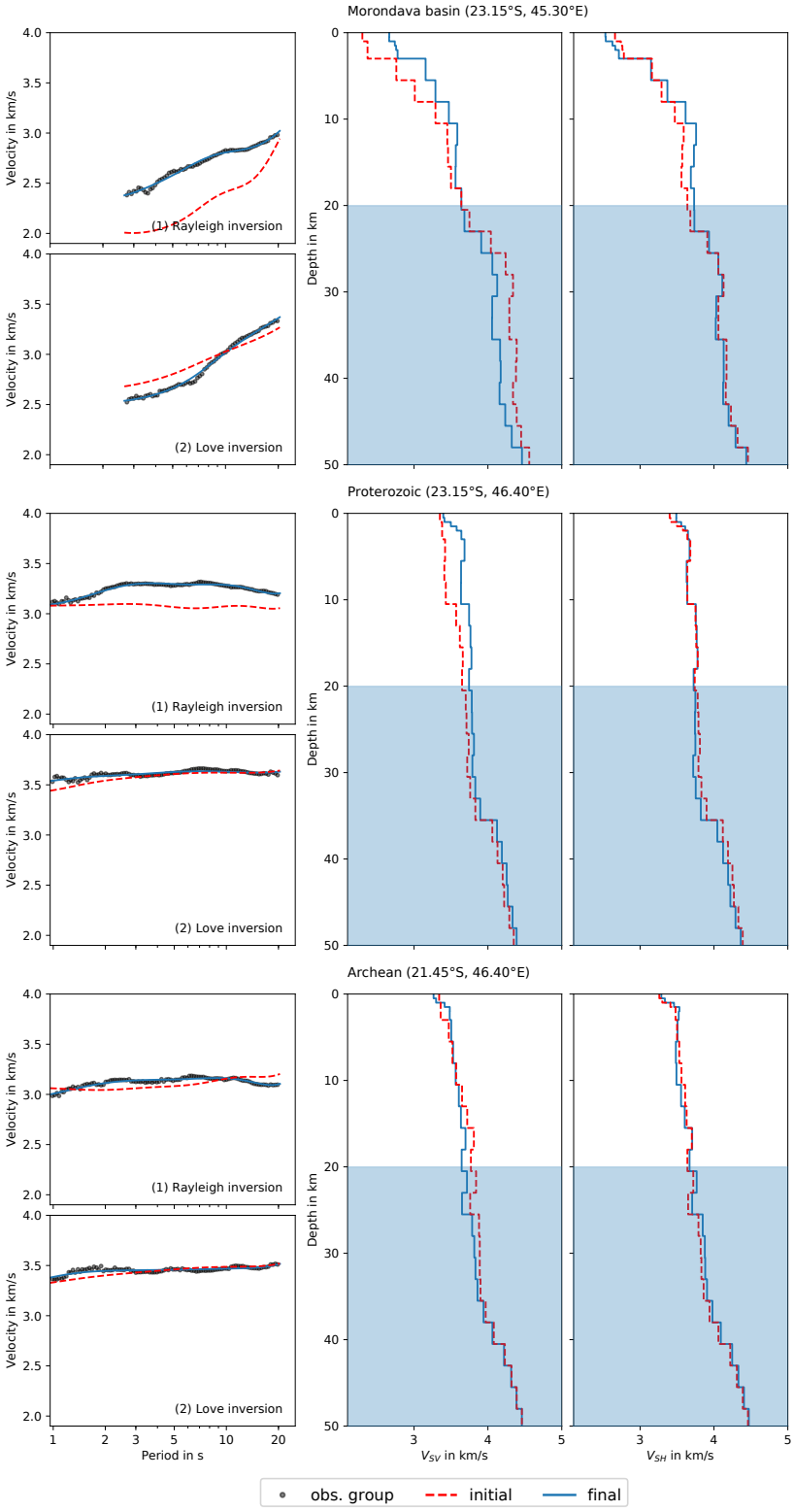

Figure I.C1: Group velocity dispersion curve inversion (R→L) for three grid nodes in the Morondava basin, Proterozoic and Archean region. (left) Initial and final dispersion curves and (right) corresponding V_{SV}- and V_{SH}-depth structures. Blue shaded area marks depths of low sensitivity.

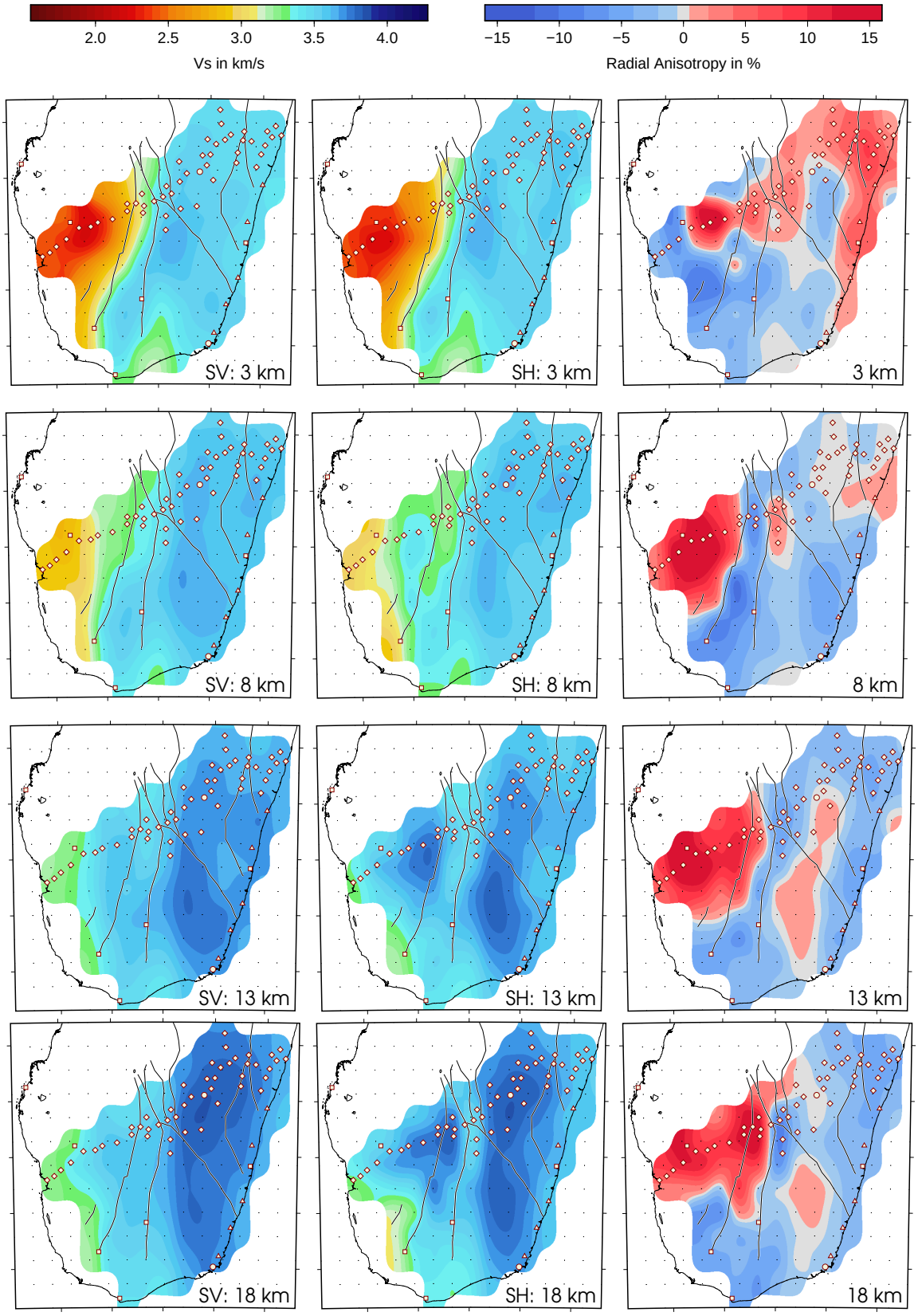

Figure I.C2: V_{SV}, V_{SH} and RA at 3, 8, 13 and 18 km of depth. RA is negative if $V_{SV}>V_{SH}$ and positive if $V_{SV}<V_{SH}$.

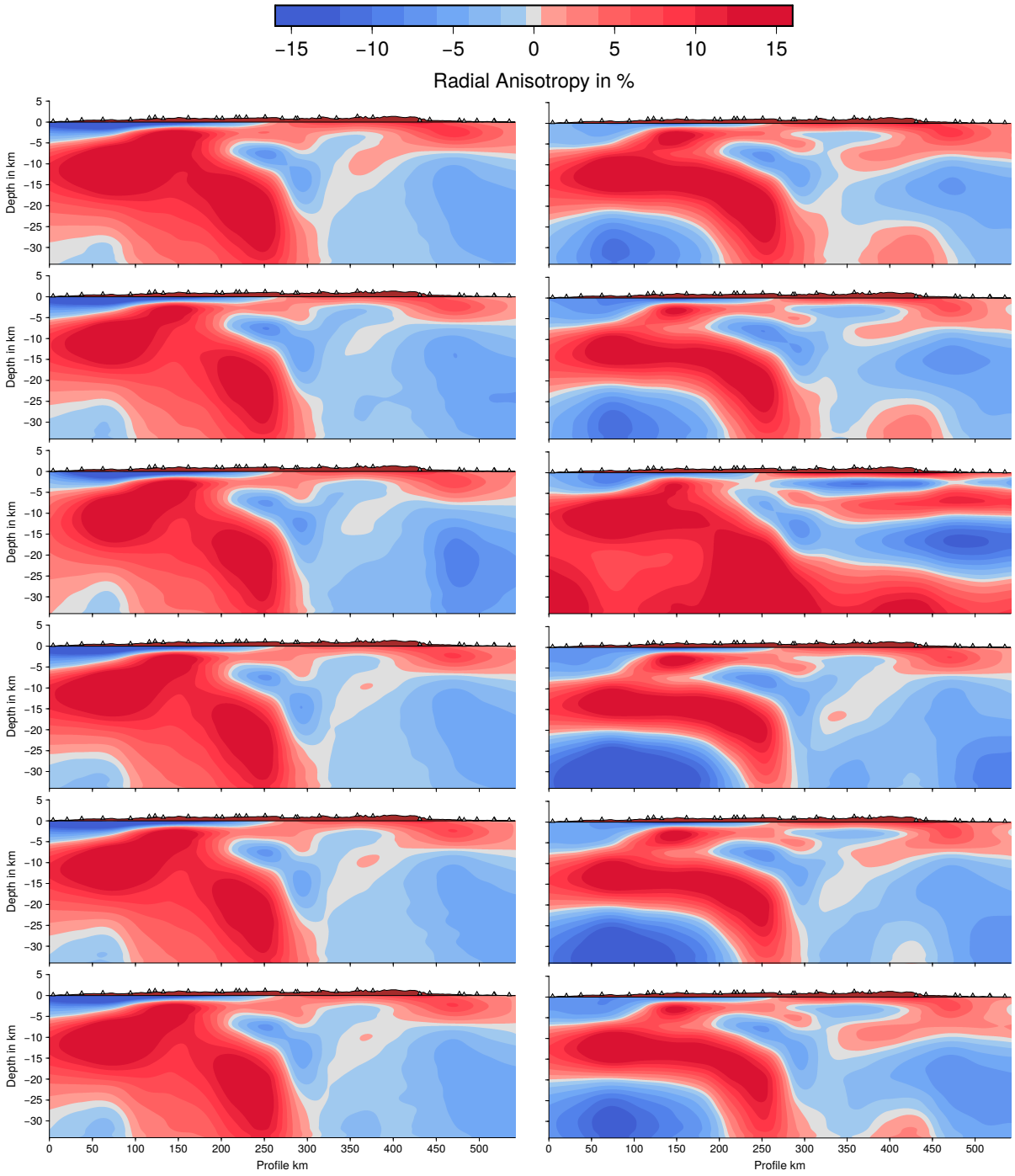

Figure I.C3: Cross sections along profile A (location as in Fig. I.1), showing radial anisotropy derived from group velocity inversion using different starting models and inversion orders. Left column shows results from R→L, right column from L→R inversion order. Initial models are from top to bottom: lgradient, sgradient, basin, proterozoic, archean and volcanics. Elevation profile is based on etopo1 (Amante and Eakins, 2009).

Joint group and phase velocity inversion

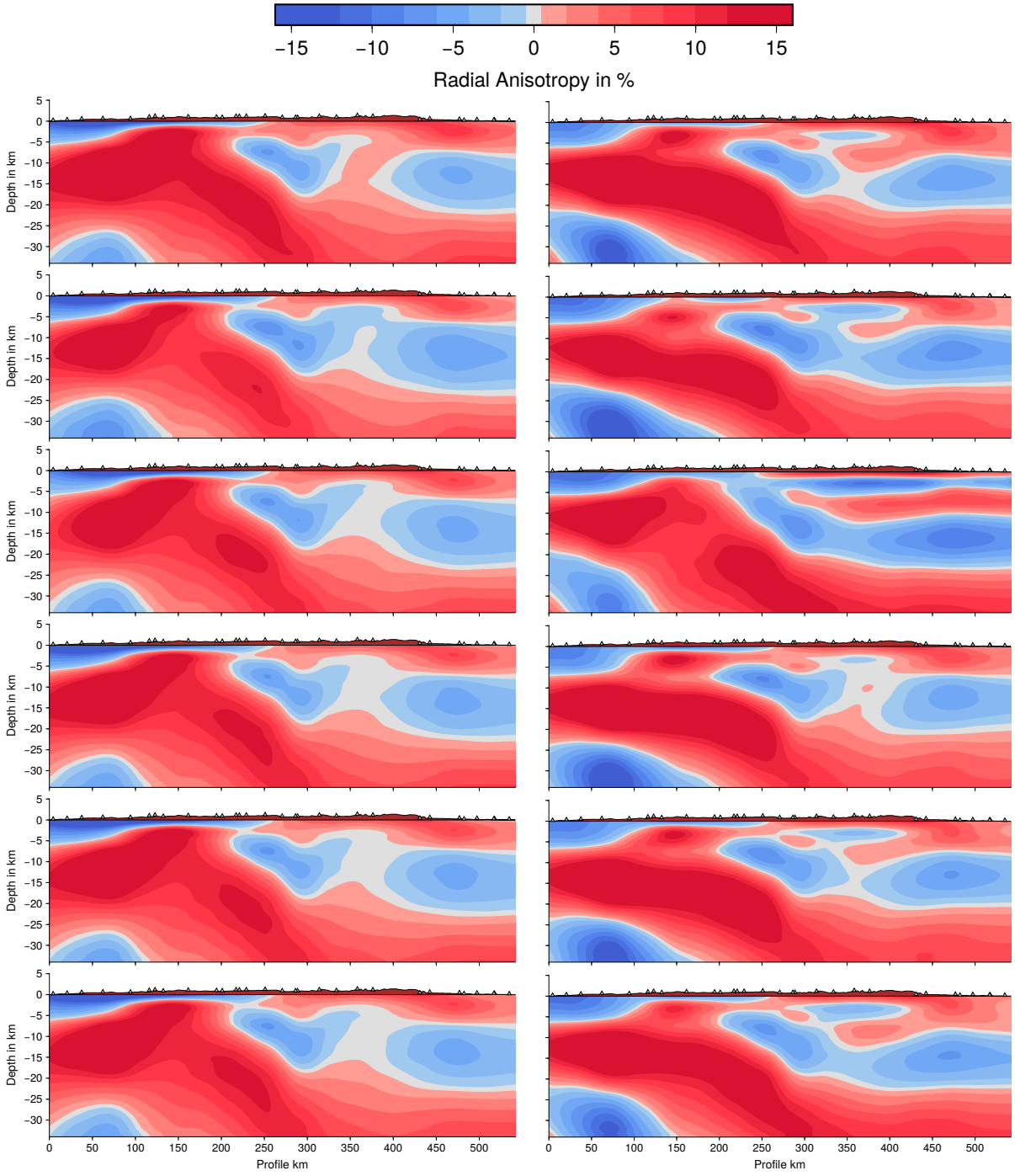

Figure I.C4: Cross sections along profile A (location as in Fig. I.1), showing radial anisotropy derived from joint group and phase velocity inversion using different starting models and inversion orders. Left column shows results from R→L, right column from L→R inversion order. Initial models are from top to bottom: lgradient, sgradient, basin, proterozoic, archean and volcanics. Elevation profile is based on etopo1 (Amante and Eakins, 2009).

II.A Station meta data

Table II.A1: Meta data for seismic stations included in part II. NW: Network, Lat: Latitude, Long: longitude, Alt: Altitude (m). Sampling rate as given in Table II.1.

NW	Station	Name	Lat	Long	Alt	Sensor type	Start time	End time
1A	SL01	Madampe	7.4922	79.8300	20	CMG-3ESP/60	2016-05-25	2017-06-30
1A	SL02	Dummala	7.5187	79.9290	34	CMG-3ESP/120	2016-05-26	2017-06-30
1A	SL03	Pugalla	7.4862	80.1062	53	CMG-3ESP/60	2016-05-26	2017-06-30
1A	SL04	Mahapitiya	7.4216	80.2961	126	CMG-3ESP/60	2016-05-27	2016-08-19
1A	SL05	Rambukkana	7.3351	80.4130	120	CMG-3ESP/60	2016-05-28	2017-06-30
1A	SL06	Medawala	7.3693	80.5588	524	CMG-3ESP/60	2016-05-28	2017-06-30
1A	SL08	Hanguranketha	7.1755	80.8353	376	CMG-3ESP/60	2016-05-29	2017-07-01
1A	SL09	Mahakale	7.2020	80.9970	127	CMG-3ESP/60	2016-05-29	2017-07-01
1A	SL10	Rideemaliyadda	7.1944	81.1248	284	CMG-3ESP/60	2016-05-29	2017-07-01
1A	SL11	Medagama	7.0931	81.2685	254	Trillium-120	2016-05-31	2017-07-01
1A	SL12	Mariarawa	6.9852	81.4065	179	CMG-3ESP/60	2016-05-31	2017-07-01
1A	SL13	Siyambalanduwa	6.9896	81.5593	95	CMG-3ESP/60	2016-06-01	2017-07-01
1A	SL14	Tharulengala	6.9302	81.6554	72	CMG-3ESP/60	2016-08-13	2017-07-02
1A	SL15	Pothuwil	6.9207	81.8168	12	CMG-3ESP/120	2016-06-01	2017-07-02
1A	SL16	Puttalam	7.9760	79.9037	56	CMG-3ESP/120	2016-06-05	2017-07-04
1A	SL17	Galgamuwa	7.9239	80.2789	97	Trillium-120	2016-06-05	2017-07-04
1A	SL18	Bakamuna	7.7931	80.8082	143	CMG-3ESP/60	2016-06-03	2017-07-04
1A	SL19	Mahaoya	7.5293	81.3533	67	CMG-3ESP/120	2016-06-03	2017-07-02
1A	SL20	Sammanthurei	7.3501	81.7896	33	Trillium-120	2016-06-02	2017-07-01
1A	SL21	Opemaduwa	8.4676	80.1710	64	CMG-3ESP/120	2016-06-03	2017-07-04
1A	SL22	Agbopura	8.3169	80.9789	62	CMG-3ESP/120	2016-05-31	2017-07-03
1A	SL23	Wakanery	7.9206	81.4362	21	CMG-3ESP/120	2016-06-02	2017-07-03
1A	SL24	Vavuniya	8.8361	80.4802	86	Trillium-120	2016-06-03	2017-07-04
1A	SL25	Morawewa	8.6618	80.9997	44	CMG-3ESP/120	2016-06-01	2017-07-03
1A	SL26	Weboda	7.0227	79.9997	38	Trillium-120	2016-06-11	2017-06-28
1A	SL27	Rathnapura	6.7120	80.5117	322	CMG-3ESP/60	2016-06-09	2017-07-03
1A	SL28	Mathugama	6.7974	81.1001	305	CMG-3ESP/120	2016-06-08	2017-07-02
1A	SL29	Katharagama	6.4008	81.3383	61	CMG-3ESP/120	2016-06-08	2017-07-04
1A	SL30	Lathpandura	6.5362	80.2101	39	CMG-3ESP/60	2016-06-07	2017-07-04
1A	SL31	Namaloya	7.3417	81.4564	115	CMG-3ESP/60	2016-06-02	2017-07-02
GE	MALK	Mahakanadarawa	8.3968	80.5425	113	STS-2/N	2010-04-10	
GE	HALK	Hakmana	6.0877	80.6806	120	STS-2/N	2011-05-12	
II	PALK	Pallekele	7.2728	80.7022	460		2000-08-22	

II.B Velocity-depth inversion

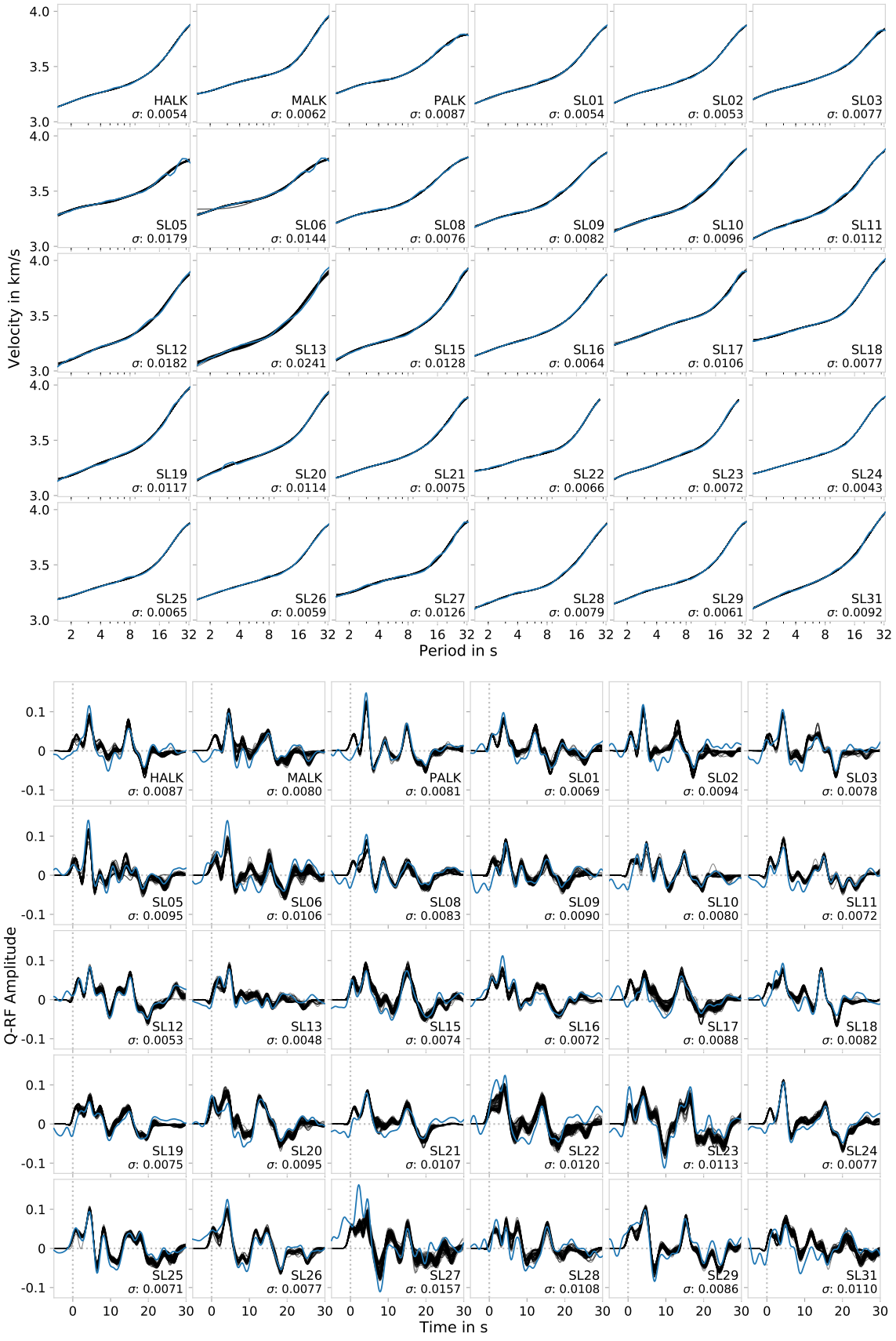

Figure II.B1: Best fit dispersion curves and receiver functions from each station and from each chain of 100 chains (except outliers chains). Blue lines represent observed data

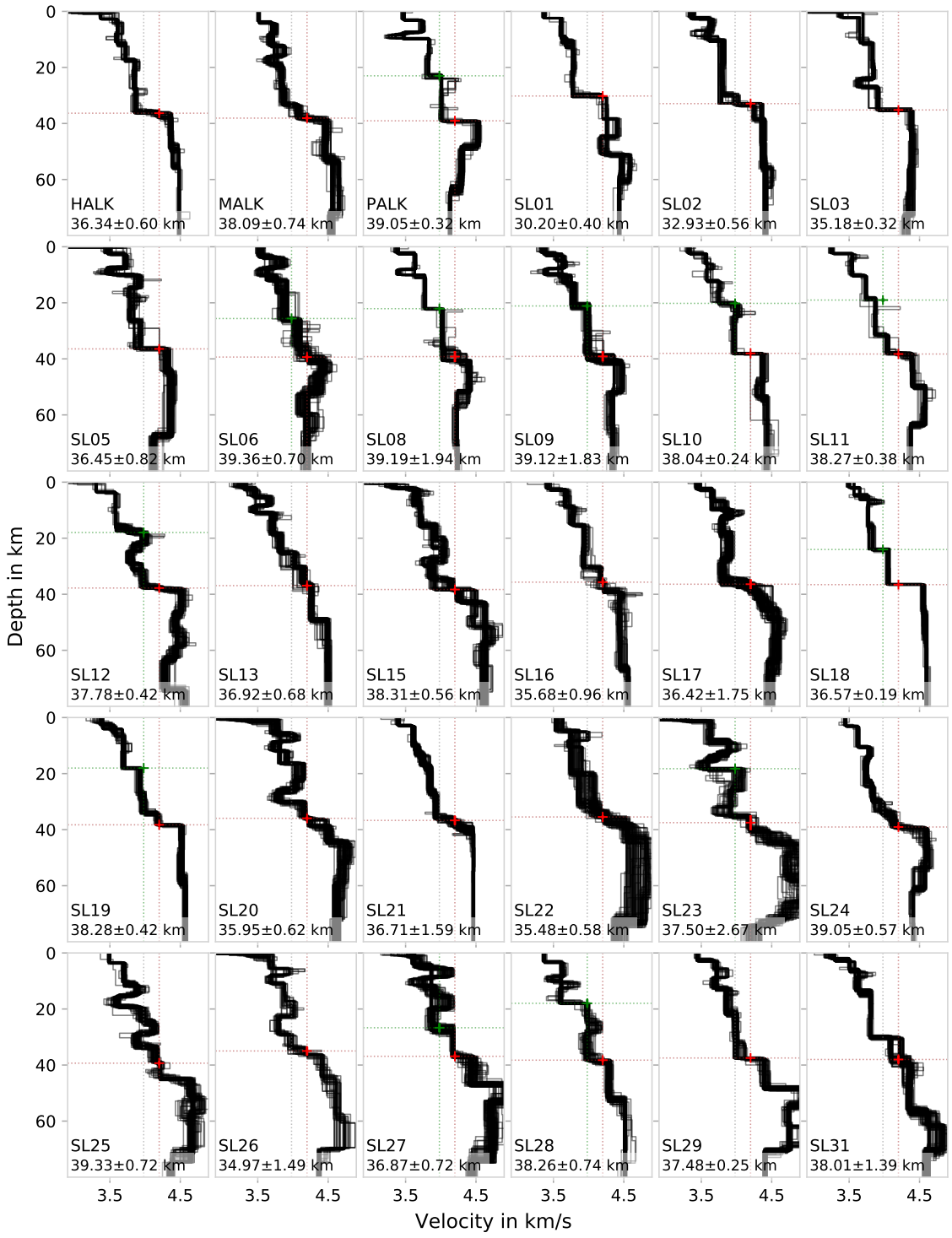

Figure II.B2: V_S-depth models corresponding to best fit dispersion curves and receiver functions from each station and from each chain of 100 chains (Fig. II.B1). Dashed vertical lines mark 4 and 4.2 km/s. Horizontal lines mark the mid-crustal interface (green) and the Moho depth (brown).

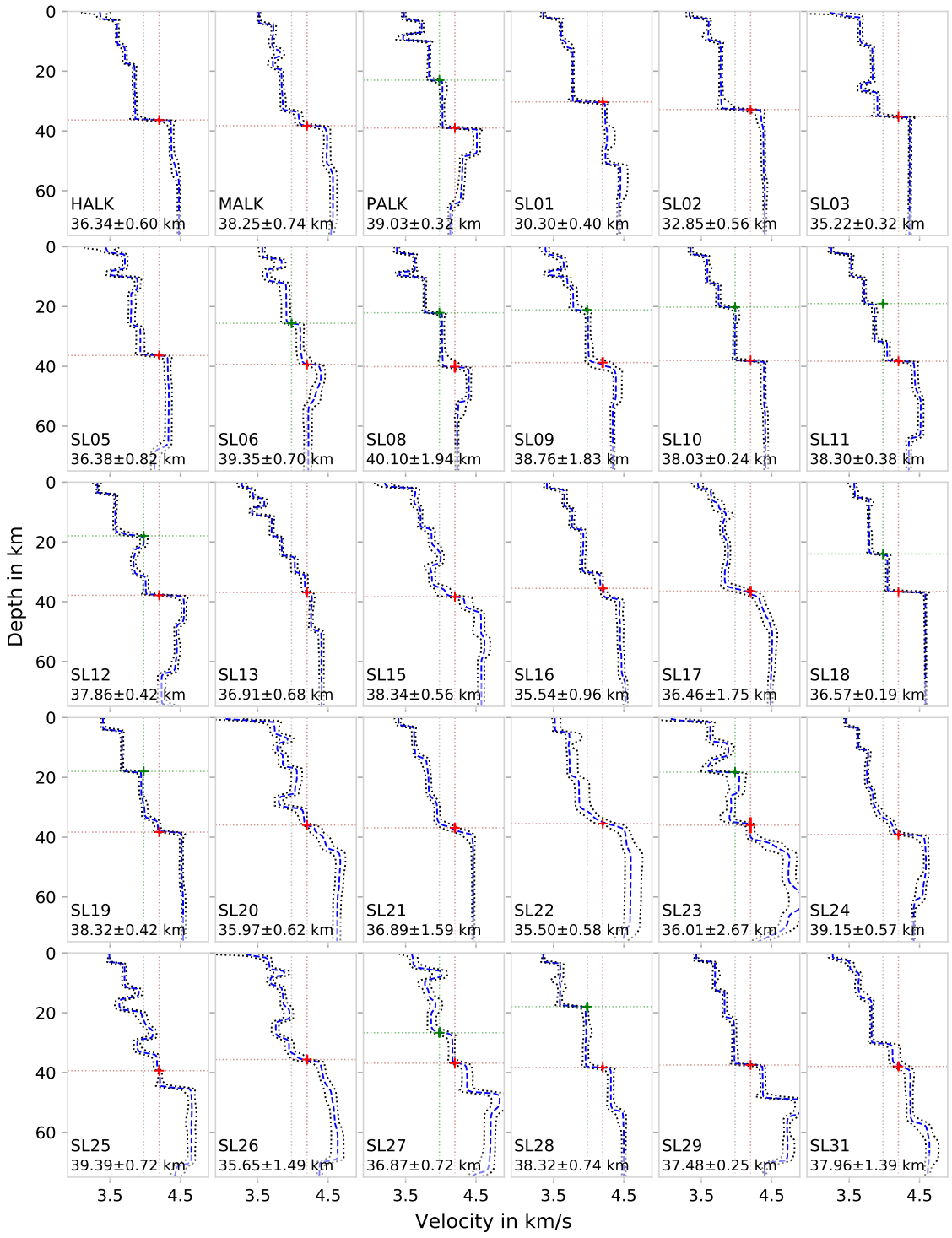

Figure II.B3: Final velocity-depth models including standard deviation for each station. Dashed vertical lines mark 4 and 4.2 km/s. Horizontal lines mark the mid-crustal interface (green) and the Moho depth (brown).

Table II.B1: Moho depths and V_P/V_S derived from Bayesian inversion and Hκ-stack grid search, and average crustal V_S and depth of mid-crustal interface (mc-int) from Bayesian inversion. Values from Hκ-stack grid search are based on binned receiver functions. Uncertainty estimated from 97.5 % contour, see Figure II.21. SL04 was excluded, but 8 events still yield a realistic result. For Bayesian inversion, the median of each posterior distribution (100,000 models) was considered. To extract the Moho depth for each station, each of the models was analyzed to find the interfaces within a pre-selected range; the crustal layer defined as the last one having a V_S <4.2 km/s. Average crustal V_S was computed based on the Moho interface depth. For estimating the depth of the mid-crustal interface with an average V_S increase from 3.75 to 4.0 km/s, same procedure as for the Moho depths was applied; for each of the twelve stations, each of the models was analyzed to find the interfaces within a pre-selected range. Results excluded are in brackets.

Code	Moho (km)	Hκ-Moho (km)	V_P/V_S	Hκ-V_P/V_S	V_S (km/s)	mc-int (km)
SL01	30.3 ± 0.4	29.5 ± 0.7	1.78 ± 0.04	1.79 ± 0.02	3.69 ± 0.01	
SL02	32.9 ± 0.6	32.8 ± 0.7	1.79 ± 0.06	1.76 ± 0.02	3.71 ± 0.02	
SL03	35.2 ± 0.3	33.2 ± 1.1	1.78 ± 0.04	1.78 ± 0.03	3.76 ± 0.02	
(SL04)		(34.75 ± 0.5)		(1.77 ± 0.02)		
SL05	36.4 ± 0.8	36.2 ± 0.6	1.84 ± 0.06	1.70 ± 0.02	3.80 ± 0.02	
SL06	39.4 ± 0.7	40.0 ± 0.7	1.69 ± 0.10	1.64 ± 0.02	3.92 ± 0.03	25.6 ± 0.6
SL08	40.1 ± 1.9	38.2 ± 0.6	1.90 ± 0.06	1.68 ± 0.02	3.82 ± 0.02	22.1 ± 0.3
SL09	38.8 ± 1.8	37.8 ± 0.9	1.92 ± 0.10	1.71 ± 0.02	3.80 ± 0.03	21.1 ± 0.8
SL10	38.0 ± 0.2	36.0 ± 0.6	1.80 ± 0.03	1.82 ± 0.02	3.79 ± 0.01	20.2 ± 0.6
SL11	38.3 ± 0.4	38.5 ± 0.5	1.78 ± 0.04	1.70 ± 0.02	3.75 ± 0.01	19.0 ± 0.7
SL12	37.9 ± 0.4	38.0 ± 0.5	1.76 ± 0.02	1.74 ± 0.02	3.74 ± 0.01	18.0 ± 0.6
SL13	36.9 ± 0.7	36.8 ± 0.5	1.80 ± 0.06	1.78 ± 0.02	3.78 ± 0.02	
(SL14)						
SL15	38.3 ± 0.6	38.2 ± 0.7	1.64 ± 0.05	1.67 ± 0.02	3.80 ± 0.03	
SL16	35.5 ± 1.0	36.8 ± 1.6	1.57 ± 0.03	1.60 ± 0.03	3.84 ± 0.02	
SL17	36.5 ± 1.7	37.2 ± 0.6	1.77 ± 0.07	1.70 ± 0.02	3.80 ± 0.03	
SL18	36.6 ± 0.2	36.0 ± 0.5	1.71 ± 0.02	1.72 ± 0.02	3.84 ± 0.01	24.0 ± 0.3
SL19	38.3 ± 0.4	37.5 ± 0.6	1.78 ± 0.03	1.71 ± 0.02	3.82 ± 0.01	18.0 ± 0.3
SL20	36.0 ± 0.6	32.8 ± 0.8	1.52 ± 0.05	1.80 ± 0.03	3.91 ± 0.04	
SL21	36.9 ± 1.6	38.2 ± 0.7	1.73 ± 0.05	1.68 ± 0.02	3.77 ± 0.02	
SL22	35.5 ± 0.6	36.0 ± 0.6	1.68 ± 0.11	1.71 ± 0.02	3.76 ± 0.04	
SL23	36.0 ± 2.7	37.0 ± 0.7	1.64 ± 0.11	1.66 ± 0.02	3.83 ± 0.06	18.3 ± 0.5
SL24	39.2 ± 0.6	39.2 ± 0.6	1.73 ± 0.03	1.69 ± 0.02	3.79 ± 0.01	
SL25	39.4 ± 0.7	38.2 ± 0.7	1.60 ± 0.05	1.71 ± 0.02	3.86 ± 0.03	
SL26	35.7 ± 1.5	36.0 ± 0.6	1.58 ± 0.06	1.71 ± 0.02	3.82 ± 0.04	
SL27	36.9 ± 0.7	37.5 ± 0.4	1.51 ± 0.04	1.75 ± 0.01	3.92 ± 0.03	26.7 ± 1.5
SL28	38.3 ± 0.7	39.2 ± 0.5	1.72 ± 0.03	1.70 ± 0.01	3.77 ± 0.02	18.0 ± 1.4
SL29	37.5 ± 0.2	38.0 ± 0.6	1.59 ± 0.03	1.73 ± 0.02	3.82 ± 0.02	
(SL30)						
SL31	38.0 ± 1.4	(33.0 ± 0.9)		(1.92 ± 0.02)	3.77 ± 0.02	
HALK	36.3 ± 0.6	37.0 ± 0.6	1.72 ± 0.02	1.72 ± 0.02	3.73 ± 0.01	
MALK	38.2 ± 0.7	37.5 ± 0.9	1.77 ± 0.03	1.74 ± 0.02	3.79 ± 0.02	
PALK	39.0 ± 0.3	38.2 ± 0.7	1.81 ± 0.05	1.67 ± 0.02	3.85 ± 0.01	23.0 ± 0.4

III.A Inversion example

```
import numpy as np
import os.path as op
from BayHunter import utils
from BayHunter import SynthObs
from BayHunter import Targets
from BayHunter import MCMC_Optimizer
from BayHunter import PlotFromStorage

# ------------------------------------------------------ obs SYNTH DATA
# Load observed data (synthetic test data)
xsw, _ysw = np.loadtxt('rdispph.dat').T
xrf, _yrf = np.loadtxt('prf.dat').T

# Create noise and add to synthetic data
ysw = _ysw + SynthObs.compute_expnoise(_ysw, corr=0, sigma=0.012)
yrf = _yrf + SynthObs.compute_gaussnoise(_yrf, corr=0.92, sigma=0.005)

#  ------------------------------------------------------------ TARGETS
# Assign data to target classes
target1 = Targets.RayleighDispersionPhase(xsw, ysw)
target2 = Targets.PReceiverFunction(xrf, yrf)
target2.moddata.plugin.set_modelparams(gauss=1.0, water=0.01, p=6.4)

# Join the targets
targets = Targets.JointTarget(targets=[target1, target2])

#  ------------------------------------------------------- PARAMETERS
# Define parameters as dictionaries ...
priors = {'vs': (2, 5),
          'layers': (1, 20),
          'vpvs': 1.73,
          'rfnoise_corr': 0.92,
          ...
          }

initparams = {'nchains': 21,
              'iter_burnin': 100000,
              'iter_main': 50000,
              ...
              }

# ... or load from file
initfile = 'config.ini'
priors, initparams = utils.load_params(initfile)

#  ------------------------------------------------- MCMC INVERSION
# Save configfile for baywatch
utils.save_baywatch_config(targets, priors=priors, initparams=initparams)
optimizer = MCMC_Optimizer(targets, initparams=initparams, priors=priors,
                           random_seed=None)
```

```
51
52 # start inversion, activate BayWatch
53 optimizer.mp_inversion(nthreads=8, baywatch=True, dtsend=1)
54
55 #  ------------------------------------------------ SAVING / PLOTTING
56 # Initiate plotting object
57 path = initparams['savepath']
58 cfile = '%s_config.pkl' % initparams['station']
59 configfile = op.join(path, 'data', cfile)
60 obj = PlotFromStorage(configfile)
61
62 # Save posterior distribution to combined files, incl. outlier detection
63 obj.save_final_distribution(maxmodels=100000, dev=0.05)
64
65 # Save a selection of important plots
66 obj.save_plots()
67 obj.merge_pdfs()
```

Eidesstattliche Erklärung

Hiermit versichere ich, dass die vorliegende Dissertation von mir selbstständig und ohne unzulässige Hilfe Dritter verfasst wurde. Ich habe nur die angegebenen Quellen und Hilfsmittel verwendet, und wörtliche und sinngemäße Zitate als solche kenntlich gemacht.

Diese Arbeit hat in gleicher oder ähnlicher Form noch keiner Prüfungsbehörde vorgelegen.

Potsdam, November 14, 2019